ESTABLISHING THE OPTIMAL CONDITIONS FOR ROTATING ARM EROSION TESTING, MATERIALS CHARACTERISATION AND COMPUTATIONAL MODELLING OF WIND TURBINE BLADE RAIN EROSION

PhD Thesis - Cameron Mackie

Supervisor - Professor David Nash

June 2020

Department of Mechanical and Aerospace Engineering
University of Strathclyde
75 Montrose St. Glasgow
G1 1XJ

This thesis is the result of the author's original research. It has been composed by the author and has not been previously submitted for examination which has led to the award of a degree.

11/06/20

Abstract

Leading edge erosion is a growing issue within the wind industry; impacting upon blade performance and efficiency. Even with the wide range of research being conducted, there are currently no apparent foolproof material solutions for the issue. The research presented here looks to develop a better understanding of lead edge erosion: firstly through the development and characterisation of an erosion test rig; then by conducting a range of parametric studies, both numerically (finite element) and experimentally, to explore the key factors and damage mechanisms associated with leading edge erosion. This work shows the importance of characterising a test rig before starting any experimental tests, through this work specifically the most optimal operating conditions can be established. Consistent results are key to transferring knowledge from the test rig to real-world applications, and this repeatability can only be reached with proper understanding of the operating conditions and aerodynamics of an erosion test rig. Reliable results were achieved at rotational speeds around 1100 and 1200rpm rather than the fastest rotational speeds, speeds greater than 1200rpm resulted in an increase in droplet breakup and less repeatable results. The development of modelling techniques alongside experimental testing allows for the physics associated with droplet impacts to be fully explored. Sub-surface imagery, through XCT scans, showed that any defects near the surface of a sample can lead to stress concentrations at the damaged area. The XCT imagery also showed that voids near the composite interface did not affect the erosion initiation or location. Subsequent modelling work also revealed that stress concentrations were the main differing factor between undamaged and damaged samples undergoing erosion, rather than a change in the peak stresses. The peak compressive and shear stresses remained similar regardless of the state of the sample, however, the stress waves became concentrated centrally, around the damaged area, once erosion had initiated. An investigation of a variety of different samples showed that currently industry struggles to find a balance between performance and consistency. Mass loss curves were established for each of the different materials tested, with the affect of number of impacts and kinetic energy also explored. Different failure mechanisms were observed: delamination causing severe damage and brittle failure most common amongst samples. Interesting work is being undertaken where coatings are optimised for certain operating conditions; showing that there is an understanding of the failure mechanisms present, though the level of understanding has not reached the stage where a significant improvement in blade lifetime can be achieved. Future work and research development aimed at further understanding the issues of blade leading edge erosion are also identified, discussed and recommendations given.

Acknowledgments

I would firstly like to give thanks to my academic supervisor Professor David Nash for his guidance, support and encouragement throughout my PhD studies. David has been a mentor as much as a supervisor and has presented me with the support and opportunity to develop and grow my expertise throughout my time as a PhD student. I would also like to thank my industrial supervisor Dr Kirsten Dyer from ORE Catapult who part funded the studentship, for her support knowledge provided throughout my PhD. Her input was always insightful and she has provide direction throughout my PhD.

I was fortunate enough to have fantastic input and support from the Energy Technology Centre. I do not want to single anyone out in particular as every single person who works there was lovely to be around and provided assistance and support throughout my time there.

I also extend thanks to fellow PhD student Grant Leishman, for his assistance in lots of different areas throughout my PhD, without his contribution much of this work wouldn't be possible.

I would like to thank everyone who helped read over sections of my PhD and correct my terrible writing, David Nash, Christine, Ali, Jake and my parents. I would especially like to thank my long suffering parents, their encouraging/nagging drove me forwards. I wouldn't be who I am today without them.

Last, but by no means least, I would like to thank Christine for all her love and support throughout the years, she provided the perfect balance between study breaks and downtime, and a forceful prod in the right direction. Without her I'm not sure this would all have been possible.

Contents

Nomenclature

c	Speed of Sound
c_d	Dilatational Velocity
c_L	Speed of Sound in the Liquid
c_R	Rayleigh Wave Velocity
c_S	Speed of Sound in the Solid
COV	Coefficient of Variation
CZM	Cohesive Zone Modelling
$DNVGL$	Det Norske Veritas - Germanischer Lloyd
d_d	Droplet Diameter
DTV	Damage Threshold Velocity
FEA	Finite Element Analysis
G	Shear Modulus
h_S	Thickness of the Specimen
I	Rain Intensity
k	Bulk Modulus
K_{IC}	Fracture Toughness of the Target Material
LEP	Leading Edge Protection
$LRTM$	Light Resin Transfer Moulding
P	Waterhammer Pressure
$PJET$	Pulsating Jet Erosion Test

R	Radius of Droplet
r_0	Minimum Radius that Cracks occur at
SR_a	Arithmetic Mean Roughness
SR_Z	Maximum Height Roughness
SPH	Smoothed Particles Hydrodynamics
V	Velocity of the impact
XCT	X-ray Computed Tomography
λ	Number of Raindrops per Unit Volume
ρ	Density of the Water
τ	Duration of High Pressure from Droplet Impact

List of Figures

List of Tables

1 Introduction

1.1 Wind Energy Development

Wind power has been utilised for centuries to mill grain and pump water however recently wind power is being employed to generate electricity. In the 1940's the first wind turbine was operated during World War II [25] providing electricity to local networks. The growth of wind turbines has continued from there with an increasing demand for sustainable energy sources leading to a rapid increase in the global installed wind capacity. The UK has committed to reducing it's carbon emissions with the EU's 2020 plan [26] and the UK's government has set it's own plans for 2030 [27]. The main energy source used to achieve these targets is wind power, with China, USA and Europe all increasing their installed capacity.

The global installed wind capacity has been increasing year on year since the turn of the millennium as can be seen in Figure 1.

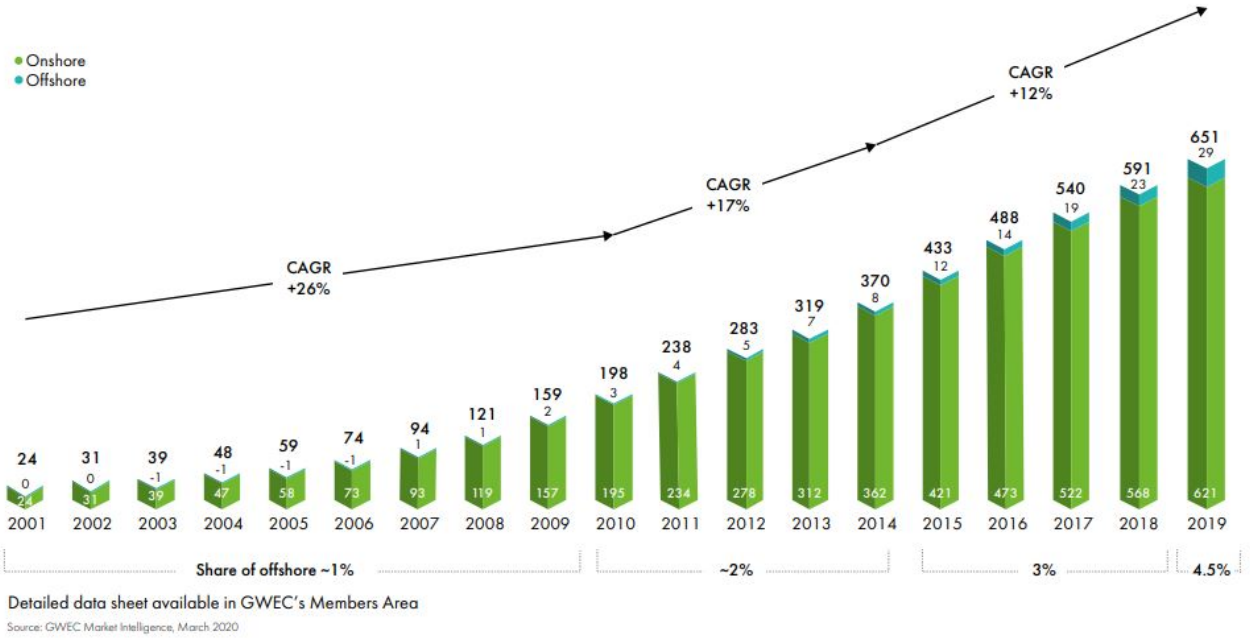

Figure 1: Global Cumulative Installed Wind Capacity 2001-2019 [1]

The installed capacity is increasing exponentially, as can be seen in Figure 1 there is a trend towards the annual installed capacity increasing each year. For a long time Europe has been the leader in wind power production but recently in the last 5-10 years Asia has seen a massive growth with countries such as China installing around 10 GW of new capacity every six months

[28]. While developed countries have a history of harnessing wind power and provide the majority of the global installed capacity it is the developing countries, particularly China and India, have quickly increased their wind capacity from a minimal capacity at the turn of the century to two of the biggest producers in the world. Developing countries are investing more in wind power [29], as their countries grow economically they will continue to spend more on wind turbines thus leading to a rapid increase in the global capacity.

Figure 2: Global Annual Installed Wind Capacity 2001-2019 [1]

Figure 2 shows how in the last 10 years the capacity installed each year has increased drastically and is continuing on an upward trend. This is down to the targets set by the international community around the world. It is also observed that from 2015 onwards there has been a significant increase in the volume of offshore wind capacity.

Northern Europe leads the expansion of offshore wind power with more than 91% of the world's offshore wind power. Other governments: Japan, China, South Korea, Taiwan and the US, have set ambitious targets for the development of offshore wind as many see it as crucial to achieve the targets they have set to reduce fossil fuels [30]. By 2030 the UK plans to increases it's installed capacity from 10GW to 40GW and many see offshore wind as the future of wind power as it currently represents one of the most stable renewable energy resources [31].

There has been a development in the wind turbine industry to increase the rotor blade diameter. This results in a larger swept area leading to a greater amount of wind energy captured, larger turbines are more cost effective per kW. As can be seen in Figures 3 and 4, the rotor diameter

has been increasing in the last 20 years.

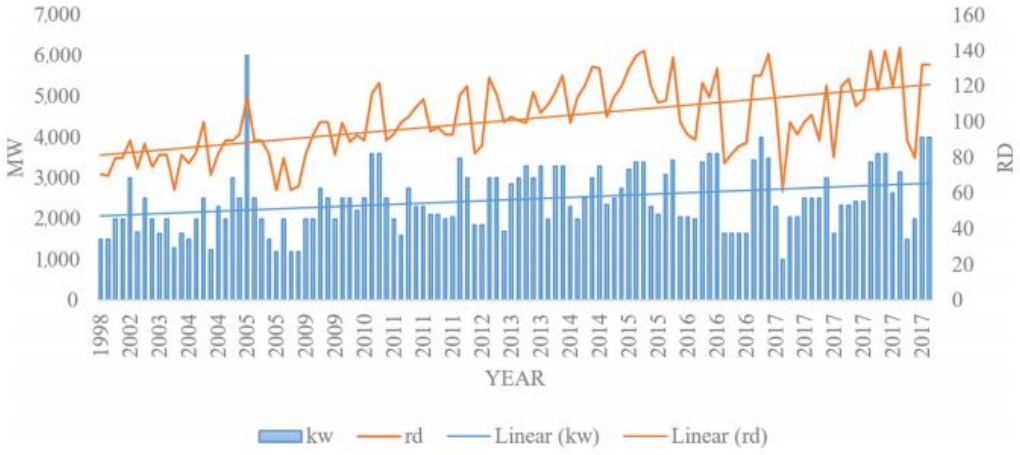

Figure 3: Development of onshore rotor diameter and nameplate capacity [2]

Figure 4: Development of offshore rotor diameter and nameplate capacity [2]

Figures 3 and 4 show the diameter and nameplate capacity of wind turbines installed each year. Multiple different turbine designs can be installed in the same year, hence the same year having multiple entries. The offshore development shows that in the last 20 years the diameter, and therefore the capacity, has doubled. This is a significantly greater increase that shown with onshore wind turbines. According to wind experts, the trend will continue as there is a limited number of developable high-quality wind resource sites requiring energy production at each site to be maximised [32]. Currently the technology is still able to facilitate this level of growth but in the future this will plateau, though this does not look likely in the near future.

The factors above are leading to erosion of wind turbine blades becoming a prominent issue. The number of wind turbines in operation is increasing, of which these turbines are increasing in size and are more likely to be located offshore. The increased diameter is causing the wind turbines to have a greater tip speed which accelerates the erosion process. By locating the wind turbines offshore they are subjected to more severe weather conditions, this again accelerates the erosion process.

1.2 Blade Erosion

Erosion is the process of the gradual destruction or diminution of something, typically due to wind, water or other natural agents. As discussed above erosion has recently become a prominent issue in the wind turbine industry, however the subject of rain erosion has been investigated for decades, by a number of researchers culminating with seminal work by Springer in the 1970's [33] who proposed a lifetime prediction model for rain erosion. Springer examined the basic physics involved in water droplet impact and discussed the forces, water hammer pressures and stresses present. He introduced concepts such as the incubation period, the time elapsed before the mass loss of the coating becomes appreciable, and the likelihood that fatigue plays an important role in the lifetime of a material experiencing erosion.

When a droplet impacts there are three main stress waves acting on the material. Firstly the compressive stress wave, which is a common occurrence for any object impacting another object. A shear wave is also present which is expected for an three dimensional system, as the impact is unlikely to impact along an axis. Finally there is the Rayleigh wave, the Rayleigh wave is an acoustic stress wave that acts along the surface of a material. The Rayleigh wave occurs in analysis of droplet impacts as the water droplet will collapse on impact causing the water to push outwards along the surface, thus a Rayleigh wave.

This covers the physics occuring with a single droplet impact, the problem occurs with multiple impacts and more importantly determining how many impacts will lead to erosion. The exact mechanism associated with erosion is unclear whether it is a fatigue-like problem where progressive loading leads to a growth in cracks or whether the impacts lead to a depression in the material causing stress concentrations and later on cracks. One of the aims of this work is to try and better understand the mechanisms involved as this will lead to a clearer picture on how erosion occurs and reducing erosion.

The problem becomes more complex when there are layers present in a leading edge protection system. Leading edge protection system is a term used a lot in industry to describe the combination of glass fibre composite, filler, coating or any extra layers such as a topcoat, all used to protect the leading edge of wind turbine blades. The introduction of layers present the added difficulty of stress waves transmitting through differing layers and reflecting off layers. This relationship can be determined by understanding the interface between the layers but there is not a large amount of work being done in this area.

This work is being undertaken to compare different blade coatings and set-ups through exper-

imental set work, time is being spent to increase the understanding of the problem. Different coatings can lead to various damage mechanisms acting on them, leading to either more brittle or ductile behaviour. This means coatings are being optimised for a certain set of experimental conditions and then failing a lot earlier than expected if a variable, such as speed, is changed. This lack of understanding even in an experimental setup makes it extremely difficult to produce leading edge protection for functioning wind turbines as there is a large variability of factors involved.

The main issue with erosion of wind turbines is the difficulty in repairing blades especially on off-shore turbines due to the lack of accessibility and the difficulty to repair blades onsite resulting in a large expenditure for companies. There is a challenge in finding and training people to perform maintenance on turbine blades in situ, combined with the difficult working environment this incurs a great cost and results in a large amount of downtime.

The downtime associated with erosion is the other major concern associated with erosion. It is estimated that erosion can translate to up to a power loss of 9% [34] and that is just due to the change in aerodynamics not including the loss in production due to downtime. There are no figures for how the downtime will affect the annual energy production as there are many external factors affecting this (location of wind turbine, erosion rate, repair method). The final point to consider is how erosion affects the lifetime, wind turbines should last 20-25 years [35]. Erosion will reduce this lifetime and affect the operational lifetime due to the repairs, however OEMs are not releasing data on how erosion affects the lifetime. The author has spoken to different employees though who anecdotally report significant erosion present on the leading edge in as little as 3-5 years for offshore wind turbines.

1.3 Experimental Blade Erosion Testing

The work contained in this thesis aims to provide a rigorous, precise and scientific approach to the experimental testing of progressively eroded samples. Since the 1940's there has been research carried out investigating the impact of precipitation. It started with the aerospace industry and has involved various techniques, from sleds being driven through rain tunnels to ice balls being fired at stationary samples.

The set-up used commonly today is the whirling arm method, where a sample is rotated at high speeds in a circular path with needles dropping water onto the sample as it rotates. This method is preferable as it allows multiple impacts to occur quickly and in a small space. The main drawback is that a large rotating arm can produce a large aerodynamic wake which in a small space can provide turbulent air for the droplets to flow through. This problem can be improved by spending time characterising the rig set up to reduce the affects of the aerodynamic wake. One solution to the problem is to only have one arm rotating rather than multiple as this obviously decreases turbulent air as there is only one body passing through the air rather than multiple.

Characterisation of the test rig is important for other reasons rather than just decreasing the aerodynamic wake. Knowing the parameters of the test rig is crucial to understanding the mechanisms taking place when erosion occurs. These parameters include droplet diameter, number of impacts and location of impacts. Understanding exactly how these parameters influence the erosion rate is a major part of the testing process and was something that considerable time was spent on, with this work.

Throughout the world there are lots of different experimental set ups, each set up will have slightly different parameters. This leads to confusion as it is very difficult to compare differing erosion rates on differing set ups. Recently Det Norske Veritas Germanischer Lloyd (DNV GL), an international accredited registrar and classification society, have produced a standard [36] to try and specify the parameters required for an erosion test. This has provided a step in the right direction. The parameters quoted in the DNV GL standard will be examined in Section 3.

Once this characterisation work has been carried out samples can then be eroded. Aluminium samples, can be used to examine the effects of speed on the erosion rate and check the repeatability of the test rig, but do not include the layers present in leading edge protection systems (LEPs). Different LEPs can be tested to determine the erosion rate as well as the erosion mech-

anism, whether it's ductile or brittle failure. Regardless of the material tested the experiment aims to establish the end of the incubation period. After this point the sample starts to change drastically and the erosion rate is a lot more difficult to predict. Experiments have been carried out to compare different materials, determining the end of incubation period for each and also how the speed affects the mass loss curve.

1.4 Finite Element Modelling of Blade Erosion

Modelling is a mathematical representation of a physical phenomenon, there are different types of modelling work being carried out, when looking at erosion. Firstly there is the lifetime prediction model, first developed by Springer [33] it aims to predict the lifetime of a given sample. Secondly there are more traditional finite element analysis (FEA) models that can model a small number of impacts. FEA is a well respected technique and there is good evidence in the literature that it can be used to model the erosion impact event, usually though explicit dynamic approaches.

The FEA models the water droplet impacting a sample. Modelling water and the process of the droplet collapsing upon impact cannot be achieved with standard FEA approaches, due to dividing the droplet into discrete elements would not allow them to separate and display lateral jetting, therefore the droplet was modelled by using smoothed particle hydrodynamics (SPH). The SPH model the water as lots of small nodes that are loosely connected but still allowed to flow and deviate from the other nodes, much like water. The SPH-FEA model allows a parameter study to be conducted, by changing criteria such as the droplet diameter and thickness of coating, to determine what the peak stress on impact is. By examining a parameter such as the coating thickness, this can analyse at which thickness the improvements plateau or looking at the droplet diameter to determine the difference larger droplets associated with heavier rain have on the coating.

FEA models also allow a small number of impacts to be modelled together, to determine the build up stress over multiple impacts, through this the recovery time can be examined between impacts. Another area modelling can help with is the study of the effect of existing damage on erosion, pits can be introduced on the surface or inbetween layers to see if this leads to any stress concentrations.

Modelling a single impact can take between 15 mins and 24 hours (for a Intel i.7 CPU @ 2.20GHz, 16GB RAM) depending on the complexity of the model and the number of layers

present. Therefore due to the computing time associated with this type of modelling it is not possible to model enough droplet impacts to see the stress levels build up to a high enough value to start failure. Therefore snapshots of the erosion process will be modelled, Figure 49 shows the mass loss curve and five different stages along the curve will be chosen. Models will be made for each of these stages incorporating the formation pits as well as any changes in material properties. Using work carried out from the experimental test rig accurate data can be provided on how the geometry and material properties change throughout the erosion process and then this is used to model the different stages of erosion.

By combining the experimental setup and modelling facilities a greater understanding of erosion can be achieved. Each area can help influence the work carried out in the other, which provides a more effective way of capturing and investigating the erosion phenomenon.

1.5 Problem Statement

The aim of this work is to build and develop an experimental test rig, the test rig will be characterised by investigating the main parameters that affect the erosion process. This characterisation work provides a more scientific and research orientated set-up than is currently available elsewhere. This leads onto a variety of different materials being eroded to determine what affect their mass loss curves and incubation periods. This develops an understanding of the two different areas of a mass loss curve, the initiation of erosion (incubation period) and the erosion rate once mass loss curves. To investigate the initiation of erosion further, sub-surface material properties and defects are explored using DMA and XCT apparatus. Modelling work can provide an insight into both: the stress waves arising from an impact; and different parameters affecting the erosion process. These parameter studies provide insight to help further develop the experimental test rig. The stress waves due to an impact can also be examined to determine the changes along the mass loss curve and how that might affect the erosion rate.

2 Literature Review

2.1 Erosion Phenomena

The erosion mechanism on blades in wind was initially studied to reduce the wear on helicopter blades, Woods [3] introduced the diagram of impact and linked that with Rayleigh waves. His diagram of the stress waves present after an impact, see Figure 5, has been referenced in many papers since and has been used as the basis for much research.

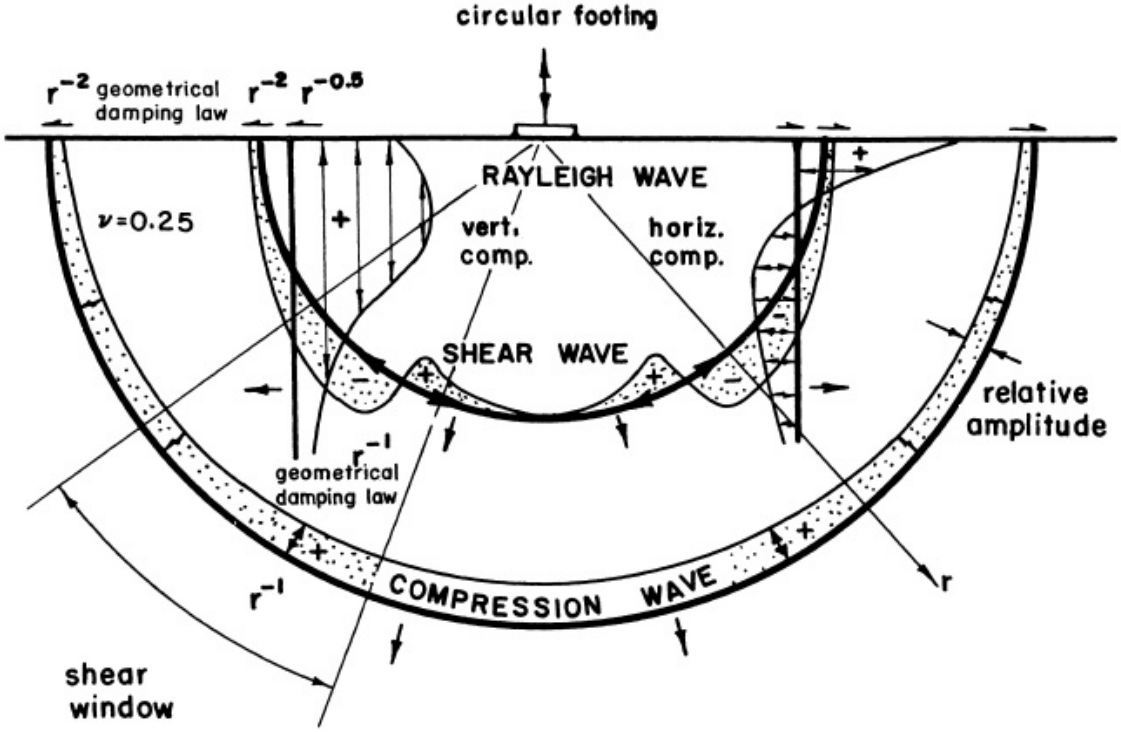

Figure 5: Distribution of Displacement Waves from a Circular Footing on a Homogenous, Isotropic, Elastic Half Space [3]

Bowden and Field [37] at a similar time were also investigating how stress waves propagated through a material. They concluded that there is a sharp peak of compressible behaviour directly after the impact, where the duration depends on the dimensions and impact velocity of the liquid mass, though this pulse only lasts for a few microseconds at most. They used high speed camera work to investigate the development of fractures and the different fracture modes. They concluded that a lot of fractures occurred near the impact location and were initiated by Rayleigh waves at locations where flaws already existed. The work carried out by Bowden and Field is used as a basis throughout research carried out in erosion.

Following on from Woods, Bowden and Field there has been a lot of research carried out by the aviation industry. Gohardani [38] was investigating high speed aero vehicles but his work can still be applied to wind turbines. He initially investigated the weather, looking into the droplet size distribution which takes the shape of a bell curve, with a droplet size of $D \approx 2mm$. Diameters similar to this are used on most experimental test rigs, which has the benefit of consistency between varying methods. Gohardani states the factors that erosive wear depends on: impact velocity, impingement angle, target material and particle characteristics (size, material etc). He also describes what constitutes erosive damage with the four factors being: change in mean volume or depth of pits; an increase in number of cracks and their sizes; loss of optical transmission in aeroplane windows and weight loss of the material.

Springer [33], then introduced the concept of the incubation period and that after the incubation period the erosion rate is constant for a period of time. The definition of the incubation period is the time elapsed before the mass loss of the coating becomes appreciable. This concept of appreciable mass loss seems imprecise but is still a term used today to measure erosion. As shown in Figure 6 he then produced a model to estimate the incubation period and the stage of steady state erosion.

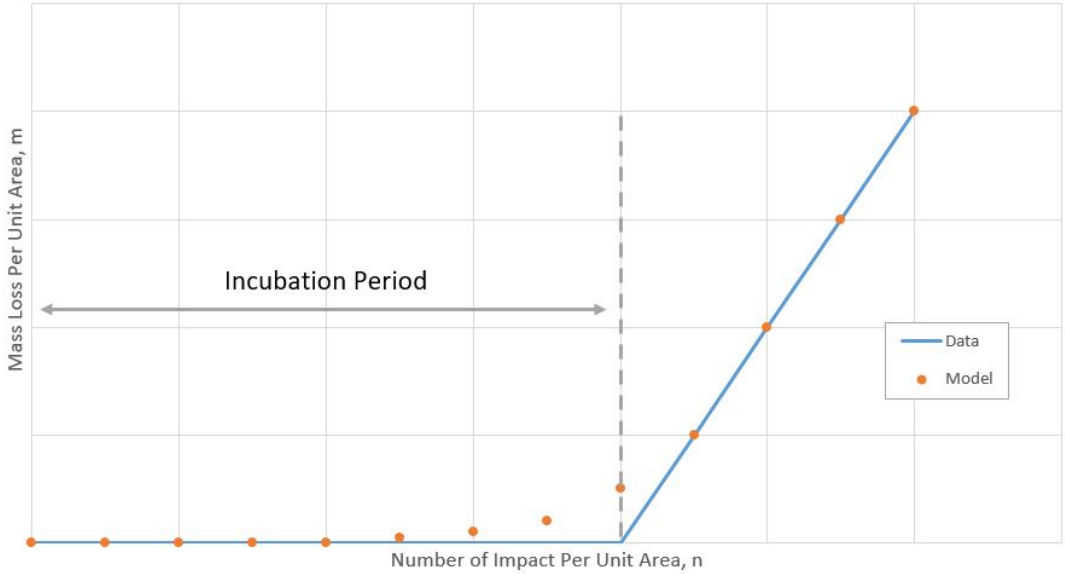

Figure 6: Experimental Results and Solution Model of Mass Loss

Rayleigh waves and the waves present with water droplet impact were examined closely by Slot et al [39], who determined that the application of surface layers or coatings introduced the possibility of the waves reflecting thus increasing stress and strain, this can be overcome by applying coatings of sufficient thickness. Negligible wave reflections develop when $t_S > t_L$, the

calculations for t_S and t_L are as follows:

$$t_L = \frac{2d_d}{c_L}$$

$$t_S = \frac{h_S}{c_S}$$

where d_d = droplet diameter, h_S = thickness of the specimen, c_L = speed of sound of the liquid and c_S = speed of sound of the solid.

Dear and Field [40], carried on similar work and discussed the expression for a waterhammer pressure, the pressure present on impact, where P is the waterhammer pressure, ρ is the density of the water, C is the speed of sound and V is the velocity of the impact.

$$P = \rho C V$$

The accuracy of the pressure can be increased by using the modified waterhammer pressure. This is used when the solid is not rigid, which is the case with the composites used in wind turbine blades. The equation for waterhammer pressure is shown below where V is the impact velocity, ρ is the density, c is the speed of sound and the subscripts l and s reference the liquid and solid bodies respectively.

$$P = \frac{V \rho_l c_l \rho_s c_s}{\rho_l c_l + \rho_s c_s}$$

This more accurately represents the initial pressure on the material. This pressure leads to an initial regime of compressible behaviour where the contact periphery initially expands supersonically, with respect to the shock wave. The contact radius r for the compressible stage is given by:

$$r = \frac{RV}{C}$$

where R is the radius of the droplet in the contact area. V is the velocity and C is the speed of sound. The duration of this high pressure τ is given by:

$$\tau = \frac{3RV}{2C^2}$$

where this high pressure stage is ended by lateral jetting and the pressures fall to those typical of incompressible flow.

Liu et al [41], states that most fractures occur within a small distance of the impact. They then calculate the minimum radius that ring cracks or cracks occur in:

$$r_0 = \frac{2h}{[(c_d/c_R)^2]^{1/2}}$$

where h is the thickness of the target, c_d and c_R are the dilatational velocity and Rayleigh wave velocity respectively. The Rayleigh wave velocity is calculated as:

$$c_R = \sqrt{\frac{G}{\rho}}$$

where G is the shear modulus ρ is the density of the target material. Finally they stated the damage threshold velocity, which is the lowest impact velocity at which damage could occur. A theoretical expression is given by:

$$DTV = 1.41\Big(\frac{K_{IC}^2 c_R}{\rho^2 c_w^2 d}\Big)^{1/3}$$

where K_{IC} is the fracture toughness of the target material. C_w is the compressive wave velocity, which relates to the material properties.

$$c_w = \sqrt{\frac{k + \frac{4}{3}G}{\rho}}$$

G and k are the shear modulus and bulk modulus of the target material, respectively.

All of these above equations help to predict damage, gaining a better understanding of the erosion process. They also show how the thickness of the coating affects the erosion and the speed of waves after impact. These are all useful in understanding single impacts but now multiple impacts will be explored as this is one of the main area that requires research.

Slot et al [39], discusses the likelihood than the erosion mechanism is related to fatigue, as when the impact of one water droplet occurs there is primarily compressive surface stresses present with a thin band of tensile stress (the diameter of this band is dependent on droplet diameter and velocity). For thick ductile coatings (as seen on wind turbine blades) a single water droplet cannot initiate failure regardless of droplet diameter or velocity, however the repeated large strains present may lead to erosion through a fatigue mechanism. For brittle materials the impact will initiate short stress peaks that last for less than a micro second, this band of tensile stresses causes failure even with a few droplets assuming the droplet velocity is relatively high.

Slot et al, suggests that fatigue is the dominant wear mechanism which is primarily combated by reducing water pressure. This is achieved by: (1) applying a surface of low modulus elasticity; (2) applying a coating with adjustable compressive stresses or adjustable hardness and (3) preventing impurities and defects in the layer. They also speculate that it might be repeated high strains that lead to fatigue initiation rather than high stress.

This failure mechanism was schematically presented, by Lee et al [4], in Figure 7 it can be seen that the coating was initially deformed by the water droplet. As more impacts struck the surface the depression increased the curvature leading to a concentration of tensile stresses at the bend. This causes cracks to form and the circumferential fracture of the coating. From this you can see that cumulative impacts lead to erosive wear. This shows how any existing defects will have a large effect on the erosion rate, as they will introduce stress concentrations a lot earlier into the lifetime of the blade.

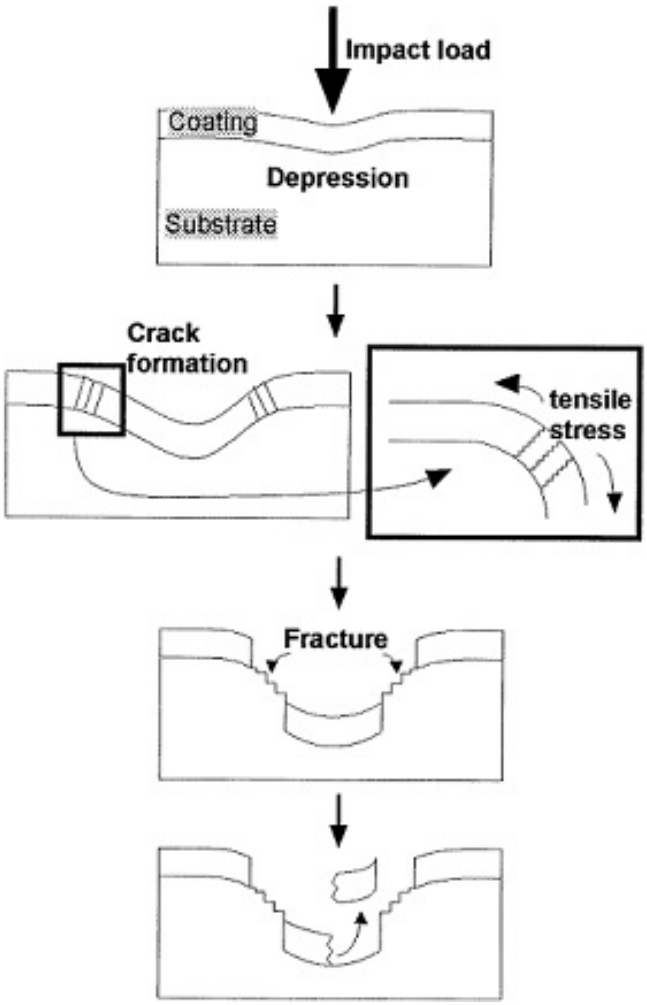

Figure 7: Liquid Impact Erosion Mechanism of TiN Coating [4]

Zhang et al [42], also hypothesised the presence of defects and how they accelerate the erosion process. They spent time experimenting with different impact velocities and frequencies to determine there is a critical velocity and frequency at which erosion occurs. These are useful to determine as ideally wind turbines would operate below these speeds, or improve material properties to increase this minimum value. Another solution is for operators to pause operations during the bad storms that lead to erosion thus increasing the lifetime drastically.

Valaker [5], proposes that it is the inclusion of defects that is then escalated by lateral jetting. As shown in Figure 8 the lateral jetting will target the miniscule defects on the surface, tearing out new sections of material. This escalates the problem and shows that the initial mass loss/defect provides the trigger to rapidly increase the erosion rate.

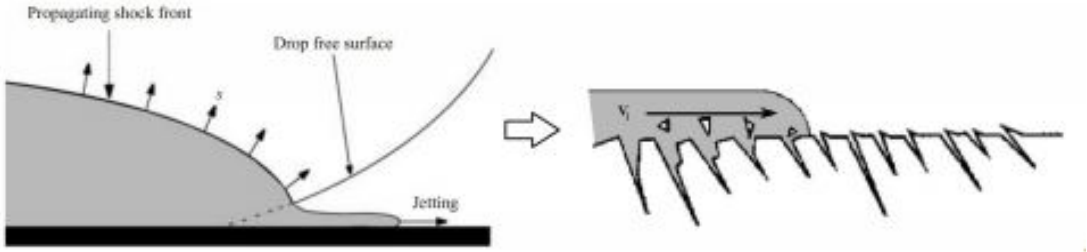

Figure 8: Propagation of lateral jetting [5]

Gaudern [6] tried to approximate what the different stages of erosion looked like, using inspection reports and photographs taken onsite to try and assign a representative diameter, depth and location of pits for each erosion stage. When comparing to photographs the patterns represent defining features of the erosion but are more uniform and do not capture the features, roughness and randomness of the erosion process. These patterns can be used in both experimental and modelling work, experimentally they can be used to quantify erosion samples and when modelling the patterns could be introduced to model damage.

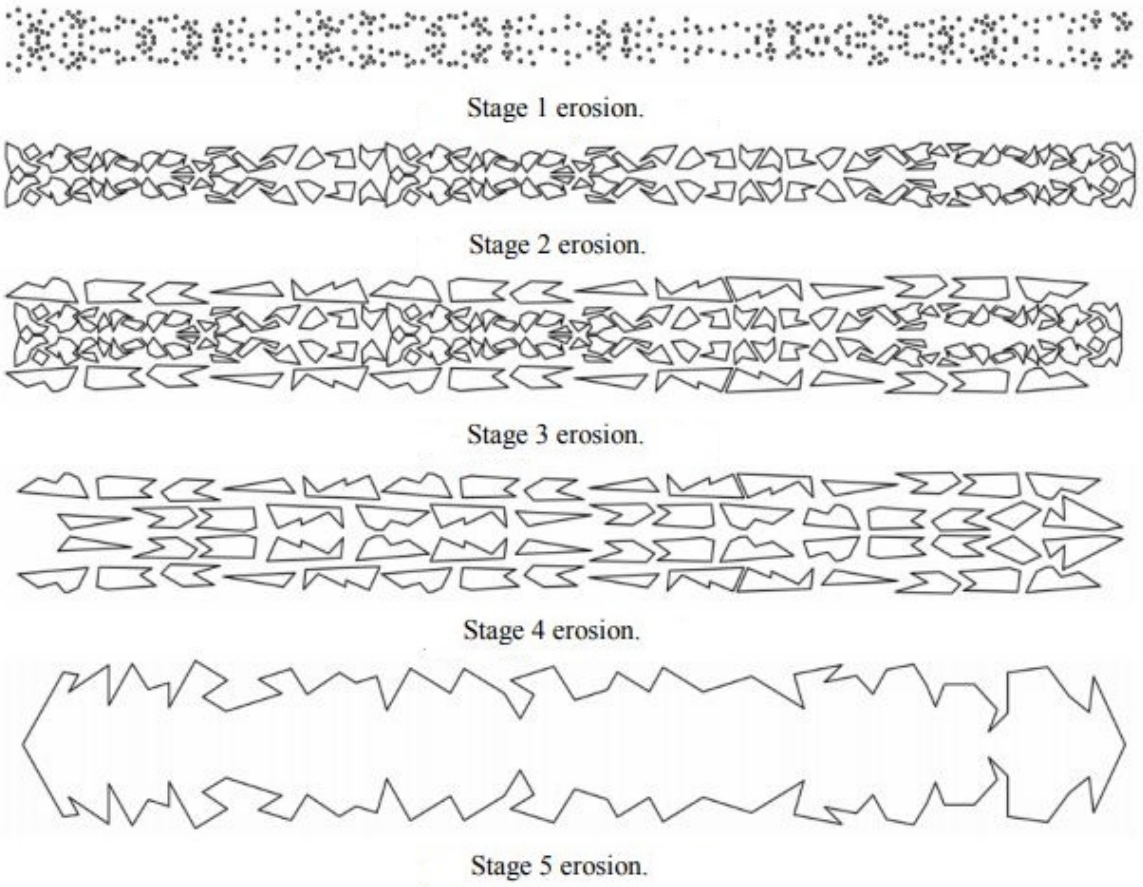

Figure 9: Stages of Erosion Throughout Lifetime [6]

Zhang [42] also states that the seawater aerosols present on offshore wind turbine conditions increases the erosion rate drastically and that in offshore conditions the erosion rate is double. Zhang also discovered that impact velocity and frequency are the two most influential parameters in erosion rate and as with other research also found that defects play an important role in the erosion mechanism.

Another weather condition that leads to erosion is hail, Keegan [43] discusses the impact hail has on erosion. The peak stress associated with hail impact is vastly greater than water impact, however this is achieved with hailstone diameters of up to 15mm (much larger than rain). These are extremely rare, even in the extreme conditions offshore. While there is potential for a short hail storm to cause damage, the infrequency of hail points towards rain still being the main contributor to erosion though it could be wise to pause operations during heavy hail storms.

MacDonald [14] conducted more extensive analysis of hail impact, ranging the hailstone diameter from 5mm to 20mm. Finding that the hailstone diameter had a large effect on the damage noted, the diameters of 15mm and 20mm both recorded severe damage after only a small number of impacts. The work carried out by MacDonald does indicate that hailstone impact could potentially be a cause of erosion initiation even if for the majority of the blade's lifetime it is subjected to rain impacts.

2.2 Blade/Coating Materials

There are a variety of different coatings being tested for their erosion performance. Different manufactures will favour ductile or brittle coatings to provide the best result, but manufacturers are secretive about the chemical composition. This limits the research carried out into coatings as it is unclear what the current coatings are made of.

Chen et al [44], provides an overview of protection technology. The protective layer can be achieved by a gelcoat or surface coating. Wind turbine blades are composed of fibre reinforced epoxy resin matrix composites therefore an in mould gelcoat are often applied in the current market. The polyurethane gelcoat is preferred to the epoxy gelcoat due to its advantages in flexibility and weatherability.

Chen states that coatings for wind turbines should have the following properties: (1) weatherability; (2) high and low temperature flexibility; (3) rain erosion resistance; (4) acid and alkali corrosion resistance; (5) wear resistance; (6) excellent adhesion; (7) salt spray resistance and

moist heat resistance; (8) anti-icing; (9) good construction performance; (10) low environmental pollution. From this list the complexity of designing a coating can be seen, coatings that would preform best in erosion resistance might not necessarily perform well in some of the other categories. This range of criteria adds more complexity to the problem and makes a solution for erosion resistance more challenging.

Valaker et al [5], mentions the current trend towards polyurethane used as leading edge protection, both as coatings and tape. Valaker explores four different coatings: an unspecified industry coating; one pure polyurethane, one reinforced with particles internally developed and one reinforced with silicon carbide particles. When examining the coatings for adhesion, surface finish and material loss the industry coating performs much worse on the adhesion and material loss experiments. The coating reinforced with silicon carbide particles actually performs the best and shows no signs of erosion when the industry coating has already failed. They also observed "craters" in the coatings, most likely linked to air bubbles being trapped in the coating during application. These bubble could be initiation points for erosion and cause the initial defects that trigger the material loss as mentioned in Section 2.1.

O'Carroll [7] tested a range of six polymetric materials: Poly methyl methacrylate (PMMA), Polycarbonate (PC), Polyethylene (PE), Polyethylen eterephthalate (PET) and Polypropylene (PP). The PMMA was tested in two configurations cast (PMMA-C) and extruded (PMMA-E). While these materials do not provide a comprehensive list of materials it does provide a range of materials to test.

When eroding the samples there is a clear difference between half the samples. PMMA-C, PMMA-E and PET perform much worse, as shown in Figure 10. PC, PE and PP performed much better and O'Carroll observed that even with the difference in time both groups seemed to fail due to brittle fracture. The damage begins with thin shallow strips of material being ripped from the surface. These groves then provide a discontinuity for the lateral jetting to attack, over time these groves lengthen due to lateral jetting.

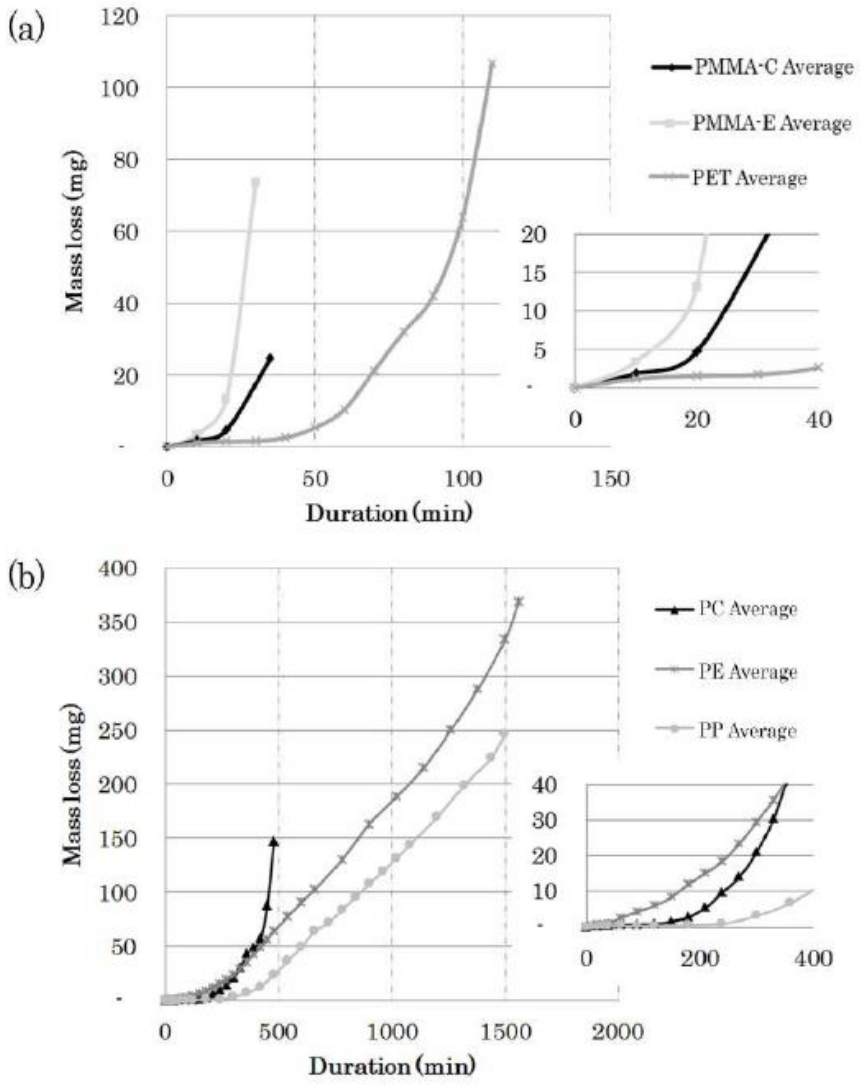

Figure 10: Cumulative mass loss of (a) PMMA-C, PMMA-E and PET and (b) PC, PE and PP. Cut-out images show early stages of testing in greater detail [7]

Armada [8], explored homogenously distributing reinforcing into coatings to increase the erosion resistance. The particles were nanosized ceramic particulate additives. The samples were tested at a low speed of 14.3m/s and the mass loss was measured to determine erosion rates. All tests were run for 2 hours. Figure 11 shows that there is a strong correlation with the amount of reinforced particles and mass loss. The reference material is unaltered and then the percentages show what percentage of the coatings is reinforced particles.

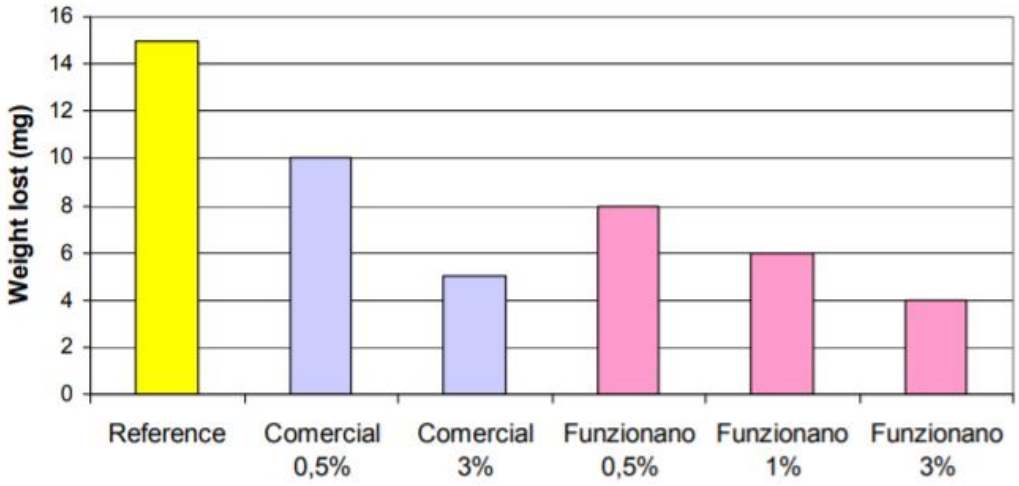

Figure 11: Mass loss of different modified coatings [8]

2.3 Manufacturing, Repairs and Detection

A resin infusion moulding process is used to manufacture wind turbine blades. Figure 12 shows a schematic of the process, the blade is sealed inside a vacuum bag and then the resin is sucked through the reinforced fibres to create the high quality composite material.

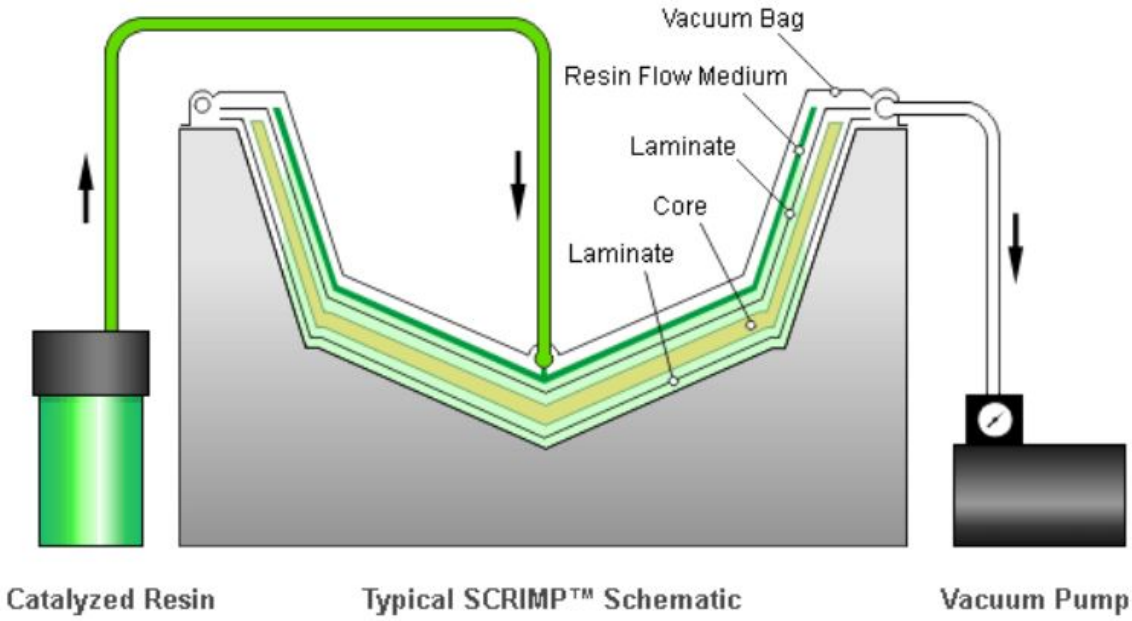

Figure 12: Resin Infusion Molding Process [9]

Nolet [9], discusses that materials are the primary driver in system performance both in terms of the fibres and the resins. The fibres can be made from glass, carbon or others, such as aramids. Glass fibres are preferred due to the low cost to high specific strength. There is a similar situation with the resin, with epoxies, vinyl/polyesteres or "toughened resins" all being possible resins but epoxies are the primary resin used in most European blade manufacturing but vinyl-esters are attracting interest from blade designers looking for alternative options.

They discussed how there is room for innovative design but this is a multidisciplinary exercise that requires coordination between aero engineers, material engineers, structural engineers and manufacturing engineers. With this multitude of areas to consider it is not surprising that erosion is not the main consideration when discussing material selection.

Finally Nolet [9] discusses the manufacturing process and the move in industry towards automation. Currently the automation is limited to cutting the ply and finishing (including coating application). The next steps are in the form of fibre placement, prepreg or dry fabric

robotoic application as well as the use of carbon fibre. These improvements will make the blades cheaper to manufacture and stronger while hopefully limiting defects in the blades due to manufacturing. This reduction in defects should help the blades withstand erosion.

Hutchinson [45] discusses light resin transfer moulding (LRTM) as an alternative to the typical vacuum infusion. The LRTM offers the possibility of better tooling and part thickness control than traditional vacuum infusion. The main benefits of the LRTM is the potential for 3% cost saving and reduction in infusion time of 25%. These benefits will not improve the erosion resistance but LRTM also offers a decrease in void formation (0.9%) which could be crucial. The defects or voids in manufacturing are often considered to be the catalyst for erosion, by reducing these it is possible to see an increase in performance.

Marsh [10], discusses the challenge of repairing wind turbine. Around 10 years ago wind farm operators did not inspect turbines frequently enough but are realising the importance now, even surface roughness can spoil the aerodynamic efficiency of the blades. Therefore the process of repairing quickly is crucial, for offshore turbines this can be especially difficult as you can need 2 to 3 days of clear weather, this makes it critical that the repair process is as good as possible.

For small repairs a mono-component resin acts as a filler and adhesive, it is ejected from a cartridge gun and then UV light is used to cure from a portable UV lamp. With this method the curing process only lasts minutes. For repairing more significant damage, when the laminate needs attention, prepregs are used. The repair patches are made up of stacked prepreg plys and can be relatively thick. Again the repair is cured by a UV lamp and a 5mm thick section can be cured by the lamp in a few minutes. For repairs deeper than 5mm, the cure is achieved by building up and curing the repair laminate in multiples of 5mm.

In Figure 13 the stages of this repair process are shown, the pictures were taken from a demonstration by Gurit UK. The area that is still unclear is how effective the repair methods are at protecting the blade. The current trend is towards quicker application times and isn't as concerned with how long these repairs will last.

Figure 13: Stages of blade repair [10]

The detection of damage is crucial as filling small pits is quicker and will maintain the structural integrity better than larger repairs. Ciang et all [46] are exploring various damage detection methods the first method explored is acoustic emission events detection method. Processes such as cracking, deformation, delamination and others, all produce localised transient changes in stored elastic energy with a broad spectral content. Tests revealed an audible cracking sound and identified the damage area of failure, the system can also detect much weaker signals in the non-audible domain. Another test method is that of thermal imaging. Thermal imaging detects subsurface defects by relating the difference in thermal diffusivity between the undamaged blade and damaged blade. Ultrasonics is a well established method for investigating the inner structures of solid objects. In the simplest arrangement, the transmitter and receiver are placed on opposite surfaces of the material but when investigating on field turbines a different technique may be applied with a single/receiver transducer in a pulse-echo mode. Ultrasound probing will typically reveal delaminations oriented perpendicular to the direction of the sound wave propagation [47].

Modal-based approaches are the most common damage detection methods principally because they are simple to implement. Structures can be excited by ambient energy and embedded strain gauges, piezoceramics or accelerometers can be used to monitor the structural dynamic responses. The basic idea behind this technology is that the modal parameters (frequencies, mode shapes and modal damping) are functions of the physical properties of the structure. Therefore changes in the physical properties, such as reductions in stiffness resulting from cracks, will cause detectable changes in the modal properties. While these technologies will provide detection, whether they have the deftness to detect the minute changes due to the initiation of erosion is unclear. Some wind farm operators are even attaching these technologies to drones [48], the thermal imaging works especially well as it does not require contact with the blade.

2.4 Blade Erosion Test Rigs

Experimental testing of erosion has been conducted since the 1940's where the main focus was in the aeronautical industry, the leading edge of high speed jets or helicopter rotors. Hurley and Schmitt [49] started looking at rain erosion of samples travelling at Mach speed to use on US military planes. They list all of the previous military tests that have been carried out by the US air force with a range of speeds from 265-1650mph. The limitations of these set ups was the lack of control of the rainfall simulation, which is what the new apparatus designed by Hurley and Schmitt was aiming to improve on. Their main area of improvement was the introduction of control of the pressure head and therefore the flowrate of the water. This same setup has been improved upon but is still broadly the same today [11], Figure 14 shows the set up.

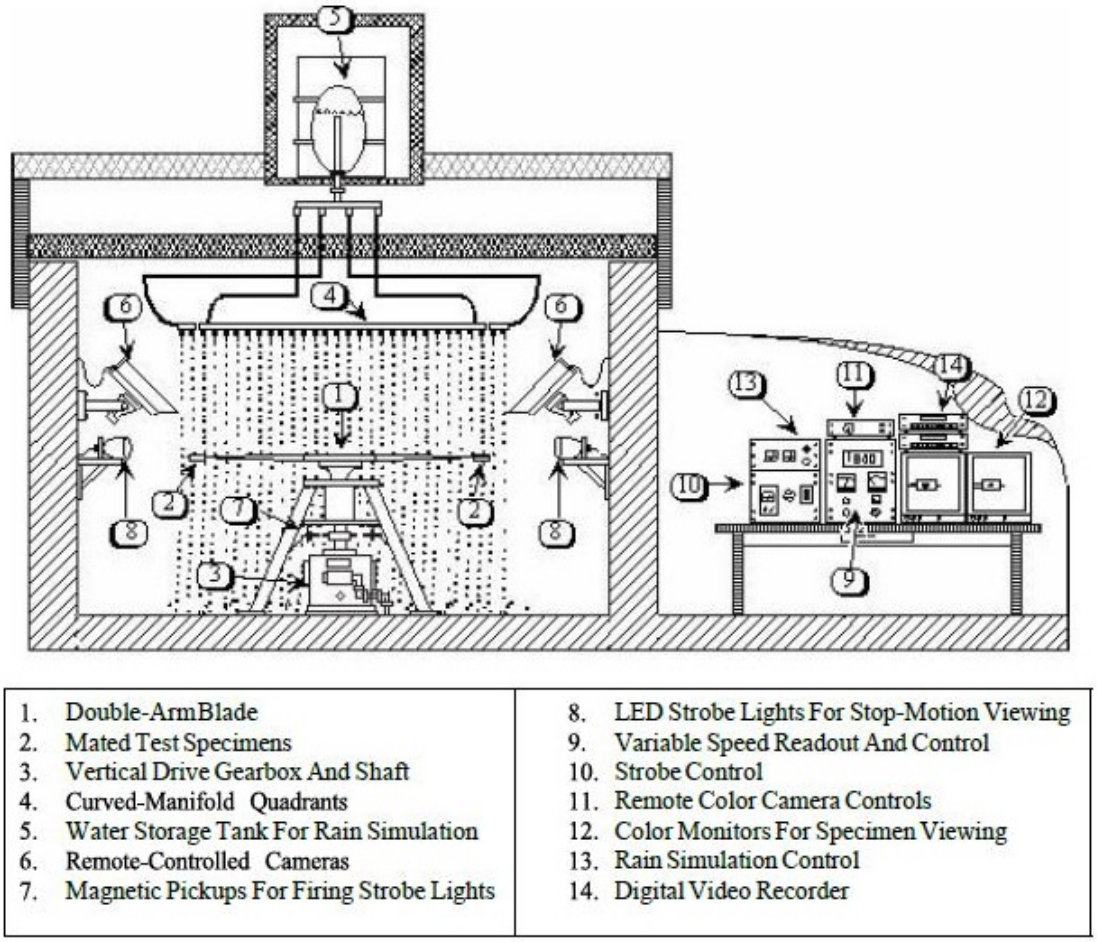

Figure 14: AFRL Rain Erosion Test Apparatus [11]

Adler [12], describes the three main methods for testing water droplet impacts which are rotating arms, rocket sleds and ballistic ranges. Rocket sleds can be used to propel an array of test specimens through an extended sprinkler system. These tests are carried out a very high speeds, similar to that of an aerospace vehicle in flight. With proper planning consistent data can be achieved with this method but the area used is vast and the number of impacts in a test is not enough with respect to wind turbines and is more associated with the speeds of aircraft.

Ballistic ranges have a specimen mounted to the front end of a sabot which is propelled down the range to impact a falling water droplet. Work on the GRCI Hydrometeor Facility carries out this work, Figure 15 shows the set-up where the speciman moves from left to right.

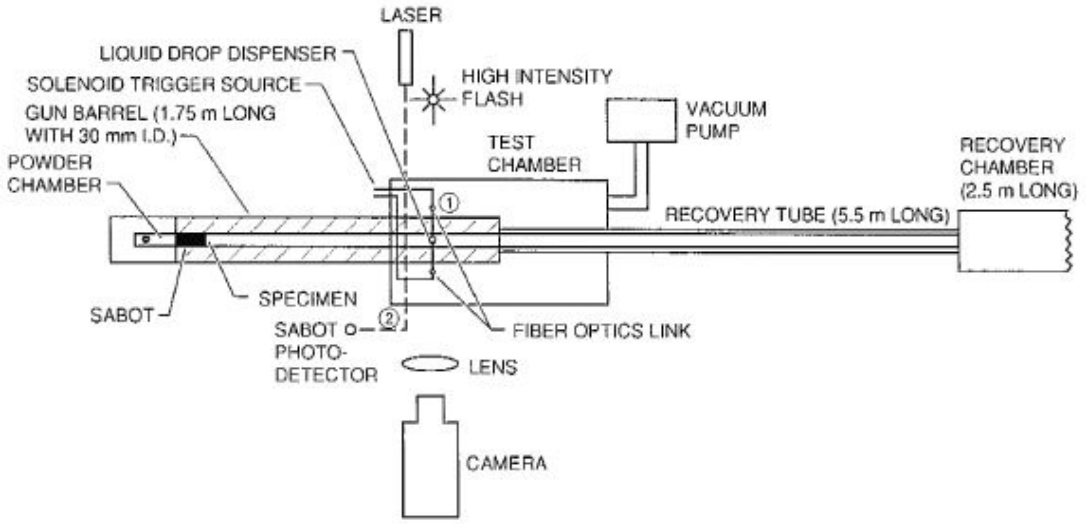

Figure 15: Schematic of GRCI Setup [12]

This set up allow speeds of up to 1000m/s and diameters of 1.5 to 5mm to be achieved and the droplets remain spherical even at these speeds. This is due to the complex set up with the experiments being conducted in a helium atmosphere and lasers setup to trigger the exact moment to release droplets to achieve impact. Finally the laser also triggers a camera which records photograph of the impact. This apparatus is clearly designed to be incredibly accurate and controlled over a range of speeds, diameters and even impact angles, however it will not provide the number of impacts to be useful for wind turbine simulations.

Adler also discusses impacts that do not involve dropping water but rather propelled onto the sample, the main method being waterjet impact. Waterjet impacts provide a simplier method of water collisions onto a surface and the use of waterjets is based on the fact that the loading a droplet imparts on a surface is due to the pressure between the two surfaces. The pressure is sustained until lateral jetting takes place, the lateral jetting occurs relatively early in the impact so that essentially only a portion of the droplet contributes to imparting an impulse to the surface. The remainder of the droplet is less effective in producing any damage.

Water droplets cannot be propelled at a target as they break up and lose their spherical nature even at low velocities. If the jet of water has a rounded front it should, according to the mechanics of liquid impact, impart the same loading as a droplet with the same diameter. Tobin et al [13] compared the erosion rates of water drop impacts and waterjet impacts on a rotating arm setup. Tobin did break the jet into waterjet segments to create more similarities to the droplet impact, known as Pulsating Jet Erosion Test (PJET). The method for achieving this is to rotate a disc with a whole in it, thus cutting the jet at a predetermined rate, as shown

in Figure 16.

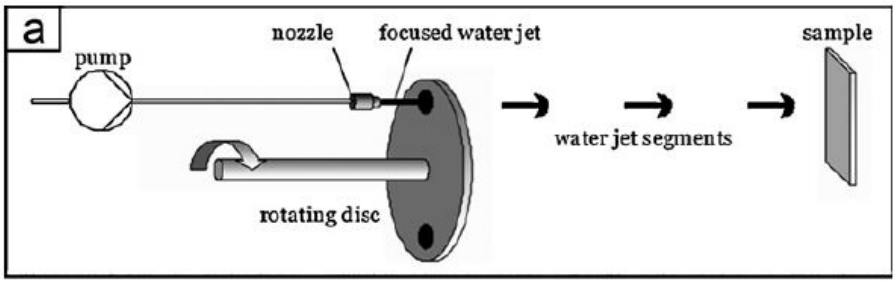

Figure 16: Schematic of Waterjet Segments Apparatus [13]

The comparison of the two methods was achieved by looking at the surface roughness, using an optical microscope and SEM images. The rotating arm was operating at 177m/s with a rainfall rate of 25.4 mm/hr. The PJET was operated with a jet velocity of 180m/s and a disk frequency of 20Hz. Both setups had droplet diameters of 2mm and the same samples were used on both. Values of arithmetic mean roughness (SR_a) and maximum height roughness (SR_z) were used to analyse the results, as shown in Figure 17. The ratio or correlation factor is roughly 1000 impacts (PJET) to 15 min test duration (rotating arm). The impact site on the PJET sample is approximately 1mm whereas the impact site for the rotating arm is 500 times larger. Looking at Figure 17 it can be seen, for SR_a values below $2\mu m$ that the correlation is very clear, this stage of testing is in the incubation period or shortly afterwards.

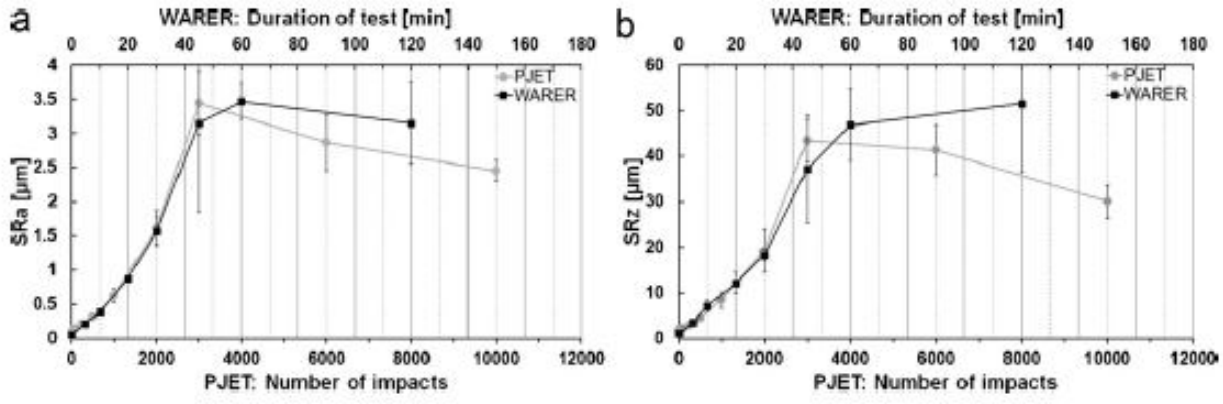

Figure 17: Comparison of roughness values taken from both sets of results: (a) SR_a, (b) SR_z [13]

A similar method to waterjets can also being used for erosion test but instead using ice rather than water. MacDonald [14], impinged hailstones on composite samples. Hailstones were fired vertically at the samples, as displayed in Figure 18. Variable speeds could be achieved by

altering the pressure level in the pressure vessel. Hailstones of different sizes could be fired through the use of detachable barrels of differing diameters.

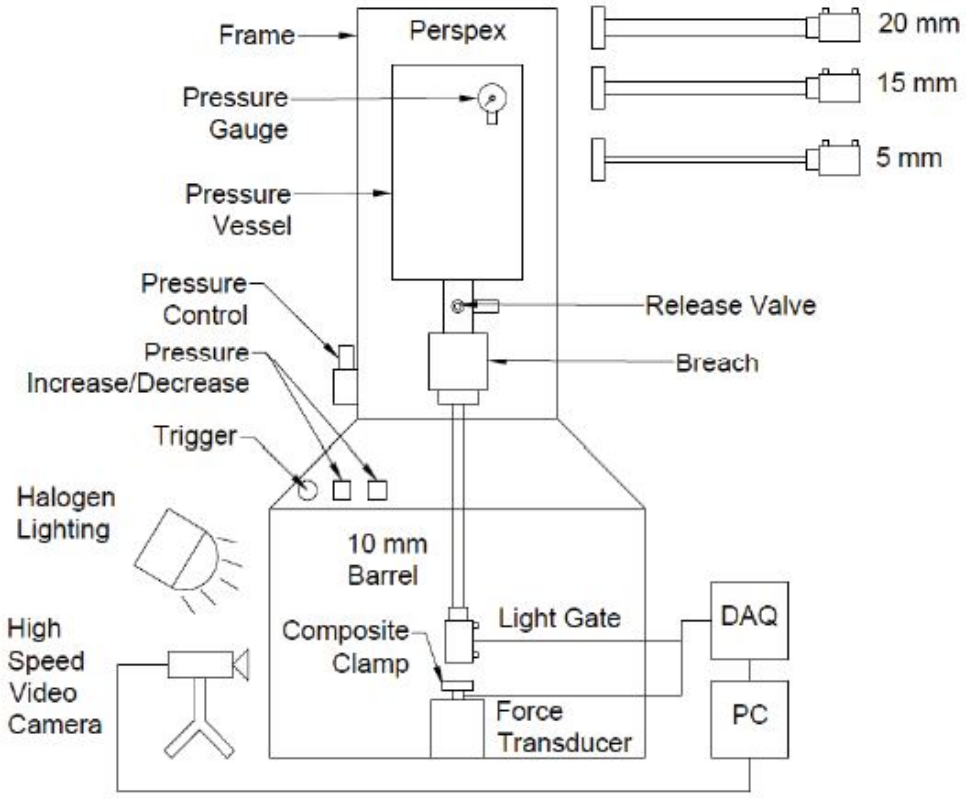

Figure 18: Schematic of hailstone impact experimental rig [14]

Spherical moulds were manufactured to create simulated hail at differing diameters of 5mm, 10mm, 15mm and 20mm. The main flaw with the work was that at the smaller diameters, the most prevalent according to weather statistics, the hailstone would start to melt in the process of the experiment, therefore the integrity of the hail is questioned. As mentioned in Section 2.1, there is a belief that hail impact has minimal cause for erosion and rain impacts are causing the most damage.

This has lead to the majority of experimental apparatus being rotating arms with water droplets falling on them. This set-up is the most space economic, lower cost and repeatable of any mentioned before. Currently R&D A/S manufactures erosion test rigs in Europe [50], they have sold their "rain erosion tester" to various companies including ORE Catapult and LM Wind. This set-up has three arms rotating at the same time, 600 needles, can alter the test specimen from 63-173 m/s and has a drop height of 200-400mm. They also have high ability of control over the rainfall, the diameter can be between 2-3.5mm, the rain intensity 29-53mm/hr

and the water temperature between 4-30°C.

There are a multitude of different rotating arm test rigs available, Saab [51] have a single arm rig that can reach extremely high speeds but only has 6 rain generators, a rain generator looks similar to a hypodermic needle. The University of Limerick [7], also possess their own erosion test rig, it is a contained structure with 2mm droplets and a rainfall rate of 25mm/hr. This test procedure is based upon the ASTM G73-10 [52].

The test rig owned by the Energy Technology Centre and located at East Kilbride, near Glasgow, is where this author carried out the majority of his experimental work. The experimental rig has a singular rotating arm and uses a small aerofoil sample which is being impacted by 72 needles spaced 5°apart. It is noted that, all of the rotating arm apparatus have similar designs but variations in parameters, as shown in Table 1.

	R&D A/S	**Saab**	**Uni of Limerick**	**ETC**	**Uni of Dayton**
Number of arms	3	1	1	1	2
Number of needles	600	6	36	72	96
Tip Speed Velocity (m/s)	63-173	0-300	0-178	0-150	44-290
Droplet Diameter (mm)	2-3.5	1.2, 1.6 or 2	2	2.3	1.8-2.2
Rainfall Rate	29-53 mm/hr	1.41-35 mm/hr	25 mm/hr	0-6 L/hr	6 to 7 drops/s
Water Temperature (°C)	4-30	-	18	19	-
Drop Height (mm)	200-400	-	-	50-350	-
Sample Shape	Aerofoil	Circular	Circular	Aerofoil	-
Sample Size	420mm width	50mm diameter	-	60mm width	-

Table 1: Parameters of Various Rotating Arm Test Rigs

The main differences in the parameters are: the number of needles on the R&D A/S rig is far greater but they also have longer samples; the Saab rig lacks needles but does have a greater maximum speed which is probably because their rig is not aimed at exclusively wind turbine blade testing. The range of parameters is down to there being two standards, ASTM G73-10 [52] and DNV GL-RP-0171 [36].

The ASTM G73-10 standard focuses on calibration and achieving the incubation time for materials, it also specifies that a minimum of 3 samples should be tested for each variation. There is no mention on standardising the rainfall conditions, be that droplet diameter, rainfall rate or number of impacts. The standard is not aimed at solely wind turbine blades, as it does discuss testing window materials used on aircraft. This has led the wind turbine industry to favour the DNV-GL Standard.

The DNV-GL Standard is based on the R&D A/S set-up as the standard suggests parameters which are similar to the R&D A/S set-up. The drop height of 200mm is stated in the standard, even though it does state the aerodynamic effects are not understood. The aerodynamic effects will be explored in Section 3.3

2.5 Computational Modelling of the Erosion Phenonmenon

Modelling of erosion can be split into two different categories, individual droplet impacts or lifetime simulations. FEA software can be used to model individual, or a small number of, impacts from this peak stresses, recovery time and lots of other factors can be explored. Whereas lifetime simulations will focus purely on determining the lifetime of the sample and how certain material properties affect this. Both have pros and cons and this work focuses on the individual droplet impacts as there is not the material data available to accurately predict the lifetime of samples. Adler [15] started modelling a single water droplet impact for use in the aerospace industry, he used DYNA3D (finite element software which is the predecessor to LSDYNA). Adler used elements to model the solid material as well as the water droplet, as shown in Figure 19.

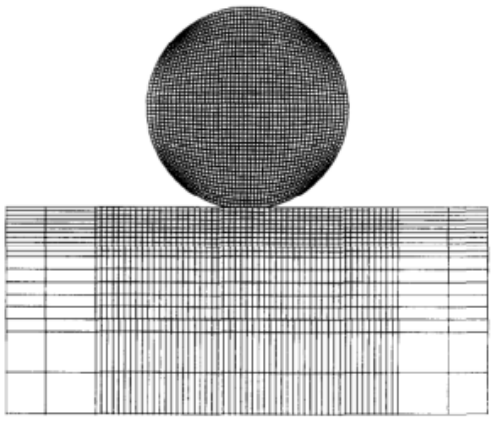

Figure 19: Finite element mesh for waterdrop [15]

Adler's modelling approach captures the shockwave propagation through the droplet and target material, as well as the lateral jetting phenomena. However once lateral jetting occurs the squeezing and stretching of the elements can be observed in the droplet geometry, as shown in Figure 20. Adler [15] states that the simulations remain stable onto later stages of the lateral jetting, but there is a loss of accuracy and an increase in computing time.

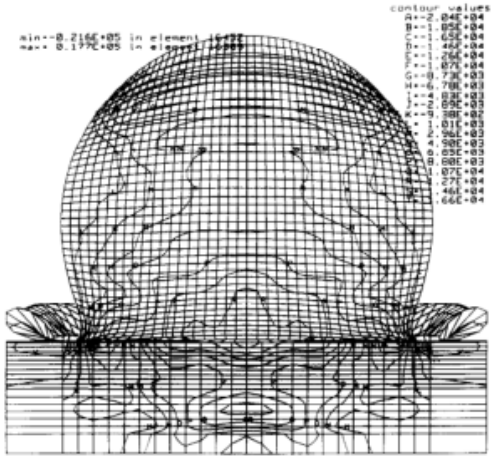

Figure 20: Finite element mesh as lateral jetting occurs [15]

DeBotton [16], also carried out some early work on high velocity water droplet impacts on targets with thin protective layers. DeBotton developed a model that describes the pressure field at the liquid solid interface during the impact of a water droplet on a solid target. The work determines the axial deflections, axial stress, radial stress, tangential stress and shear stress, radial stress as shown in Figure 21. From this analysis you can characterise the failure mechanisms by linking the experimental results with data available from literature. Rayleigh surface waves; variation of the loading with the impact velocity; the pattern of the damage and the in-plane shear stresses are all elements that affect erosion. This shows how modelling work can be used to help lead other aspects of the research.

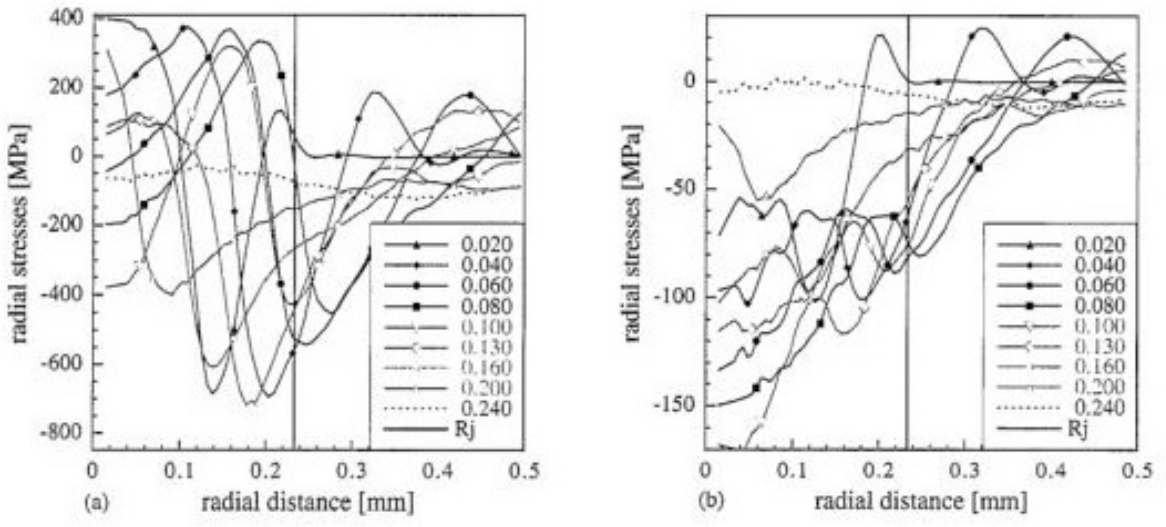

Figure 21: Distribution of radial stress at the diamond side (a) and silicon side (b) during impact of a 2mm droplet as functions of the distance from the centre of the impact site [16].

Keegan et al [17], carried out a lot of novel work on the modelling droplet impacts. He also used LS-DYNA, a finite element software which has specialist capabilities for the modelling of high speed impacts. They introduced the idea of using smoothed particle hydrodynamics (SPH), to model the water after exploring the advantages of an Eulerian approach and SPH. SPH was initially developed to simulate nonaxisymmetric phenomena in astrophysics [53] but recently has found applications in modelling water [54].

SPH does not use elements, per se, rather the droplet is split into nodes. Keegan [17] preferred this to an eulerian method because when the droplet spreads, as shown in Figure 22, SPH remain stable as the nodes are not stretched.

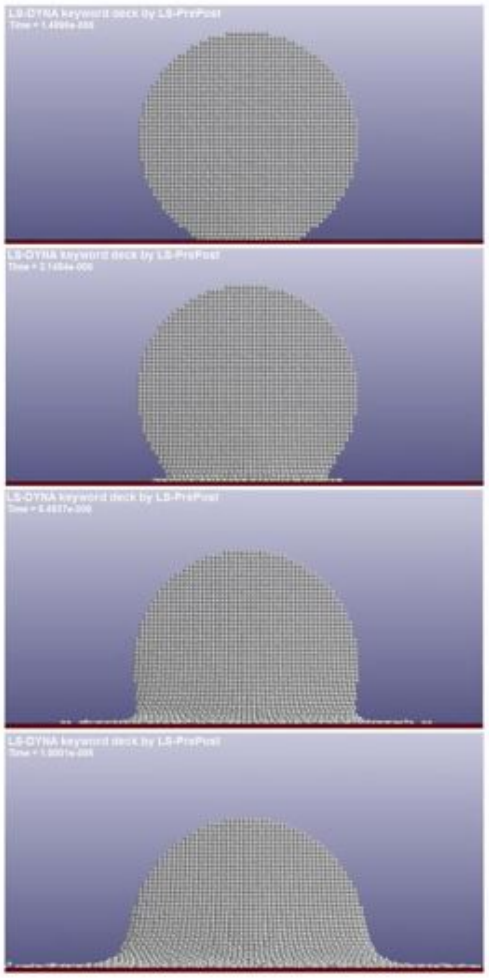

Figure 22: Droplet spreading behaviour using SPH method [17]

Mabrouki et al [55], used Lagrangian and Eulerian coupling to model the droplet impact using finite elements. The Eulerian/Lagrangian coupling is based on momentum conservation, hence the lagrangian structure has the ability to move though the Eulerian grid. Coupling is achieved by constrained methods defined between special points of the Lagrangian structure (slave group) and Eulerian nodes (master group). Mabrouki does not compare this coupled method to other ways of modelling the droplet impact so it is difficult to tell if the results differ drastically however this method does add a layer of complexity while also still having the same instability issues present when meshing the lateral jetting of the droplet. Therefore the SPH method conducted by Keegan, seems to provide a simpler and more reliable approach.

Li et al [18,56], uses one dimensional modelling to provide insight into the water erosion problem. In Figure 23, the impact velocity was varied along with the impact load duration, this was modelled with rectangular pulses rather than a water droplet. The tensile and compressive

stress changes with varying impact velocities, there is also wavy trend with the tensile stress. This wavy trend shows there is a worst-case for impact duration, where the peak stress is around 50% greater than the regular tensile stress. While this model is only one dimensional it does provide useful data that could be explored further either experimentally or numerically.

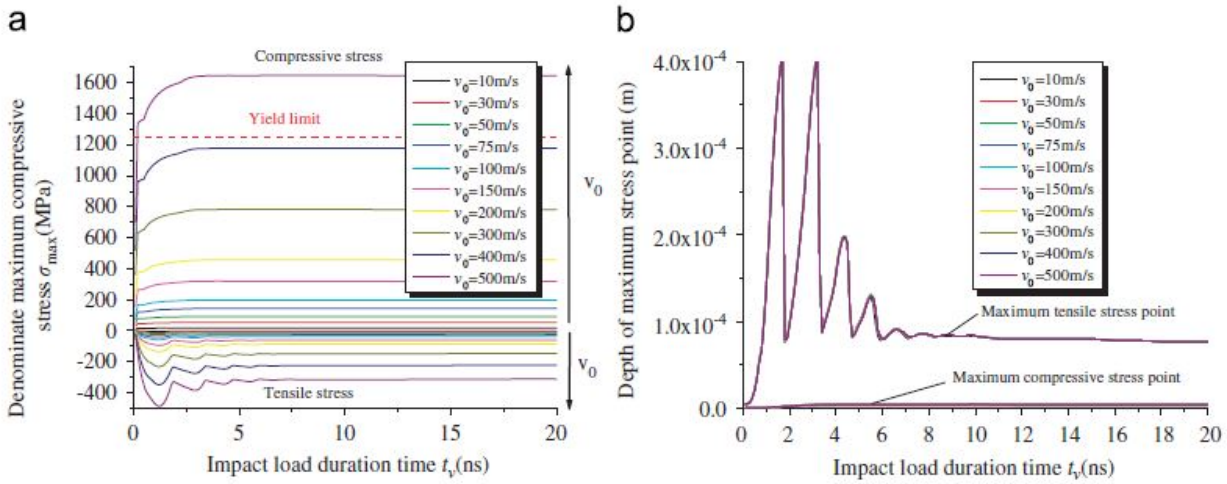

Figure 23: (a) The dimensional maximum compressive and tensile stresses and (b) The position of maximum stress point [18]

Amirzadeh et al [19, 20], looked at rain data to develop three-dimensional fields of raindrops consistent with the rainfall history. They developed a model to predict an expected number of raindrops per unit volume λ, can be calculated as a function of rain intensity. This relationship is shown in Figure 24 where the model is similar to the equation below. λ has a power relationship with I as follows:

$$\lambda = 48.88 I^{0.15}$$

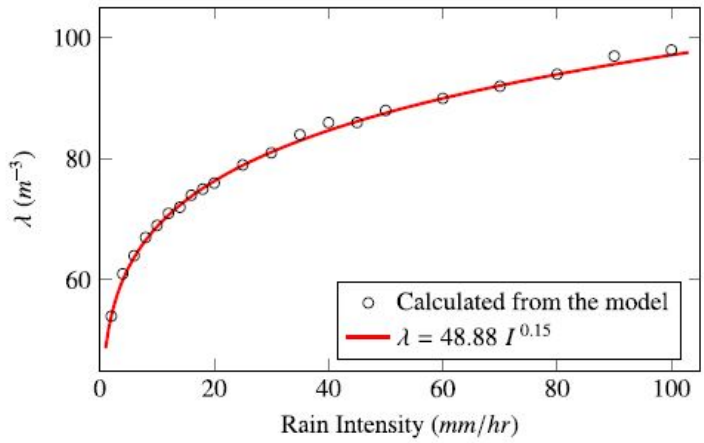

Figure 24: Expected number of raindrops per m^3 vs rain intensity [19]

This provides an accurate rain model with can be used when simulating erosion. This work helps relate numerical modelling to real world applications. Amirzadeh [20] explored the peak stress over time and the evolution of the impact pressure profile. These provide tools to help validate future modelling work.

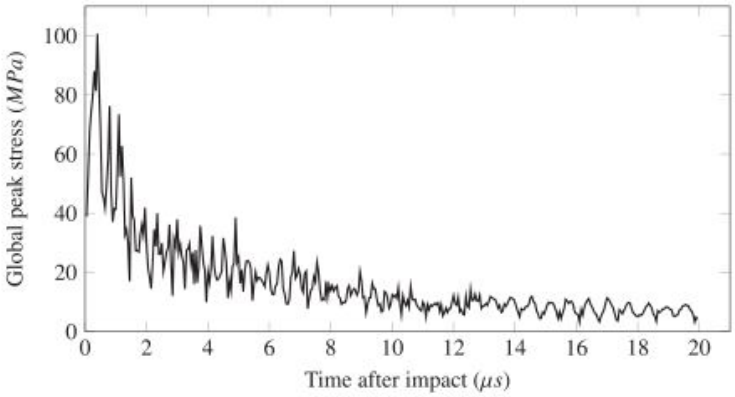

Figure 25: Global peak stress in the coating layer vs time [20]

Cortes et al [57], researched the layers involved in wind turbine coatings and how the stress waves transmit and reflect. Reflections can cause the new wave to now advance into the coating at a different amplitude depending on the acoustic impedances of the coating and substrate. Delamination is one of the main mechanisms for failure and to successfully model erosion, multilayered systems have to be modelled. Cortes introduces the concept of Cohesive Zone Modelling (CZM) to model the interface between the different layers. CZM is a 1D model that includes the impedances of the different layers, the parameters for CZM are defined by means

of both physical pull-off and peeling tests.

Mishnaevsky et al [21], developed a micromechanical model of coatings to take into account their micro and nanoscale structures. From these models it has been demonstrated particles and voids in the protective coatings have critical effect on the crack initiation in the coatings under multiple impact loading. Figure 26 shows the stress concentrations around the voids especially near the area where lateral jetting occurs.

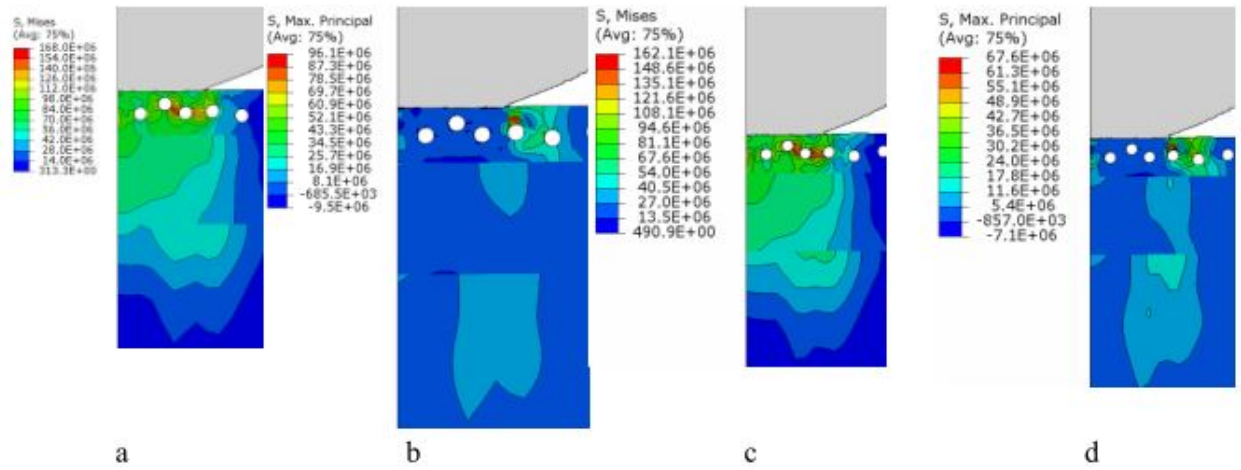

Figure 26: Stress distribution in coating with voids. (a) Elastic, Von Mises, (b) Elastic, Max Principal Stress, (c) Viscoelastic, Von Mises, (d) Viscoelastic, Max Principal Stress [21]

The work by Cortes and Mishnaevsky shows that the problem is more complicated than just a liquid impacting a solid. The potential manufacturing defects have a large effect on erosion performance. Certain coatings also experience delamination as the main failure mechanism but currently not many models consider this. These models also increase the level of complexity, which is crucial for long term development and to reach modelling that simulates experimental or field results.

2.6 Summary

The first research of erosion was conducted by the aviation industry, with the focus on the physics of the problem. This led to the theory of droplets causing compressive, shear and Rayleigh waves, these stress waves combined with the lateral jetting that occurs, when the droplet collapses. There has also been work studying damaged samples and how phenomena such as lateral jetting can accelerate mass loss. However, there does not seem to be much

research on the physics that results in the initial mass loss, as this is the crucial step that changes from the individual impacts and the stress involved to the acceleration of mass loss. This is also observed with the work conducted by Springer where he introduced the concept of the incubation period and the steady state mass loss afterwards. Whereas, to fully understand the erosion process, the time between these two stages is most important, the time right at the end of the incubation period. The state of the sample at the initiation of mass loss is crucial and something this work looks to explore.

In more recent times, the development of coating has occurred with polyeurathane being a common choice of material. The results for coatings has been mixed with the majority of samples failing due to brittle failure. To test the samples many unique test rigs have been developed. There is a wide range of test rigs available, DNV-GL and ASTM both have introduced standards to try and standardise the development of these test rigs, though there are shortcomings with both standards. By DNV-GL basing a standard off a particular test rig design, it is limiting the development of other, potentially beneficial designs. The DNV-GL standard, and no other research, has put enough importance on the aerodynamics involved in an erosion test rig. The main difference between real-world turbines and experimental test rigs is the faster rotational speeds of the experimental set-ups, and the aerodynamic differences due to this will greatly affect the droplets trajectories and impacts.

Modelling is another tool used to investigate erosion, with lots of research into different areas though most are adopting a finite element approach to investigate the stress waves present with the droplet impact. SPH offers a novel and accurate method for modelling droplets that was not available when initial modelling of droplet impacts began. The research conducted by Cortes into Cohesive Zone Modelling provides an interesting method for modelling the interface between layers. However, this is currently a one dimensional method and as shown with the work by Woods and Springer on the physics of a droplet impact, the shear stress is an important parameter to study which one dimensional analysis cannot adequately represent. Currently the modelling work of droplet impacts is still at early stages and greater detail needs to be applied to models to allow the results to be useful to either experimental set-ups or real-world applications.

3 Characterisation of a Whirling Arm Erosion Test Rig

3.1 Test Rig Specification

The present work uses an experimental test rig to explore different damage mechanisms with different coatings and rotational speeds. This provides a better understanding of the overall rig erosion rate. The Whirling Arm Erosion test rig was designed, built and characterised at the Energy Technology Centre (ETC) in East Kilbride, UK. ETC has been investigating erosion since 2015 supported by the Offshore Renewable Energy (ORE) Catapult but prior to this work no test rig had been built. Only a few needles were operational with experiments being carried out on a small scale, investigating needle gauges and the aerodynamics of the arm.

ETC has experimented with both a single and double arm arrangement, to analyse whether the aerodynamic wake with two arms would be more detrimental than the benefit of two samples. It was discovered that using just one arm produced more repeatable results, as the aerodynamic wake produced by an arm influences the air for approximately two thirds of a rotation. Therefore a second arm would induce turbulent air thus making droplet formation and trajectory unpredictable, for these reasons a set up with only one arm was decided as optimal [58]. Next an aerofoil was also attached to the arm in order to decrease the drag which increases the droplets stability allowing the arm to rotate at a faster rotational speed.

Examining different needle gauges, from 19 gauge to 30 gauge, determined which needles provided the most consistent diameter over a variety of pressures, while also providing a diameter similar to the average rain droplet ($\sim$ 2mm). A needle gauge of 27 was found to provide the most accurate droplet diameter over a range of pressures. Another improvement was to include plastic shrouds to protect the droplets while they form on the needle and through work with a high speed camera it has been demonstrated that the plastic shrouds increased the number of droplets forming and in turn the number of droplet impacts. Without the plastic shrouds a lot of premature droplet breakup was observed. Premature breakup causes the droplets to implode, due to turbulent air, and split into lots of tiny droplets. This subsequently adds an element of uncertainty to the results as the tiny droplets cannot be quantified as easily as fully formed droplets. This makes it difficult to accurately quantify fractions of droplets in observations.

The water flowrate is controlled using a pressure head from a water tank on the wall. To increase or decrease the flowrate, water is removed or added to the tank. This process is controlled using an ABB Pressure Sensor which keeps the pressure constant throughout the

experiment. The pressure sensor measures the pressure change due to the changing pressure head then the corresponding pressures is set to the correct head height.

Finally, leg adjustment was added to the ETC rig to allow for varying standoff heights. The standoff height is defined as the distance between the tip of the needle and the centre of the leading edge of the sample. A DNV GL standard was published [36] that stated the minimum standoff height should be 200mm. This was investigated to determine which height caused the least disruption to the droplets. The reason for choosing a distance of 200mm is that it is believed that outside this distance the air is no longer turbulent. Theoretically this means that droplets can form and gain momentum before reaching the turbulent zone thus increasing the chance of the droplet remaining intact and following a straight trajectory. As mentioned previously a test was conducted to investigate if this was true, the results are in Section 3.3.7.

Figure 27: Experimental Set Up of Test Rig at ETC

This previous work has led to the test rig being configured as shown in Figure 27. There is a single rotating arm that can spin up to 1400 rpm, with tip speed of 150 m/s. Table 2 shows the conversion from rotational speed to linear speed. There are 72 needles spaced 5°apart, mounted on a frame that can be adjusted to change the height of the needles and the water pressure is determined by the pressure head on the tank, which is attached to the wall. There is a sample holder that can fit samples of 60mm in length. The needles are attached to a PVC pipe manifold which delivers a 14mm variance in the strike location due to the manufacturing process. The manifold is the ring round the test rig that the water is collected in before being expelled out the needles.

Speed (RPM)	**Speed (m/s)**
700 RPM	75.1 m/s
800 RPM	85.9 m/s
900 RPM	96.6 m/s
1000 RPM	107.3 m/s
1100 RPM	118.1 m/s
1200 RPM	128.8 m/s
1300 RPM	139.5 m/s
1400 RPM	150.3 m/s

Table 2: Converting rotational speed to linear speed

It is noted that the test rig was upgraded towards the end of the programme of work reported with this thesis with a hollow metal section replacing the PVC pipe manifold. This creates a more secure connection between the needles and the manifold as the needles are screwing into a sturdier material, which will reduce the likelihood of leakage. Leaks can cause large droplets to fall and potentially impact the sample. The other upgrade to the test rig was an inclusion of a purge system, this allows the water to be forced through the test rig at a high pressure. By doing this it should clean the needles and stop any debris from fully or partially blocking the needles. How these upgrades affected the characterisation will be discussed later in Section 3.3.

3.2 Methodology

The previous work carried out by ETC has allowed the test rig to be fully controllable and provide repeatable tests. Other commercial test rigs carry out their testing using a standard time to failure method and in general simply compare samples, rather than fully understanding the droplet impacts. The ETC test rig has been designed to be a more research focused rig through the work undertaken to characterise the droplet impacts. This characterisation can, within a certain accuracy, determine the exact number of droplet impacts for any given stage of erosion. The knowledge of number of droplet impact plus the location where they impact the sample is what separates the ETC rig from the other test rigs in the literature. Throughout all of the characterisation tests used below the test rig was operated at varying speeds from 700rpm to 1400rpm.

3.2.1 Vibration Analysis

When operating the test rig, the tone of the vibration changes as the test rig hits a natural frequency. Therefore an accelerometer was attached to the underside of the top plate of the motor as shown in Figure 28. The test rig was tested from 0-1400rpm increasing in steps of 50rpm, where the max acceleration was recorded at each rotational speed.

This test was carried out after the majority of the characterisation work, where the speed of 1000rpm was avoided due to health and safety reasons as resonance occurs around this area. Therefore most of the other characterisation work will avoid the speed of 1000rpm.

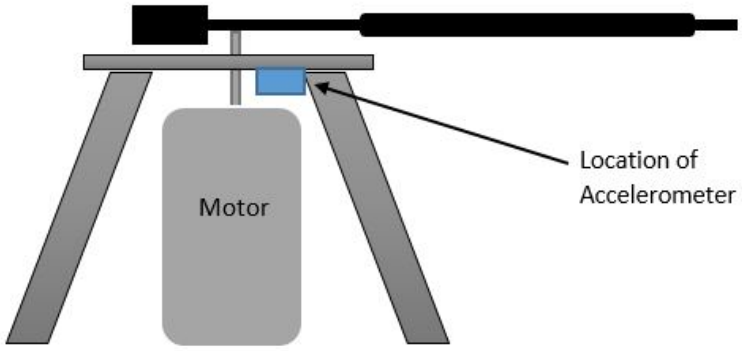

Figure 28: Schematic showing location of Accelerometer

3.2.2 Droplet Forming and Impacts

The Photron FASTCAM SA-X2, high speed camera, was operated at 2000fps to quantify the number of droplets forming and the number of droplet impacts on the sample. Each clip recorded by the high speed camera lasted 3.639s, three needles from the test rig where visible within the frame of the footage. This time per clip was based on the frame size, resolution and video clip size, where the time used was an agreeable balance between all three parameters. The aim of this characterisation was to determine if any of the speeds or pressure heads resulted in unreliable results, most likely due to the turbulent air. The aim of the ETC rig is to be highly accurate as well as repeatable, therefore it is important to test it at a range of conditions to determine if any combinations of speed and water pressure would result in unreliable results. This measurement of the droplet impacts will also help determine at which speed and pressure head the most severe case of erosion occurred.

3.2.3 Strike Location

The high speed camera was then used to film droplets at up to 40,000 frames per second to track the droplet trajectories and strike locations. All of this data was then analysed to gain a greater understanding of the operating conditions. Firstly the high speed camera was used to count the number of droplets formed as well as the number of strikes, measured using varying speeds and pressures. Next the strike location was analysed with the sample being divided into five bins, as shown in Figure 29. The majority of erosion occurs on the leading edge, therefore it is important for the experimental set-up to replicate this. The strike location was studied from both the radial and tangential perspective, the tangential view was split into three bins rather than five; the inner, middle and outer thirds. Again the ideal strike location would be in the middle of the sample when looking tangentially as that is the line that the droplets are falling on. If droplets are impacting on either the inside or the outside this shows that the aerodynamic wake produced by the rotating arm is altering the trajectory of the droplets. An increase in the aerodynamic wake, or turbulent air, will negatively affect the erosion results as turbulent air causes premature droplet breakup.

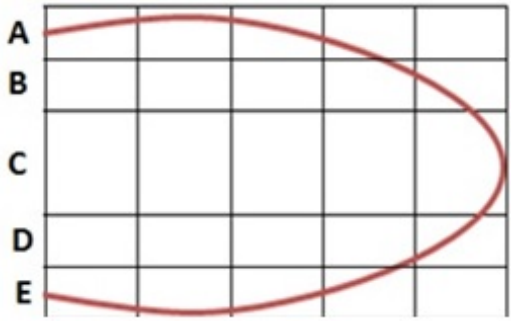

Figure 29: Bins for Droplet Strike Location

3.2.4 Droplet Diameter

A DSLR camera was used to take photographs of the droplets, with the arm rotating and not rotating, to determine the droplet diameters. Each photograph could fit three needles into the frame, the same three needles were used for all measurements of droplet diameters. The reason the diameters were measured with the rig operating and stationary is to determine how the aerodynamic wake affected the droplets. The stationary tests should provide accurate results with the uniform conditions and then the measurements with the rig operating will show the amount of variation present with the rig rotating.

The droplet diameters were measured, using a DSLR camera set on burst mode to capture droplets. The number of pixels were counted for each droplet from which an accurate droplet diameter was calculated. The droplet diameters were measured with and without the arm spinning, and as expected the measurements taken without an aerodynamic wake present were more accurate. When measuring the diameters with the arm spinning, the horizontal and vertical diameters were taken as the wake can cause the droplets to become misshapen. While this is not an ideal solution it was deemed that this was preferable to ignoring deformed droplets as they would still cause impacts.

The droplet diameters were measured with all 72 needles operating as well as 36 and 24 needles operating. This is crucial as the test rig will be operated in these conditions to reduce the erosion rate. The potential change in diameter, due to the number of needles operating, needs to be quantified to preserve the scientific nature of the test rig. After analysing all of the photographs a distribution of the diameters was created, this will not only show the mean diameter but also the standard deviation. The mean and standard deviation can be compared for different pressures as well as the number of needles operating. Finally the three different needles were analysed to see what the variation between them was, as the needles are required

to all produce similar diameters for results to be quantifiable. Too great a variation and it will provide a level of uncertainty that is undesirable for an accurate test rig.

3.2.5 Needle Flowrate

The flowrate of the needles was analysed at 16 different needles spread around the manifold. A DSLR camera was used to record 60s of footage of four needles and this was repeated at four different quadrants around the manifold. The reason for checking in four different quadrants was to make sure there were no problems with the manifold that would result in higher pressures in different areas.

The flowrate was measured at various different pressures to determine how the pressure head affected the flowrate. The footage could also be used to determine if any needles were malfunctioning as their flowrate was much lower than the rest. As the needle diameter is very small, any foreign particles in the water could block or restrict the flow. By running this test, needles that are performing differently can be located and either cleared or replaced. Again as with the majority of these tests this is to achieve consistent conditions which will lead to reliable results.

After the manifold upgrade the flowrate was measured again, the method used was changed as it was a quicker process. This time a beaker was placed under 4 needles for 60s and the total volume of water collected was measured. The total number of droplets falling in 60s was also measured, this allows a more direct comparison with previous flowrate and allows an average droplet diameter to be calculated.

3.2.6 Needle Radial Position

The radial position of the needle is also important to determine as this measurement will quantify the erosion area. The needles should all be 1025mm from the centre of the test rig but due to manufacturing there could be some variation. By measuring all 72 needles the innermost and outermost needles can be determined, this provides the range that droplets fall in. The aerodynamic wake will deflect the droplet path slightly but the area that erosion could occur on the sample can be determined.

The radial position of the needles was measured by attaching digital calipers to the end of the arm and measuring the distance to the needle. After the manifold was changed the same

process was carried out again.

3.2.7 Standoff Height

Finally the optimum standoff height was explored. The standoff height is defined as the distance between the tip of the needle and the centre of the leading edge of the sample, as shown in Figure 30. A high speed camera was used to determine the droplets' trajectories at varying standoff heights. The results were separated into four categories: droplets that fall straight; droplets with a slight deflection but still strike the sample; droplets that are deflected greatly and miss the sample and droplets that break up due to the wake causing them to explode into many smaller droplets.

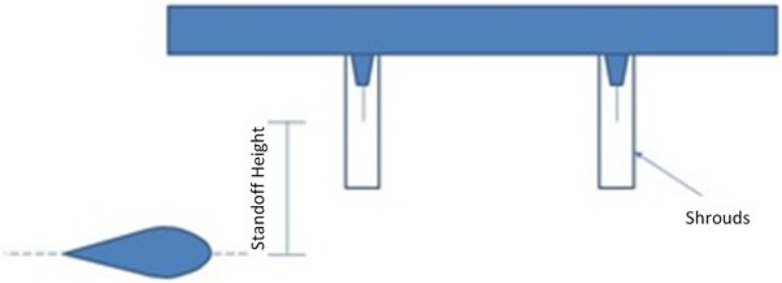

Figure 30: Diagram of Needle Arrangement

The deflection and break up was explored for both a radial and tangential view as from different perspectives there will be different droplet trajectories. Afterwards the height at which the droplet started to deflect or break up was examined with varying stand off heights. This determines whether there is a band of aerodynamic wake acting around the rotating arm. If this is the case most droplets would deflect and break up at a similar height.

Finally the location of the arm at deflection or break up was explored, this is to determine if certain conditions lead to break up or deflection. The question arises, does a droplet just missing an impact result in it more likely breaking up? To determine this the location of the arm was used, by counting the number of frames the arm had travelled from passing the needle to when the droplet started to deflect or break up. Using this combined with the rotational speed to calculate where the arm was situated around the circle. Analysing these results determines whether the arm location is different with break up or deflection and therefore how close the droplet was to the sample when it initially fell.

3.3 Characterisation Results

As discussed in the Methodology section a series of tested were undertaken ranging from rotational speeds of 700-1500RPM. The pressure head could also be altered from 50mm to 350mm. The test are investigating: the vibration of the test; droplet formation and impacts; strike location onto the sample; droplet diameter measurements; needle flowrate; needle radial position and standoff height. All of these different parameters were explored as each area will have a slight effect on other areas. The test rig's aim of being highly controlled is only possible with a full understanding of each of these areas.

3.3.1 Vibrational Analysis

The vibrational analysis as conducted to determine resonance occurred at a particular rotational speed. This was tested by incrementally increasing the rotational speed from 0 up to 1500rpm, at steps of 50rpm. Figure 31 plots the acceleration detected against rotational speed.

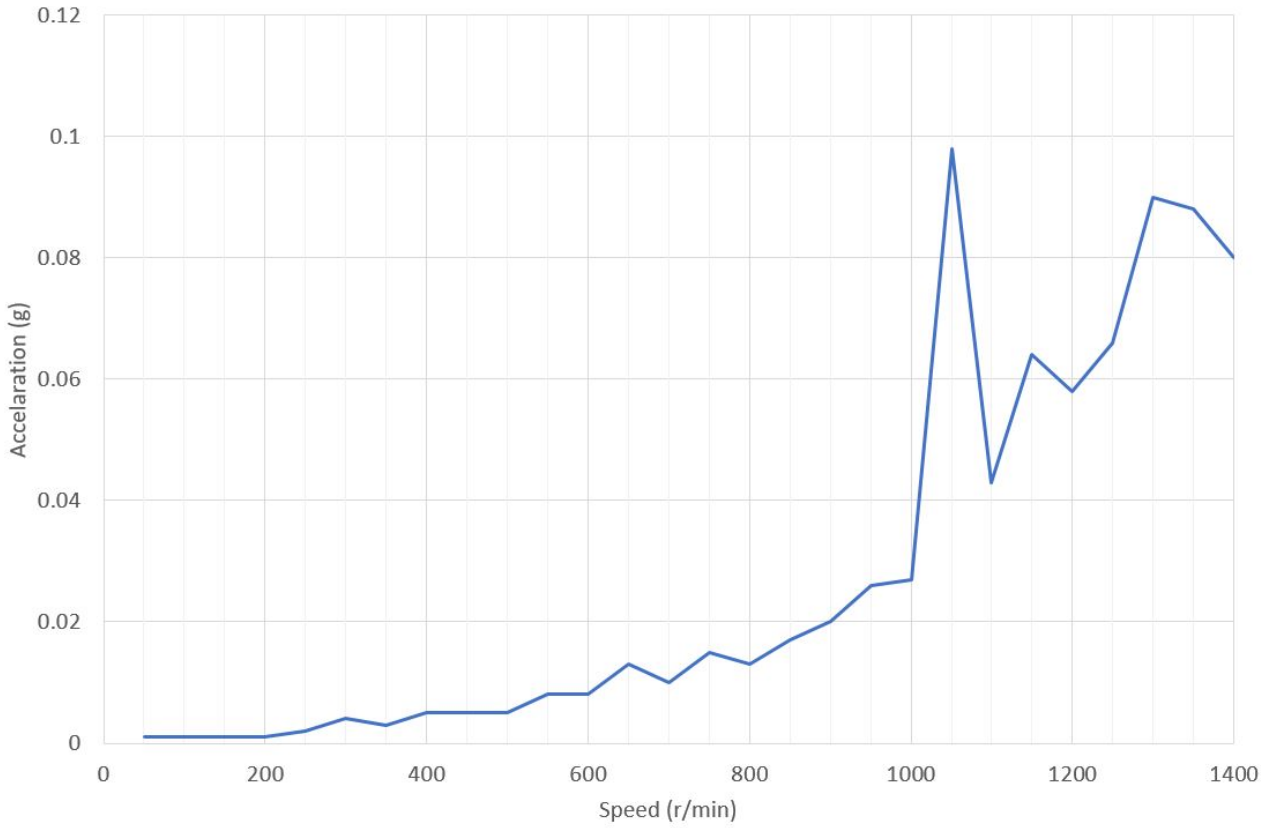

Figure 31: Acceleration at Varying Speeds

Figure 31 plots the vibrational acceleration against rotational speed showing a clear spike at 1050rpm, even greater than the vibration reached at the 1400rpm. This clearly signifies that at, or close to, 1050rpm the test rig is operating at resonance. Operating at resonance will damage the motor and therefore the speed of 1050rpm should be avoided.

3.3.2 Droplet Forming and Impacts

The number of droplets forming and number of impacts, is one of, if not the most important parameter to understand. No other test can quantify this information and obtaining it will allow erosion to be measure against number of impacts and not just time. The number of impacts were examined for rotational speeds ranging from 700rpm to 1400rpm, as shown in Figure 32.

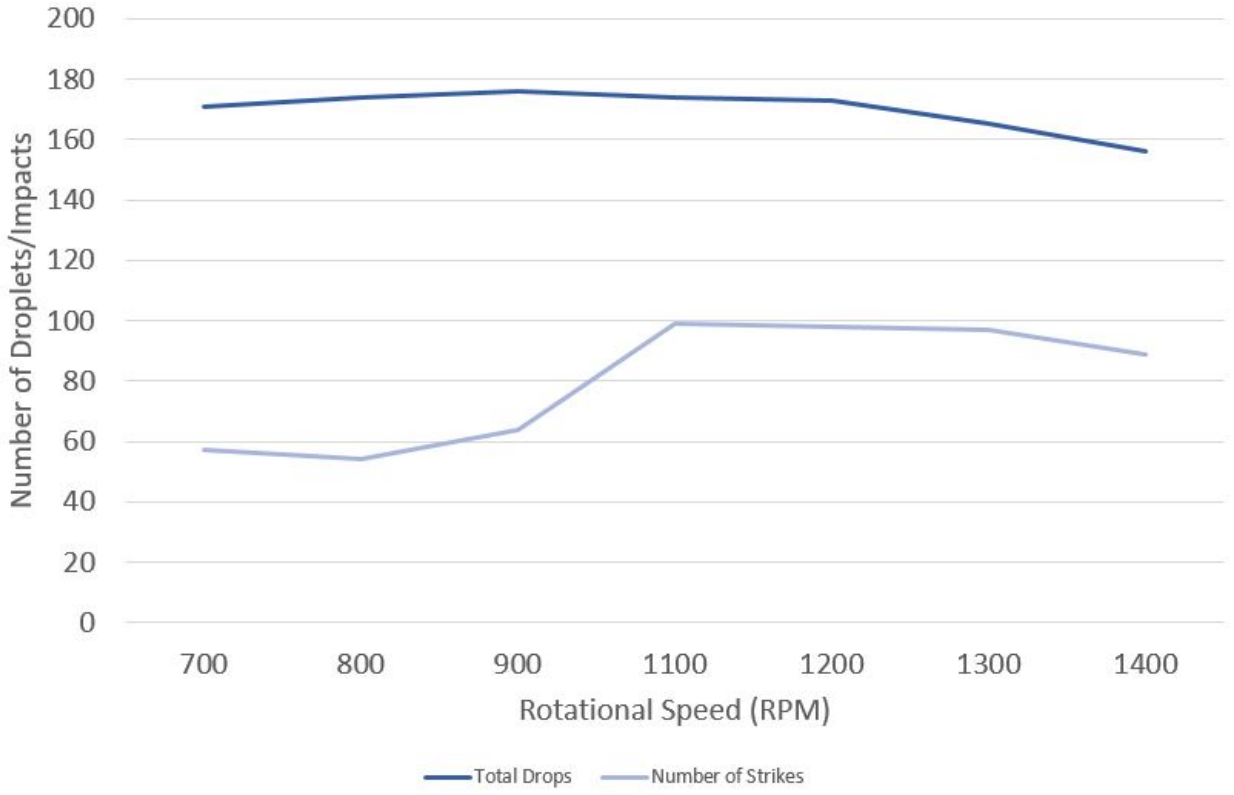

Figure 32: Number of droplets and strikes at varying speeds

Figure 32, shows that the total number of droplets formed with the dark blue line and the number of impacts is shown by the light blue line. Each of the different pressure heads was measured for the 3.639s as stated above, therefore the total values are the summation of all

pressure heads and lasts for a time of 25.47s. The total droplets formed remains fairly constant regardless of the rotational speed. There is a slight decrease in droplet formation at higher speeds, which is due to the aerodynamic wake present which causes droplets to break up before they have a chance to form fully. In Figure 32 it is shown the number of strikes is close to constant between 700-900RPM and then an increase in the number of impacts at speeds of 1100RPM and greater. The increase in number of impacts at the speed of 1100RPM is due to the arm rotating faster therefore not allowing enough time for any droplets to fall far enough that they miss the sample. Droplets either impact the samples or are deflected or broken up by the aerodynamic wake. The curve flattens as once the speed of 1100RPM is reached the time between rotations is short enough that increasing the speed does not make any difference.

Table 3 shows as expected that as the pressure increases the number of droplets formed increases, this makes logical sense as greater water head pressure will mean an increase in flowrate and therefore more droplets being produced.

	50 mm	**100 mm**	**150 mm**	**200 mm**	**250 mm**	**300 mm**	**350 mm**	**Total**
700 RPM	18	20	22	23	24	32	32	171
800 RPM	18	20	21	24	26	33	32	174
900 RPM	18	20	20	25	26	33	34	176
1100 RPM	19	21	21	24	26	33	31	174
1200 RPM	19	20	22	23	25	32	32	173
1300 RPM	17	18	19	24	25	30	32	165
1400 RPM	19	18	19	20	21	31	28	156

Table 3: Number of Droplet Formed at Different Rotational Speeds and Pressure Heads per 25.47s

The total number of impacts provides the most useful result. As can be seen in Table 4 the maximum number of impacts occurs at a rotational speed of 1100rpm. However there was not much difference between 1100rpm, 1200rpm and 1300rpm. It is expected that as the rotational speed increases there would be an increase in the number of impacts, due to there being more passes in an equal time frame.

	50 mm	100 mm	150 mm	200 mm	250 mm	300 mm	350 mm	Total
700 RPM	7	6	7	7	7	9	14	57
800 RPM	5	4	5	10	10	9	11	54
900 RPM	4	6	6	11	12	13	12	64
1100 RPM	9	10	11	15	17	18	19	99
1200 RPM	6	8	10	15	14	21	24	98
1300 RPM	8	6	8	19	13	21	22	97
1400 RPM	6	8	16	7	13	20	19	89

Table 4: Number of Impacts at Different Rotational Speeds and Pressure Heads per 25.47s

Table 5 examines the average number of impacts per pass it can be seen that it is fairly constant through all the speeds tested with only a slight drop off once the highest speeds are reached. This decrease this is due to less droplets forming as noted above. This illustrates why a greater number of impacts are expected at higher speeds.

Speed	**Impacts Per Pass**
700 RPM	1.34
800 RPM	1.11
900 RPM	1.17
1100 RPM	1.48
1200 RPM	1.35
1300 RPM	1.23
1400 RPM	1.05

Table 5: Impacts per Pass

From Figure 32 the strike rate can also be calculated, as shown in Table 6, this is a less useful metric as it is the total number of impacts that will ultimately contribute more to erosion rather than the rate at which they impact. However a lower percentage of strikes will result in an increase in the droplets caught in the aerodynamic wake, more "near misses" will lead to more droplets exploding due to the turbulent air. The droplet explosions cause lots of tiny droplets to enter the air, which can still be impact the sample. These tiny droplets can be difficult to quantity, firstly in terms of the number of them that impact the sample and secondly how much bearing these exploded droplets have on the overall erosion of the sample. While it is not expected for the minuscule droplets to have a large bearing, over an 8 hour test they could add

to a significant affect over time.

	50 mm	100 mm	150 mm	200 mm	250 mm	300 mm	350 mm	Average
700 RPM	38.9%	30%	31.8%	30.4%	29.2%	28.1%	43.8%	33.3%
800 RPM	27.8%	20%	23.8%	41.7%	38.5%	27.3%	34.4%	31%
900 RPM	22.2%	30%	30%	44%	46.2%	39.4%	35.3%	36.4%
1100 RPM	47.4%	47.6%	52.4%	62.5%	65.4%	56.3%	61.3%	56.9%
1200 RPM	31.6%	40%	45.5%	65.2%	56%	65.6%	75%	56.6%
1300 RPM	47.1%	33.3%	42.1%	79.2%	52%	70%	68.8%	58.8%
1400 RPM	31.6%	44.4%	84.2%	35%	61.9%	64.5%	67.9%	57.1%

Table 6: Strike Percentage with respect to Speed and Pressure

3.3.3 Strike Location

A high speed camera was used to detect the strike location of the droplets. Figure 33 shows a still image of the footage used, where two droplets can be clearly seen. As the sample passes the strike location of the impacts can be easily determined.

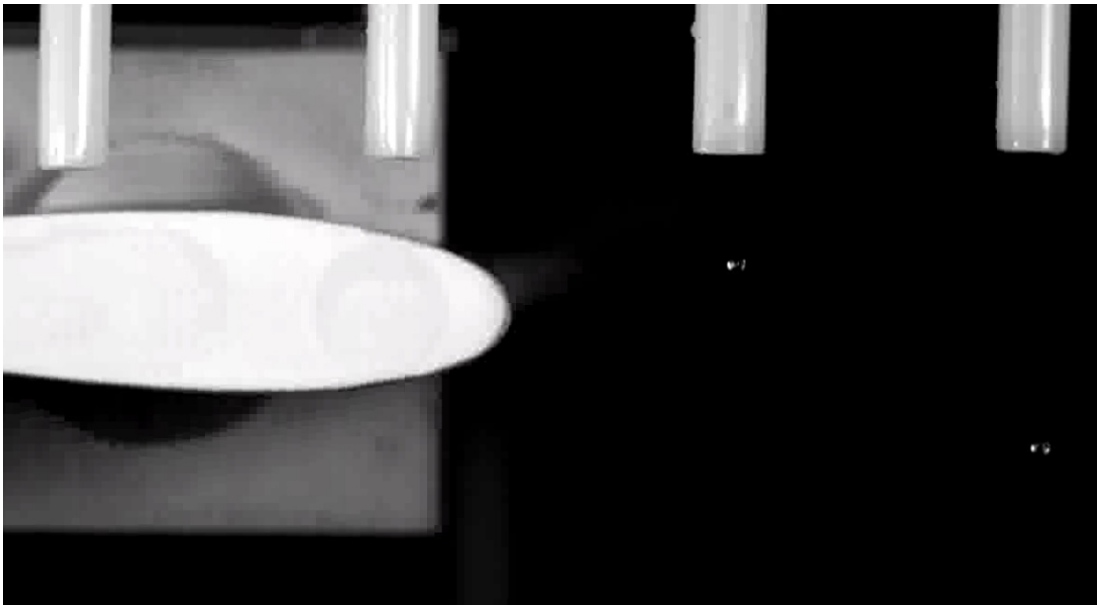

Figure 33: Screenshot of High Speed Camera Footage used to Determine Strike Location

The droplet strike location, shown in Figure 34, shows that at all speeds the highest number of impacts in the centre occurred at 1100rpm when analysing the radial direction. From analysing the footage you can see at slower speeds that a portion of the droplets are not close to impacting

as the rotational speed is slow enough that the rate of droplet formation is quicker than the rate it takes the arm to complete a full rotation. Therefore as the rotation speed increases there is greater parity between droplet formation and time between passes of the arm. While this does not directly relate to impacts in the centre of the sample a greater number of total impacts will increase the odds of impacts in the centre. Table 6 shows that the average percentage of strikes does not change much from 1100-1400RPM. The reason the same number of impacts in the centre are not seen at the higher speeds is due to the aerodynamics. At these higher speeds there is more turbulent air present which leads to early droplet collapse, an implosion of the droplet due to varying air pressure, or the droplet trajectories being more variable.

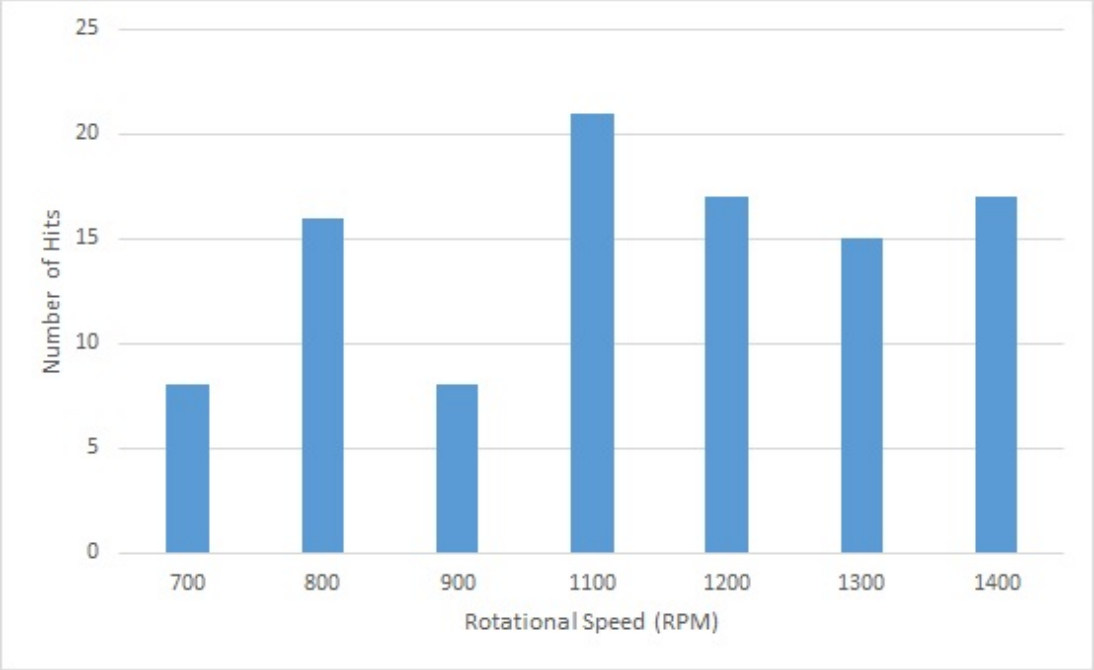

Figure 34: Number of impacts in the centre of the sample when viewed radially

Table 7 shows the percentage of impacts in each of the bin locations as shown in Figure 29. The number of impacts in the centre is fairly constant regardless of the rotational speed, the main difference is at higher speeds the number of impacts on the underside of the aerofoil section decreases. Bins D and E represent the underside of the aerofoil, for speeds of 1100 RPM and above a maximum of 17.5% impacts the underside of the sample. This is due to the arm rotating quicker, which means there is not as much time for droplets to fall before they are impacted by the arm. The full results on the strike location are found in Appendix B.

	A	B	C	D	E
700 RPM	4.8%	28.6%	38.1%	14.3%	14.3%
800 RPM	10.3%	10.3%	55.2%	17.2%	6.9%
900 RPM	14.7%	20.6%	23.5%	26.5%	14.7%
1100 RPM	11.4%	29.5%	47.7%	11.4%	0%
1200 RPM	15%	25%	42.5%	12.5%	5%
1300 RPM	18.9%	32.4%	40.5%	5.4%	2.7%
1400 RPM	18.2%	27.3%	38.6%	11.4%	4.5%

Table 7: Strike Rate for each location at Varying Speeds

Again as noticed in the number of strikes, the higher speeds will result in more turbulent air which will push and distort the droplet shape. However, when considering the tangential view, shown in Figure 35, it can be seen that 1100rpm represents the speed with the greatest number of impacts which do not occur in the centre, documented as 20%. By contrast, at the three slowest speeds all droplets impacted the centre.

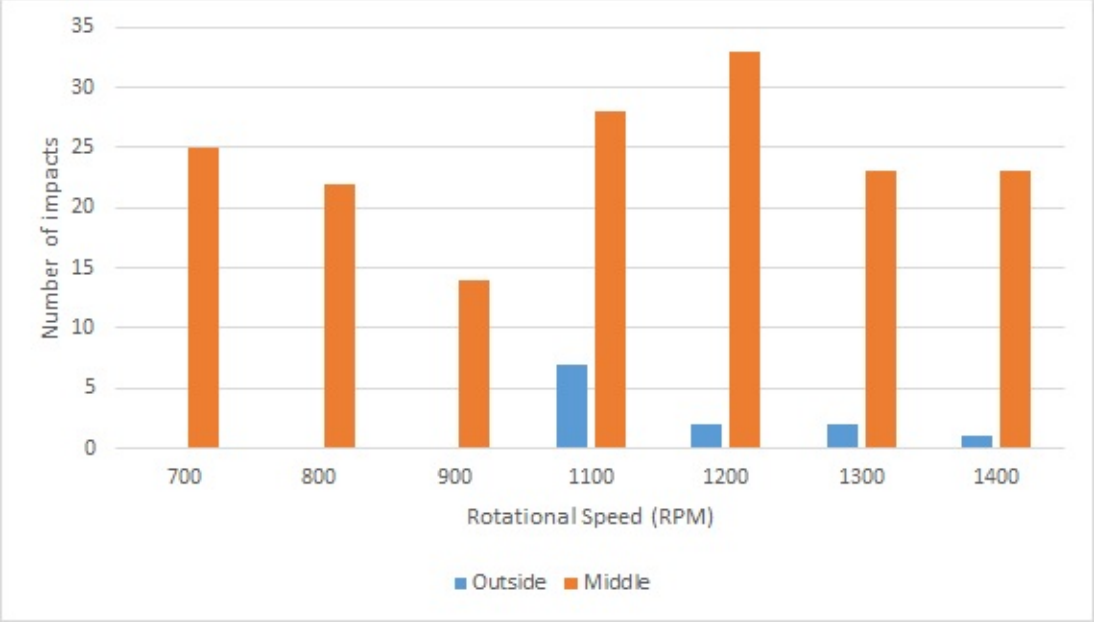

Figure 35: Location of impacts from tangential view

As discussed before the higher rotational speeds leads to more turbulent air which affects the droplet trajectories. As can be seen there is a speed where the aerodynamic wake is strong enough to force occasionally droplets outwards and impact the outside third of the sample.

This has a lesser effect than the radial view though as the number of droplets forced away from the centre is less.

3.3.4 Droplet Diameter

The droplet diameter is an important characteristic to quantify, firstly to provide consistent values and secondly to make sure the diameters are similar to rain droplets. Before any measurements were taken, a picture of a ruler was taken. Then the number of pixels over 30cm could be counted, this could be converted into the length of a single pixel. The tripod was fixed to the floor using weights to ensure it wouldn't move with the test rig operating. The calculation of pixel length can only be used for that exact camera location as once the camera is moved the pixel will not cover the same distance.

Firstly, with a static test rig, a fairly predictable result was achieved showing a linear trend between low pressure and greater droplet diameters. This is due to lower pressures having a smaller droplet flowrate thus allowing more water to fill the droplet before the force of the water flowing into the needle overcomes the adhesion of the water. In Figure 36, the blue line represents the diameters when 100% of the needles are switched on. The orange and grey lines show the diameters at 50% and 33% respectively.

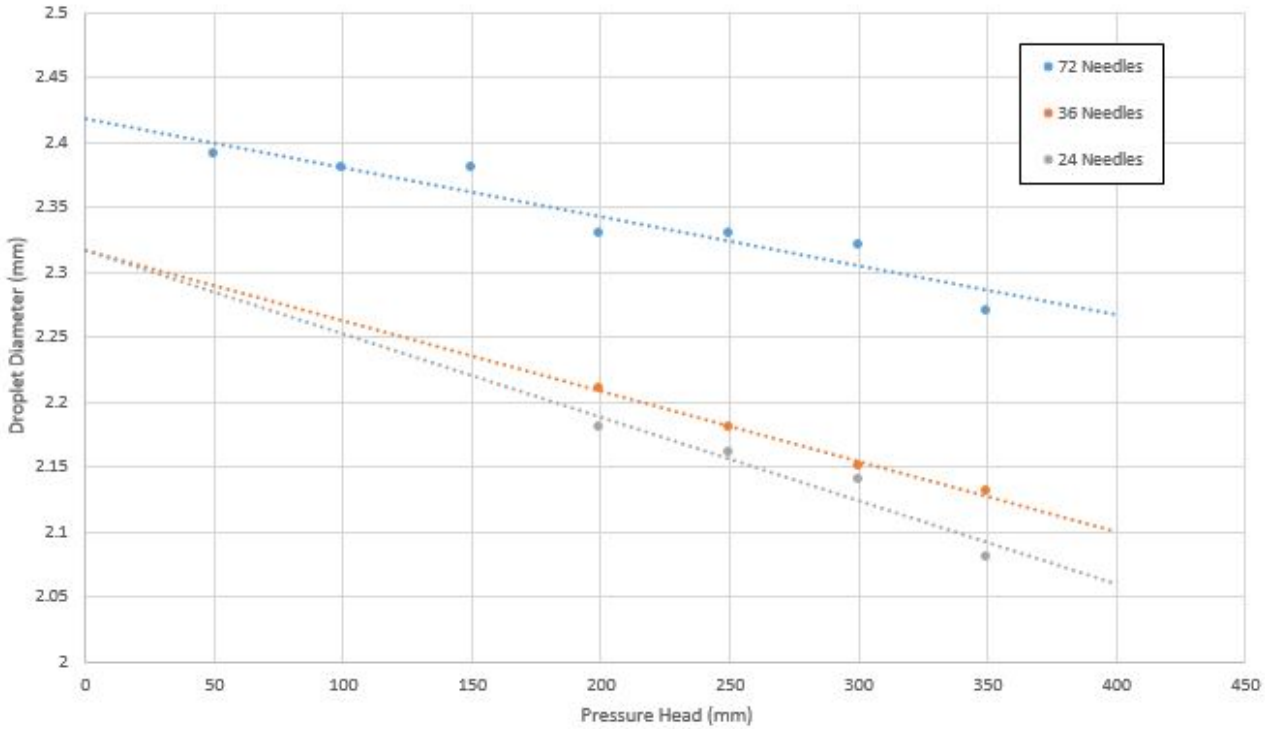

Figure 36: Droplet Diameter for Varying Pressure and Speeds

When less needles are used the pressure in the remaining needles will increase as the same volume of water now has the output area halved therefore the flow will need to increase to balance this. A greater pressure will force the droplets forming on the end of the needle to fall sooner, resulting in a smaller diameter droplet. Therefore, as shown in Figure 36 the fewer needles that are used the smaller the droplet diameter.

Examining the droplet distribution in Figure 37 allows this trend to be studied even more. The graph shows a distribution curve of the droplet diameters, with a pressure head of 350mm, including the results for different number of needles operating. The x-axis displays the droplet diameter and the y-axis is the probability of that diameter occurring. Usually the probability ranges between 0 and 1 but as this test can produce multiple droplets at the same diameter it results in a probability of greater than 1 occurring.

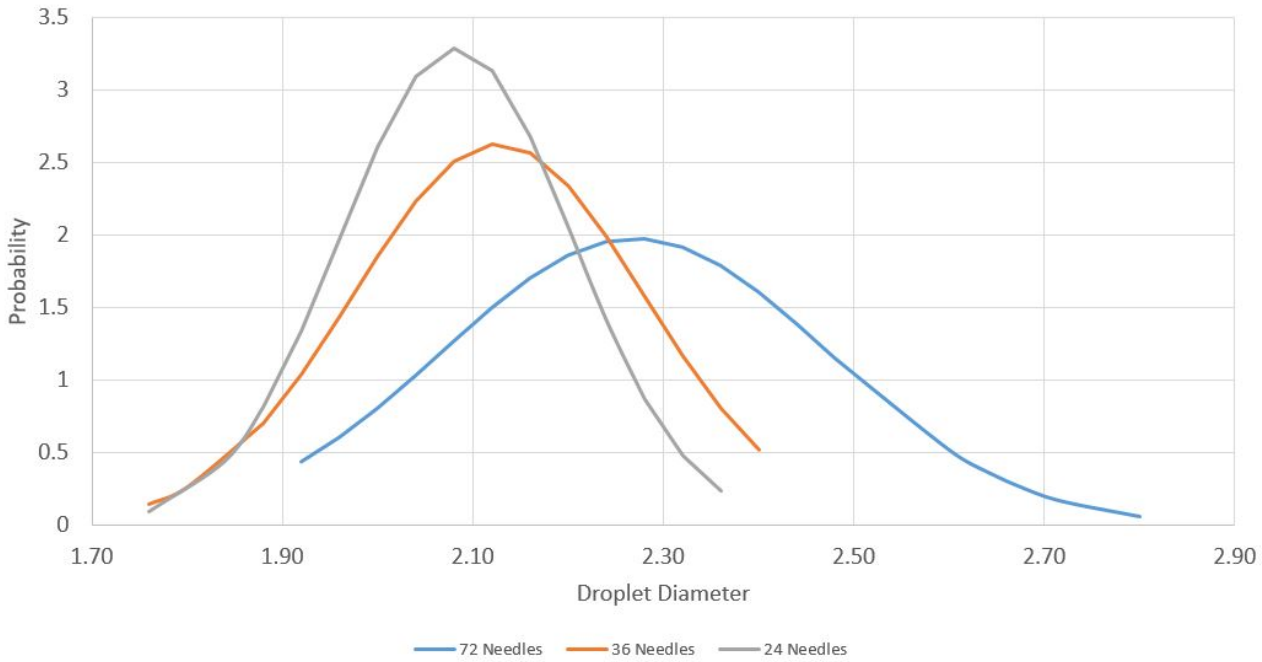

Figure 37: Distribution of Droplet Diameters at 350mm Pressure Head

As discussed the mean diameter decreases with decreasing needles, also the standard deviation decreases with decreasing number of needles (a smaller standard deviation results in a narrower spread of results). It is unclear whether the standard deviation is affected by the change in number of needles operating or flowrate. When examining Figure 38, which shows the distribution of droplet diameter at varying pressures for a constant number of needles, it is shown that the standard deviation for the different pressures is close to constant. This leads to the conclusion that the change in standard deviation could be as much down to the sample size not being large enough rather than the pressure affecting the standard deviation.

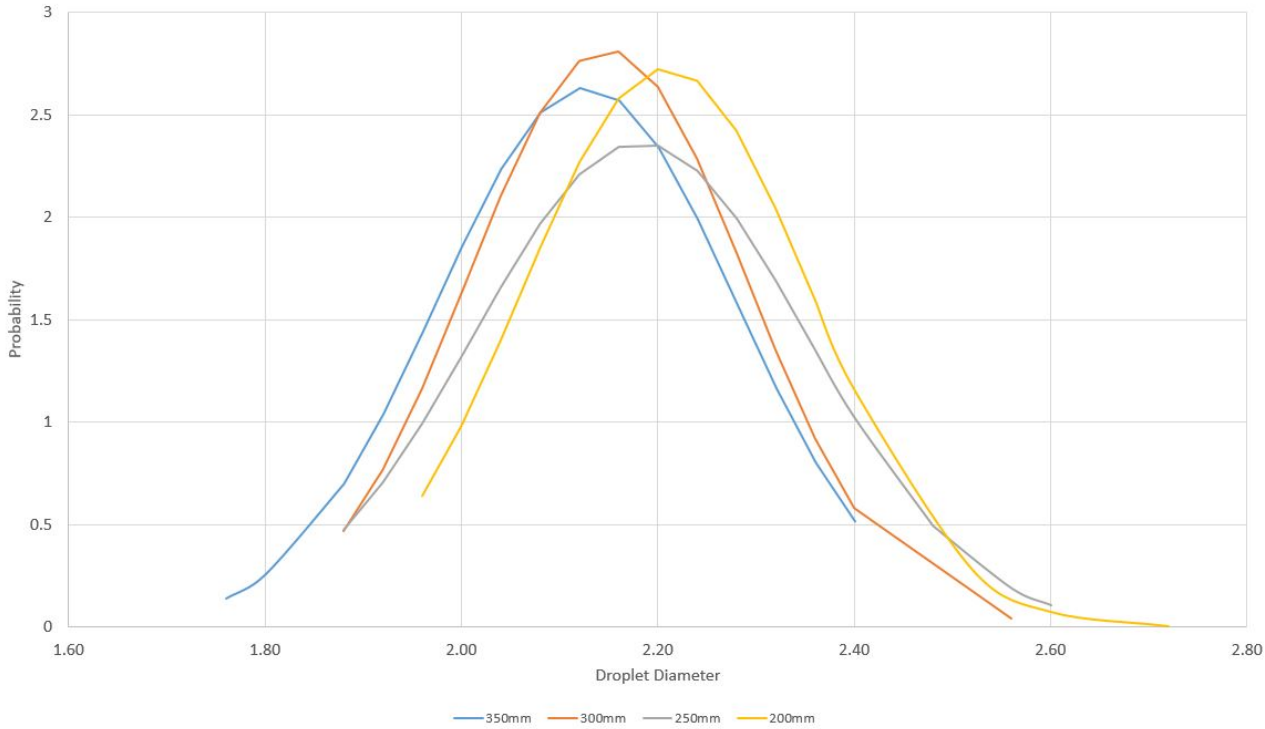

Figure 38: Distribution of Droplet Diameters for 36 Needles

Table 8 compares the mean and standard deviation over all the varying pressure heads and needles. The standard deviation is fairly constant across all the different variations. The small changes in standard deviation will be due to the slight randomness in the results and we can assume that the standard deviation is constant for differing pressures and needles.

		350mm	**300mm**	**250mm**	**200mm**
72 Needles	Mean	2.27	2.32	2.33	2.33
	SD	0.2	0.16	0.14	0.14
36 Needles	Mean	2.13	2.15	2.18	2.21
	SD	0.15	0.14	0.17	0.15
24 Needles	Mean	2.08	2.14	2.16	2.18
	SD	0.12	0.12	0.11	0.12

Table 8: Mean and Standard Deviation of Droplet Diameters for Varying Pressure Heads and Needles

Another consideration is that individual needles might produce different diameter droplets. Examining Table 9, Needle 2 always produces smaller diameter droplets than the other two regardless of the pressure or number of needles. There are a couple of reasons this could occur,

firstly there could be some tolerances in the manufacturing, the needles are meant to have an inner diameter of 0.21mm [59] but just a minuscule change could affect the droplet diameter. Secondly while the water used is filtered there could still be tiny particles that are contained in the water and potentially partially block the needles. However from experience usually blocked needles result in a greater reduction in flowrate rather than a small change in diameter so seems more likely to be the manufacturing tolerances. It is unclear whether this range in diameters is consistent across all 72 needles and these three needles provide a fair representative or whether needle 2 is an outlier. There was a time constraint on measuring the droplets and all photographs were taken before they were analysed, therefore it was unknown if the three needles chosen would represent all 72 needles.

Another point of interest is that with the setup of the DSLR camera, needle 2 was situated in the middle and therefore in focus. Whereas the other two needles were slightly out of focus, this means that firstly there is a larger sample size for needle 2 as occasional droplets were too out of focus to take a reading for needles 1 and 3. Secondly there are more accurate measurements of needle 2 droplets as it is a clearer image, while the other needles can still be seen with a clear image each pixel represents 0.04mm which is around 2% of the diameter, this will not change the results massively it might provide a slight variation.

Number of Needles	**Head Pressure**	**Needle 1**	**Needle 2**	**Needle 3**
72 Needles	350	2.36	2.17	2.33
	300	2.38	2.23	2.38
	250	2.39	2.28	2.33
	200	2.41	2.24	2.36
36 Needles	350	2.22	2.01	2.18
	300	2.26	2.03	2.20
	250	2.30	2.09	2.21
	200	2.24	2.15	2.26
24 Needles	350	2.14	2.01	2.14
	300	2.20	2.07	2.17
	250	2.20	2.10	2.22
	200	2.20	2.12	2.26

Table 9: Droplet Diameters for each of the Needles

When analysing the droplets while the test rig was operating, there is more variance in the diameters. As can be seen in Figure 39, the majority of droplets are between 2.4 and 2.8mm, with a few outliers as well. In this situation, the pressure does not show the same trend as with a static rig.

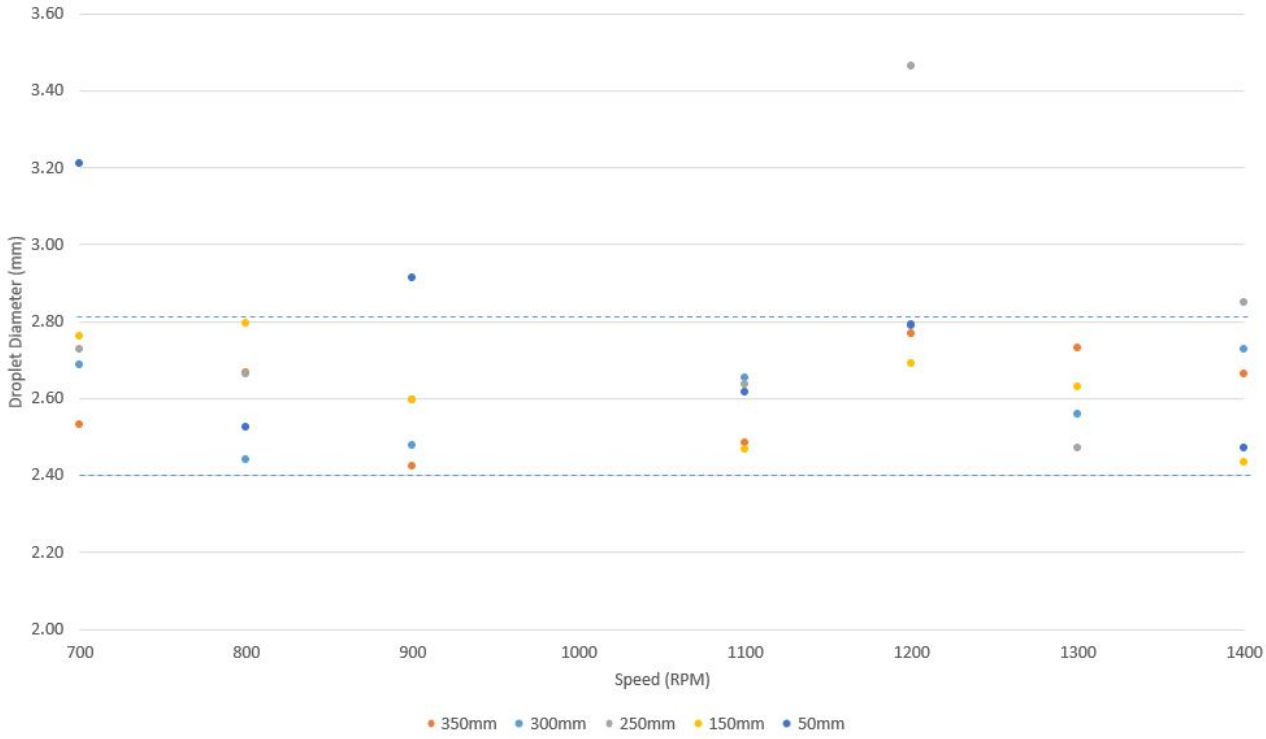

Figure 39: Average Droplet Diameter with Varying Pressures and Speeds

The reason for the greater variation in results when the rig is running is due to the aerodynamic wake. With the rig stationary droplets are formed by water filling the needle and collecting on the end, the cohesion of the water droplet molecules cause them to stick together and the adhesion of the whole droplet causes it to stick to the needle. Then when enough water collects on the needle the weight of the water is greater than the adhesion and the droplet falls. However when the rig is operating the aerodynamic wake causes lateral forces to act on the droplet thus pushing it off the needle earlier.

Another factor in the variation of the results is the method used to measure the droplet diameters. Firstly the measurements are taken from a 2D photo while the droplets are three dimensional. The turbulent air present inside the erosion test rig can cause the droplets to be distorted and a 2D representation of this can lead to faulty measurements. If a droplet is stretched in a certain axis then the photograph will not be able to pick this up leading to a greater variation in droplet diameter measurement. Secondly the photos were taken at random

times as the technology was not accessible to time photographs to coincide with droplet formation. This leads to a variety of different sample sizes for the different speeds and pressures. In Figure 39, at 1200RPM and a pressure head of 250mm there is an outlier in the droplet diameter, nearly 3.5mm. The reason this average is so high is that there is a sample size of one. Meaning only one photograph was taken that fits these exact pressures and speeds. This combined with the issue of distorted droplets can lead to unexpected results.

The inclusion of shrouds protecting the needles means that you'd assume the droplet diameters leaving the needle would be the same as shown without the arm spinning. The change between Figure 36 and Figure 39 is due to the aerodynamics distorting droplets. It is expected that even with the arm spinning the high pressures will result in smaller droplets and the lack of accurate measurement and smaller sample size is causing this range of values. Therefore for any future calculations the droplet diameters measured from the static rig will be used.

3.3.5 Needle Flowrate

The next part of the test rig to characterise is the needle flowrate. Sixteen needles were measured in total, four needles in each of the four different quadrants. The number of droplets formed in 60s were counted and then an average was taken over all 16 needles as well as the standard deviation to check the accuracy of the results. Table 10 examines these results from a pressure head of 50mm to 350mm in 50mm increments. As shown, as the pressure head increases by 50mm this increases the flowrate by around 10%.

Pressure Head	**Mean**	**Standard Deviation**	**Mean Increase**
50mm	99.4	20.6	-
100mm	112.1	17.2	9.8%
150mm	121.9	23.3	8.5%
200mm	133.6	25.3	9.7%
250mm	147.4	26.9	10.5%
300mm	162.9	30.7	10.7%
350mm	173.1	35.6	8.6%

Table 10: Needle Flowrate at Varying Pressure Heads

The volumetric flowrate can be determined by using the equation for the volume of a sphere.

$V = 4/3\pi r^3$, where the radius is half of the diameter calculated in 3.3.4, though the diameter is calculated using the equation of the line of best fit. Then the volume of one droplet is multiplied by the number of droplets forming in a minute before dividing by 60 to give the volume per second. The results of this can be shown in Table 11. The results are also shown in l/hr as that is a convention used by the DNV GL standard. The pressure head can be converted into a pressure measured in Pascals by using the equation: $P = \rho gh$. Where the height is the pressure head in the tank plus the datum height. The datum height is the distance from the bottom of the tank to the needle height, this was measured as 590mm. These values can be useful when comparing the test rig to other test rigs or to real world scenarios. Rainfall is not measured in number of droplets and different test rigs have vastly different number of needles and therefore cannot be directly compared without these values.

Pressure Head (mm)	**Pressure** (Pa)	**Volumetric Flowrate** (mm^3/s)	**Volumetric Flowrate** (l/hr)
50	6278	11.97	0.043
100	6769	13.16	0.047
150	7259	13.96	0.050
200	7750	14.91	0.054
250	8240	16.03	0.058
300	8731	17.27	0.062
350	9221	17.88	0.064

Table 11: Volumetric Flowrate vs Pressure Head

These values for the volumetric flowrate are for a singular needle, to calculate the flowrate for the test the value for the singular needle is multiplied by 72 . At the highest pressure head, this gives a volumetric flowrate of 4.63 L/hr for the whole test rig.

Once the manifold had been changed the flowrate was checked to determine if the test rig still had similar operating conditions. This time a beaker captured the water falling from a needle for 60s and the number of droplets were counted. This method could be used to check the flowrate and the droplet diameter. The diameter was calculated by dividing the total water collected by the number of droplets. These measurements were taken for 4 different needles around the manifold and the results are in Table 12.

Nozzle ID	**No of Droplets**	**Nozzle Volumetric Flowrate** (l/hr)	**Total Volumetric Flowrate** (l/hr)	**Mean Droplet Diameter** (mm)
10	244	0.0921	6.63	2.29
28	234	0.0885	6.37	2.29
45	211	0.0812	5.85	2.31
64	238	0.0734	5.29	2.14
Mean	232	0.0838	6.03	2.26

Table 12: New Manifold Calibration Results

Table 12 shows that the droplet diameter remains very similar to the diameter determined in Section 3.3.4 with only a 0.01mm difference. However there is quite a big difference in the volumetric flowrate, the original experiment calculated $4.63L/hr$ whereas this new measurement reads $6.03L/hr$. Looking at the calculations this is solely down to a difference in the number of droplets recorded. The previous measurement recorded an average of 173 droplets per minute whereas the new reading was 232 droplets per minute. When the changes to the test rig were applied, new needles would have been attached, these new needles will not have any minuscule particles blocking them and slowing down the flow. Also the new rig set-up included a purge system, which is used to force water through at a high pressure at the start of each test. This again cleans out the needles and therefore should provide consistent flowrate. This leads to the conclusion that the new measurement of flowrate is more accurate and will be used going forward.

3.3.6 Nozzle Radial Position

Figure 40 shows the changes in radius around the circle. The graph shows the distance each needle is from the average position. The average position is represented by the dotted line. The maximum positive distance, which relates to a greater radius, is 6.12mm and the greatest negative distance is 7.88mm, resulting in a range of 14mm for the radial needle position.

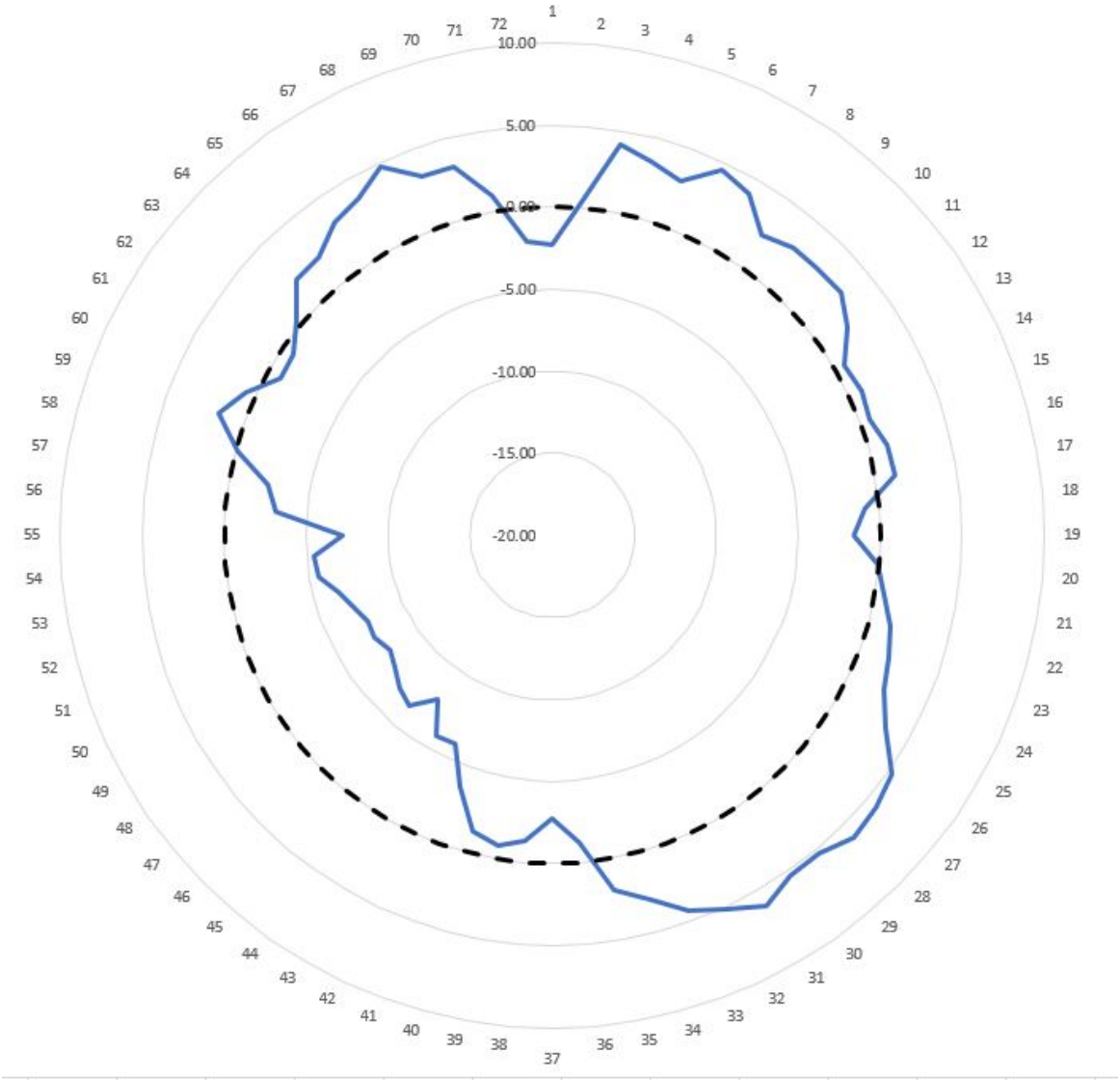

Figure 40: Radial Position of all 72 Needles

The manifold was upgraded to metal which resulted in improved accuracy of the needle positions. Figure 41 shows the comparison between the old PVC pipe manifold and the new metal manifold.

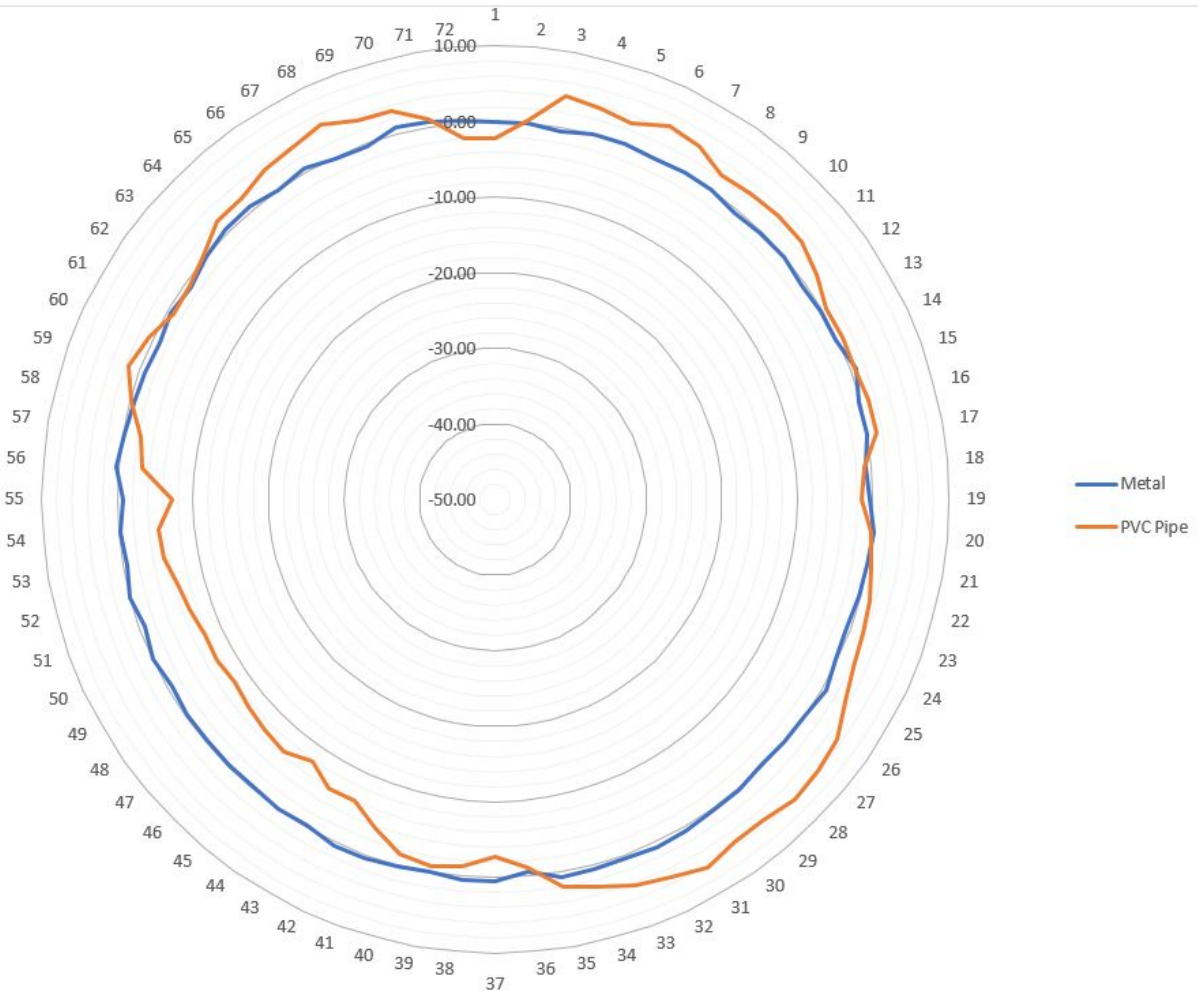

Figure 41: Radial Position of all 72 Needles - Upgraded Version

The new manifold only has a range of 2mm. With a distance of 1.05mm in the negative direction and 0.95mm in the positive direction. This is a significantly smaller range when compared to the previous set up, the aerodynamic wake will cause the droplets to move therefore it does not have too great a difference on the erosion rate, work carried out in Section 4 will show this.

3.3.7 Standoff Height

As can be seen in Figure 42, the standoff height characterisation displays results that contradict the DNV GL standard that above 200mm standoff is preferential. The vertical axis is the percentage of impacts that fall into each of the groups and on the horizontal axis are the different standoff heights and speeds at each of those heights. It can be seen that at a standoff height of 50mm the majority of droplets fall directly straight. The fact that the plastic shroud surrounding the needle is 35mm long means that the droplet is only in the air free stream for 15mm. The use of plastic shrouds are not specified in the DNV GL standard, this could clarify why this erosion test rig operates more accurately at smaller standoff heights.

Another interesting point to note is that the slower speeds result in more droplets falling straight regardless of the standoff height and at 140m/s this provided the lowest number of straight droplets for every standoff height, demonstrating it's the aerodynamic wake acting off the back of the arm that is causing the disturbance to the droplets. Figure 42 examines the validity of DNV GL's 200mm standoff rule. At heights above 200mm, more droplets start to fall straight again whereas at the heights of 100, 150, 200mm the results contain quite an even distribution across the four different bins. The importance of the shrouds is clear here as even above 200mm the higher speeds still result in a lot of droplets that break up or deflect whereas at 50mm standoff even at 1400RPM the majority of droplets fall straight.

Looking at a standoff height of 50mm another interesting point arises, there are no droplets that fall into the category of deflecting out of the path of the sample. The vast majority of samples fall straight and then a few are deflected slightly or break up. This is due to the small distance between the needle and the sample, there is not enough time for the droplet to get deflected out of the path of the sample. This is another benefit of having a standoff height of 50mm, you guarantee all droplets will either hit the sample or be broken up.

The results show that, with the inclusion of shrouds, a standoff of 50mm is preferable, as it results in a far greater number of droplets falling straight. Without the use of shrouds then increasing the standoff height above 200mm increases the rate of straight falling droplets. However, from the results in this study it is clear that the use of shrouds should be strongly advised as it presents a dramatic increase in droplets impacting the sample. The use of shrouds also allows the droplets to gain momentum out with the airstream, thus resulting in more spherical droplets.

Next by looking at the radial view in Figure 43, it can be seen this forms a very similar picture

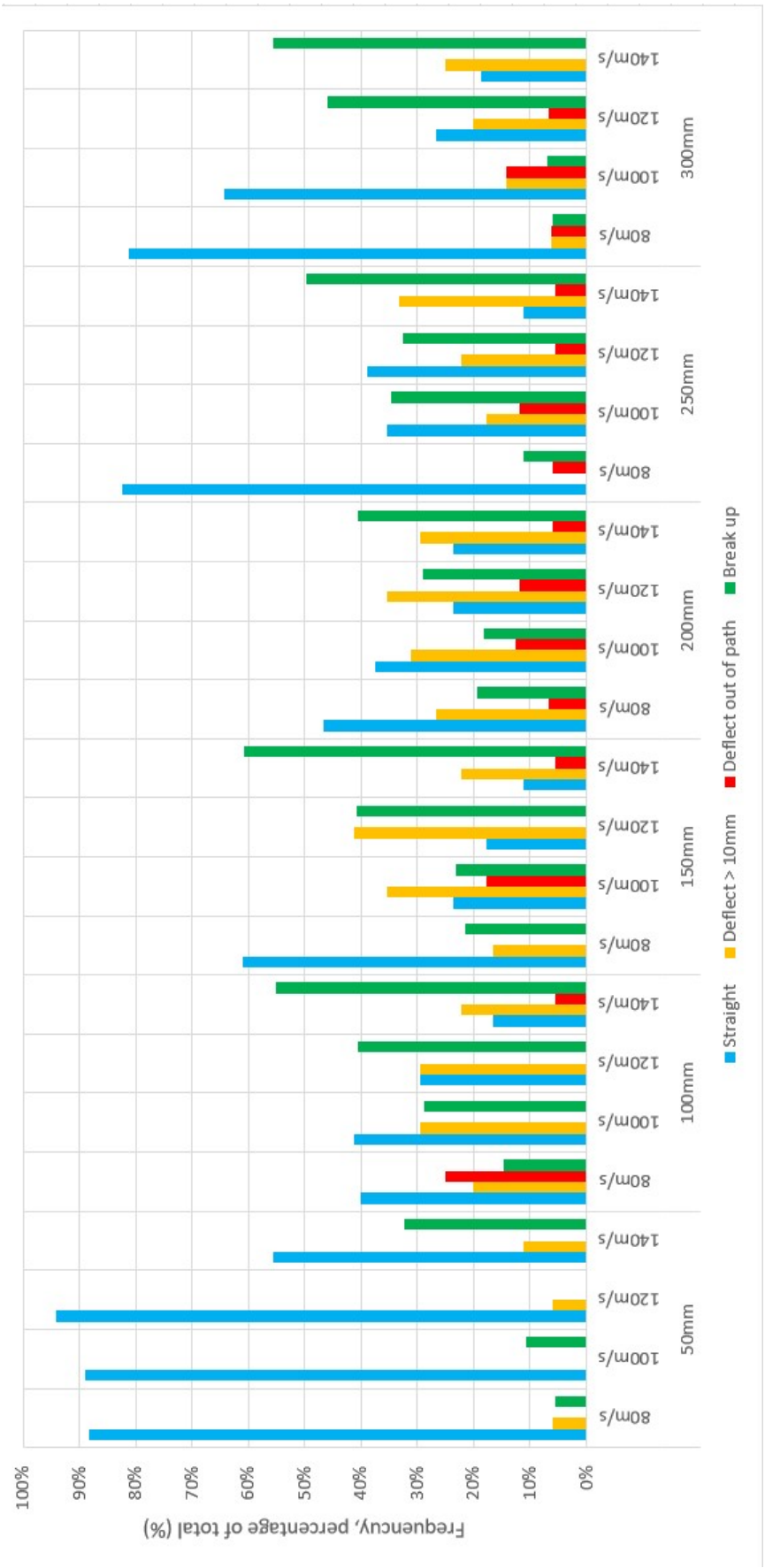

Figure 42: Tangential Droplet Trajectories at Varying Standoff Heights and Speeds

to the tangential direction. This time the results are only split into three bins; straight, deflect or break up. The standoff height of 50mm again has the majority of droplets falling straight, this time interestingly the speed does not seem to affect the droplet trajectories to the same extent as before.

Figure 44 shows the average break up height or average height that the droplet starts to deflect for each of the different standoff heights. This was to examine the presence of a band of aerodynamic air, as this was the assumed reason that DNV GL introduced their standard that said a 200mm standoff height was required. If it is observed that the majority of droplets break up and deflect at the same height then it would be understood the need to avoid this standoff height. Excluding the 50mm standoff height the average height at which break up occurred was 61mm. Figure 44 shows that the breakup height does not seem to be affected by the standoff height, excluding 50mm. This implies that break up is more affected by a strong enough wake to cause the droplet to collapse and that is irrelevant of standoff height.

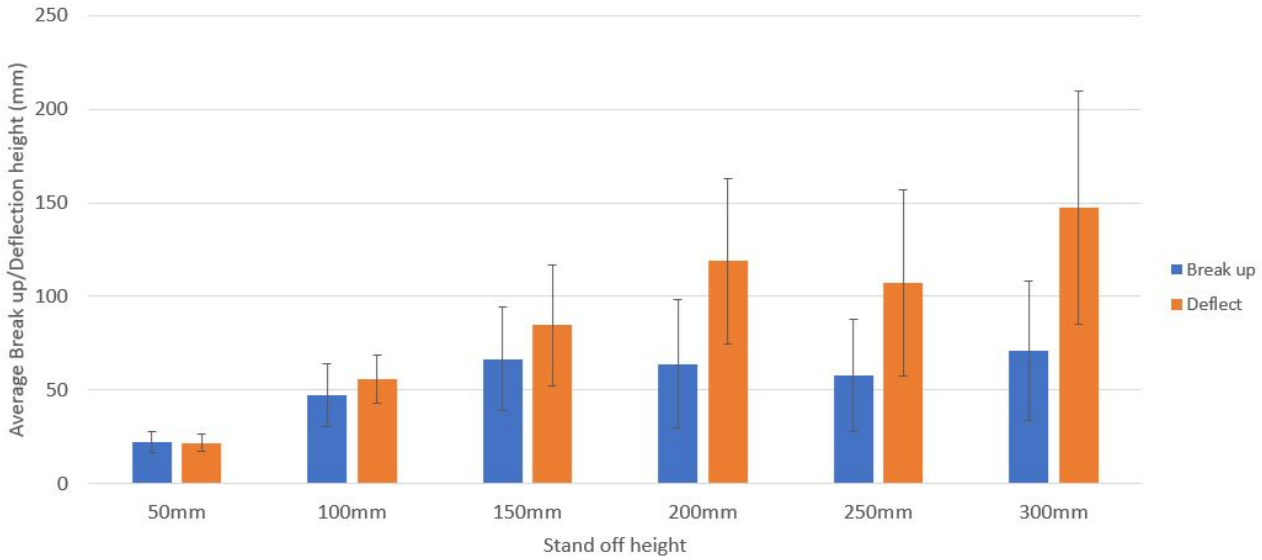

Figure 44: Average height of droplet deflection or break up for varying standoff heights

There is a difference however when looking at the deflection, Figure 44 shows a linear increase in the deflection height from a standoff of 50mm to 200mm and after that point the deflection height plateaus and from 200mm to 300mm there isn't much difference in deflection height or at least a small enough difference to account for random variance. This does provide some validity to the DNV GL standard that it looks like there is a band of turbulent air around 200mm wide which has a greater effect on the droplets, it looks like droplets starting at higher than that fall and then deflect when they reach 200mm above the sample.

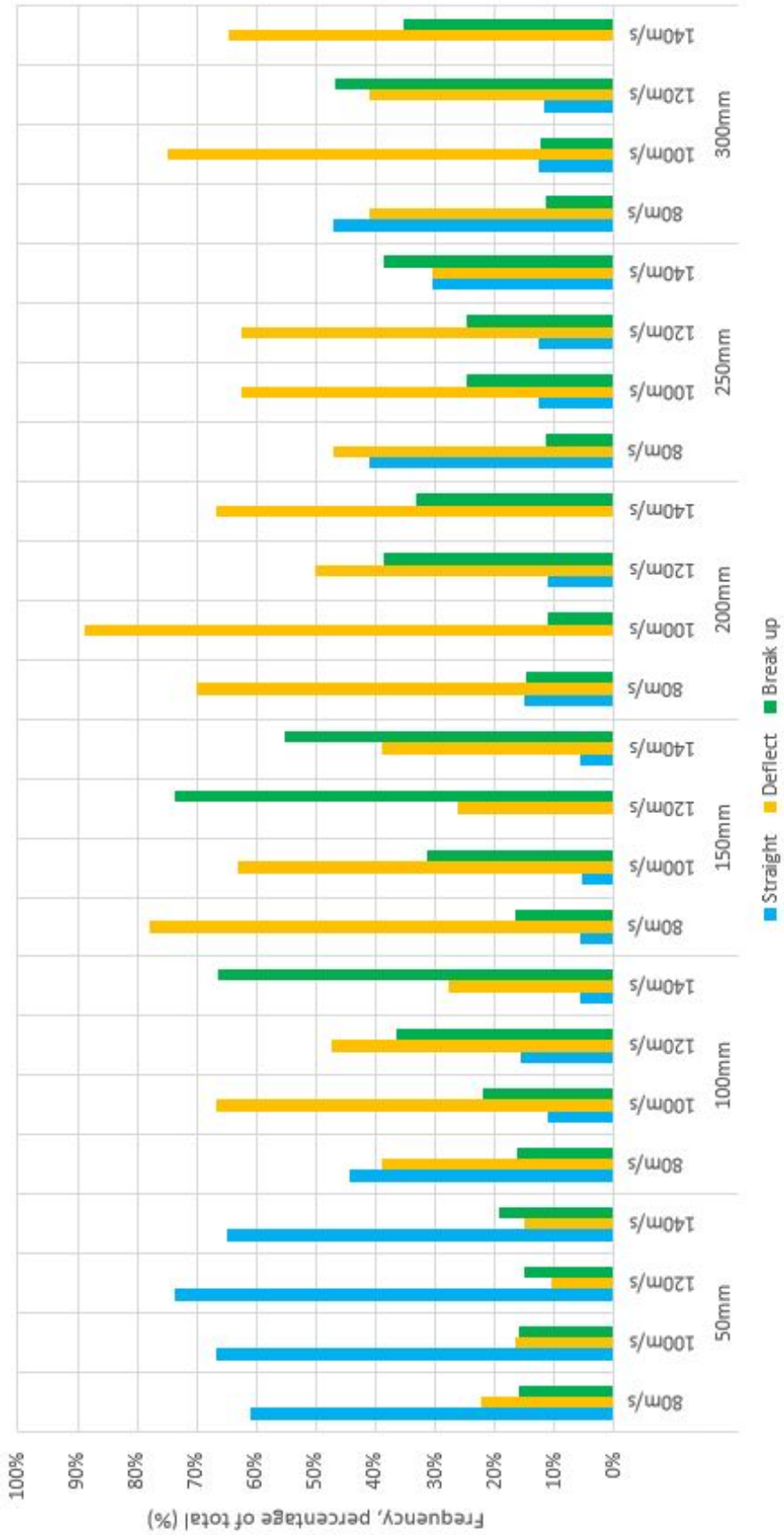

Figure 43: Radial Droplet Trajectories at Varying Standoff Heights and Speeds

The position of the arm when droplets were either deflected or broken up was examined. In Figure 45 a plot is constructed of the probability of droplets deflecting or breaking up for each location of the arm around the full 360°.

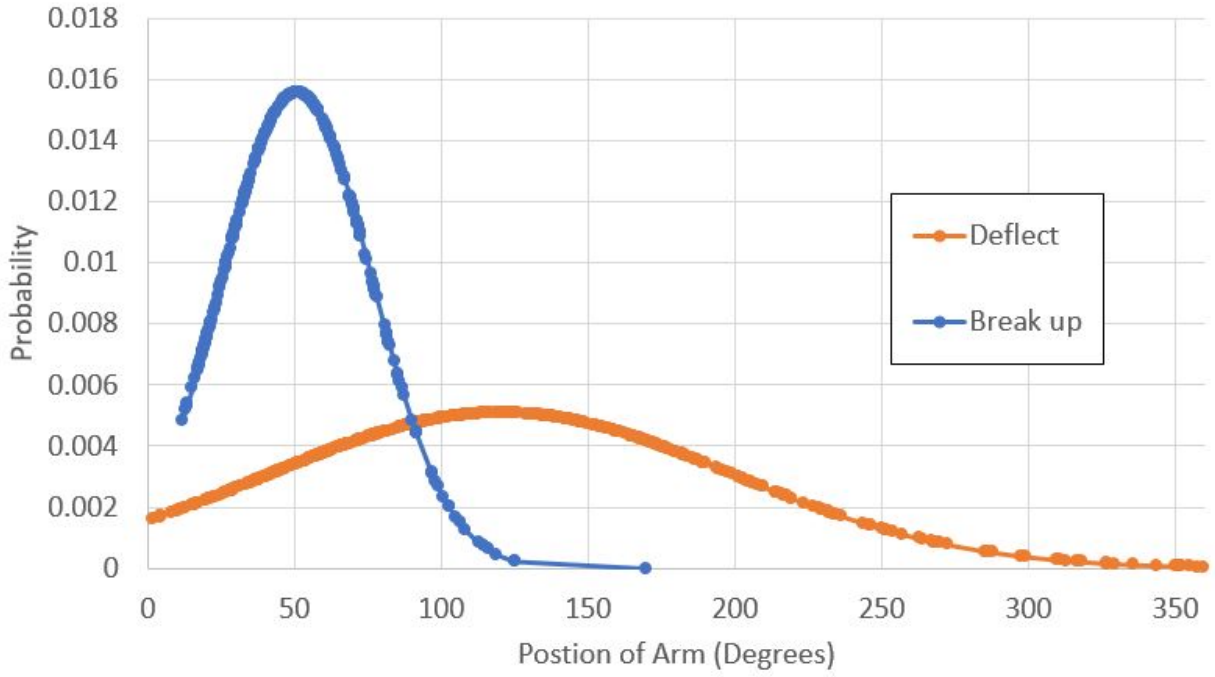

Figure 45: Position of Arm when Droplets Deflect or Break Up

Figure 45 shows that droplets deflect for the full rotation of the arm whereas break up occurs shortly after the arm has passed. The mean position of the arm for droplets that were deflected is 120°, compared the mean value of 50°, for droplet break up. As discussed before, for break up to occur a greater force is required therefore this occurs when the arm has recently passed and the aerodynamic wake is stronger, once the arm has passed 180°, no break up will occur.

The plots shown in Figure 45 were created using a best fit curve from the raw data. Histograms (Figures 46 and 47) show the data for the position of the arm for deflection and break up. The histograms are very similar to the best fit plots as expected, the only real difference is in Figure 46, where the best fit tends to zero at angles above 200°, there are still deflections occurring on the histogram. Whereas the best fit plots imply that there are close to no deflections occurring when the arm reaches the end of it's rotation.

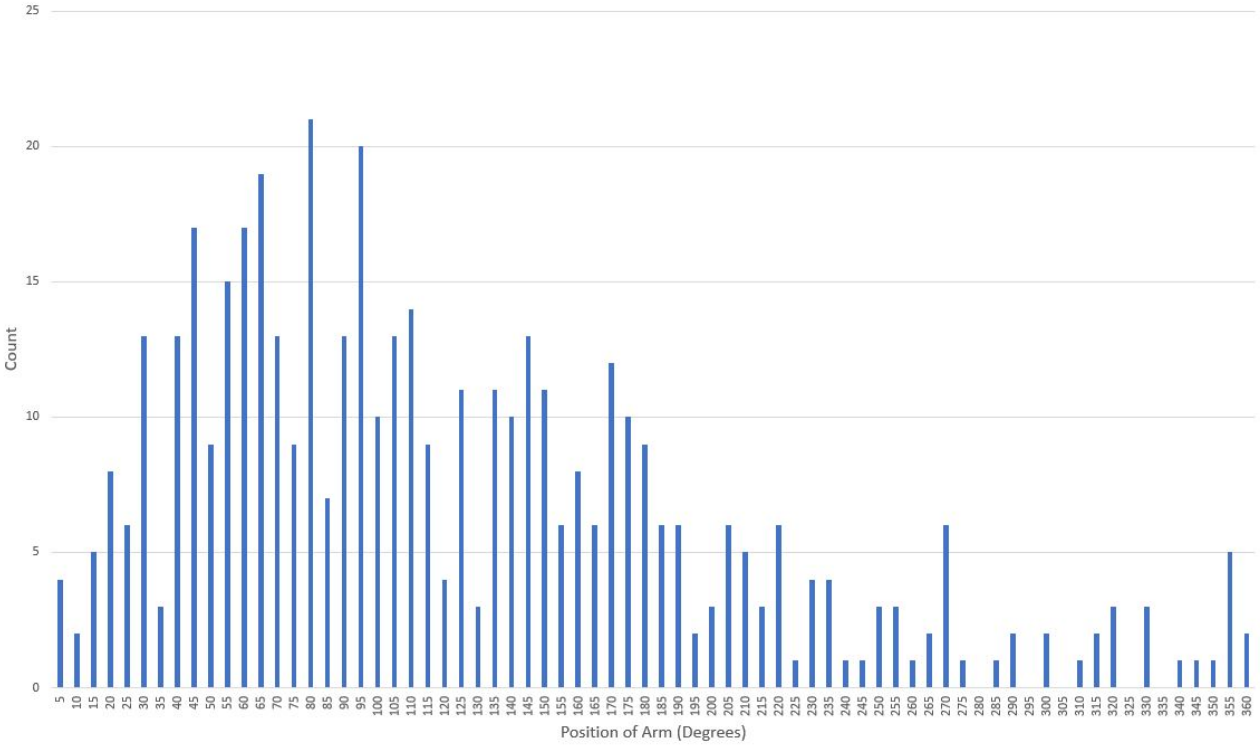

Figure 46: Histogram showing Position of Arm when Droplets Deflect

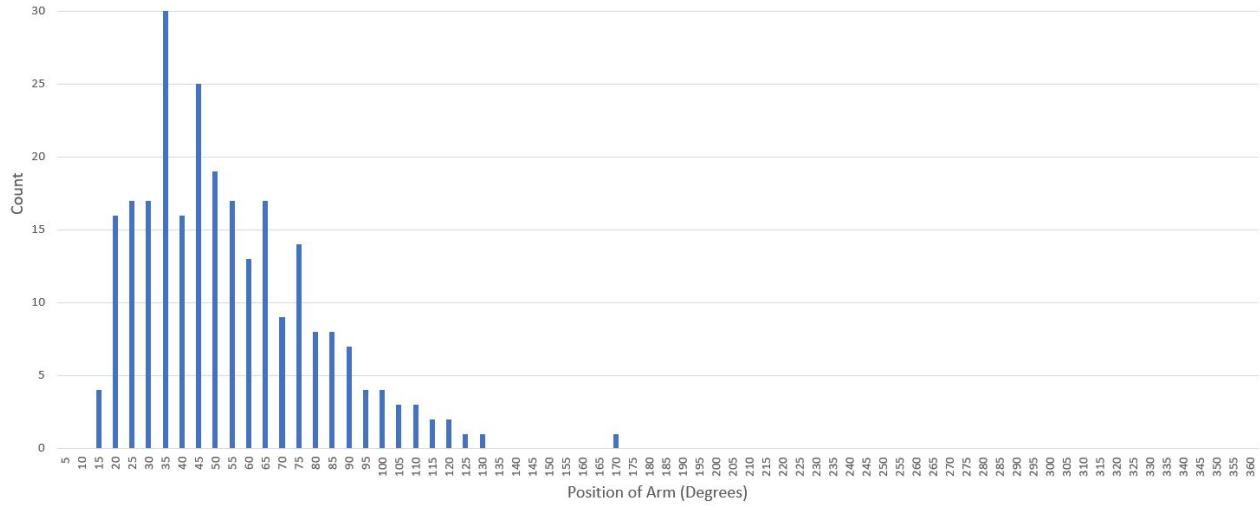

Figure 47: Histogram showing Position of Arm when Droplets Break Up

3.4 Scaling to Full Rig

The majority of the parameters investigated were measured using a few needles and will be affected with the whole test rig operating. This section discusses how to scale the characterisation results to full scale operation. Firstly, the vibrational analysis; nozzle radial position and droplet diameter were measured taking the full rig set-up into account, therefore they will not be changed.

The number of droplets forming and the number of impacts can easily be converted to include the whole rig. The original results were measured for three needles over 25.47s. Therefore it can be easily converted for impacts over the whole test rig. Determining the total number of droplets formed is not an important parameter as this does not affect the erosion rate. The number of impacts for the whole test rig is important to quantify. Table 13 converts the number of impacts from three needles over the 25.47s to impacts per second. Then that value is divided by three to determine the value for a single needle but also changed to be over a minute rather than a second. Finally this is multiplied by 72 to calculate the number of impacts for the whole test rig every minute.

Speed RPM	**Impacts**	**Impacts per needle per second**	**Impacts per needle per minute**	**Impacts per minute (Full rig)**
700	57	2.24	44.76	3222
800	54	2.12	42.40	3053
900	64	2.51	50.25	3618
1100	99	3.89	77.73	5597
1200	98	3.85	76.94	5540
1300	97	3.81	76.16	5484
1400	89	3.49	69.88	5031

Table 13: Converting impacts to impacts per minute for the full rig

The rig was commonly operated at 1200 rpm which corresponds to 5540 impacts per minute. Multiplying this value by 60 determines the number of impacts per hour, 335,820 impacts. Converting the impacts to impacts her hour is useful just to get a sense of scale, as most samples tested will as a minimum last close to an hour. Table 14 shows the impacts per hour for the different rotational speeds.

Speed RPM	Impacts per hour
700	193,320
800	183,180
900	217,080
1100	335,820
1200	332,400
1300	329,040
1400	301,860

Table 14: Impacts per hour for varying speeds

The strike location should be unaffected by the change from three needles to seventy two needles. There might be a slight change in the aerodynamics with all needles operating but this would be very insignificant and would not affect the strike locations. The strike locations were measured as a percentage therefore it is possible to determine how many droplets impact each area of the sample for a given time. Using the results from Table 14 in Table 15 demonstrates the impacts per location. These values can be utilised when examining the experimental results.

	A	B	C	D	E
700 RPM	9,206	55,234	73,646	27,617	27,617
800 RPM	18,950	18,950	101,065	31,583	12,633
900 RPM	31,924	44,693	51,078	57,462	31,924
1100 RPM	38,161	99,220	160,278	38,161	0
1200 RPM	49,860	83,100	141,270	41,550	16,620
1300 RPM	62,251	106,716	133,395	17,786	8,893
1400 RPM	54,884	82,326	116,628	34,302	13,721

Table 15: Strikes per Location at Varying Speeds over One Hour of Testing

In Section 3.3.5 the needle flowrate was given as the flowrate for a singular needle, by multiplying this value by 72 the flowrate for the whole test rig can be calculated, as shown in Table 16. As discussed in Section 3.3.5, after the test rig was upgraded a more accurate reading has been taken. The author used the same linear gradient on the previous volumetric flowrate and then transposed off the new reading for 350mm pressure head, of $6.03 L/hr$.

Pressure Head (mm)	**Volumetric Flowrate (l/hr)**	**Upgraded Volumetric Flowrate (l/hr)**
50	3.10	4.17
100	3.41	4.48
150	3.62	4.79
200	3.87	5.10
250	4.16	5.41
300	4.48	5.72
350	4.63	6.03

Table 16: Volumetric Flowrate of the Whole Test Rig

Finally the standoff height calculations are unaffected as they were evaluated with the whole test rig operating.

3.5 DNV-GL Standard

As mentioned in Section 2.4 the DNV-GL Standard is based on the R&D A/S test rig design. This leads to some of the specifications not agreeing with the optimal method for testing, as shown in Charactersation section. Firstly the standard states that there should be a minimum of three rotating arms that carry a sample. Previous work commissioned by ORE on the ETC rig [60] shows that the aerodynamic wake off a rotating arm lasts more than 180°. The results showing the position of the arm when droplets break up or deflection, as shown in Figure 45, also shows that droplets are deflected when the sample is past 180°. Therefore this means that even a set-up with 2 arms rotating may still see effects from the previous arm, never mind the three arms suggested by the DNV GL Standard. This CFD study was carried out on the ETC set-up therefore is not directly transferable to all test rigs, to determine the effects of extra arms characterisation should be conducted. Different radii and maximum rotational speeds will affect the aerodynamic wake and extensive characterisation work should be conducted to determine these effects, though from the work conducted in this thesis the author thinks it's highly unlikely that a three arm set-up could be designed where the aerodynamic wake isn't altering the droplets trajectories.

The Standard states the radius of the rotating arm should be a minimum of 1m, it is unclear why this is specified and a distance of 1m is chosen. As long as the tangential speed is comparable to a wind turbine then the radius does not matter. The radius could be important when considering the aerodynamic wake, as discussed above. Smaller radii will result in quicker rotations which will result in a short time between passes, whereas a longer arm won't have to rotate as fast to reach the same tip speed resulting in a longer time between passes. Instead of recommending a minimum distance for the radii of test rigs, the standard should consider the aerodynamic wake. A combination of maximum rotational speed, radius of arm and number of arms could be used to determine if the aerodynamic wake from a previous arm will affect any other arms and whether decreasing or increasing one parameter would improve this.

The Standard also discusses the inclusion of a side wall, again proper CFD analysis should be carried out to determine if the proposed side wall will affect the aerodynamics and how far away the side wall should be to avoid this. The Standard does state any influence of the side wall should be avoided but the author feels this should be clearer and have a quantifiable measurement. Next the Standard states that the angle of incidence of the sample should be 90°, this stops the aerofoil providing any lift which is crucial to the safety of operation.

The Standard states a minimum standoff height of 200mm but as explored in Section 3.3.7 this statement is not backed by experimental results. Figure 42 shows that the most preferable results occur with a standoff height of 50mm. This could be largely due to the inclusion of the plastic shrouds, as they allow the droplets to form while protected from the turbulent air. Above heights of 200mm, Figure 42 shows, the number of droplets falling straight does increase when compared to standoff heights of 100mm and 150mm. This demonstrates that there is some basis for the standard suggesting standoff heights greater than 200mm but they failed to consider the use of shrouds. The small standoff height with the inclusion of shrouds results in the droplet passing through free air for only 15mm, which greatly reduces the possibility of the trajectory being altered. Especially at speeds greater than 100m/s, with a standoff of 50mm, the shrouds offer an improvement on straight falling droplets of more than double compared to the greater standoff heights. This should be a section of the Standard DNV GL should consider changing as while this test was carried out on one particular set-up, the author does not see why varying set-ups would show any different results.

The Standard also states that the samples should have a gauge zone of at least 200mm. The gauge zone is the area on the specimen where erosion performance is evaluated, this is to avoid edge effects. The gauge zone also has to be smaller than the exposure zone, the exposure zone is the area the rain is distributed on. The exposure zone may be smaller or larger than the sample length. All of this leads to the sample being required to be greater than 200mm in length. Again there does not seem to be any numerical reasoning for this length, it just seems to be following the design of the R&D A/S test rig. The benefit of this system is that you get a range of speeds acting on the same sample and in theory can track the erosion rate as it spreads down the sample. However if you consider the potential issue with turbulent air as mentioned above then you will not accurately be able to quantify this. Currently different lengths of the sample correspond to a certain speed based on the radius and rotational speed. Then the rate of erosion can be tracked by watching where on the sample erosion is present, at the end where it has a faster linear speed the effects of erosion will be present earlier. Therefore rather than running multiple tests at different speeds, one test will, in theory, incorporate all the different speeds. The three arm system should result in more turbulent air which will affect the droplets trajectories therefore droplets will be pushed out of the way, meaning that tracking the erosion rate will not be as accurate. While there is no negative side to having a longer sample, it is unclear why a minimum size of 200mm is specified. Depending on the aim of experimental set-up having a smaller sample can also be of benefit.

The water droplet statistics are vague in the DNV GL, the only parameter specified is the

droplet diameter. For the droplet diameter the Standard states that the diameter should be $\sim 2mm$. The standard deviation for the droplet size is just "to be monitored". The Standard does state that the droplet size does have a large influence on the erosion behaviour. Therefore the standard deviation should be specified as well, currently there could be a range of droplets between 0-4mm but as long as the mean size is $\sim 2mm$ this would still meet the criteria. A standard deviation that makes the droplets consistent and similar to rainfall should be stated. The rain intensity is "to be measured" and the needles radial position is unspecified. These parameters should not be fixed, as different experiments will require a difference in these parameters. A better understanding of the problem will lead to clear guidelines on these parameters, so maybe this will be clarified in the future. Though some boundaries could be defined to make results easier to compare between different test rigs.

Finally the DNV GL Standard states the definition of incubation period as " The incubation period is defined as the exposure time until the first damage is visually detectable on the outer surface of the test specimen". This is different to the previous definition by Springer [33] as appreciable mass loss signifying the end of the incubation period. While the DNV GL definition does offer a clearer end point than Springer, "visually detectable" could still be improved on. Depending on the operators eye sight they will see a different result, under an optical microscope damage can be seen a lot earlier, this would still be classified as "visually detectable". A numerical reading that signifies the end of the incubation period would be beneficial, as this would clarify the long term confusion.

3.6 Discussion

The work carried out allows there to be a higher level of understanding of the test rig's operation, performance and influencing factors, while also providing data to determine the preferable operating conditions. When examining the number of strikes, the rotational speeds of 1100 and 1200 rpm provided the highest number of impacts which shows that avoiding the highest rotational speeds can be beneficial. The only reason the higher speeds were detrimental is that the aerodynamics caused more droplets to break up or deflect. Therefore if wanting to run at higher speeds more work would need to be carried out to decrease the aerodynamic wake. The same conclusion can be drawn when examining the standoff height, as findings suggest that avoiding 140m/s will provide more consistent results.

In addition the higher speeds lead to a far greater proportion of deflected droplets and droplet break up. Broken up droplets can affect the accurate measurement of the erosion rate, when droplets break up they form lots of smaller droplets, these smaller droplets can still impact the sample but will not be counted as they are less clear on the camera footage. This means that the number of impacts is not as accurate as it could be, there is almost a need to include fractions of droplets to categorise the broken up drops. However this is too difficult to achieve with the technology available. This shows the importance of avoiding break up, as it just leads to uncertainty when characterising the impacts. The erosion rate can be measured with respect to the kinetic energy imparted by the droplets but this is still difficult to assign values to partial droplets.

From the experiments carried out it can be seen that break up only occurs shortly after the arm has passed. Once the arm has passed 180°, no droplets will receive a great enough force from the aerodynamic wake to cause them to implode and break into smaller pieces. As discussed before, droplets that break up can still be impacted by the sample, which leads to difficulty in characterising those impacts. Therefore the test rigs could be controlled to switch off needles immediately after the arm has passed and then switch them back on when the arm is approaching. This would eliminate the potential from droplet break up and make the characterising process more consistent.

Looking at the droplet strike locations a mixed picture is observed, the radial view and tangential view provide opposing ideas on the preferable speed. Though both views do have 1100rpm and 1200rpm as the top two in terms of number of droplets impacting the centre. Above speeds of 1100rpm then there are a similar number of impacts in the centre of the sample. At these

higher speeds a smaller number of droplets impact the bottom third of the samples. To obtain a clearer picture, a larger sample size is required.

The mean droplet diameter when the test rig was stationary, with a pressure head of 350mm, is 2.27mm. A linear trend can be seen as the pressure head changes with respect to the droplet diameters, this is due to the slower flowrate allowing more water to collect in the droplet before it falls from the needle. When the test rig is operating the picture is not as clear, the average for a pressure head of 350mm is 2.61mm. This increase in diameter compared to the static set-up is due to the droplet being distorted by the aerodynamic wake present when the test rig is operating. The droplets can be warped by the aerodynamic wake and it is difficult to obtain an understanding of the droplet dimensions as we can only see a 2D image. The outliers on the diameter measurements, when the arm is spinning, are quite often down to limited clear pictures at that speed and pressure. Therefore these images have a greater impact on the average, with a very small sample size, and provide misleading results. The experimental method could also be improved as the DSLR camera was set to burst mode and therefore randomly taking photographs and not guaranteeing any images of droplets. Another difficulty was the droplets moving closer or further away from the camera thus becoming out of focus, this reduced the number of usable photos that could be used to measure the diameter. An improved method would have a camera set up in the radial and tangential direction therefore giving a clearer idea of how the droplets are distorting.

Another improvement in testing procedure, could be that droplets are characterised by volume instead of diameter. Currently the DNV GL standard and the ASTM standard both classify droplets in terms of diameter. However as shown with the droplet diameter study, when a test rig is operating the aerodynamics of the rotating arm causes the droplets to distort. Therefore depending on what axis you take a measurement of diameter will greatly affect the result. This problem could be overcome by changing the parameter recorded to droplet volume. When droplets become distorted they keep the same volume, therefore the measurements are consistent with the test rig operating or not. It would be easy to measure this you just need a beaker or measuring cylinder to collect the droplets, though this might be more challenging if you want to measure a singular droplet. It would be easier to measure droplets for a longer period of time and take an average. Regardless measuring droplet diameters is still a difficult task and changing this to volume would provide more consistent measurements.

The original manifold design saw a range of 14mm for the needle radial position and after the upgrades to the test rig this improved to a range of 2mm. This is a significant improvement

from the original design. There is a worry that this change in the impact area would influence the erosion rate but carried out on aluminium, the erosion rate seemed very similar. This is due to the turbulent air deflecting the path of the droplets, therefore this will create a spread of droplets regardless.

The flowrate experiments show an increase of around 10% in number of droplets for each 50mm increase in the pressure head. By converting these values into a volumetric flowrate, a maximum flowrate of 4.63L/hr was calculated. When the new manifold was used the flowrate measurements were taken again, with a flowrate of 6.03 L/hr measured. The difference in the flowrate is due to the new system having a purge system and therefore clearing the needles of any blockages. This new measurement was also useful in clarifying that the droplet diameter hadn't changed as there was only 0.01mm difference from the previous measurement. Flowrate is an important value to quantify and should be done periodically and this value is used to determine the number of impacts. The aim for the ETC test rig is to be scientific and accurate so these measurements are important to quantify the erosion rate by linking stages of erosion to number of impacts.

When analysing the DNV GL standard, it can be seen that there is some validity to the standoff height requirement as between 100mm and 200mm the results show no trends and the majority of droplets are deflected. Above heights of 200mm, the number of droplets falling straight does increase again. The reason the test rig at ETC performs better at a standoff height of 50mm is due to the plastic shroud. The plastic shrouds mean the droplets only have to travel a short distance in disturbed air. The aerodynamics in the ETC rig show that 50mm is the best standoff height for that rig. The DNV GL standard which gives minimum standoff height of 200mm is based on the R&D AS test rig which has different aerodynamic airflow and is correct for the R&D AS test rig design. This explain why the ETC rig is contradicting the DNV GL standard. The standard does have other areas where it could be more clear.

All of the results point towards the test rig operating at speeds of around 1100-1200rpm with a standoff height of 50mm to provide the greatest number of droplet impacts in the centre of the sample. The pressure head present in the test rig does not seem to affect the reliability of the results and raising the pressure increases the droplet flowrate thus increasing impacts.

The rigorous characterisation work has provided a platform to test samples for erosion, giving the user the fullest confidence in the impact frequency and what loading will occur. This is a crucial step that most other test rigs have not undergone, thus adding a level of uncertainty to the erosion results.

4 Understanding Erosion

Industry uses a standard test as a means of assessing a blade coating system by testing a single material and hence characterising it's erosion. However, to better understand erosion a variety of materials need to be tested, as different materials will lead to different failure mechanisms therefore conclusions should not be drawn from investigating only one material. In the present work, the approach is to firstly test aluminium samples, to analyse the effect of the impact velocity on the erosion rate. Thereafter a series of coated composite samples is examined and their characteristic erosion resistance assessed.

Examples of the aluminium samples tested are as shown in Figure 48, with (a) showing the erosion of an aluminium sample after 3 hours and (b) after 6 hours. While testing the aluminium samples mass loss curves were developed to examine the incubation period and erosion rate. Once the aluminium samples have been tested to gain an understanding of the erosion rate inflicted by the test rig, an XCT will be used to examine what occurs sub-surface. The XCT images provide a useful insight into an area of erosion that is not usually explored. Sub-surface defects could play a crucial part in erosion initiation and studying their affect will help increase the lifetime of coatings.

(a) Aluminium sample after 3 hours (b) Aluminium sample after 6 hours

Figure 48: Aluminium samples being tested at a rotational speed of 1200RPM

The characterisation results from Section 3.3, can be used to determine the operating conditions for experimental tests and then can be used to quantify the number of impacts, location of impacts etc. This knowledge can provide a basis for the experimental results, rather than just stating a sample lasted for a fixed period of time in a test rig, the results can be stated having experienced a certain number of impacts and each droplet having a certain diameter. The results

from the characterisation section provide context, which provides a greater understanding of the experimental results.

The characterisation tests were run at various speeds, which showed rotational speeds of 1100 and 1200 RPM to provide the most consistent result, in terms of number of impacts, when compared with faster speeds which were associated with more turbulence and thus, increased droplet break up. The water pressure head of 350mm was used for all tests and if the tests required a slower erosion rate then the number of needles was reduced. From the previous characterisation work, in Section 3.3.4, the droplet diameters for each of the number of needles is as follows: 72 needles - 2.27mm, 36 needles - 2.13mm and 24 needles - 2.08mm.

For experiments of the aluminium samples the rotational speed changed in 50RPM increments due to the this being a more appropriate step size for the aluminium samples, however the characterisation work was completed earlier. This means certain statistics such as impacts etc, are not available therefore an average is taken from the values either side of the required speed. For example, at 1200RPM 24 impacts were recorded over the given time period and at 1300RPM 22 impacts were recorded. Henceforth at the rotational speed of 1250RPM, 23 impacts was used. Due to the overall variability in the experiments, this represents a reasonable averaging of the data sets.

The kinetic energy of each impact is calculated as it can be a useful metric to compare mass loss curves. The kinetic energy is calculated by using the droplet diameter to determine the volume of an individual droplet, then multiplying that by the density of water to convert it to mass of a droplet. Then by using the number of impacts determined in Section 3.3.2 the kinetic energy per minute of testing can be determined. This process was undertaken for all the different rotational speeds as well as the different number of needles operating, the results are shown in Table 17.

The range of kinetic energy present in Table 17 shows the importance of the characterisation work. Even a small change in number of impacts is shown to have a great effect, though the rotational speed does have the greatest effect on the kinetic energy.

Another point of note, is that the manifold of the test rig was upgraded during the latter stages of the testing programme as mentioned in Section 3.3.6. This happened during the testing of the aluminium samples so these are the only results that will be effected. The manifold was altered after samples tested at 1100 and 1150 RPM had been tested to 7 hours. This could affect the mass loss curves but will be discussed further in Section 4.1.

Rotational Speed (RPM)	Linear Velocity (m/s)	Number of Needles	Droplet Diameter (mm)	Impacts per 3.639s for 3 Needles	Impacts per Minute for 72 Needles	Volume of Droplet (m^3)	Mass of Droplet (kg)	Kinetic Energy of Droplet (J)	Kinetic Energy per Minute (J)
1000	107.3	72	2.27	12	4749	$6.12X10^{-9}$	$6.10X10^{-6}$	0.035	167.04
1100	118.1			19	7519			0.042	320.01
1150	123.4			21.5	8508			0.047	395.79
1200	128.8			24	9497			0.051	481.06
1250	134.2			23	9101			0.055	500.24
1300	139.5			22	8706			0.059	517.53
1000	107.3	36	2.13	12	2374	$5.06X10^{-9}$	$5.05X10^{-6}$	0.029	69.00
1100	118.1			19	3759			0.035	132.19
1150	123.4			21.5	4254			0.038	163.49
1200	128.8			24	4749			0.042	198.72
1250	134.2			23	4551			0.045	206.64
1300	139.5			22	4353			0.049	213.78
1000	107.3	24	2.08	12	1583	$4.71X10^{-9}$	$4.70X10^{-6}$	0.027	42.84
1100	118.1			19	2506			0.033	82.07
1150	123.4			21.5	2836			0.036	101.50
1200	128.8			24	3166			0.039	123.37
1250	134.2			23	3034			0.042	128.28
1300	139.5			22	2902			0.046	132.72

Table 17: Kinetic Energy for Droplet Impacts

4.1 Droplet Speed Study

The impact velocity is one of the main parameters that affects the erosion rate, therefore analysing it's effect is crucial to understanding the problem. It is expected that increased impact velocity will result in a higher erosion rate but it is unclear what trend this will follow. Aluminium samples were used to investigate the impact velocity as it is a homogeneous, isotropic material, as well as lacking any defects that might be present when manufacturing composite materials. This makes aluminium a repeatable material that should provide consistent results, meaning that the only variable being altered in these tests, is the impact velocity and not any factors associated with the material properties.

The method used for determining erosion rate is to measure the mass loss, which results in a plot of the mass loss vs number of impacts as shown in Figure 49.

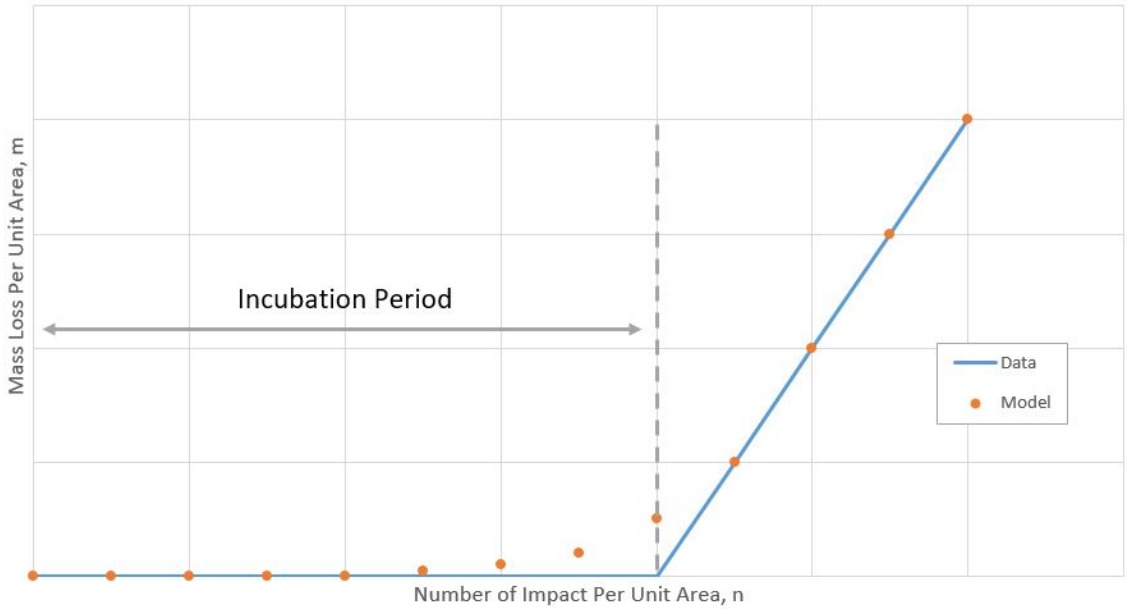

Figure 49: Mass loss vs Number of Impacts

From Figure 49 important conclusions about the erosion rate can be determined. Firstly the time or number of impacts until the end of incubation period is determined, this is an important point to classify as it is the last point the material can be said to be undamaged. Therefore repairs can be carried out easily, before the erosion rate accelerates and quickly becomes severely damaged. Also from the mass loss vs number of impacts plot, the gradient of the curve (the erosion rate) is calculated and the change in erosion rate is an important parameter to determine. This could be used to control wind turbines, by slowing down the turbine and

therefore reducing the number of impacts hence prolonging the lifetime of a wind turbine to allow sufficient time to repair it.

4.1.1 Aluminium Sample Results

The aluminium samples used are 3003 grade aluminium as specified in the DNV GL standard [36]. The samples were weighed using electronic scales that could achieve an accuracy of 0.0001g. Ideally the samples should be dried out, by using an oven or something similar, at a low heat to extract any moisture from inside the sample. This makes the mass loss measurement more accurate, as the initial mass was measured without the presence of water so all future measurements should be carried out at the same state. This option was not available to the author, as the samples also had to be transported from ETC to the university, as ETC did not have scales to the required degree of accuracy. The lack of options on drying out the samples plus the potential for damage on transportation means that there could be some minor errors introduced to the mass measurements. However this should only affect the mass during the incubation period as once the mass loss becomes considerable, these small changes will not have much effect. This means that the measurements taken during the incubation period will be effected and therefore it was decided for any value below a mass loss of 0.005g is effectively zero as changes less than that could be due to the other factors mentioned. Also during the incubation period occasionally there was an increase in the mass due to the factors mentioned above.

The aluminium samples were eroded at varying speeds from 1100RPM - 1300RPM in 50RPM increments. Samples were also measured at speeds of 1000RPM but after 9 hours of testing there were no signs of erosion and the mass loss had not changed significantly. Due to a lack of time the samples at 1000RPM were ignored, the speed of 1050RPM was also ignored as this is a speed at which resonance occurs, as mentioned in Section 3.3.1.

As mentioned before in Section 3.3.6 the manifold was changed during the droplet speed study. The samples tested at 1100 and 1150 RPM had been tested for 7 hours and the first of the 1200RPM samples had been fully tested before the alterations. When studying the results, the effect this alteration might have had will be discussed further.

Table 18 shows the mass of all samples at the various speeds. Initially the mass was recorded at times of 3, 5, 7, 9 and 11 hours and with initial measurements, at speeds of 1100RPM these times showed enough points on the mass loss curve. Whereas when speeds of 1300RPM

were explored, at 3 hours there was already a significant mass loss, therefore the mass loss was measured more frequently.

Sample	Speed (RPM)	Initial Mass (g)	Mass at 1 hour (g)	Mass at 2 hours (g)	Mass at 3 hours (g)	Mass at 4 hours (g)	Mass at 5 hours (g)	Mass at 7 hours (g)	Mass at 9 hours (g)	Mass at 11 hours (g)
AL003	1100	44.0069	-	-	44.0056	-	44.0062	44.0078	43.9984	43.9611
AL004	1100	44.0756	-	-	44.0738	-	44.0750	44.0771	44.0688	44.0330
AL010	1150	44.0873	-	-	44.0873	-	44.0890	44.0613	44.0179	-
AL011	1150	44.1521	-	-	44.1516	-	44.1514	44.1142	44.0749	-
AL006	1200	43.9544	-	-	43.9531	-	43.9392	43.8830	43.8279	-
AL018	1200	43.9762	-	-	43.9728	-	43.9265	43.8586	-	-
AL022	1200	43.8049	-	-	43.8004	-	43.7311	43.6898	-	-
AL024	1250	43.9429	-	-	43.9212	-	43.8659	-	-	-
AL025	1250	43.7653	-	-	43.7406	-	43.6870	-	-	-
AL021	1250	44.0468	-	44.0434	-	-	-	-	-	-
AL019	1300	43.8461	43.8460	43.8360	43.8059	43.7738	-	-	-	-
AL020	1300	44.1368	-	-	44.0871	44.0530	-	-	-	-

Table 18: Results for Droplet Speed Study

Table 18 shows how as the impact speed increases it takes a shorter time to reach a similar mass loss. All experiments were stopped when considerable mass loss was achieved, around 0.05g. It was important when carrying out the experiments to capture a point around the end of the incubation period, as once the sample has passed this point the mass loss will accelerate quickly before settling on a constant gradient.

Table 19 shows the mass loss of the aluminium samples at an impact speed of 1100RPM. The results are consistent across the two samples with the mass loss being similar at all time measurements. After around 9 hours the mass loss rate increases as until then the mass loss is effectively zero. Interestingly at 7 hours there is an increase in mass, which as mentioned before is attributed to the samples not drying out properly.

Sample	**Mass Loss 3 hours (g)**	**Mass Loss 5 hours (g)**	**Mass Loss 7 hours(g)**	**Mass Loss 9 hours(g)**	**Mass Loss 11 hours(g)**
AL003	0.0013	0.0007	-0.0009	0.0085	0.0458
AL004	0.0018	0.0006	-0.0015	0.0068	0.0426
Average	0.00155	0.00065	-0.0012	0.00765	0.0442

Table 19: Mass Loss for Aluminium Samples at 1100RPM

Table 20 shows the mass loss of the aluminium samples at an impact speed of 1150RPM. Again the results are consistent across all time measurements though a bigger divergence at 7 and

9 hours is observed. The incubation period will be between 5 and 7 hours as this is where the mass loss changes from negligible to significant. Ideally a measurement of 6 hours would have been recorded as that would give a more accurate representation of the end of incubation period.

Sample	**Mass Loss 3 hours (g)**	**Mass Loss 5 hours (g)**	**Mass Loss 7 hours(g)**	**Mass Loss 9 hours(g)**
AL010	0.000	-0.0017	0.026	0.0694
AL011	0.005	0.0007	0.0379	0.0772
Average	0.00025	-0.0005	0.03195	0.0733

Table 20: Mass Loss for Aluminium Samples at 1150RPM

Table 21 shows the mass loss of the aluminium samples at an impact speed of 1200RPM. For this speed three samples were used, as AL006 was completed and then the test rig set up was changed, this showing that the test rig is more erosive with the improved set up. All samples were examined but the difference between AL006 and the rest were noted at various stages. Another interesting anomaly is the big difference in mass loss between AL018 and AL022 at 5 hours before reaching a similar mass loss at 7 hours. It is unclear why this has happened, potentially there could be a defect in sample AL022 that caused a stress concentration, thus accelerating the erosion rate. Once this defect has caused the mass loss in that area, the sample then returned to a normal erosion rate. Again the incubation period is between 3 and 5 hours and measuring the mass loss at 4 hours would have been preferable with a longer time frame.

Sample	**Mass Loss 3 hours (g)**	**Mass Loss 5 hours (g)**	**Mass Loss 7 hours(g)**
AL006	0.0013	0.0152	0.0714
AL018	0.0034	0.0497	0.1176
AL022	0.0045	0.0738	0.1151
Average	0.0031	0.0462	0.1014

Table 21: Mass Loss for Aluminium Samples at 1200RPM

Table 22 shows the mass loss of the aluminium samples at an impact speed of 1250RPM. When measuring the erosion rate, the samples had already passed the end of the incubation period

by the time the first measurement was taken at 3 hours. Therefore with the short time frame it was decided to run a singular sample, stopping it at 2 hours to get a clearer picture of when the incubation period occurs. Samples AL024 and AL025 both provided consistent results with a similar mass loss at all times.

Sample	**Mass Loss 2 hours (g)**	**Mass Loss 3 hours (g)**	**Mass Loss 5 hours(g)**
AL021	0.0034	-	-
AL024	-	0.0217	0.077
AL025	-	0.0247	0.0783
Average	0.0034	0.0232	0.07765

Table 22: Mass Loss for Aluminium Samples at 1250RPM

Table 23 shows the mass loss of the aluminium samples at an impact speed of 1300RPM. Again sample AL020 was eroded to three hours before measuring the mass loss, this means it is significantly past the incubation period. Therefore sample AL019 was measured at hourly intervals to more accurately detect the incubation period.

Sample	**Mass Loss 1 hour (g)**	**Mass Loss 2 hours (g)**	**Mass Loss 3 hours(g)**	**Mass Loss 4 hours(g)**
AL019	0.0001	0.0101	0.0402	0.0723
AL020	-	-	0.0497	0.0838
Average	0.0001	0.0101	0.04495	0.07805

Table 23: Mass Loss for Aluminium Samples at 1300RPM

All of the above mass loss measurements can be combined to create Figure 50, showing the curves for rotational speeds, from 1100-1300RPM. This figure shows the incubation period, where mass loss is negligible, and the erosion rate (gradient of the line). This can be used to compare the varying speeds for these different factors.

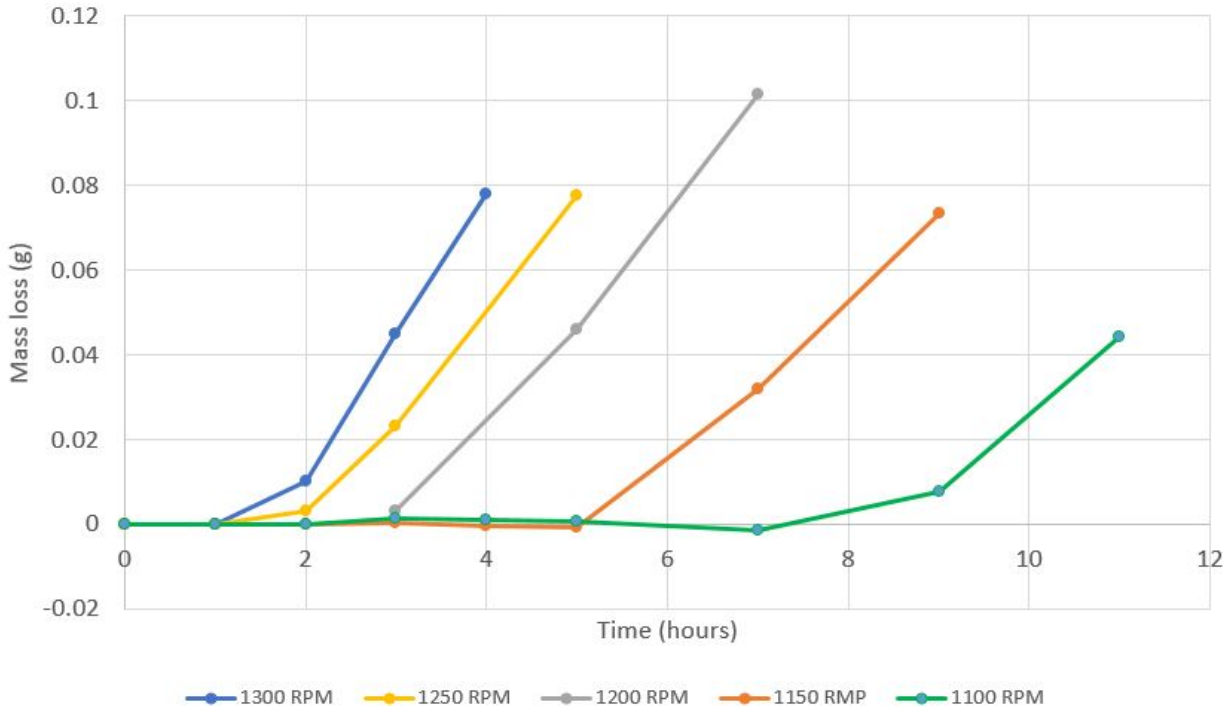

Figure 50: Mass loss vs Time for all impact speeds

As expected the quicker the rotational speed, the shorter the incubation period and the steeper the gradient. Once the end of incubation period has been reached the gradient of the line increases rapidly and should be constant, as stated in Springer [33]. For speeds 1150RPM and 1200RPM there is a near constant gradient due to the times the mass was recorded being close to the end of incubation period. Whereas with other speeds it is less clear where the incubation period ends and so, to combat this calculations can be used to determine the end of incubation period. Each plot has a minimum of two points on the steep gradient, these points can be used to calculate the end of the incubation period, using the assumption that the gradient is constant.

4.1.2 Predicting Mass Loss Curves

Plotting the two points gives a linear equation for the line between them, in the form of y=mx+c. As the incubation period ends when mass loss becomes significant it is assumed this occurs when $y \sim 0$. This process can be continued for all rotational speeds, with the results being shown below in Table 25.

Speed (RPM)	1100	1150	1200	1250	1300
End of Incubation Period (hrs)	8.57	5.45	3.32	2.15	1.69

Table 24: Calculated times for end of Incubation Period

Using these values, the mass loss curves can be plotted again giving a more accurate representation of what is occurring. Figure 51 shows this with the estimations of incubation period included.

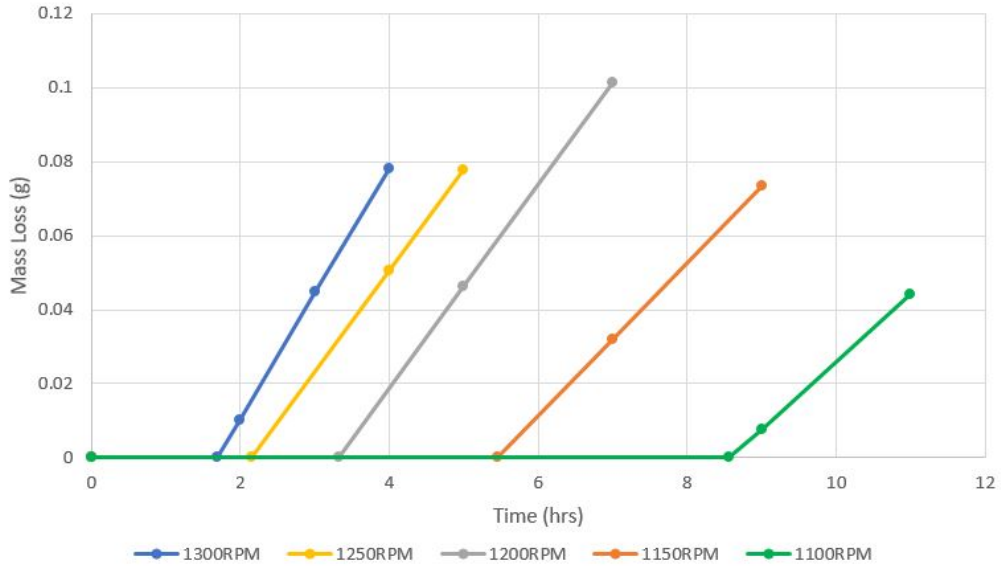

Figure 51: Mass loss curves, using estimations to determine the incubation period

From this similar trends in the gradient and the incubation period are apparent. From the graphs used to estimate the end of incubation period the gradient can be determined, therefore the trend can be plotted to predict what the mass loss curves would look like for other rotational speeds. Table 25 shows the measurements taken for the incubation period and gradient for 1100-1300RPM as well as the predicted values.

Speed (RPM)	End of Incubation Period (hrs)	Gradient of curve
1500	0.48	0.063
1450	0.73	0.054
1400	1.08	0.047
1350	1.61	0.04
1300	1.69	0.034
1250	2.15	0.027
1200	3.32	0.028
1150	5.45	0.021
1100	8.57	0.018
1050	17.79	0.016
1000	26.54	0.014
950	39.60	0.012
900	59.07	0.01
850	88.13	0.009
800	131.47	0.008
750	196.13	0.007
700	292.60	0.006

Table 25: Calculated times for end of Incubation Period and Projections for Slower and Faster Speeds

Table 25 displays a method for predicting the mass loss curves for rotational speeds that have not been tested. Figure 52 shows the mass loss curves from 1500RPM to 1200RPM. From incubation period and gradient it can be seen that the incubation period grows exponentially, plotting the line of best fit gives an equation of:

$$T_I = 79126e^{-0.008\omega}$$

where T_I is the time to the end of incubation period and ω is the rotational speed. This equation only accurately predicts the time to the end of the incubation period for this set-up, a different test rig would require its own estimation to be developed. Figure 52 plots the estimations of the mass loss curves for the speeds from 1500RPM to 1350RPM and also includes the curves for 1300, 1250 and 1200RPM as a comparison.

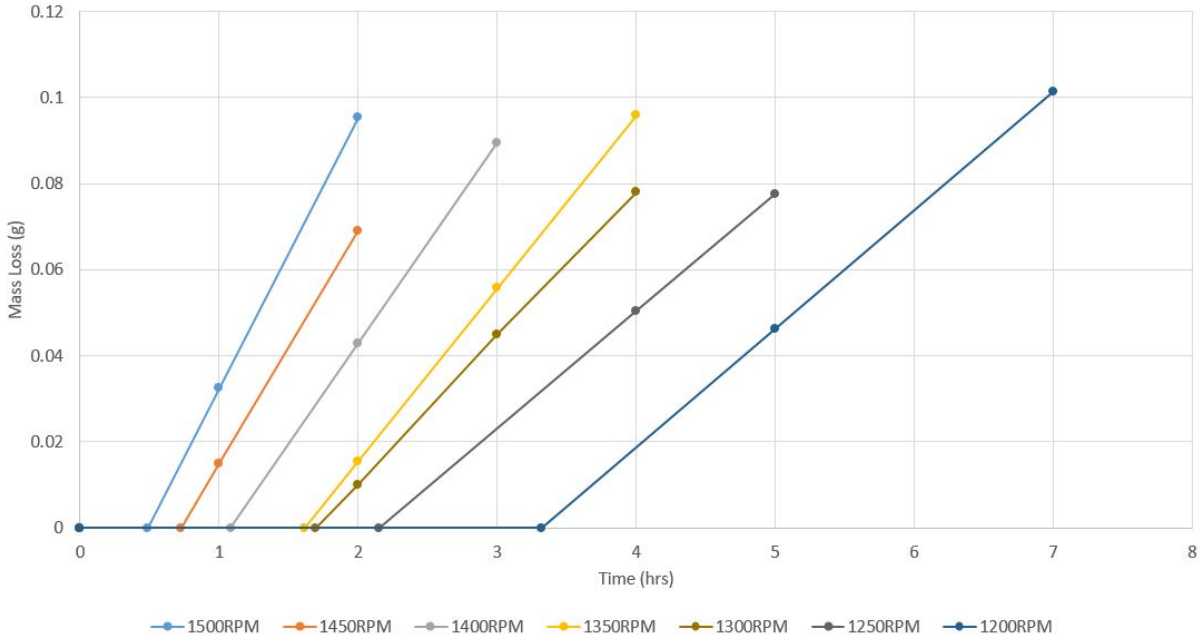

Figure 52: Predicted mass loss curves, for rotational speeds greater than the ones tested

Figure 52 shows that the gradient is steeper for higher rotational speeds even with the predictions which aligns with the measured results. This confirms that increased rotational speed directly relates to the rate of mass loss. Further to this, the mass loss curves were then analysed with respect to the number of impacts rather than time passed, in order to compare trends between the variable factors.

4.1.3 Number of Impacts

Using the number of impacts calculated in Section 3.3.2 these values can replace the time passed on the mass loss curves. Figure 53 shows the mass loss vs number of impacts curve, it is very similar to Figure 50 with only the gradients being slightly different.

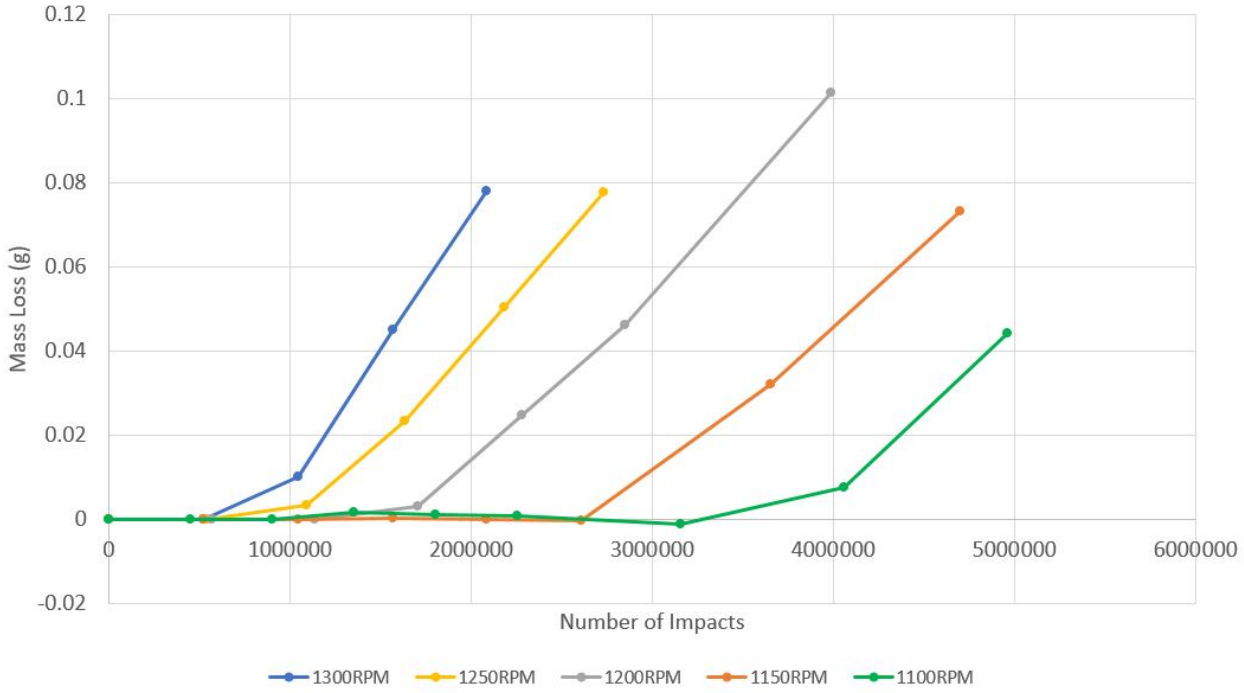

Figure 53: Mass loss vs Number of Impacts for all rotational speeds

As with the previous mass loss curves, with time on the x-axis the incubation period can be determined by assuming the mass loss curve is linear after the end of incubation period.

Speed (RPM)	**Number of Impacts**
1100	3,870,554
1150	2,849,852
1200	1,773,762
1250	1,173,403
1300	885,554

Table 26: Number of Impacts to reach the end of Incubation Period for varying Rotational Speeds

The results displayed in Table 26 present very similar results to Figure 51. The Figure using number of impacts rather than time is almost identical therefore there is no need to display it as well.

4.1.4 Kinetic Energy

Another method for displaying and representing mass loss curves is to use kinetic energy as the x axis. The rationale behind this is that damage or wear inflicted on a material will be due to work done on the material, thus measuring the droplets by kinetic energy could be more effective in predicting the lifetime of a material. The calculations in Table 17 are used to determine the kinetic energy per droplet impact. The use of kinetic energy to quantify the mass loss should result in different curves to those seen in Figures 50 and 53 as there is a v^2 component to the kinetic energy equation. The mass loss curves using kinetic energy are shown in Figure 54.

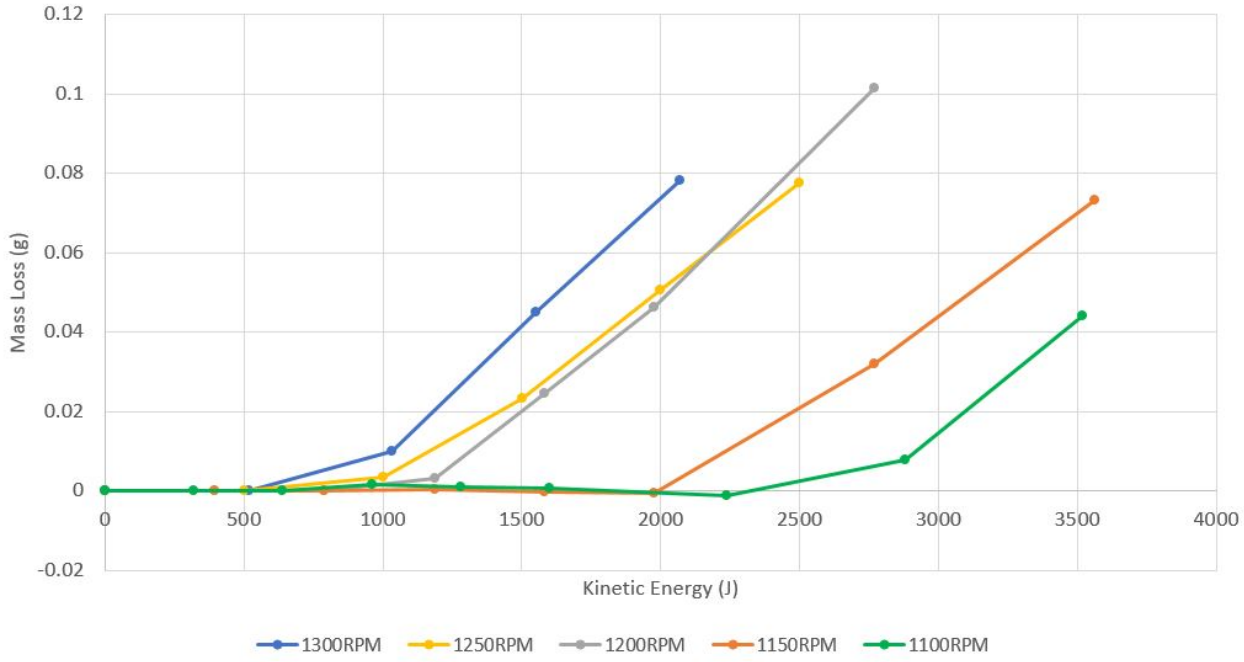

Figure 54: Mass loss vs Kinetic Energy for varying rotational speeds

Figure 54 shows different mass loss curves than the others. Firstly the gradient of the curves does not fall the same trend, the rotational speed of 1200RPM has a steeper gradient than the others. Secondly the end of the incubation period does not occur as evenly spaced. The speeds of 1300, 1250 and 1200RPM are more tightly grouped. As mentioned in Section 4 the tests at speeds of 1100 and 1150RPM were mainly tested before the rig was altered. This means that potentially the kinetic energy required to reach the end of the incubation period is similar regardless of rotational speed, looking at 1200, 1250 and 1300 this holds true.

Using the same method as before the end of incubation period can be predicted, the results are

shown in Table 27. From the predicted times, it is shown that there is still a tight grouping between the rotational speeds from 1200RPM to 1300RPM.

Speed (RPM)	Kinetic Energy (J)
1100	2,746
1150	2,161
1200	1,148
1250	1,075
1300	878

Table 27: Kinetic Energy to reach the end of Incubation Period for varying Rotational Speeds

Using the values shown in Table 27, the mass loss curves can be predicted. Figure 55 displays the mass loss curves with the calculated representation of the end of incubation period and the same gradient as the results.

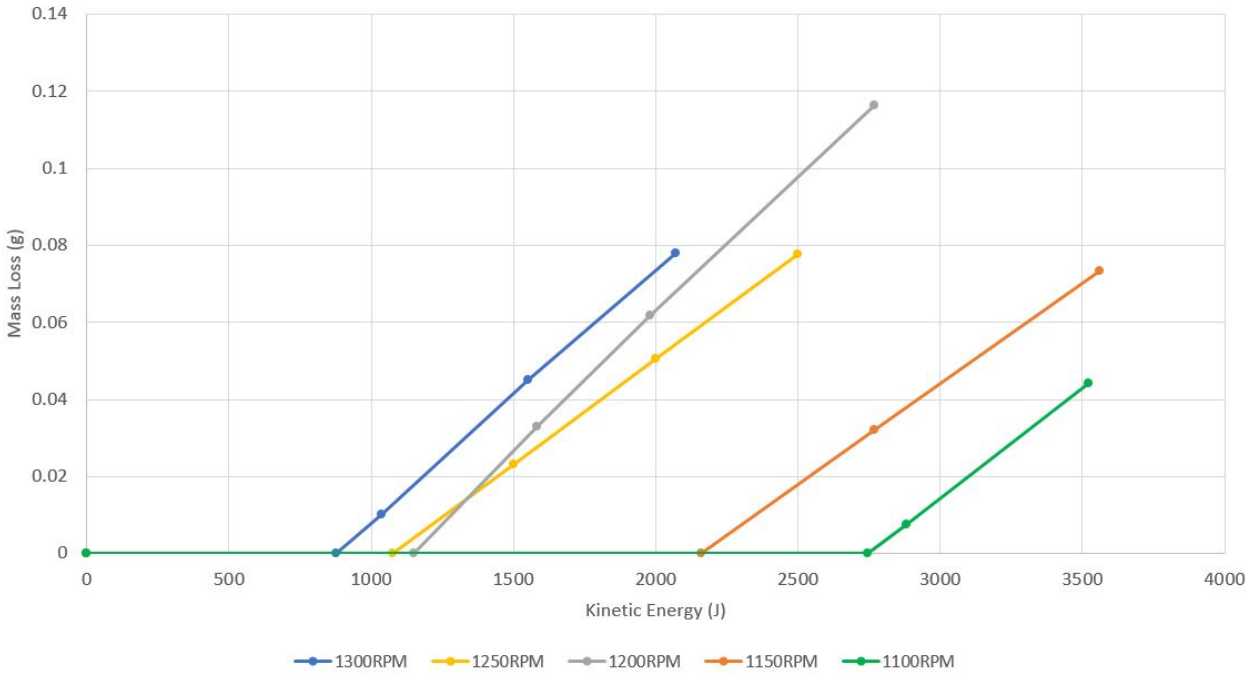

Figure 55: Estimation of mass loss curves for all rotational speeds

From Figure 55, the speed of 1200RPM provides the most interesting result. The erosion rate (gradient) is the steepest of all samples, this leads to one of two possibilities. Either the results for 1200RPM are incorrect, for some reason potentially the altering of the test rig, and the mass loss curves follow a similar pattern to the previous version that used time and number of

impacts to quantify the curve. The other option is that the 1200RPM shows that when using kinetic energy to plot mass loss curves there is not the same trend as before and that a similar mass loss curve will be present regardless of rotational speed. This would be a very useful result as the end of incubation period could be quantified before testing, however further tests need to be conducted to check if this is true.

4.1.5 Incubation Period

Plotting mass loss against the number of impacts is still useful as it is a preferable method for comparing different test rig set-ups. Different set-ups can having varying numbers of needles and various lengths of impact areas, using number of impacts will make results more comparable than a simple time measurement. The DNV GL standard recommends results are displayed with axis of impact velocity and number of impacts, to plot the time taken to reach the end of incubation period.

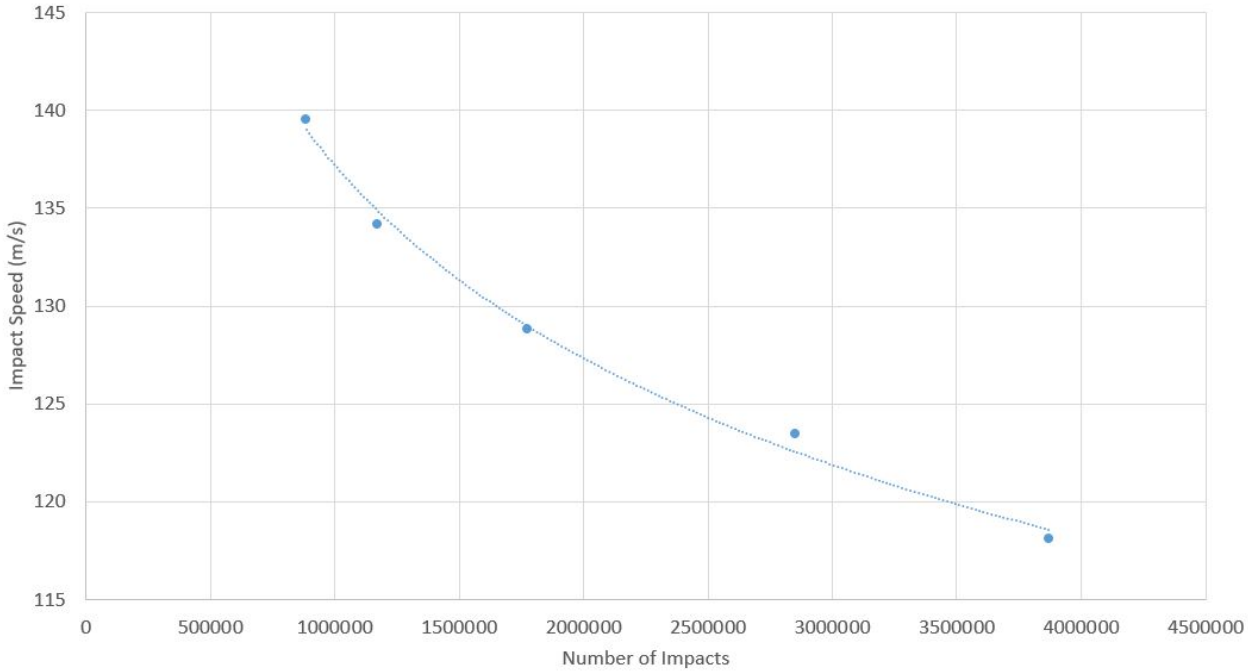

Figure 56: End of Incubation Period for impact speeds of 140-115 m/s

Figure 56 plots the end of incubation period for a variety of rotational speeds. The speed is now given as a linear impact speed, as Figure 56 would be used to compare test rigs, rotational speed would not be as preferable as different test rigs would have different radii. Plotting a curve of best fit, gives a power curve with the equation $V = 608.12I^{-0.10777}$ where V is rotational speed

and I is the number of impacts. The end of incubation period can be predicted using this best fit curve for a wider range of rotational speeds.

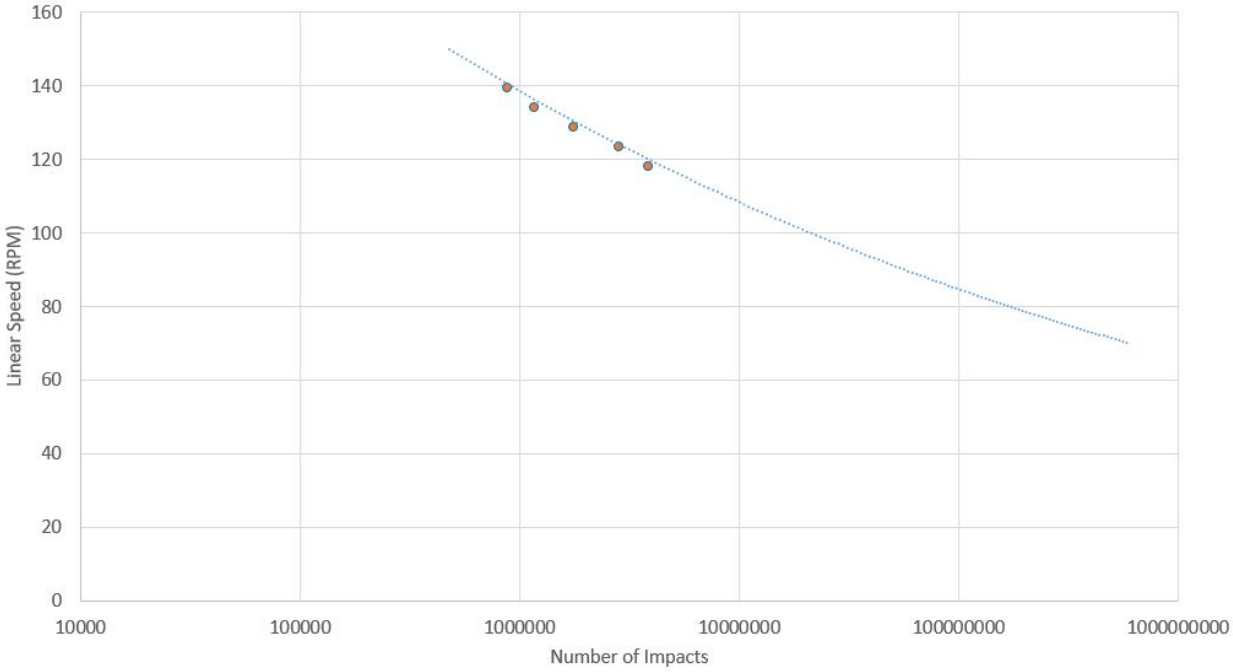

Figure 57: Prediciton of End of Incubation Period for impact speeds of 150-70 m/s with x-axis in a logarithmic scale

Figure 57 displays the result with a logarithmic scale in the x-axis, showing the logarithmic nature of the trend. The minimum speed of 70m/s was chosen was at speeds lower than that the time would be so great it becomes difficult to quantify. For an impact speed of 70m/s the number of impacts required to reach the end of incubation period is 5.95×10^8. Taking the 14 impacts per 3.639s, determined in Section 3.3.2, this leads to 1790.7 days of constant testing. Using the equation for the best curve fit, the number of impacts at a rotational speed of 50m/s to reach the end of incubation is 41,563 days of constant testing. This shows at the speed of 50m/s the lifetime is much greater than the expected usage of a wind turbine. At a rotational speed of 150m/s the number of impacts required is 480,054 which equates to roughly 27 minutes of testing. These values show the extremes of the testing and how an S-N style curve could be produced for erosion as used in fatigue testing.

Instead of using number of impacts to plot end of incubation period, kinetic energy can be used. Figure 58 plots rotational speed against kinetic energy for the time to reach the end of incubation period.

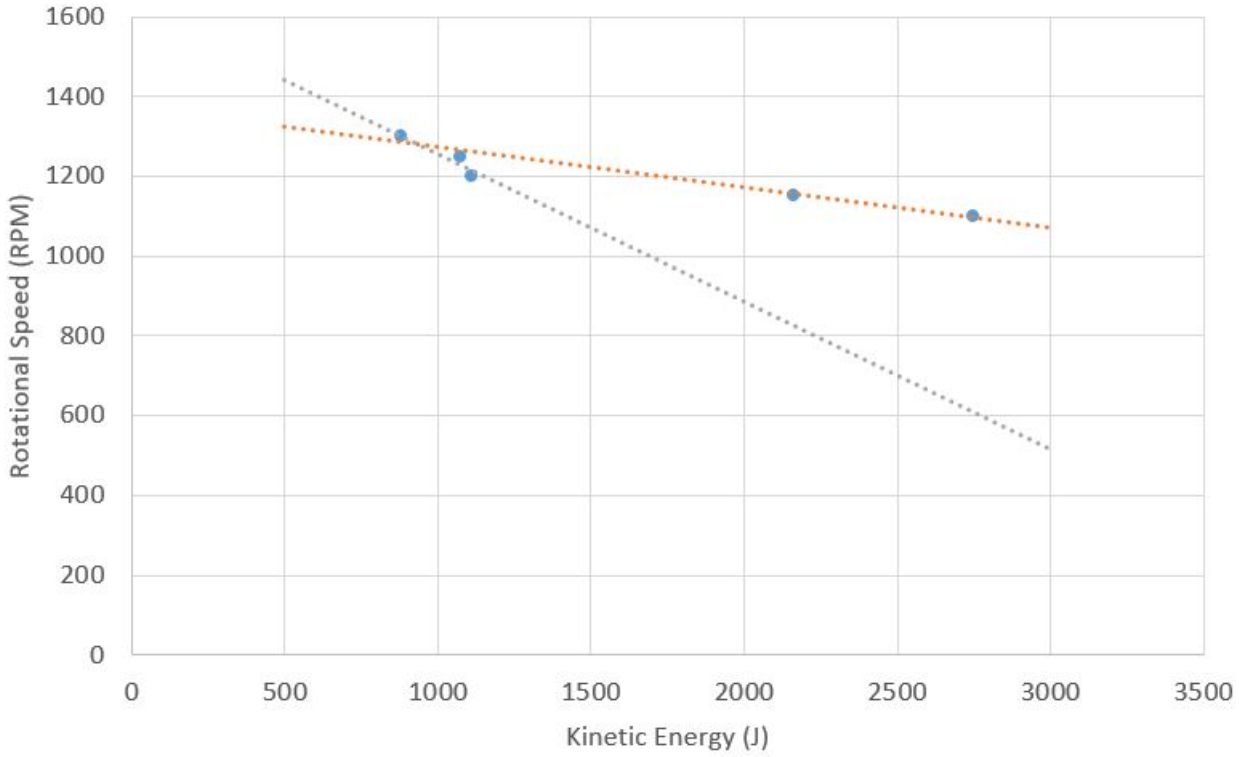

Figure 58: End of Incubation Period for rotational speeds of 1300-1100RPM using Kinetic Energy as x-axis with two options of best fit curve included

Figure 58 shows the points measured in the experiments and includes two lines of best fit. As mentioned before the change in experimental set-up makes it unclear whether the measurements for 1150 and 1100RPM are accurate. Figure 58 plots two differing lines of best fit, which are significantly different. The orange best fit line includes the lower rotational speeds and the grey line does not. Further work would be required to clarify which of these two scenarios is correct but given the very high speeds at the upper end of the range is well beyond the operating speeds ot the main bulk of the tests, this is deemed not part of the current work and should be considered in future work.

4.1.6 Repeatability

Aluminium samples are used as a calibration tool to investigate parameters such as impact velocity and impact frequency. To insure that the parameter study is reliable the results need to be repeatable. The DNV GL standard states that calibration tests using aluminium specimen should lead to a coefficient of variation, COV of less than 20%.

$$COV(N_{fit}(v_{ref})) = \frac{s(N_{fit}(v_{ref}))}{\overline{\mathrm{x}}(N_{fit}(v_{ref}))}$$

with

s = standard deviation for specific number of impacts, N

$\overline{\mathrm{x}}$ = mean value for specific number of impacts, N

v_{ref} = reference impact speed of droplet with sample

$N_{fit,j}$ = specific number of impacts N following the best fit reference line for the data points of sample "j"

To determine the COV, the mass loss curves for each individual sample are produced, see Appendix C for mass loss curves. The results are taken from Tables 19 - 23. From this the incubation period for each sample can be calculated. Then the standard deviation and mean values are calculated which results in the COV. The COV for each rotational speed is shown in Table 28.

Speed (RPM)	**COV (%)**
1100	0.62
1150	9.47
1200	56.78
1250	4.50
1300	8.83

Table 28: Coefficient of Variation Results for each Rotational Speed

Table 28 shows that apart from at the rotational speed of 1200RPM the COV is below 20%. As mentioned before, during the 1200RPM experiments the test rig was altered. This will

effect the results and will have an impact on the standard deviation. However ignoring sample, AL006, a value of 54% is calculated for the COV, showing that this doesn't have a great affect on results. It is unclear why the results from 1200RPM have a large variability, considering there is a small variability for the rest.

4.1.7 Reproducibility

Comparing results between test rigs is important to furthering understanding of the problem. The DNV GL standard states that every test rig should provide results that lie within a reference band of ±50% of the mean line. Figure 59 plots the graph showing the mean line and reference band, the mean line is taken from the line of best fit from Figure 57.

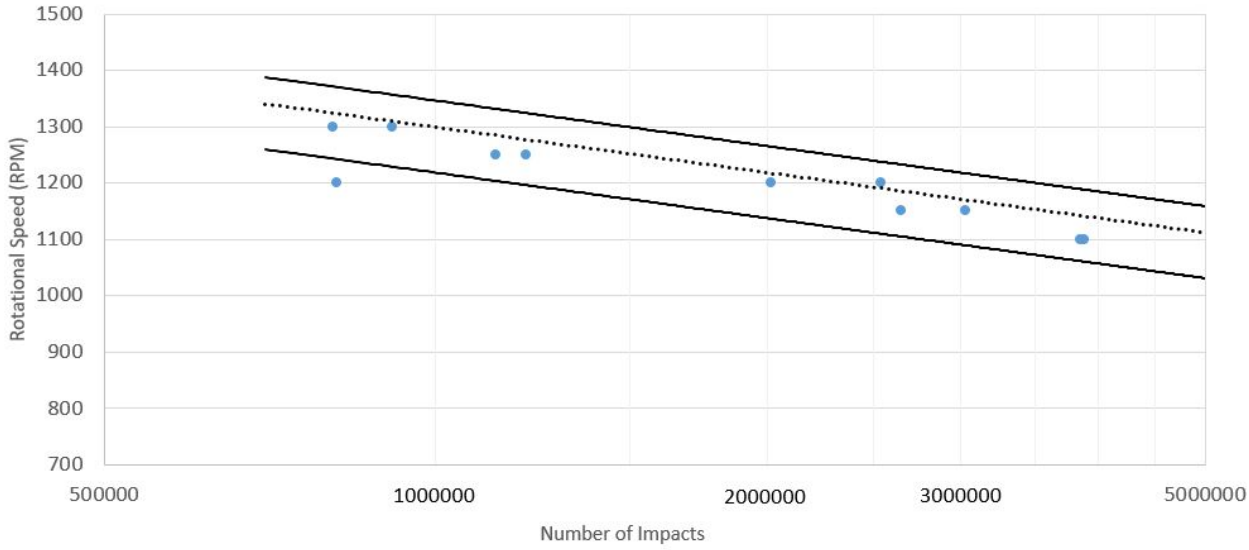

Figure 59: Aluminium calibration test results (end of incubation period) for all test. Dotted line is mean curve and solid lines are reference bands of ±50% error

Figure 59 displays that only the one sample at 1200RPM lies outside of the reference lines. The rest all fall comfortably inside. While this graph's purpose is to compare multiple test rigs, it is also a useful prediction tool. This band creates a clear limit that the vast majority of samples will fall within, which can be scaled up or down to investigate different speeds.

4.2 Erosion examined in XCT

X-ray Computed Tomography (XCT) is a non-destructive technique for visualising interior features within solid objects [61]. An XCT image is typically called a slice as it corresponds to what the object would look like if it was sliced along a plane. A good analogy is a slice from a loaf of bread, because just as a slice of bread has a thickness, and an XCT scan also corresponds to a certain thickness of the object being scanned though the XCT slices are a lot thinner.

One of the current uncertainties with erosion damage is what is occurring below the surface of the samples. It is unclear whether erosion is initiated on the surface or whether sub-surface damage can lead to stress concentrations and mass loss. Also the manufacturing and application of coatings can lead to voids occurring in between layers and the contribution of these voids to initiation of erosion is as yet unknown.

To study the sub-surface effects of erosion samples are examined using the XCT technique to assess for sub-surface damage at different stages in the erosion process. Deciding when to stop the samples and test in the XCT is crucial, as it is not possible to test the samples frequently in the XCT due to time and costs. Figure 60 plots the mass loss vs time curve and the five stages chosen to test the samples at.

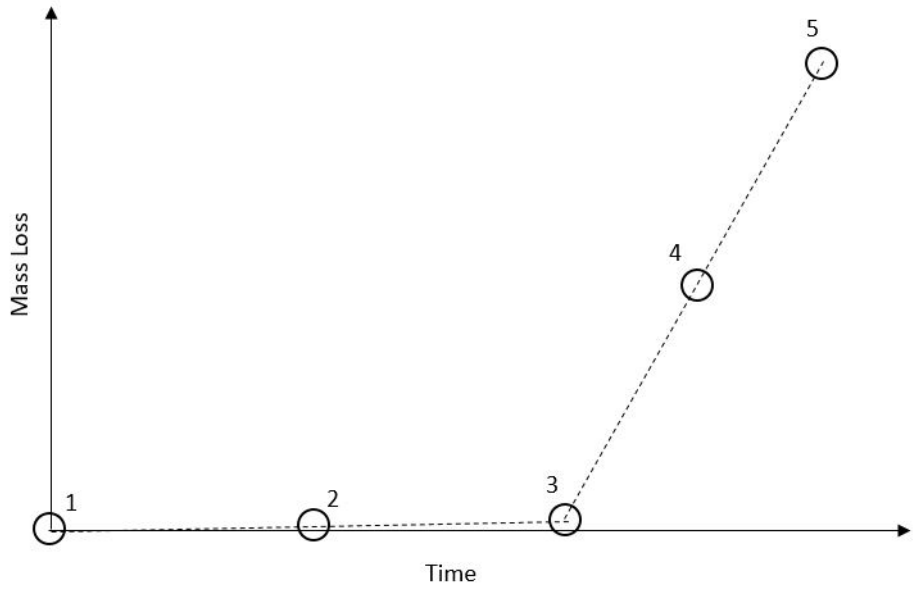

Figure 60: Five stages of erosion used for XCT samples

Stage 1 represents the time before the sample has been tested, which will be useful to determine

if there is any pre-existing defects or voids below the surface and how these affect the materials ability to resist erosion. Stage 2 is halfway through the incubation period, at this time there will be no damage visible on the surface of the sample but will be interesting to see if there is any defects or voids that have grown or been initiated by the erosion process. Stage 3 is at the end of the incubation period, ideally just before the increase in erosion rate occurs. This will hopefully show the changes in the sample that lead to the significant increase in mass loss. It can be difficult to stop the testing exactly at the end of the incubation period, therefore a cautious approach will be taken to make sure the sample is tested before significant mass loss occurs. Stage 4 is during the steady rate of mass loss to look at how the sample is changing during this time and where the mass loss is occurring. Finally Stage 5 is classified as the point where the composite substrate is showing, at this point the sample is damaged beyond repair and the mass loss will no longer be consistent.

Stage 2 and 4 are both determined by being halfway to stage 3 and halfway between Stage 3 and 5 respectively. Therefore a number of test samples were used beforehand to determine these points and gain a knowledge of the rough timescale as well as an idea of what to visually expect at these stages.

With other samples tested, such as the aluminium, there was a very regimented testing procedure where the sample testing was stopped at the same increments each time. However with these samples they all started with 20 minute intervals between stoppages but this decreased down to the 10 minutes and then 5 minutes as more erosion occurred. The shorter time between stoppages was needed to pick up subtle changes that occur quicker later on in the erosion process. The time taken to reach each of the stages for each of the samples is shown in Table 29.

Sample	**Stage 2**	**Stage 3**	**Stage 4**	**Stage 5**
A007	-	-	60 mins	-
A010	60 mins	100 mins	110 mins	120 mins
A030	60 mins	90 mins	115 mins	120 mins
A035	80 mins	120 mins	140 mins	145 mins
A038	60 mins	100 mins	120 mins	130 mins

Table 29: Time to reach each erosion stage for the five samples

The time taken to reach each stage is fairly consistent, as shown in Table 29, apart from sample

A007. This sample displayed no signs of erosion and then suddenly jumped to a Stage 4 erosion where a lot of the filler was uncovered.

The samples used for this experiment were flat samples rather than the usual aerofoil shape, this is due to the requirement of the samples fitting in the XCT system holder. Since an aerofoil shape was not possible, this does mean that the results from the Characterisation section cannot be directly applied to these results. For these tests knowing the number of impacts is not crucial as it is the sub surface defects that are being investigated and it is more important to track the changes for the same sample rather than know the specific number of impacts.

Finally the samples were coated in a commercial coating which is a multi-layered LEP. This LEP has a coating layer and a filler layer that are on top of the composite substrate. The white coating and grey filler layers can be seen in Figure 61.

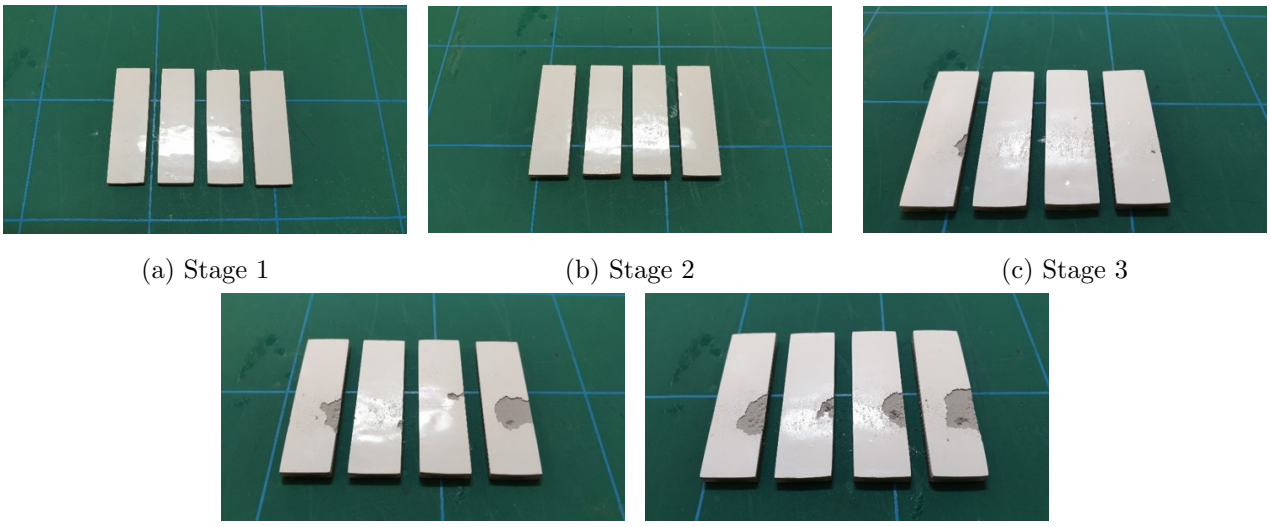

(a) Stage 1 (b) Stage 2 (c) Stage 3

(d) Stage 4 (e) Stage 5

Figure 61: Different stages of erosion for samples that were tested in the XCT

Figure 61 displays the results for the five different stages of erosion. The results are fairly consistent across the different samples though at Stage 3 it would be preferred to not have any filler showing, as can be observed in Figure 61 (c). Sample A007 was omitted due to it failing early and exhibiting a different failure mechanism. Although the samples at Stage 4 have wide range of filler showing, what cannot be seen from the photographs is that the samples with less damage do have deeper pits and therefore were deemed to have reached Stage 4.

To investigate how the quality of the samples affected the erosion results, the total void volume was calculated. The total volume of the sample was also calculated and then the void volume

given as a percentage of the sample's volume, due to there potentially being different volumes for each sample. The void volume included all three layers of the sample (composite, filler and coating) so provides an empirical value to the quality of the sample. Higher quality composites will be fully infused until no air pockets are present, the same with the application of the filler and the coating as ideally there will be no air bubbles present. Therefore taking a measurement of void volume will provide a means of comparing the samples. Table 30 shows the void volume percentage for each of the samples available.

Sample	**Void Percentage**
A007	4.22 %
A010	7.97 %
A030	5.39 %
A035	6.14 %
A038	8.88 %

Table 30: Void Volume Percentage of Full Sample at Stage 1 before Erosion Occurs

The values in Table 30 do not show any trend when compared with the lifetime, shown in Table 29. Sample A007 lasted the shortest amount of time even though it had the smallest void volume and Sample A035 lasted the longest but has an average number of void volume. Sample A038 lasted 130 minutes compared to the 120 minutes of both A010 and A030. Sample A038 has the greatest volume of voids yet it lasted longer than A010 and A030. In addition A010 and A030 lasted the same length of time even though the void volume was quite different. In summary the void volume or quality of the samples, did not have any effect on the time taken to reach Stage 5 erosion. This indicates that the sub surface voids were not important to the lifetime and that the failure mechanism has more effect on the lifetime.

When examining the samples under XCT, two different failure mechanisms were apparent, brittle fracture and delamination. These failure mechanisms are examined separately.

4.2.1 Delamination

The reason for sample A007 failing rapidly and unexpectedly is due to delamination. When this sample was tested there appeared to be no damage on the surface and then suddenly severe damage had occurred, as shown in Figure 62.

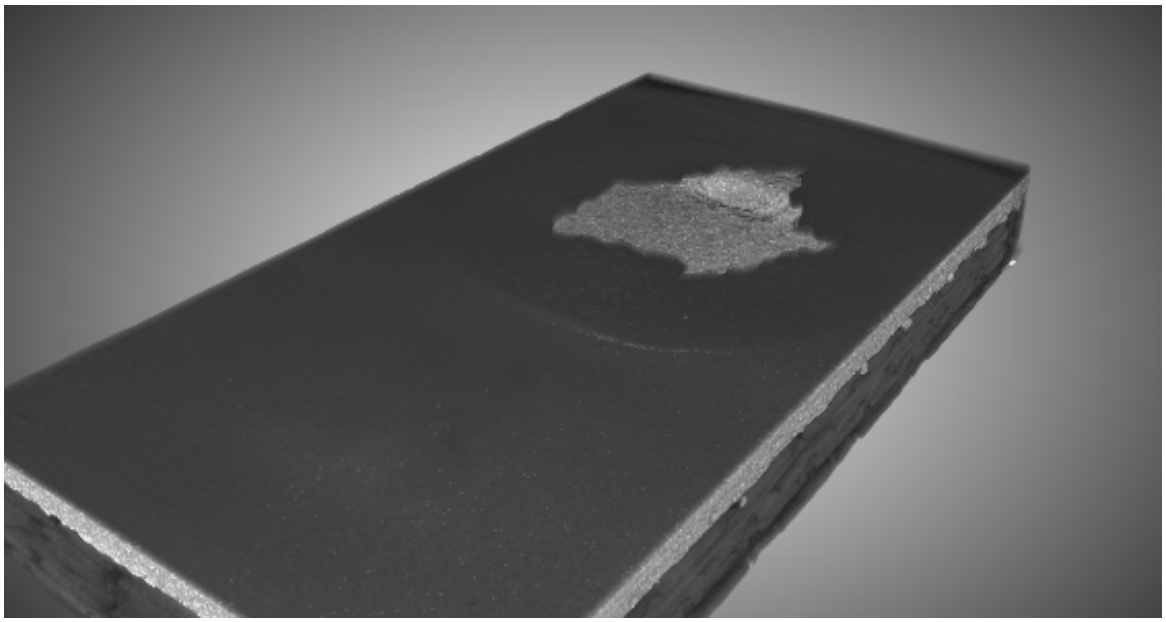

Figure 62: XCT Image of Sample A007 showing damage occurred

Figure 62 shows the extent of the damage. The test had been stopped at 20 minute intervals and at both 20 and 40 minutes there had been no visible damage, then when the test was stopped again at 60 minutes the damage, as shown in Figure 62 was present. This demonstrates the major issue with delamination, as changes are taking place sub-surface the extent of the damage is unknown until suddenly severe mass loss occurs.

From Figure 62 a faint circle can be detected marking the outer edge of the delaminated zone. This indicates the area which water has penetrated under the top layer and causes the coating and filler to separate. This can be best shown with a cross sectional view of the sample as shown in Figure 63.

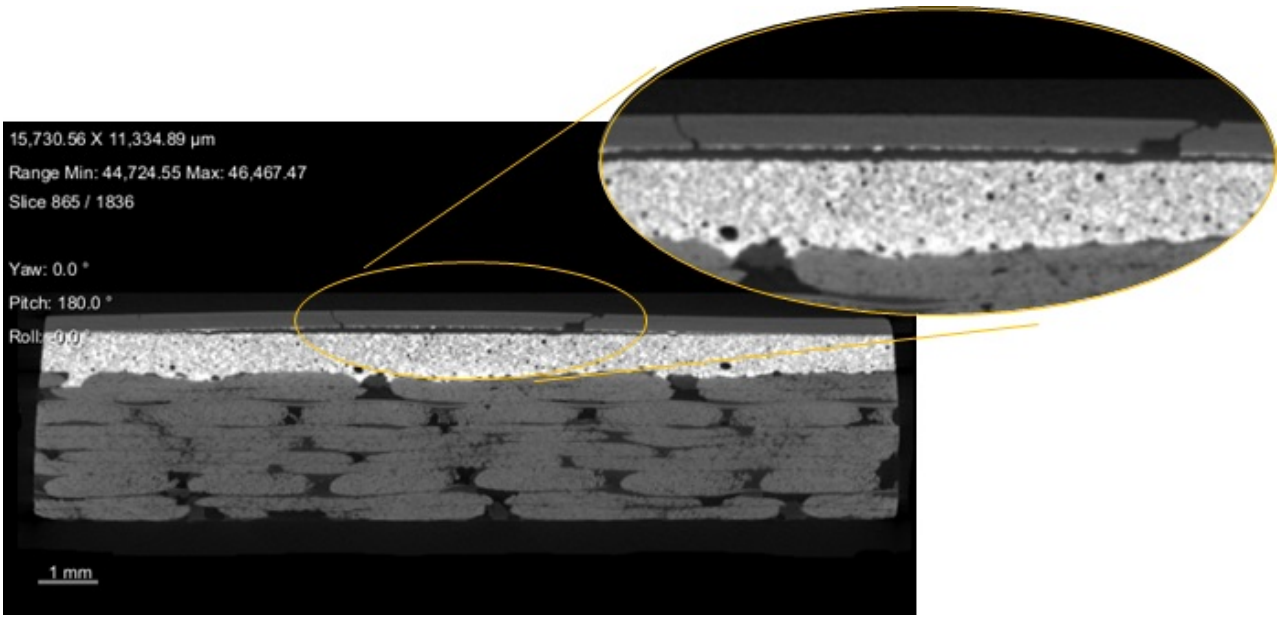

Figure 63: Cracks and Delamination present after sample A007 had been tested for 60 mins

Figure 63 displays the full cross section with a section zoomed in on the two cracks. It is clearly shown that the coating has separated from the filler, which is a classic sign of delamination. This delamination occurs by water travelling down the cracks and forcing its way between the two layers, causing them to split. This causes the coating to become loose and large areas to fall off, resulting in rapid mass loss.

This image was taken at Stage 4 at the edge of the eroded area, therefore these are not the exact cracks that lead to the delamination but the earlier process has been replicated. Unfortunately the nature of delamination and the rapid changes mean that Stages 2 and 3 were missed.

To understand why Sample A007 failed due to delamination, it is important to analyse initial XCT images. From these images, plus the notes taken in the log book, a depression towards the top of the sample was noted before any testing had taken place. Figure 64 shows a plan view and side-on view of the sample where this depression can be observed.

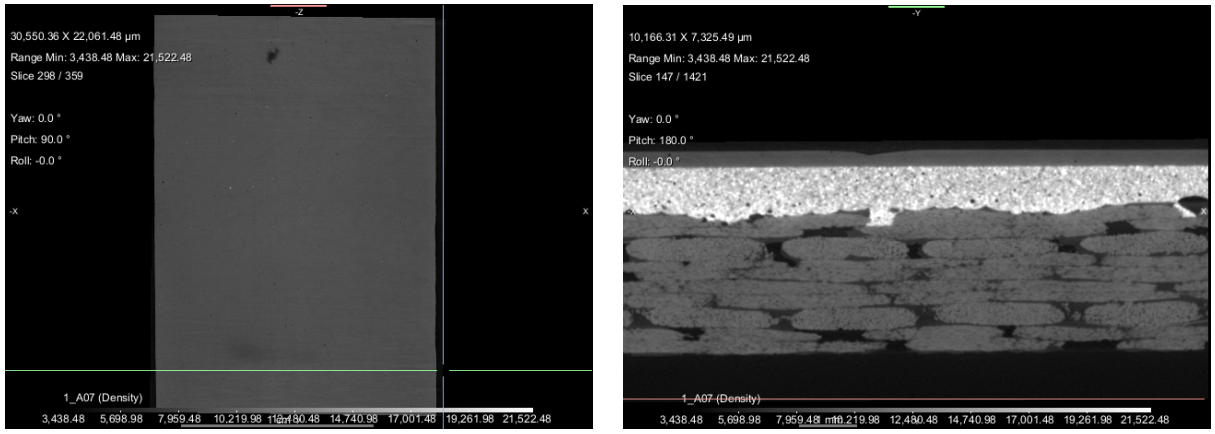

(a) Plan View (b) Side-on View

Figure 64: Sample A007 before any testing, showing the depression in the sample from a plan and side-on view

The depression in Figure 64 is at the edge of the damaged area as shown in Figure 62. This signifies that the dip could cause stress concentrations to form at this area, leading to cracks. As these cracks propagate through the coating, this can cause water to seep between the layers and cause delamination.

From the work in Section 4.2 with the void volume showing that sub surface voids did not seem to affect erosion rates. This shows that surface damage or irregularities have a greater effect on the erosion rate and extra care should be taken to avoid them.

4.2.2 Brittle Fracture

Materials that fracture are usually categorised into two different fracture modes, either ductile or brittle. Ductile fracture involves extensive deformation and the crack is stable unless there is applied stress. Whereas brittle fracture have relatively little deformation and the crack is unstable and can propagate rapidly without an increase in stress. This process is more of a sliding scale rather than black or white depending on material properties and the applied stress. Erosion relates more to brittle fracture, since there is a constant applied load so deformation is minimal and there can be sudden cracks that lead to mass loss.

Samples A010, A030, A035 and A038 all experienced brittle fracture. The rate of erosion might change between samples but they all experience a similar method of failure where mass loss occurs rapidly and without any deformation. Using the XCT images the sub surface changes of brittle fracture can be explored as well as looking at the initial condition of samples and how that affects brittle fracture.

The brittle nature of the fracture is evident when the progression of erosion is assessed over time. In Figure 65 the erosion in the coating is shown from Stage 3 to 5.

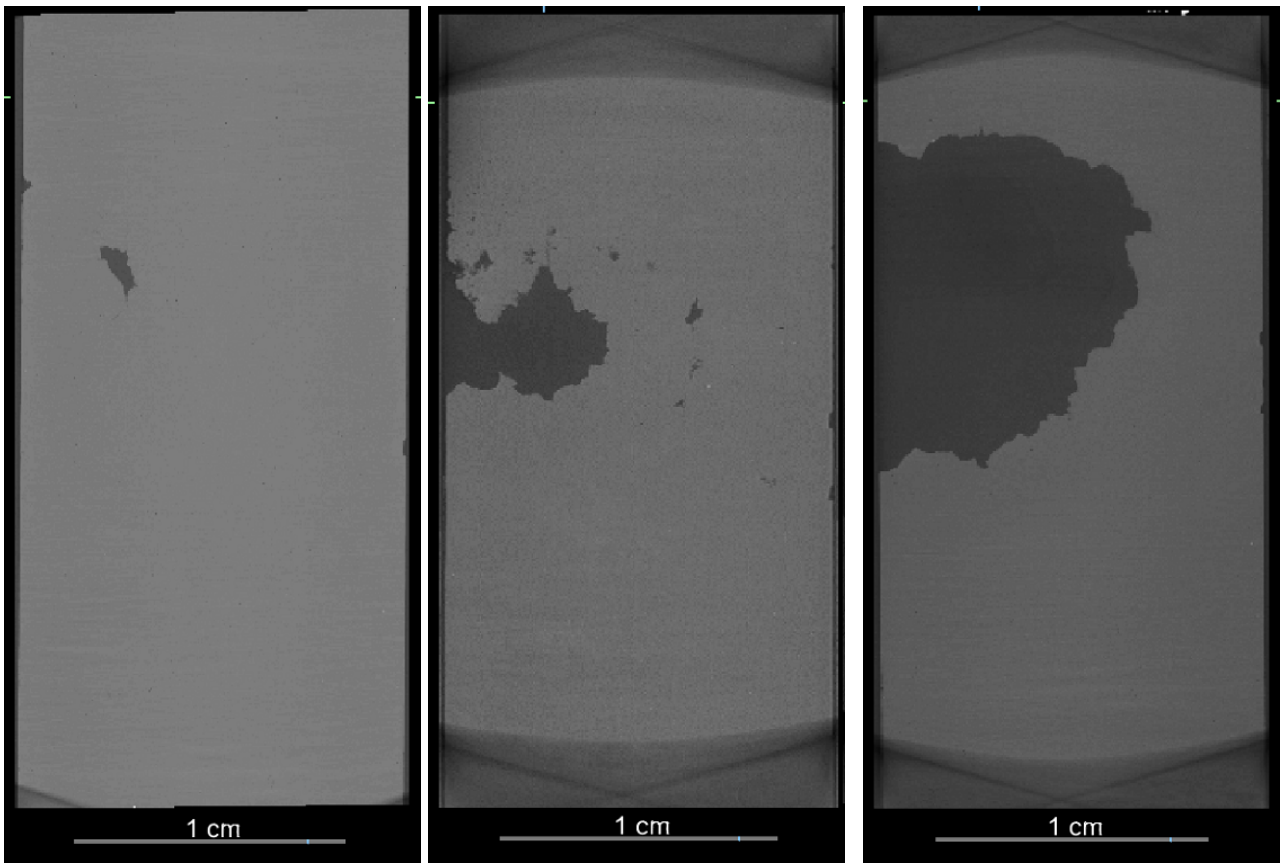

(a) Stage 3 (b) Stage 4 (c) Stage 5

Figure 65: Progression of Erosion from Stage 3-5 in Sample A10

The photographs taken in Figure 65 were all taken 10 minutes apart, and it is clear that in these intervals the damage had significantly increased. Another sign of the brittle nature of the fracture is the jagged edges to the damaged area, this is customary in brittle fracture due to chunks of material falling off at a time. If the failure was more ductile a slower erosion rate would be present. The effects of brittle fracture is explored along with the reasons behind it acting on these samples.

One theory is that sub-surface voids provide weak points in the material that leads to stress concentrating at that area. These stress concentrations will increase the likelihood of fracture occurring in a particular area. To investigate this theory the sample was examined at all five stages, looking to detect the largest voids near the coating/filler interface. Figure 66 shows these voids for stages 2, 3 and 4. Stage 1 and 2 showed the same pattern of voids therefore only the image for Stage 2 is displayed.

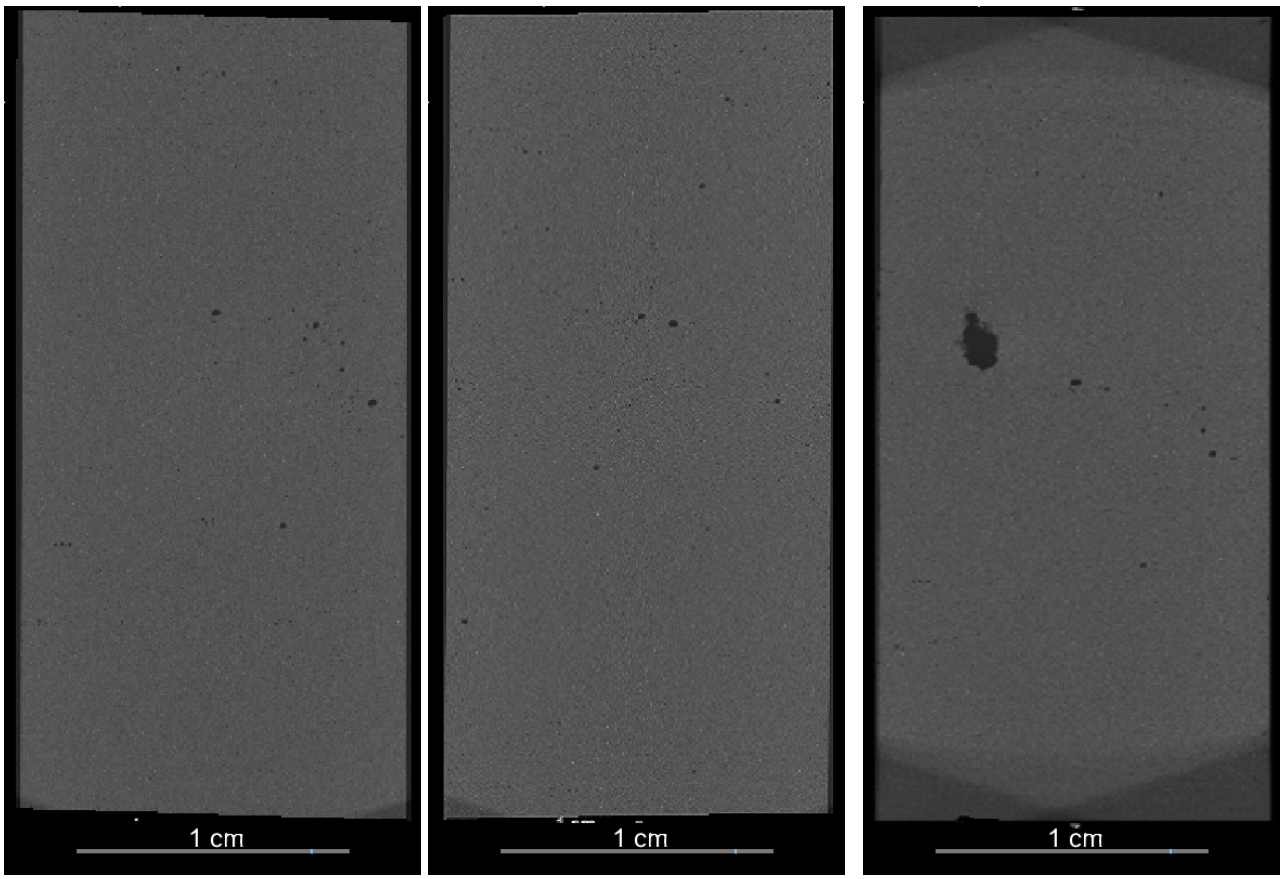

(a) Stage 2 (b) Stage 3 (c) Stage 4

Figure 66: Voids in the centre of the Filler layer for Sample A10

Figure 66 shows the location of the biggest voids and at Stage 4 the large damage on the left hand side is due to the erosion reaching this level. This dark area represents the air left by the erosion removing most of the filler layer. This area of damage shows where the erosion was initiated and it has no link to the location of the large voids. Regardless of where the largest voids or a collection of voids are located, the erosion is consistently initiated at another part of the sample. The same situation happens with the other samples and these images can be found in Appendix F. This shows that voids are no accelerating the erosion process in these samples, and the location of the impact is vastly more important than the location of the voids.

Another area of interest is where the voids are located in the sample, determining if the voids are near the composite or the coating. Photographs were taken at varying depths through the filler layer starting at the composite interface (0%) and increasing in (20%) intervals until it reaches the coating interface (100%). Figure 67 displays these images through the depth of the filler.

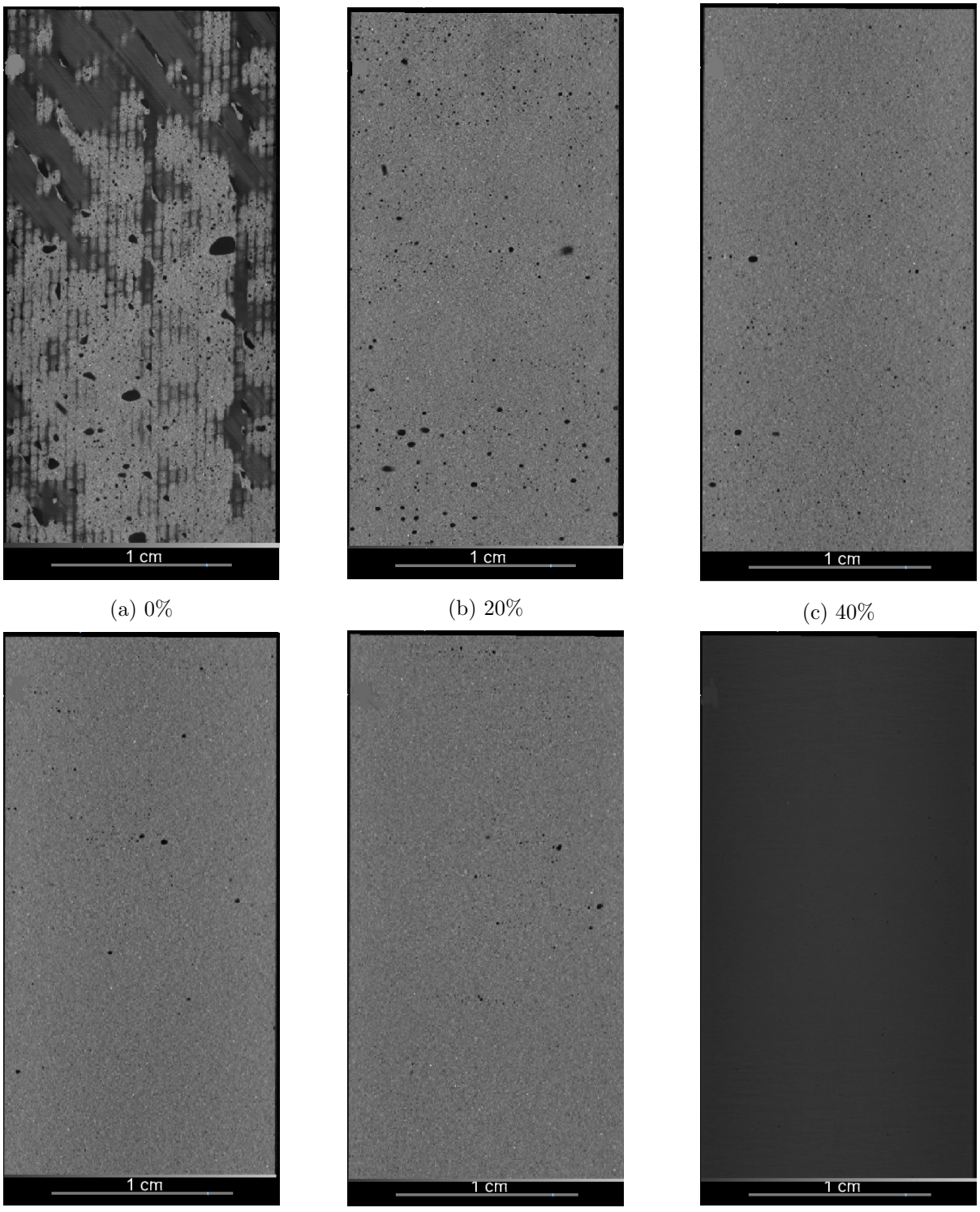

(a) 0% (b) 20% (c) 40%

(d) 60% (e) 80% (f) 100%

Figure 67: Voids through Filler layer for Sample A10 at Stage 1, starting at composite interface (0%) through to coating interface (100%)

Starting at Figure 67 (a) the number of voids is unclear due to the composite fibres but some large voids are still visible through the composite layer. In (b) there are many voids of varying sizes spread over the full area of the sample. Moving up through the layers the number and frequency of the voids diminishes until at (f) there are none remaining. Figure (f) is darker in colour as it is at the coating interface.

It is evident that more voids are present near the composite substrate rather than near the surface of the sample. This is due to the manufacturing of the composite not being to the highest standard, from Figure 67 (a) the gaps between the different fibre strands are evident. If the infusion process is not carried out properly this can lead to gaps/air bubbles in the composite. These air bubbles can penetrate into the filler layer, this cause more voids to be evident at the composite.

As the voids are not near the surface of the sample they will have less of an effect on the erosion rate, and as shown in Table 30 the total void volume does not seem to affect the sample's lifetime. Therefore while it would be preferable to manufacture the highest quality samples the voids present do not seem to have a direct correlation to the sample lifetime.

Another area of interest, is whether there are any sub-surface changes during the erosion process. To investigate this the void volume was measured throughout the erosion process, in both the filler layer and the coating layer. The same process was carried out as before, with the total void volume in Section 4.2 this time isolating just the filler and coating. Table 31 shows the void volume in the coating layer, through all five stages of erosion.

Sample	**Stage 1**	**Stage 2**	**Stage 3**	**Stage 4**	**Stage 5**
A10	0.38%	1.64%	1.37%	6.30%	30.66%
A30	0.36%	2.75%	6.30%	11.09%	36.78%
A35	0.71%	2.99%	4.81%	6.97%	12.78%
A38	0.27%	2.84%	3.44%	7.62%	56.10%

Table 31: Void Volume in Coating Layer

The results in Table 31 show that the void volume increases throughout the erosion process. This is to be expected with the coating as erosion occurs on this layer first, so by the time Stage 5 is reached there can be significant mass loss, which is shown by the large volume shown. The process for determining void volume is to measure the air present in the sample, therefore it could be slightly inaccurate due to identifying both voids and erosion on the surface. The main

point of interest for the coating is what occurs at Stage 2, as there should be no erosion present on the surface however there is some erosion seen from these results. This means that even if not visible to the naked eye there will be microscopic pits forming on the surface that then grow to be visible by Stage 3. Unfortunately the resolution of the XCT scans is not accurate enough to detect these microscopic pits at the earlier stages.

While the measurement of the voids in the coating might be affected by erosion as early as Stage 2, the filler should remain undamaged until probably Stage 4 and definitely Stage 3. Table 32 shows the void volume in the filler layer for all five erosion stages.

Sample	**Stage 1**	**Stage 2**	**Stage 3**	**Stage 4**	**Stage 5**
A010	0.63%	0.84%	1.83%	1.40%	4.52%
A030	0.92%	0.94%	1.14%	1.77%	4.65%
A035	0.69%	0.76%	1.31%	1.29%	3.11%
A038	0.52%	0.93%	1.03%	1.00%	8.22%

Table 32: Void Volume in Filler Layer

Clearly there is an increase in void volume as the sample erodes. It can be seen at stages 1-3 (the filler will not have experienced any mass loss at this stage), there is an considerable increase. For samples such as A010, the void volume trebles from Stage 1 to 3, whereas for sample A030 there is only a small increase but there is consistently evidence of an increase in void volume regardless of the sample.

This is an interesting observation, as it should not be possible for new voids to be formed during the erosion process. This suggests that the original voids are somehow increasing in volume. One suggestion for how this occurs is that tiny voids next to each other in the sample will merge together, by multiple stress waves breaking down the small wall between them. This will then increase the total volume measured. Another option is that the filler layer has some particulate matter present in it, these particulate could cause stress concentrations which lead to minute cracks forming, thus increase the total void volume.

For most samples there is a slight drop in the void volume at stage 4, which will be due to the samples being measured in a different orientation for Stages 4 and 5. Thus making it difficult to measure the same volume of the sample, as if a slightly smaller volume is measured this could result in the anomaly in the results.

4.2.3 Discussion

The aluminium samples have been shown to provide the ideal calibration as they produce repeatable results, this makes them ideal to investigate the effect of impact speed or frequency. However after these initial tests it is still useful to investigate speed and frequency for multi-layered composite samples as they are more comparable to real-world use. The one speed that does not provide the same repeatable results, is when the aluminium samples are tested at 1200rpm. The mass loss curves for the samples tested at 1200rpm is very different both in terms of end of incubation period and erosion rate, this is shown when measuring the coefficient of variation for that speed as it is far greater than any other speeds.

The reason for 1200rpm being much more variable than any other speed could be due to the test rig changing design part of the way through the testing process. However the two samples that were tested after the change (AL018 and AL022) are still not very similar when comparing the mass loss curves. Another theory on the variability present could be that a rotational speed of 1200rpm reach some sort of sweet spot, like a resonance, for this set-up providing the chance for the stress waves to amplify. Though this would probably see a more uniform drop in erosion lifetime rather than produce such a range. The main area to improve is the sample size, but due to time constraints only three samples were measured but if this was increased to ten samples a clearer picture would be achieved.

A useful outcome from the study of the aluminium samples was using the results to predict mass loss curves. Both in terms of predicting the curve for a given speed but only requiring a few data points and extrapolating the data from a few different speeds to predict the lifetime for a range of speeds. As the aluminium provides such repeatable results, this allows even a small number of samples to be used to gain an understanding (with a high degree of accuracy) of a range of speeds. From this you can extrapolate down to slow enough impact speeds that the lifetime starts to become greater than the lifetime of a wind turbine. Ideally understanding of multi-layered coatings could reach a high enough level that this same extrapolation could be achieved with them, thus creating a lifetime prediction model.

Using kinetic energy rather than time to plot the mass loss curve shows an interesting result, as shown in Figure 54. There is tight grouping for the end of the incubation period apart from the samples tested at 1100rpm and 1150rpm. The reason these speeds could be different is due to the test rig being altered after they had already been tested. If these two speeds do prove to be outliers then this could provide a small window for which the kinetic energy

required to reach the end of incubation period would fall in. The other option is that 1200rpm is providing samples that are not as reliable, again a larger sample size would clarify this. Also the re-testing of the slower speeds is important to determine if they provide similar results to the other speeds.

Similarly to the aluminium samples, the flat commercial coating tested in the XCT also provided fairly consistent results. Calculating the coefficient of variation to reach the end of incubation period gives a value of 12.2%. Comparing this to the results for the aluminium samples in Table 28 it is shown that the COV is relatively similar. This calculation of the COV was excluding Sample A007 as no time measurement was taken at Stage 3 (end of incubation period). In fact the main variation with these samples is when the failure mechanism changed, as with Sample A007.

The delamination seen in Sample A007 clearly was initiated by the depression in the sample due to manufacturing or damage during transportation. While stages 2 and 3 were missed and not allowed to be examined in the XCT, the cracks seen at the edge of the damaged area clearly point towards delamination. Also the large circular area around the damaged area, where the coating had separated from the filler, was another clear sign of delamination. The depression initially seen on the sample was near the edge of the sample and not in the area directly impacted by the sample. Regardless, this still caused the delamination and shortened lifetime. Studying the voids present sub-surface, even voids close to the impact area does not seem to have a great affect on the erosion lifetime. Illustrating that damage on the surface is vastly more detrimental to the lifetime than sub-surface defects.

The majority of the samples tested in the XCT failed due to brittle fracture, evident by the jagged fracture around the edge of the damaged area. The main focus of this section was to study the voids in the sample to determine how they affected the erosion lifetime. Initially the total void volume was examined, as a method in quantifying sample quality, however the results indicated no correlation between the "sample quality" and the lifetime. The void location was also examined, showing that the majority of voids were near the composite interface. This leads to a potential conclusion on why the "sample quality" did not correlate to lifetime, as the voids measured were mainly near the bottom of the filler thus not being close enough to the surface to affect the erosion results.

Another important point with regards to the void location, is in relation to the location of the droplet impact. When studying the void location near the surface, there was never an occasion whether the void location was near the area which was damaged. However the ETC test rig

does not have a range of impact locations, the test rig has a 2mm range in the needle location's radius. This results in a very specific impact location therefore if large voids are not near that location then it would be unlikely for them to affect the erosion. These XCT tests should be carried out on samples from a test rig that has range of impact location as this would provide a clearer picture on whether the voids will lead to any initiation of erosion.

Finally the changes in void volume during the erosion stages were examined. It was found that as the sample experienced impacts the void volume increased. For the coating layer this is to be expected as mass loss is experienced on the surface. However the filler layer also showed an increase in void volume, even when no mass loss in the filler layer would be possible. There are two possible reasons as to how this occurs: that microscopic voids in the materials merge together due to the stress waves breaking down the walls between them thus increasing the void volume; or that particulates in the filler are leading to minute crack initiation. Interestingly the void volume increasing during erosion contradicts the earlier finding that the total void volume (sample quality) did not affect the lifetime of the sample. The reason for this contradiction is unclear.

The combined work of examining the aluminium samples and the commercial coating helps to provide a better understanding of what is physically occurring during erosion. Firstly the impact speed against number of impacts produces a logarithmic curve for the results. Meaning that a predictable sample, such as aluminium, leads to repeatable and easily extrapolated results. The challenge therefore is to design a stable coating system that provides the same reliable results. As shown with the XCT work, there is still a lot that is not understood when studying multi-layered LEPs especially how the sub-surface voids affect the erosion rate. One important conclusion to draw is that the surface of the sample having no existing defects is important to increasing the lifetime.

5 Multi-layered Leading Edge Protection Systems

The aluminium mass loss measurements provide a consistent reading, but wind turbines are not manufactured from solid metal. The make-up of modern turbine blades is generally a glass fibre composite with some leading edge protection (LEP). These LEPs are multi-layered systems used to protect the composite substrate from the erosion process. The multi-layer approach adds complexity as the manufacturing process is not as consistent, as manufacturing solid metal, which can lead to potential defects or voids between the layers. This results in multi-layer system's response to the erosion mechanism being a lot less consistent and repeatable than the aluminium samples.

In this section, two multi-layered LEPs will be explored. Firstly, a long-standing elastic industry standard LEP which is a three layered system, with a topcoat, filler and substrate, this coating will be referred to as, LEP 1, for the rest of the thesis. Then there is the a newer highly flexible visco-elastic LEP, which is a four layered system with the inclusion of a primer between the topcoat and filler, this will be referred to as LEP 2. The inclusion of the primer is to reduce the chance of delamination occurring. These two LEPs will be examined individually to observe how they react to droplet impacts as well as their common failure mechanism. There will also be a slight comparison between the two samples, where applicable as not every factor can be kept exactly the same for both.

The incubation period is still used to measure the erosion process, as this remains useful to determine as it allows repairs to be made before damage becomes severe. For multi-layered measurements the time to erode through each layer will also be measured, so for LEP 2 that has four layers: this means the time taken to reach the filler layer will be measured. Finally for both samples, the time to breakthrough will be measured, which is defined in the DNV GL standard as the time until the composite substrate is exposed. Using these terms allows the erosion rate to be quantified and provides the ability to compare different LEPs.

5.1 Long-standing elastic LEP

The first LEP to be examined has a topcoat and filler on top of the composite. The chemical make up of the LEP is unknown but is thought to have a polyurethane base. Through parallel work with ORE Catapult and Bristol University, the top coat chemical structure was altered with a polyhedral oligomeric silsesquioxane (POSS) nanoparticle variant inserted by a fellow

PhD student [62]. This results in two variations of LEPs being tested, with unmodified and modified topcoats.

The samples were tested at a range of speeds, 900rpm, 1100rpm and 1200rpm, also with the test rig operating 24, 36 and 72 needles. The samples were tested in five minute intervals with a three minute break in between to check the sample and take photographs. There were only twelve samples available to test which limits the sample size of the results but it should be possible to still gain information on how the coating reacts to different impact speeds and frequency.

Figure 68 shows the photographs taken at the 5 minute intervals, though only photographs every 20 minutes are shown. Using the photographs the end of incubation period and breakthrough can be determined and used to quantify the erosion rather than mass loss. The end of incubation period occurs when there is noticeable damage on the leading edge and the topcoat is starting to erode away, so a tiny bit of filler could be visible. Breakthrough is classified as the erosion getting through to the substrate, i.e. both the topcoat and the filler have been eroded. These two points can be used to construct a mass loss curve, as seen before in Section 4.1.2, with the end of the incubation period being the point where the steady erosion begins and breakthrough being when steady erosion ends and the mass loss curve is no longer linear.

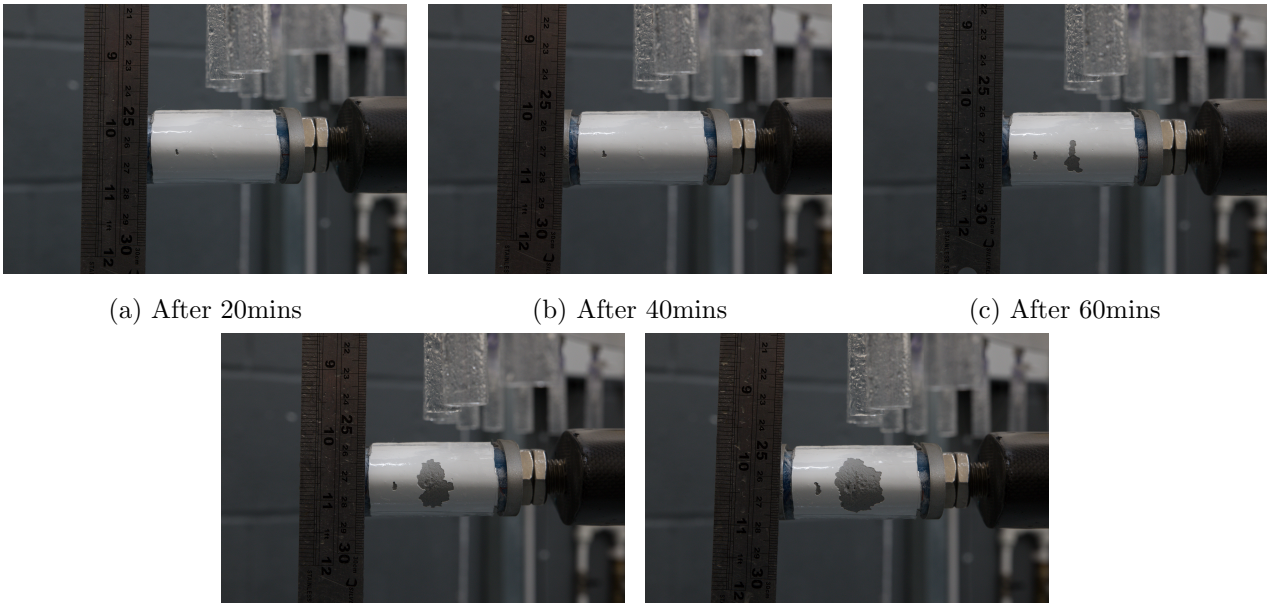

(a) After 20mins (b) After 40mins (c) After 60mins

(d) After 80mins (e) After 100mins

Figure 68: Composite samples being tested at a rotational speed of 1200RPM with 24 needles operating for Sample 6

Figure 68 displays the photographs taken for Sample 6. Photographs were taken every 5 minutes but only every 20 minutes have been selected, as they provide a representation of the erosion phenomenon. Examining the photos, results can be obtained for all samples as shown in Table 33.

Sample Number	**Speed (RPM)**	**Number of Needles**	**Time to End of Incubation Period (mins)**	**Time to Breakthrough (mins)**
1	1200	72	25	35
2	1200	72	15	25
12 (Modified)	1200	72	10	15
10 (Modified)	1200	72	10	35
5	1100	72	65	90
8 (Modified)	1100	72	55	65
4	900	72	-	-
7 (Modified)	900	72	180	240
3	1200	36	45	50
9 (Modified)	1200	36	40	60
6	1200	24	45	100
11 (Modified)	1200	24	55	70

Table 33: Results for LEP 1 Samples

For each rotational speed and number of needles there is at least one modified and unmodified sample. The first thing to notice is that the unmodified samples appear to show slower erosion rates compared to modified sample. However the exception is the time to reach end of incubation period with 24 needles operating, though this is then corrected when the samples are measured to breakthrough. This abnormality is most likely due to a defect in the topcoat causing it to erode quicker than anticipated.

The other result that is unexpected is regarding Sample 4 in Table 33, as there are no results for this sample. This is due to the samples being tested for 400 mins and showing no sign of erosion. Therefore the test was stopped and the result deemed to be an outlier.

Figure 69 plots the time to reach end of incubation period for both the modified and unmodified samples, with an average taken for any rotational speeds that have more than one reading at that point. The number of impacts is taken from Table 17.

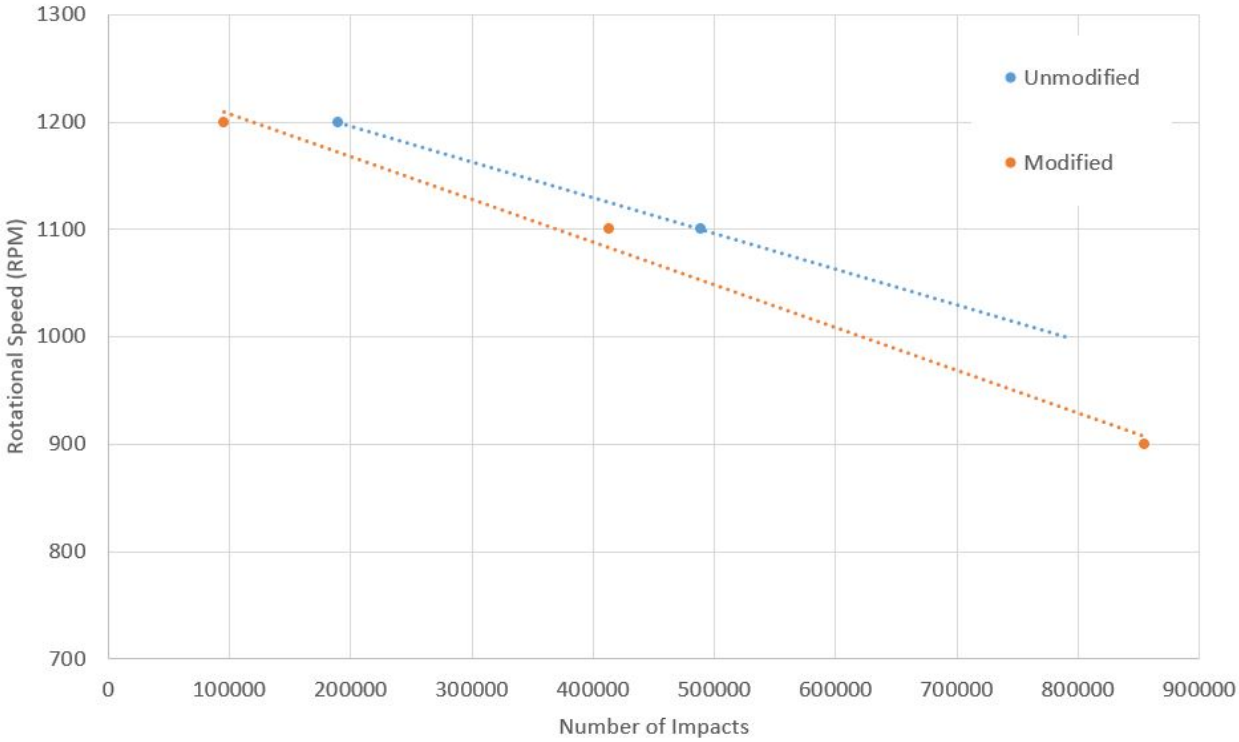

Figure 69: Number of Impacts to reach End of Incubation Period for Different Rotational Speeds

Figure 69 shows a linear trend between the rotational speed and number of impacts to reach the end of the incubation period. The orange line represents the modified samples and the blue line is the unmodified samples. The gradient of the two lines of best fit are very similar although the modified samples always require around 100,000 impacts less to reach the end of incubation compared to the unmodified samples. Both lines displaying a similar gradient shows that the modifications made did not change the failure criteria, just decreased the erosion lifetime.

Figure 70 plots the number of impacts required to reach breakthrough for each rotational speed.

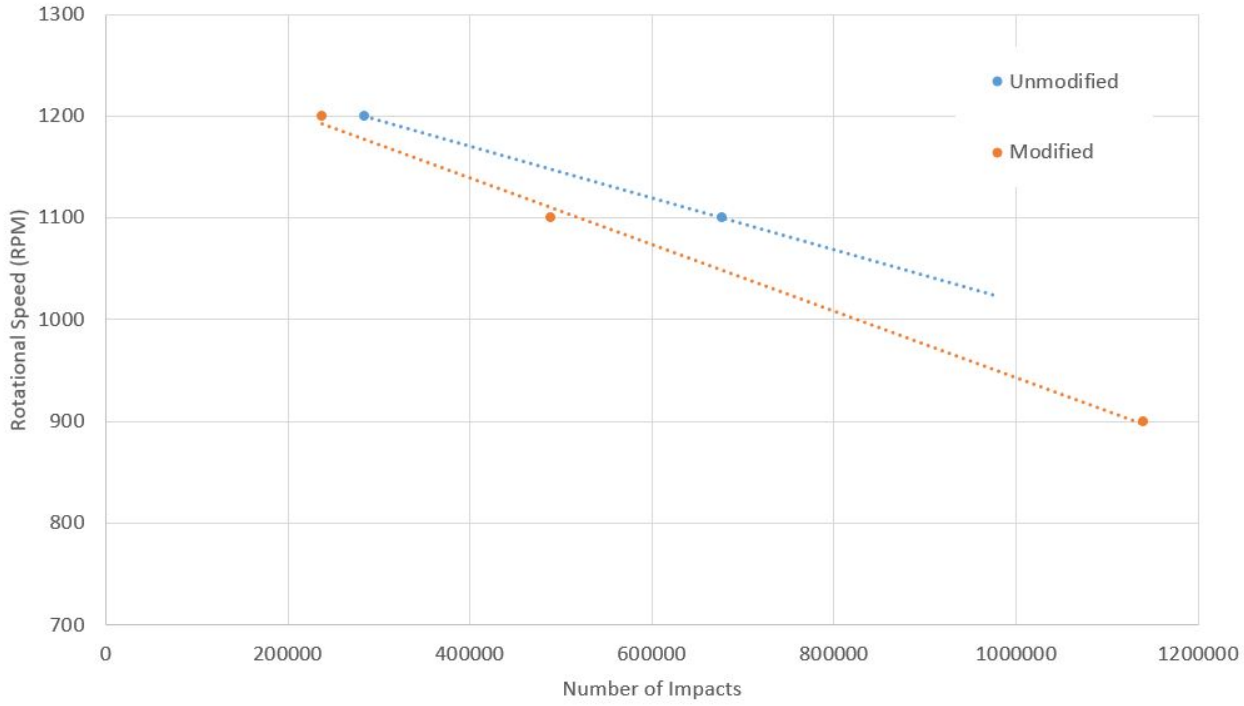

Figure 70: Number of Impacts to reach Breakthrough for Different Rotational Speeds

Figure 70 again has the unmodified samples in orange and the modified samples in blue. Similarly to Figure 69 there is a linear trend between rotational speed and number of impacts. However this time the best fit lines diverge indicating that the impacts required to reach breakthrough will be similar at higher rotational speeds. This result would be expected for Figure 69 not just Figure 70 but the lack of a reading at 900RPM makes this more difficult to determine, as well as a smaller sample size being another obstacle. This suggests that the modifications made were targeting improvement at higher speeds, which does not relate to improvements at lower speeds.

The modified and unmodified samples can also be compared for the kinetic energy required to reach the end of incubation and breakthrough. Figure 71 plots the kinetic energy required to reach the end of the incubation period, Figure 72 plots the kinetic energy required to reach the breakthrough.

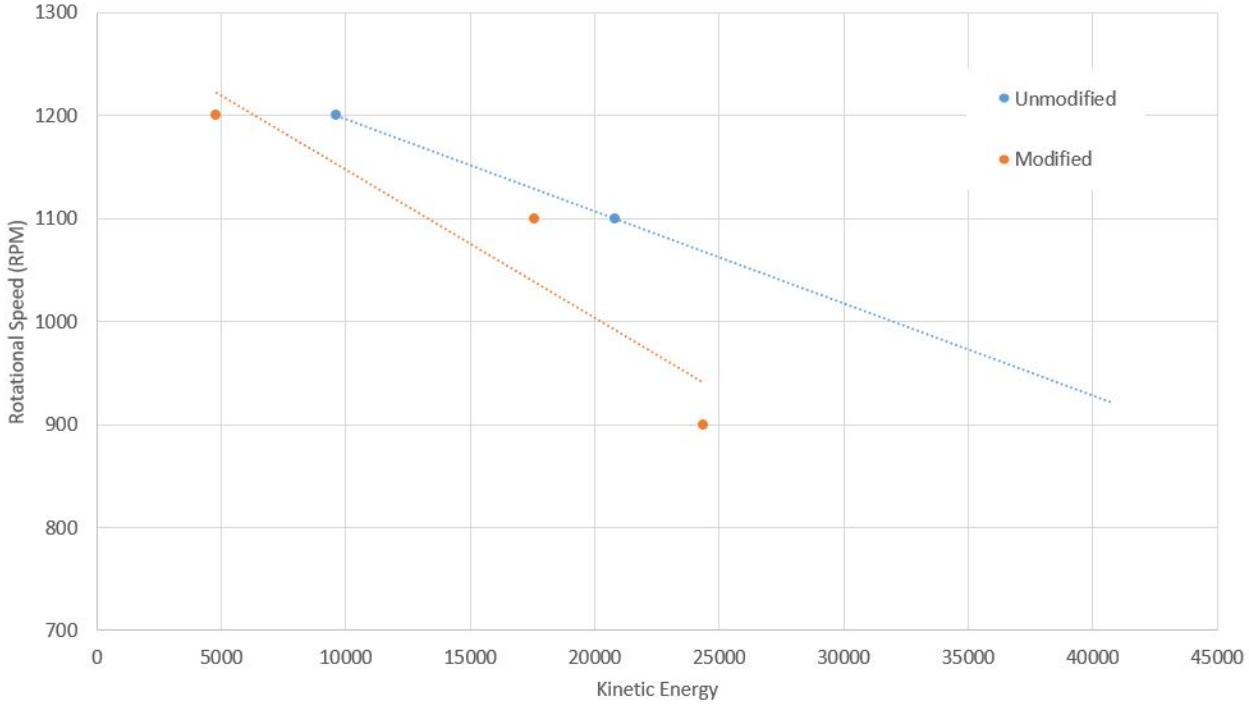

Figure 71: Kinetic Energy vs Rotational Speed to reach end of Incubation Period

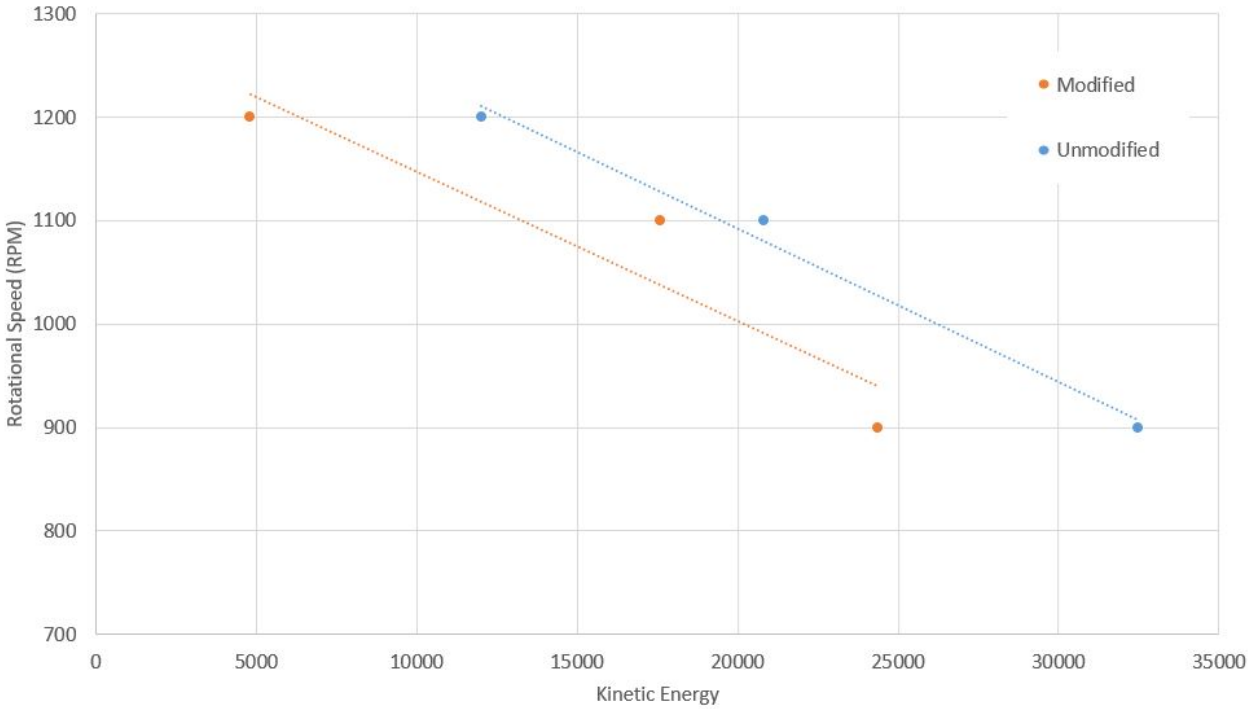

Figure 72: Kinetic Energy vs Rotational Speed to reach Breakthrough

Figures 71 and 72 display a similar trend to the plot with number of impacts, the main difference being that the goodness-of-fit for the data is worse than the number of impacts, this is especially

apparent with the modified samples.

Another area of interest is how the impact frequency affects the erosion, which can be studied by examining the number of needles operating. If data is compared for number of impacts or kinetic energy instead of time, the frequency of impacts can be investigated. Figure 73 plots the number of needles against the number of impacts to reach both the end of incubation period and breakthrough.

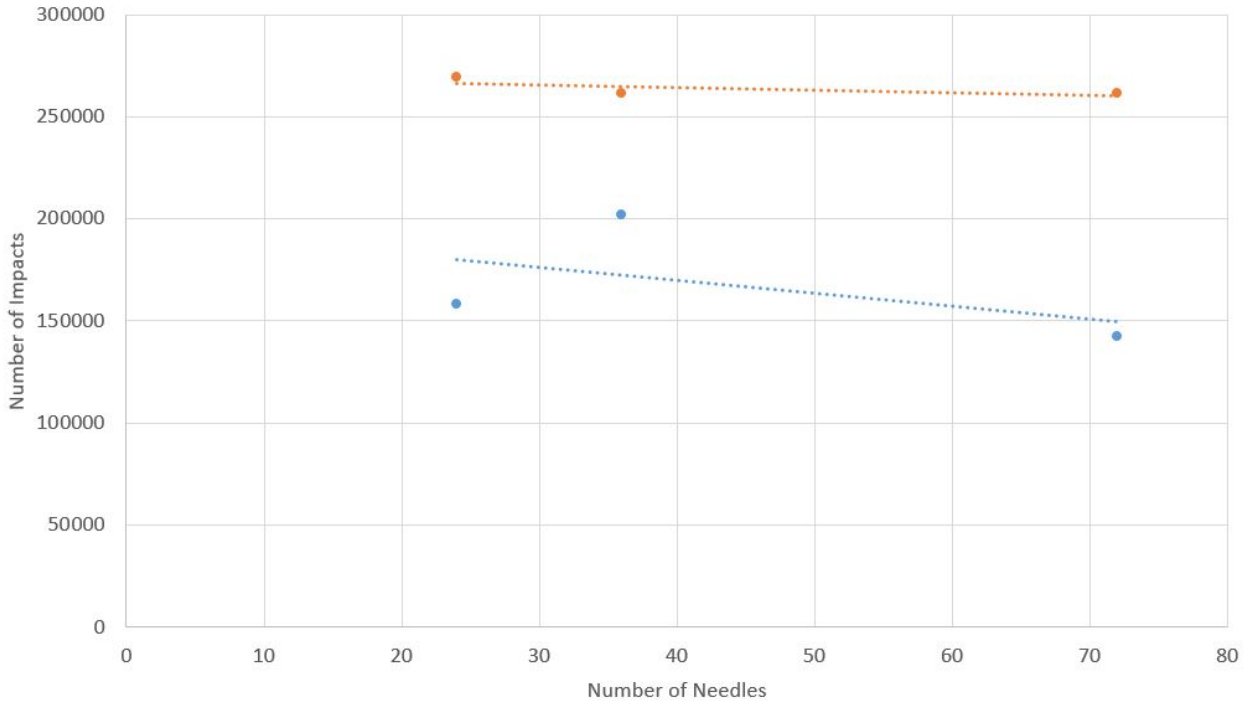

Figure 73: Number of Needles vs Number of Impacts to reach the end of Incubation Period (blue) and Breakthrough (orange)

Figure 73 shows that the number of impacts is close to constant regardless of the number of needles operating. A similar result can be seen with respect to kinetic energy, the graph of which is in the appendix. While less needles operating does result in a longer time to reach the end of incubation and breakthrough this is purely down to the slower rate of droplet production and when comparing to the total number of impacts a samples receives the results remain constant regardless of needles. This result confirms that impact frequency has minimal effect on the lifetime of erosion, and from previous work with the aluminium samples and the XCT samples it is clear that the impact velocity has a greater effect.

5.2 Highly Flexible Visco-Elastic LEP

LEP 2 has an extra layer compared to LEP 1, there is a clear topcoat, then a red primer layer, underneath this a filler before reaching the composite substrate. The chemical make up of this LEP is also unknown.

The samples were tested at speeds of 1200, 1100 and 1000rpm. Another set of samples was also tested with 36 needles operating (with a rotational speed of 1200RPM) to explore the effect of impact frequency. The tests were operated with the samples being checked every 10 minutes, this resulted in a 5 minute downtime to check the sample and take a photograph. The speeds used were different to LEP 1, as after the vibrational analysis characterisation carried out in Section 3.3.1, the speed of 1000RPM was deemed safe. Plus after some preliminary testing, LEP 2 lasted longer than the time available in a day at a speed of 900RPM so the speed was increased to 1000RPM. This also links to the reason why the time intervals were increased, as LEP 2 was lasting longer. Therefore to make the process more efficient and to fit the testing into one day, the time intervals were increased.

The results for all samples are shown in Table 34:

Sample	Speed (RPM)	Number of Needles	Time to End of Incubation Period (mins)	Time to Filler (mins)	Time to Breakthrough (mins)
C007	1200	72	10	30	40
C014	1200	72	90	110	120
C015	1200	72	30	40	50
Average	1200	72	43	60	70
C008	1100	72	40	60	150
C009	1100	72	60	90	110
Average	1100	72	50	75	130
C012	1000	72	-	-	-
C013	1000	72	30	180	370
C016	1000	72	300	480	1200
Average	1000	72	165	330	785
C010	1200	36	70	80	130
C011	1200	36	60	80	100
Average	1200	36	65	80	115

Table 34: Results for LEP 2 Samples

The results can be considered in the following groupings: 1. the time to reach the end of incubation period, which was judged as erosion through the clear topcoat; 2. then time to reach the filler i.e. erosion through the red primer layer; 3. time to breakthrough, which is signified by reaching the composite substrate. Sample C012 does not display any results as after 400mins of testing the sample appeared untouched and there were no signs of erosion. This time was chosen due to the amount of testing possible to fit in a day. Therefore the testing was stopped and the set up checked as it was unclear whether this was due to a malfunction or the sample performing exceptionally well.

Figure 74 displays the photographs taken during the testing of C007. The decision on whether the erosion had reached the end of incubation period, filler or breakthrough was an empirical decision and judged when the samples were examined real time. The decision was made this way as it was easier to determine the erosion stage from eye sight rather than a photograph. The clear topcoat combined with the lighting can make it difficult to determine the erosion damage as the topcoat reflects the light and makes the smaller defects difficult to spot. However in

person even the smallest damage can be spotted, thus making the end of incubation period straight forward to determine.

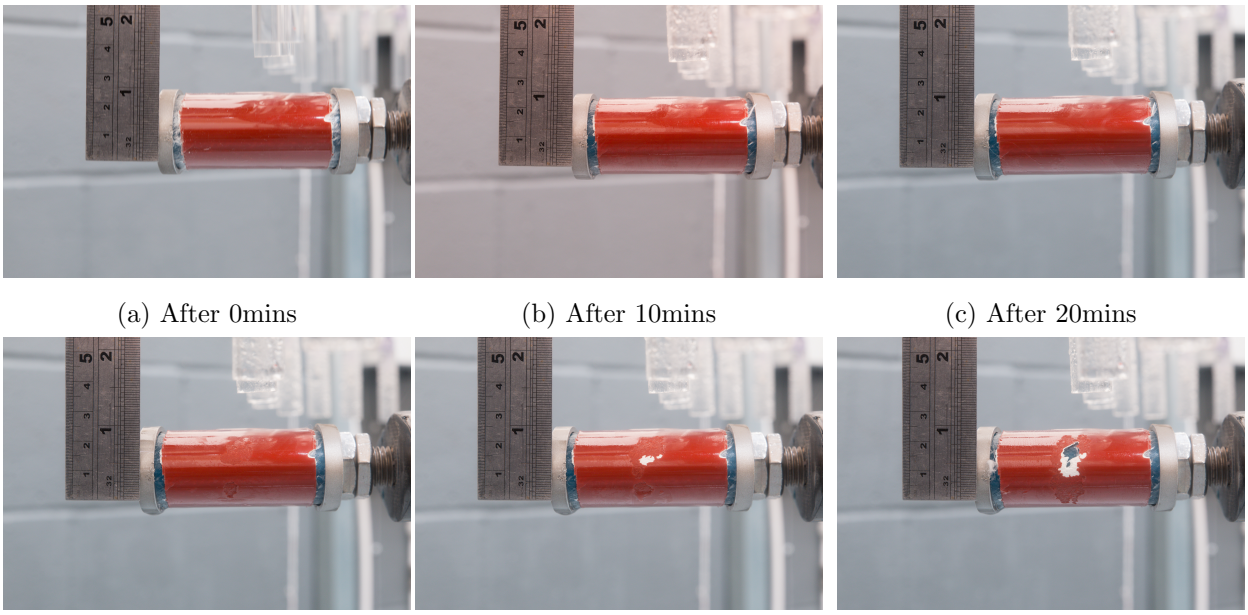

(a) After 0mins (b) After 10mins (c) After 20mins

(d) After 30mins (e) After 40mins (f) After 50mins

Figure 74: Composite samples being tested at a rotational speed of 1200RPM with 72 needles operating for C007

From the results in Table 34 the time to reach each of the stages can be plotted against the different rotational speeds, this is shown in Figure 75.

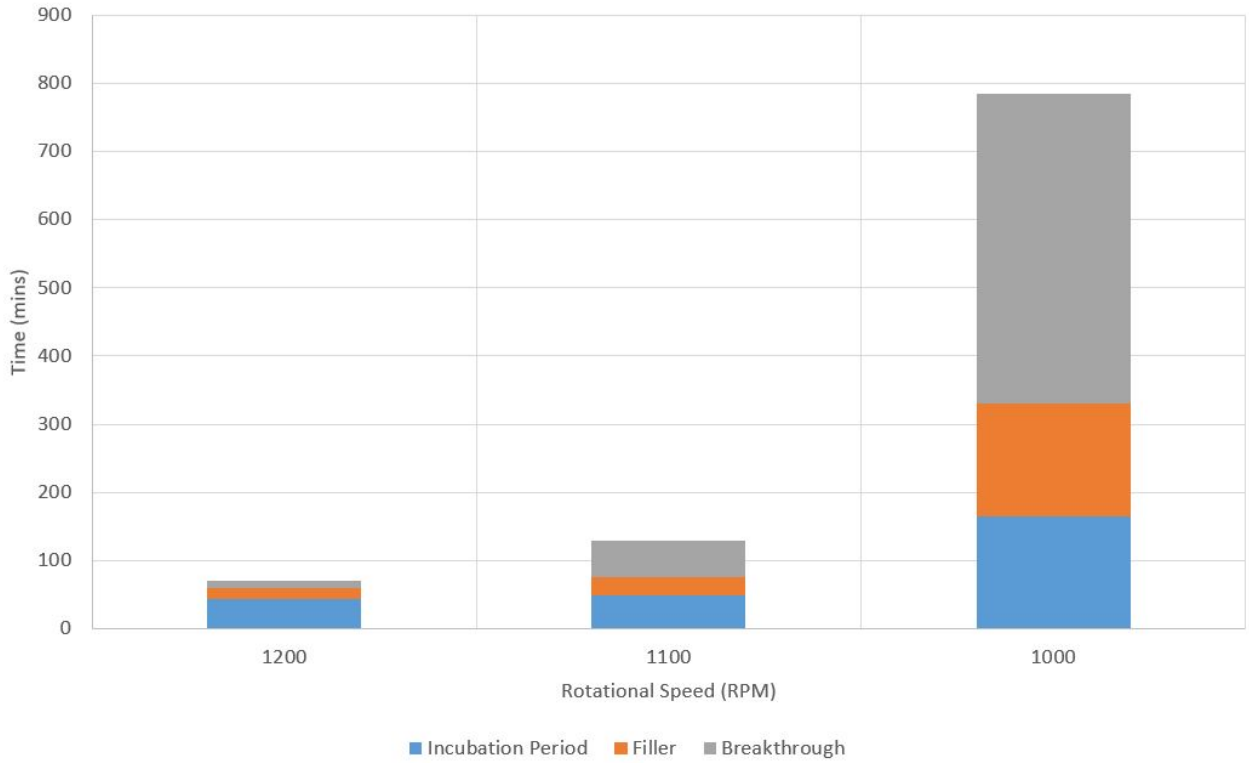

Figure 75: Stacked bar chart showing time to reach end of incubation period, erosion of the filler layer and breakthrough for various rotational speeds

Figure 75 shows several interesting findings: firstly as expected the faster impact speeds result in quicker erosion regardless of the stage of erosion. More interestingly, the ratio of times for each stage is not consistent across the different rotational speeds. As the rotational speeds get slower, and the times longer, the time taken to reach the end of incubation period does not increase at the same rate. Table 35 shows the percentage of the total time to reach each erosion stage and as discussed: the percentage time to reach the end of incubation period steadily decreases as the speed decreases, as well as the percentage time to reach the filler.

Rotational Speed	**End of Incubation Period**	**Reach Filler**	**Breakthrough**
1200	61.9 %	85.7 %	100 %
1100	38.5 %	57.7 %	100 %
1000	21.0 %	42.0 %	100 %

Table 35: Cumulative Percentage of Time to reach that stage of Erosion

The total time to reach the end of the incubation period increases as the speed decreases but a larger percentage increase is seen with incubation period when compated to other layers. For

LEP 2 the incubation period is related to how long the topcoat lasts, the topcoat being the layer that is primarily designed to combat and resist erosion. Therefore it would be expected that the topcoat would perform better, compared to the other layers. This could be due to breakthrough taking less time as the speed increases as the droplet impacts on the filler layer are more destructive. The filler layer is not designed to receive impacts whereas the topcoat is. This means the ratio of time between incubation period and breakthrough shifts to appear as though the topcoat is performing better at higher speeds. It is unclear whether this is the case or whether the topcoat performs better at greater impact speeds.

5.2.1 Number of Impacts

Number of impacts is a better parameter to use when comparing varying impact speeds, as each speed will result in a differing number of impacts per time increment. Figure 76 plots the number of impacts to reach each of the erosion stages for varying rotational speeds.

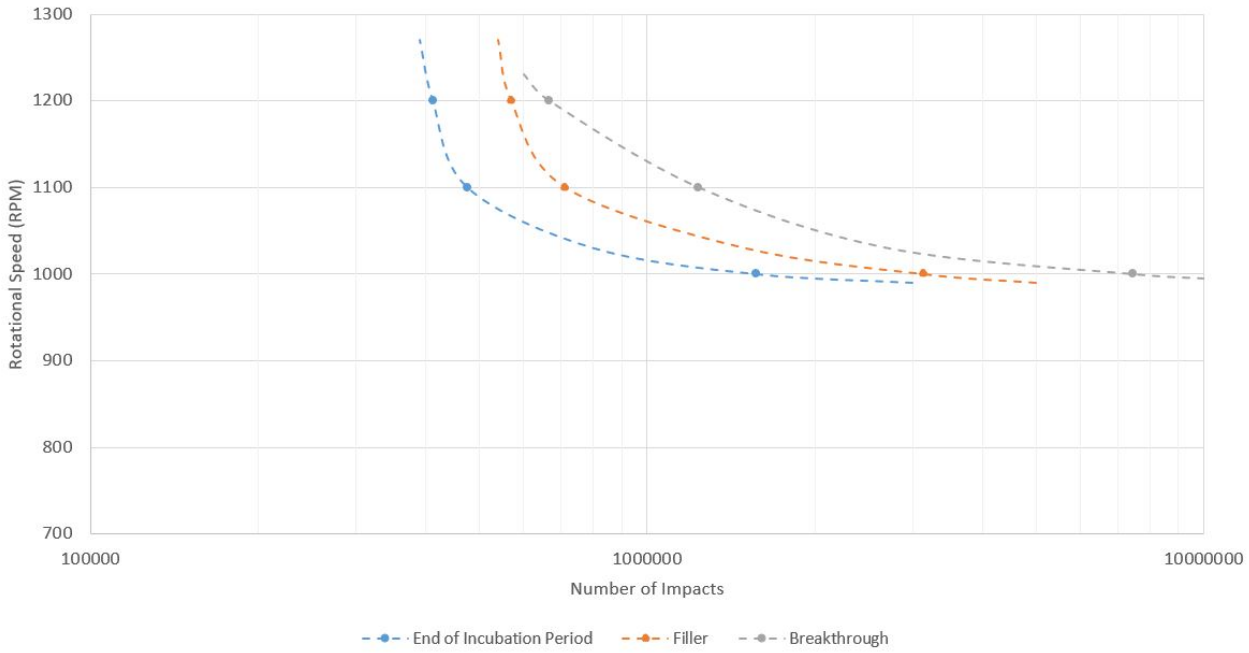

Figure 76: Number of Impacts to reach end of incubation period, erosion of the filler layer and breakthrough

As expected the quicker the impact speed the fewer impacts it takes to reach the different stages of erosion. There are similar shaped curves for incubation period and filler though the breakthrough curve is more gradual. This will be due to the filler being designed to provide a

smooth uniform surface for the LEP to be applied to and is not designed to resist erosion, hence faster speeds are more destructive, so less impacts required to achieve later stages of erosion.

The x-axis is displaying the number of impacts as a logarithmic scale and there is still a sharp decrease in the number of impacts as the speed increases. Comparing this to the aluminium samples, as shown in Figure 57, it is observed that LEP 2 samples are more greatly affected by the change in rotational speed. The aluminium samples displayed a close to logarithmic curve, whereas LEP 2 samples display an even more severe change in number of impacts for a small change in rotational speed. This result shows that a homogenous material will provide consistent results that are easy to predict whereas multi-layered LEPs that have the potential for defects in manufacturing will be less predictable.

5.2.2 Kinetic Energy

The kinetic energy required to reach each stage has been analysed, as shown in Figure 77.

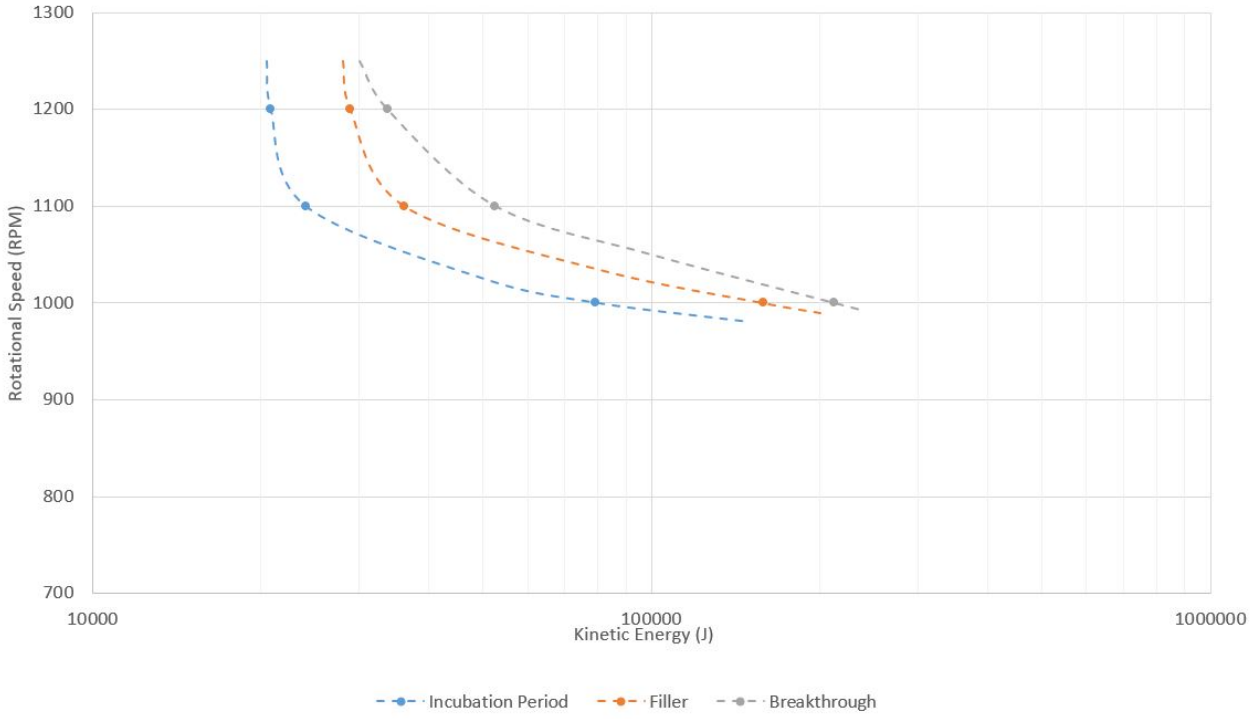

Figure 77: Kinetic Energy to reach end of incubation period, erosion of the filler layer and breakthrough

Figure 77 shows a very similar result to Figure 76, where the erosion was compared to the number of impacts. Again the kinetic energy required rapidly decreases as the impact speed increases. The similar shaped curves for number of impacts and kinetic energy provide confidence

in the results, as these measurements are expected to be similar. If they were very different, this would lead to the conclusion that there are some outliers present, or discrepancy in the results.

5.2.3 Impact Frequency

The effect of impact frequency on erosion can also be examined by comparing varying number of needles as less needles operating will result in a lower impact frequency. The results for this are displayed in Table 36.

	Number of Needles	**Time (mins)**	**Number of Impacts**	**Kinetic Energy (J)**
Incubation Period	72	43	411,542	20,846
	36	65	308,656	12,917
Filler	72	60	569,827	28,864
	36	80	379,885	15,879
Breakthrough	72	70	664,798	33,674
	36	115	546,084	22,852

Table 36: Number of Needles vs Number of Impacts for LEP 2 samples to reach different stages of Erosion

Table 36 shows the number of impacts and the kinetic energy required to reach each of the stages of erosion for both 36 and 72 needles. The time required is longer for 36 needles compared to 72 needles but surprisingly 36 needles (the smaller impact frequency) results in erosion occurring with less impacts and kinetic energy required.

A theory on why a smaller impact frequency results in more erosion per impact could be due to the LEP being a layered system. A layered system reflects and transmits the stress waves, from the impact, through the different layers of the LEP. Therefore, stress waves from the previous impact could reflect off layers and interfere with the next stress waves so this will result in an impact frequency that increases the erosion rate (constructive) and another frequency that decreases the erosion rate (destructive). Potentially the different impact frequencies associated with 36 and 72 needles result in this phenomena occurring, as compared to the effect of impact frequency on aluminium (with no multi-layers) this trend was not seen. The main difference

between the aluminium and LEP 2 is that this LEP is a multi-layered system.

5.2.4 Counting Pixels

An additional method that could be used to track erosion is counting pixels. Rather than measuring the mass loss, as implemented with the aluminium samples, the area of eroded material could be measured using pixels. With the red colour seen in LEP 2 the easiest method for achieving this would be to count the number of red pixels. So as the material erodes the amount of red pixels will decrease. A Matlab script was developed, by the author, to count the number of red pixels from the photographs taken every 10 mins, script in Appendix E. Figure 78 displays the original image and then the pixels that are detected by the Matlab script.

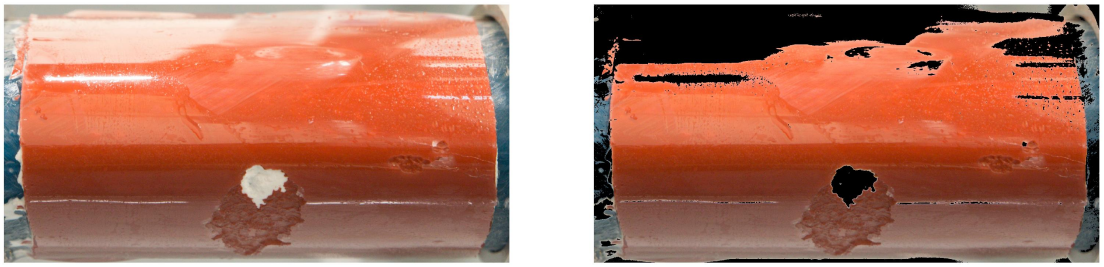

(a) Original Image (b) Matlab Processed Image

Figure 78: (a) Original cropped image and (b) Matlab image detecting red pixels

Figure 78 shows that the Matlab script does detect the majority of the red pixels, however it struggles with the top of the sample and the light reflecting off of it. One can specify colours using a vector that gives the RGB triple, where each value ranges from 0 to 255. However with the lighting the red colours will not appear as a uniform colour across the image, therefore it is necessary to provide a range for RGB of the colours to search within. From research [63] a range of ≥ 50 for R, ≤ 170 for G and ≤ 170 for B was suggested as an initial starting point. Figures 79 and 80 plot the number of red pixels for each image taken, varying the range for RGB.

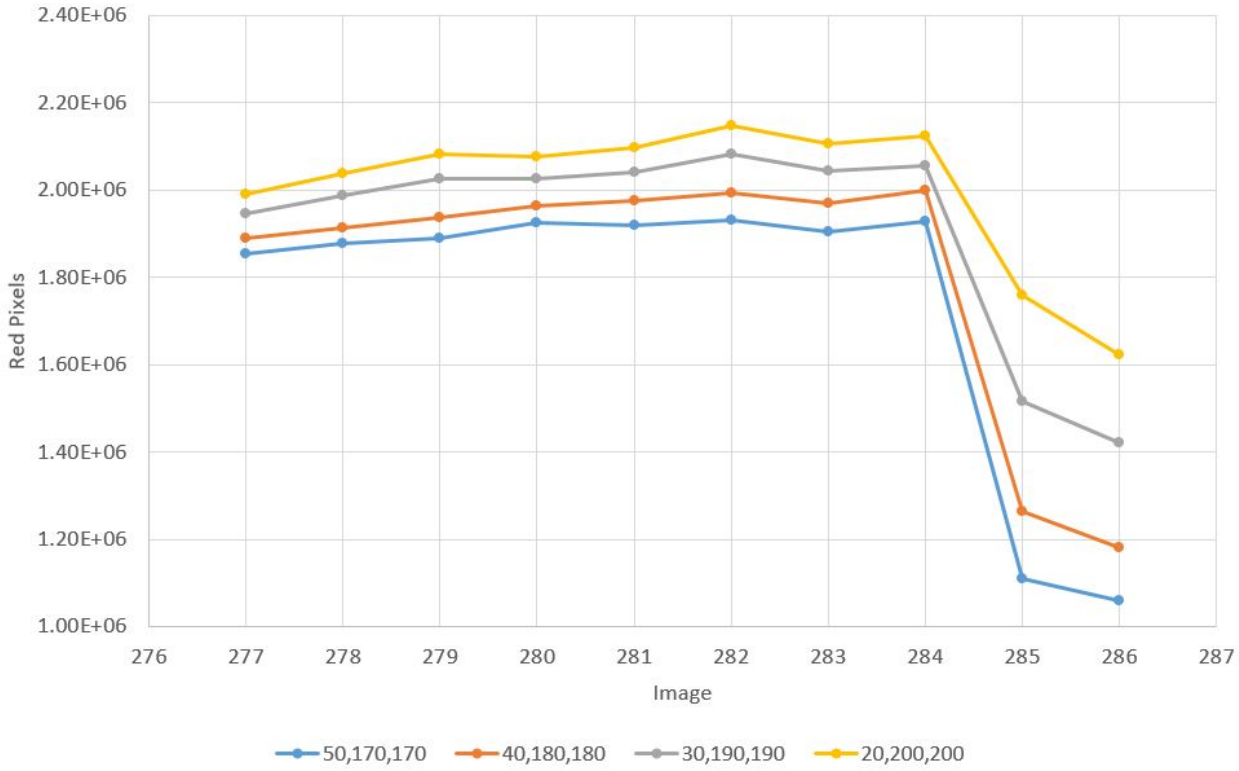

Figure 79: Red pixels vs images for the C006 sample for a variety of colour ranges

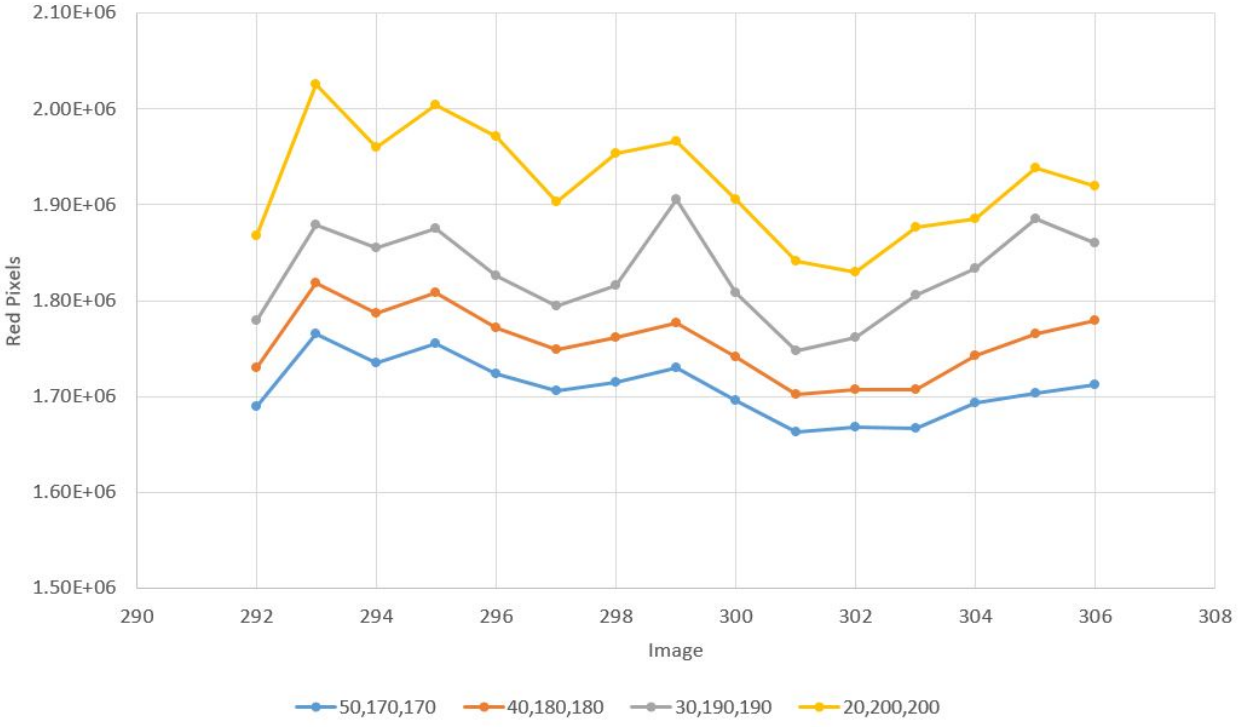

Figure 80: Red pixels vs images for the C008 sample for a variety of colour ranges

Figure 79 plots the changes for Sample C006 and Figure 80 plots the changes for Sample C008. From examining the photos the end of incubation period occurs around image 284 for Sample C006 and image 298 for Sample C008. Therefore it is shown that for sample C006 the Matlab script effectively detects erosion as there is a steep decline at the correct image, indicating the end of the incubation period and the start of steady state erosion. However, for Sample C008 it is less clear and the end of incubation period would not be able to be determined from Figure 80. Sample C006 quickly changes from undamaged to severe erosion, which makes it easier to detect whereas sample C008 occurs more gradually. The photos for both samples are in the appendix. This variation between the two samples in terms of a detectable change in red pixels is vastly different, this same trend continues when looking at other samples. It appears that rapid mass loss is required for the Matlab script to effectively detect the change, this rapid mass loss is not a common failure method so the Matlab script will not be used further as an erosion detection method.

5.3 Discussion

The analysis of LEP 1 & 2 allows the opportunity to take the knowledge gained from the previous chapter, when examining impact speed frequency, and determine if it stills applies to multi-layered systems. From the work with the XCT, it is known that LEP 1 provides fairly consistent results. This allows the modified samples to be compared against the unmodified samples with confidence that the results will be accurate. For all of the samples tested the modified samples lasted a shorter length of time.

The time difference between the two samples (modified and unmodified) to reach the end of incubation period is always around ten minutes, whereas the time to reach breakthrough has a lot larger range. Firstly it is unexpected that the difference at the end of incubation is a constant value rather than a percentage difference, it would be expected that as the length of time increased the difference between the two would increase accordingly. As the exact changes made to the modified samples are unknown it is difficult to draw conclusions on why this is occurring. The wider range of results to reach breakthrough shows how once the coating layer has been breached the erosion rate is a lot more unpredictable.

The curves plotted with rotational speed against number of impacts to reach either the end of incubation period or breakthrough show a linear trend. The aluminium samples shows a logarithmic curve when plotting the same graph. This implies that LEP 1 does not perform as well at the higher impact speeds compared with the aluminium samples. This is to be expected as the layers in LEP 1 that reflect and transmit waves, will amplify the stress waves causing the faster speeds to have a great effect. Finally the lack of samples resulted in no measurement being taken at 900rpm for the unmodified samples, this does make it difficult to draw a trend line with only two points. Depending on the result of this missing sample, it could greatly alter the shape of the curve.

When plotting the same curves using kinetic energy rather than number of impacts, the modified samples shows a difference shape with the slower speed requiring a lot less kinetic energy than expected. Again the lack of a sample at 900rpm for the unmodified samples makes it unclear if this is consistent with the unmodified samples or something has changed with the modification.

The most interesting result from LEP 1 is that the impact frequency does not affect the lifetime of the samples. Tested with 24, 36 and 72 needles, the unmodified sample requires an almost identical number of impacts to reach the end of the incubation period. Studying the impact frequency to reach breakthrough does not provide as consistent results though the number of

impacts are fairly similar.

The LEP 2 samples perform better than the LEP 1 samples, lasting longer when comparing samples for the same speed. However LEP 2 is less consistent with a much wider range of results. The fact that the speeds used for LEP 2, were 1000, 1100 and 1200rpm means that there cannot be direct comparison to LEP 1. However results from the same speed can be compared, the main conclusion being that LEP 2 samples exhibit more signs of brittle erosion. This leads to a larger range of results as the rapid mass loss associated with brittle fracture can occur at any time.

LEP 2 samples include a fourth layer in the LEP, the inclusion of a primer between the filler and topcoat. Therefore reaching the filler layer is a measurement now recorded as well as end of incubation period and breakthrough. Examining the ratio of times to reach each of these stages for varying speeds provides interesting results. The percentage of total time spent to reach the end of incubation period is greater at higher speeds, as seen in Table 35. Comparing the percentage of total time taken to reach the end of incubation period the percentage increases by roughly 20% as the speed increases. It is unclear whether this is due to the coating performing better at higher impact speeds or that the other layers erode quicker. If the coating layer could be isolated on its own, this phenomena could be explored further.

When examining the rotational speed vs number of impacts curve in Figure 76 it is observed that the curves are steeper than a logarithmic. This means that the LEP is performing better at higher impact speeds as it requires more impacts to reach each erosion stage. A similar situation is seen when examining the curves for kinetic energy. To return to the previous paragraph, this shows that potentially the coatings are designed to function better at higher speeds and that is why the percentage of time to reach the end of the incubation period increases as the speed increases.

When examining the effect of the impact frequency the results are quite different to LEP 1, for LEP 2 samples the smaller impact frequency the shorter the lifetime. This is consistent for all erosion stages and not just an anomaly with results. As stated before the layered system might be the cause for this result, with the transmission and reflection of the stress waves at certain speeds they could become constructive thus amplifying the stress waves. This is not seen in LEP 1 but each LEP would have a specific impact frequency where this phenomena occurs and that frequency might not have been tested for LEP 1.

The Matlab script designed to detect the number of red pixels was an interesting experiment

to test it's validity. The process worked well when the erosion occurred rapidly and the red primer layer was removed quickly, however the results were unclear with slower more ductile erosion. As the failure mechanism is unknown before the beginning of testing, the use of this Matlab script unfortunately could not be used. Another issue is that most LEPs do not have as distinctive a colour as LEP 2 therefore with a coating having a similar colour to the filler this set-up would not work. However it did provide some promise, though it would require more time than the author had to make it a reliable and accurate method for tracking erosion.

Both LEPs provided good alternatives to the aluminium samples. LEP 1 was close in terms of repeatability but lacked the erosive resistance to last as long. LEP 2 did show a significant improvement in terms of lifetime although this was only for certain samples, as the LEP had a large coefficient of variation, other samples only lasted for a short period of time. LEP 1 samples also portrayed a similar failure mechanism each time with the rate of mass loss fairly similar, whereas LEP 2 seemed to provide a larger range of failure, with some samples experiencing massive areas of damage and others just small areas.

6 Computationally Efficient Finite Element Erosion Model

Using finite element analysis can provide a time and cost effective method to explore the erosion process and different parameters associated with it. With respect to erosion, the large amount of testing time combined with the uncertainty associated with the testing procedure means that computer modelling provides a more efficient and potentially even more reliable method to studying parameters than by solely experimental testing. By linking the two approaches, a more thorough and deeper understanding of the phenomenon can be gained with each approach validating and informing the other.

For this computational analysis, LS-DYNA was chosen as the finite element software due to it being a leading software tool for impact analysis with a suite of capabilities and approaches for modelling turbine blade erosion problems. It also provides a variety of different material and contact models which are two of the main considerations when modelling water droplet impacts on wind turbine blades.

6.1 LS-DYNA Set Up

Firstly a basic model must be developed to increase the understanding of a new software as well as validating that the software is suitable to complete the necessary task. This basic model should still be physically representative of the samples used in experimental set ups, there are two types available in industry, either a flat sample or an aerofoil sample.

LS-DYNA controls all of the model's operations using the keyword manager, the keyword manager states all properties for the model to run: the material properties, contact, termination time, timestep etc. The only aspect of the input deck not generated by the keyword manager is the geometry.

6.1.1 Geometry and Meshing

LS-DYNA does include an in-built geometric modeller, however it is somewhat rudimentary and struggles to build more complicated shapes. Therefore for any flat samples the geometry was built in LS-DYNA whereas the aerofoil shapes were built using Solidworks and then exported into LS-DYNA as an IGES file. The geometry of the aerofoil was the same as used in

experimental testing, and as stated in the DNV GL standard.

When building a simple flat shape in LS-DYNA the number of elements can be easily set to achieve the level of accuracy required. However when importing the geometry into the program, meshing does not become as simple. The automesher tool is used to apply the mesh to the geometry, which can be progressively refined to result in a mesh fine enough for the task.

Difficulties can arise when using very thin, curved layers. As the elements can not have curved edges, therefore the curve is made of many very small straight lines (or elements). This process works perfectly well for single layer systems however when multi-layered curved shapes are modelled this can lead to some difficulties. Using linear elements, curved layers that are touching each other, when meshed, will result in overlaps between the layers as the approximations of the curves do not link up. To combat this issue there needs to be small gap left between the layers of only around 0.1mm.

6.1.2 Smoothed Particle Hydrodynamics

Smoothed particles hydrodynamics (SPH) was invented to simulate nonaxisymmetric phenomena in astrophysics [64]. The method was developed to provide a modelling process that was easy to work with and could provide reasonable accuracy, even for difficult situations. The SPH approach satisfied these requirements and also was found to be robust stably so could be extended to complicated physics without much trouble.

The SPH method is a particle method, which constructs a continuous field from a cloud of discrete particles which are property carriers. It is a meshfree method which makes it ideal to simulate problems dominated by complex boundaries or where mesh stability is difficult to achieve. Another benefit is that SPH can easily be hybridised with other modelling techniques, as well as the computational cost of SPH simulations per number of particles being significantly less than a grid based simulation when the metric of interest is related to fluid density. The modelling of water droplet impact fits these criteria.

Lui et al [65], used smoothed particles hydrodynamics for the numerical simulation of an underwater explosion. Keegan et al [17] also used SPH to model water droplet impacts, after comparing the SPH method with an Eulerian approach. Their reason for using SPH is that as a free Lagrangian method can track the moving interface between the gas produced by the explosion and the surrounding water effectively. The meshless nature of SPH overcomes the

difficulties resulting from large deformations. Vacondio et al [66], explored smoothed particle hydrodynamics in shallow water used for modelling a wide range of varying free-surface flows such as dam breaks, river floodings and tidal flows. These principles are the same reasons why SPH is beneficial to model water droplet impacts.

The main difference between SPH and classic approaches is the absence of any grid or mesh. Instead the droplet is represented by a collection of particles (or nodes) through which all the governing equations are applied. Each particles is assigned part of the mass/density of the whole body and represents a point for material properties and characteristics during modelling. The particles are not directly connected, instead they are the basis of an interpolatory system which uses a kernel function to determine the material behaviour. Figure 81 shows how SPH can be implemented with water droplet impacts [17]. This allows the large deformations present in lateral jetting, a typical characteristic of droplet impingement, to be modelled.

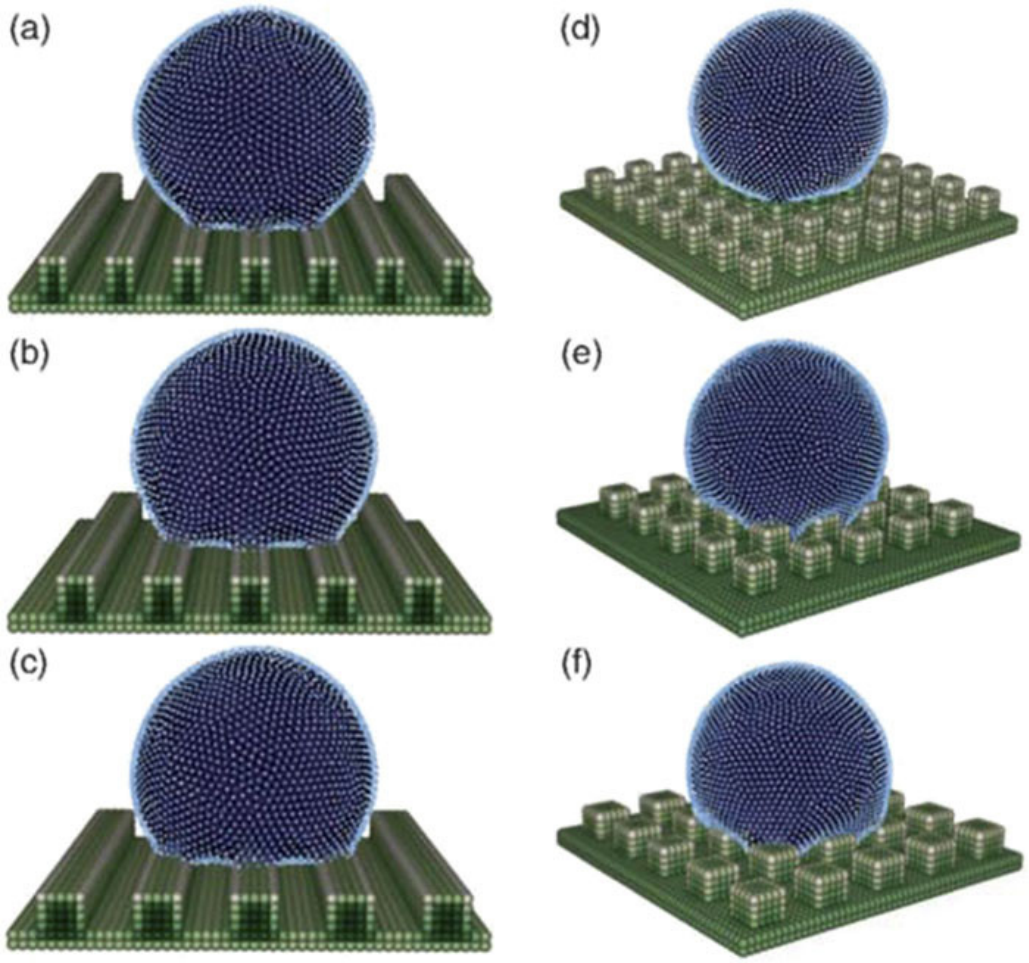

Figure 81: SPH method, analysing static contact angles of droplets on hydrophilic rectangular and dual rectangular surfaces [22]

To implement the SPH method into LS-DYNA is a reasonably straightforward process. The main parameter to change is the number of nodes in each axis, along with inputting the radius and the density of the water. An increased number of nodes will increase the accuracy of the analysis but it reaches the point of diminishing returns, in Section 6.3 a sensitivity analysis is conducted to determine the optimum number of nodes.

6.1.3 Boundary Conditions and Initial Velocity

The two main conditions set are the initial velocity of the droplet and the boundary conditions. The initial velocity is determined by the experimental set up, as the experimental set-up measures the rotational velocity this needs to be converted to the impact velocity. Table 37 shows the corresponding impact velocity to rotational speed.

Rotational Speed (RPM)	**Linear Speed (m/s)**
700	75.1
800	85.9
900	96.6
1000	107.3
1100	118.1
1200	128.8
1300	139.5
1400	150.3

Table 37: Converting Rotational Speed to Linear Speed

When the modelling work is linked to an experimental sample the impact velocity will be chosen accordingly. However for the present set of parametric studies a value will be chosen, usually the worst case scenario (150m/s).

The boundary conditions change depending on the sample being modelled. When comparing the models to the experimental setup certain edges are fixed in space. For both the flat and aerofoil sample, the sample is locked in place by an aluminium holder. Figure 82 shows the bottom surface of the sample is fixed which correspond to the experimental setup as well as showing each of the nodes initial direction.

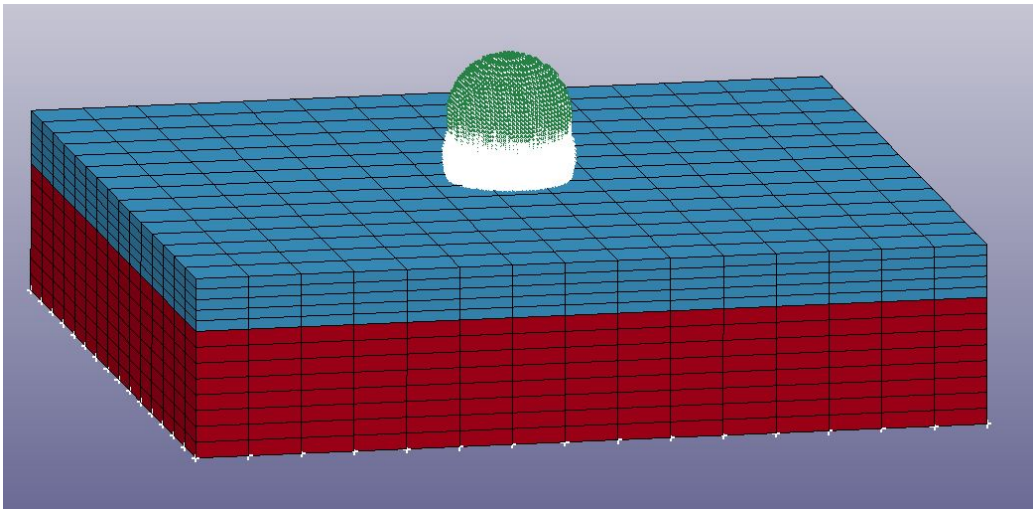

Figure 82: Boundary conditions and initial velocity applied to model

6.1.4 Material Models

LS-DYNA offers a range of different material models for any material and situation so choosing the appropriate one takes time. The main factors on choosing the material model is the material data available and the expected forces acting on the material. For example, it is expected that the shear stress will play an important part in the failure of a material, a material model that incorporates shear modulus would be important.

Firstly, modelling the water is relatively straightforward as the water is assumed only to apply force to the coating and requires only a simple material model. No physical information is required from the water other than its loading action. The material model used is MAT_NULL, this material model allows the equation of state to be considered without computing the deviatoric stresses. This means that the SPH can be bypassed in the element processing however the mass and pressure it applies is still computed. A Gruneisen equation of state is used, which relates the pressure and volume to a given temperature. These values then relate to the water-hammer pressure which is then applied to the coating.

The modelling of composites is more complicated as composite materials are anisotropic, therefore requiring more material properties. Menna et al [23], provides some data to be used to model a glass fibre composite. These values are inputted into the material model MAT_SOLID_COMPOSITE_FAILURE, this model can simulate three-dimensional behaviour and predict the initiation of three major failure modes: tensile failure, compressive failure and transverse shear failure. The values inputted into the material model are shown in Table 38 below.

Material Property	**Orientation**	**Value**
Density (kg/m^3)	-	1500
Young's Modulus (GPa)	x	26
	y	26
	z	8
Tensile Strength (MPa)	x	414
	y	414
	z	120
Compressive Strength (MPa)	x	458
	y	458
	z	500
Shear Modulus (GPa)	xy	3.8
	yz	2.8
	xz	2.8
Shear Strength (MPa)	xy	105
	yz	65
	xz	65
Poisson's Ratio	xy	0.1
	yz	0.25
	xz	0.25

Table 38: Composite substrate material properties [23]

The coating is the most important part of the LEP system and therefore the modelling of this should be carried out with attention to the detailed interaction. However there is a lack of information available as most manufacturers do not publish material property data. Littell et al [24], measured the tension, compression and shear stress-strain curves for an epoxy resin the values of these are shown in the table below:

Material Property	Value
Density (kg/m^3)	1150
Young's Modulus (GPa)	2.5
Poisson's Ratio	0.4
Tensile Yield Stress (MPa)	90
Tensile Strain at Break	0.25
Compressive Yield Stress (MPa)	120
Compressive Stress at Break (MPa)	180
Compressive Strain at Break	0.3

Table 39: Gelcoat material properties [24]

The values from Table 39 are used in the material model MAT_PLASTICITY_COMPRESSION_TENSION. However this relates to one particular coating and each coating manufacturer will provide different properties depending on the failure mechanism they are trying to avoid. It is noted that this coating is also designed for the aerospace industry and not specifically to prevent erosion but a lack of information makes it in the best available data to undertake these benchmark tests. The values for tensile and compressive stress/strains were used to make stress/strain curves, these were then inputted into the model using the DEFINE_CURVE feature in LS-DYNA.

This problem of assuming data is common across all of the different layers. The values shown above provide representative and qualitative values that can illustrate the problem and probe certain parameters but without accurate data there cannot be the complexity required to fully understand the problem.

6.1.5 Contact Models

The multi-layered systems present in most LEPs mean that the interface between the layers becomes an important area to model. As discussed in Section 1.2 the stress waves in the sample will reflect and transmit through the different layers. Depending on the connection between these layers the stress waves will transmit more or less easily and from the work with the XCT in Section 4.2 there is a large number of voids present near the interface between the composite and filler. The voids present result in the contact being imperfect though it is extremely difficult

to produce a numerical value for the quality of the contact.

For all models, the contact will be assumed to be perfect. The contact model used for the water impacting the sample is CONTACT_ AUTOMATIC_NODES_TO_SURFACE_SMOOTH and the contact between the two layers is modelled using CONTACT_AUTOMATIC_SURFACE_TO _SURFACE_TIEBREAK.

6.1.6 Base Model

Using the different material and contact models mentioned above base models can be developed, these models can be altered to see the effect of erosion. In Figure 83 a flat sample and curved sample are displayed.

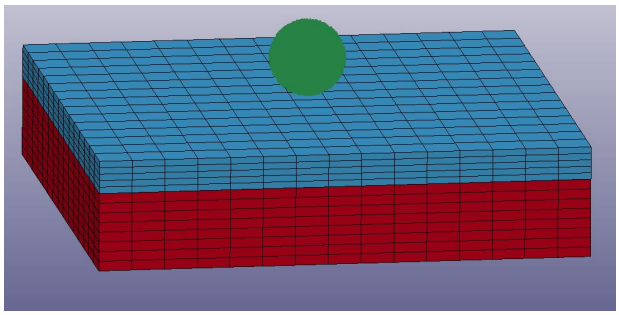

(a) Flat Sample

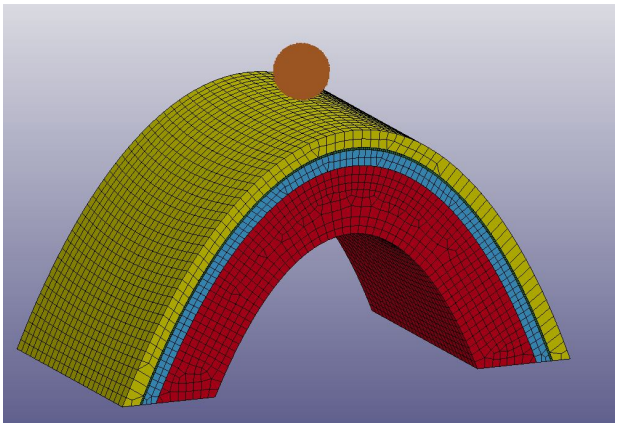

(b) Curved Sample

Figure 83: Flat sample and curved sample with varying layers

The flat sample is a simple set-up with a composite substrate and a coating layer on top of this, whereas the curved sample is aimed to replicate the LEP 2 with a topcoat, putty, filler and composite substrate. These models can provide the basis to experiment with various different parameters, and while the exact material properties may not be known useful results can still be drawn.

Figure 84 shows the stress plots for progressive time intervals, originally the droplet obscures most of the details so images are also taken with the droplets removed for the sample time steps, Appendix G contains the same stress plots for the curved sample. When examining models this is a useful tool to determine where the stress is concentrating.

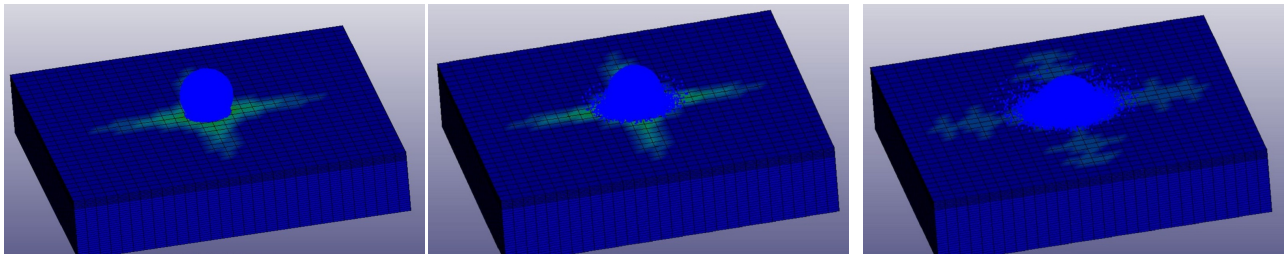

(a) Stress plot at t=1 $\times 10^{-6}$ (b) Stress plot at t=2 $\times 10^{-6}$ (c) Stress plot at t=3 $\times 10^{-6}$

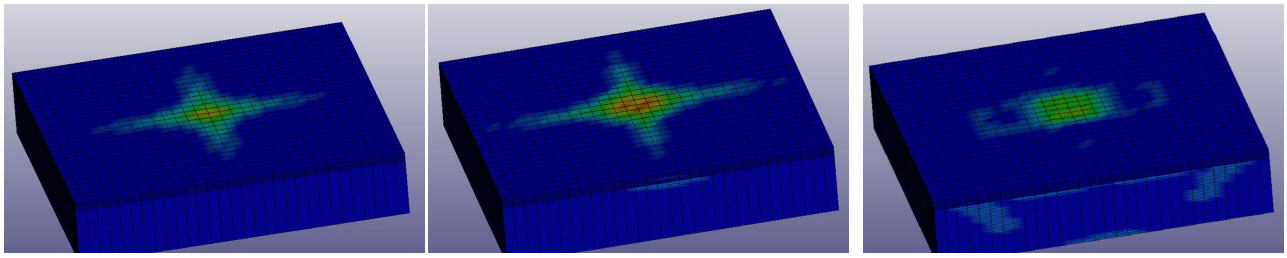

(d) Stress plot at t=1 $\times 10^{-6}$ (e) Stress plot at t=2 $\times 10^{-6}$ (f) Stress plot at t=3 $\times 10^{-6}$

Figure 84: Progression of stress plots for the base model with and without droplet

Below in Figure 85 the z-stress is plotted against time for the flat sample above. The droplet is travelling in the z-axis so the z-stress is displaying the compressive stress inflicted by the droplet. The different lines indicate how far the point measured is from the centre of the impact, starting at the middle and going out to 3mm.

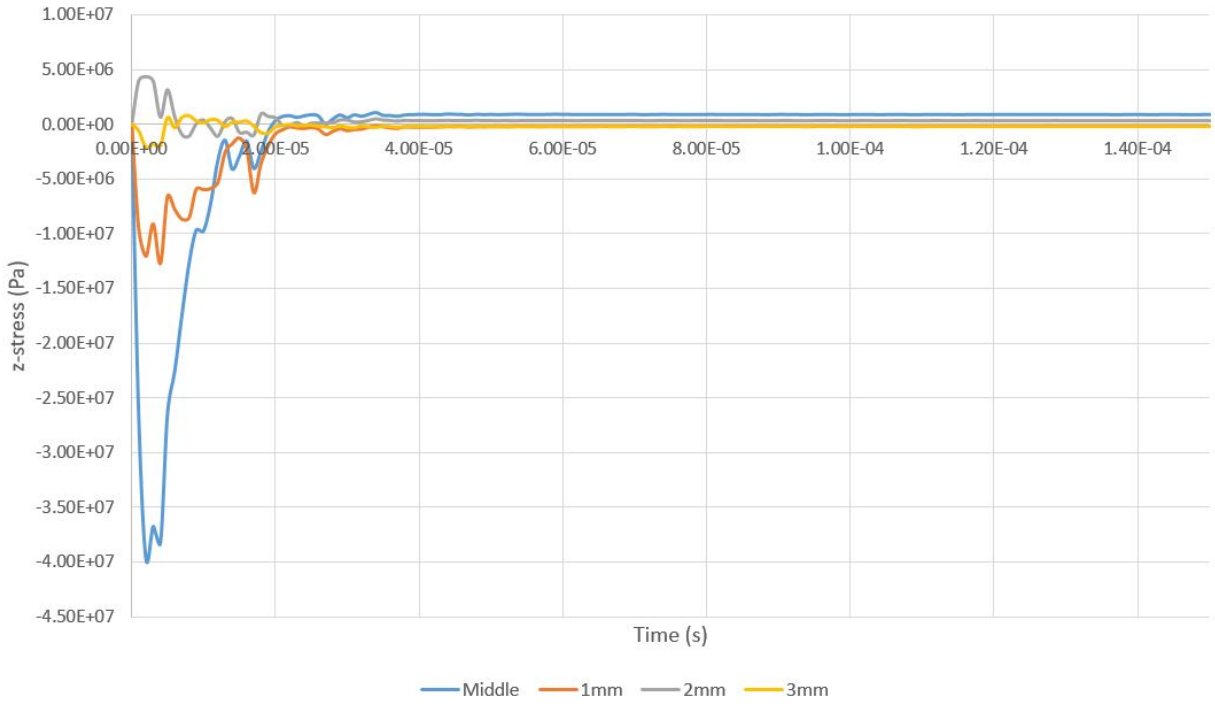

Figure 85: Z-stress against Time for a droplet impact plotted for varying radial distances

Figure 85 shows that the largest peak in compressive stress is right in the centre of the sample. Also interestingly at 2mm out there is a spike in tensile stress at the same time presumable countering the peak in compressive stress. It also shows that quite quickly, around 4×10^{-5}s, the stress levels plateau though at no distance does it return to exactly zero there is still some residual stress.

This model does lack accuracy and was used as a test to check all the different sections (material models, contacts, geometry) work together. One of the main methods for increasing the accuracy of models is to increase the number of elements or nodes however this can result in a large increase in computing time. A sensitivity analysis was conducted to investigate this, see Section 6.3.

6.2 Validation of Model

When using modelling techniques it is important to validate the model's results to check the model is a fair representation of the problem. It is impractical to measure the stresses and strains on the sample with the test rig operating at such high speeds. Therefore basic equations were used to compare against the base model, in Section 6.1.6. Keegan [67] carried out this comparison using a flat sample with the epoxy coating on top. The results from this model were compared against the waterhammer pressure mentioned in Section 1.2. The results are shown in Figure 86.

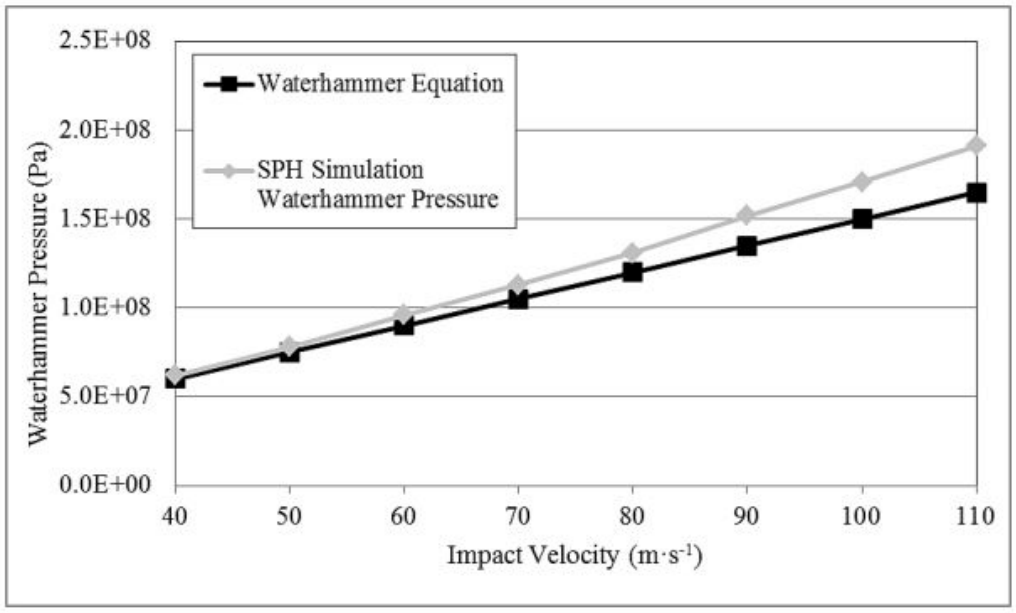

Figure 86: Comparison of calculated waterhammer pressure and Von Mises stress (determined from model) for a 3mm droplet impacting an epoxy coating.

From Figure 86 it is observed that the model closely follows the waterhammer pressure, though does slightly differ at higher impact speeds. The difference between the model and the calculations is minimal showing that the model provides an accurate representation of what is occurring.

6.3 Sensitivity Analysis

The complexity of modelling erosion is relatively high. This can lead to large computing times, while this is not an issue for individual models it adds unnecessary time with carrying out a parametric study. As such, the number of nodes used in the SPH; the number of elements used to model the sample and the material properties used for the coating are explored.

6.3.1 Number of Elements

The number of elements is crucial both to the run time and the accuracy of the model. Below in Table 40 the time taken vs the number of elements is shown.

Number of Elements	**Time**
800	18mins
3200	20mins
25600	57mins
102400	175mins

Table 40: Sensitivity Analysis of Elements in Model

When investigating how the number of elements affected the outputs from the model, it was found that the results were converging on a solution around 25,600 elements though there still was slight improvement with an increase in elements. Over the time frame of an impact the maximum variation in stress levels between 25,600 elements and 102,400 elements was only around 0.3% and considering the drastic difference in time this value was deemed acceptable. The model used to test this was a very simple one layer flat plate and the finest meshed sample already was taking roughly three hours. Therefore it was decided not to go any further as an increase of elements on top of this would not occur, as the computing time was too great.

6.3.2 SPH Nodes

A similar process was conducted investigating the number of nodes used in the SPH. Table 41 shows the number of nodes corresponding to a particular run time. The total number of nodes

correspond to a SPH with 10x10x10 nodes along each axis right up to 80x80x80 nodes in each axis.

Number of SPH Nodes	**Time**
552	1min
4224	7mins
14328	10mins
33552	18mins
65752	55mins
113104	50mins
179944	140mins
268096	242mins

Table 41: Sensitivity Analysis of SPH Nodes in Model

In Table 41 it is noticed that as expected the computational time increases as the number of nodes increases. There is an anomaly however where the time decreases for 113,104 nodes. This will be due to the model tested with 65,752 nodes taking unusually long. For example, the author uses 4 licenses at once to speed up the program if 4 licenses were not available at that time this could cause it to take longer or some computational power was occupied by something running in the background.

There is a more noticeably change when analysing the SPH nodes compared to the number of elements. Figure 87 plots the Von-Mises stress in the sample against time for the different number of nodes and Figure 88 plots the Z Force against time for the different number of nodes. The lines correspond to n=10 up to n=80 where n=10 is a SPH with 10x10x10 nodes.

From both figures it is observed that around the n=40 mark there seems to be no noticeable difference in the results for any increase in nodes. This corresponds to a total number of nodes of 33,552 which takes a reasonable amount of time to run, therefore this was deemed the ideal number of nodes to include in the SPH.

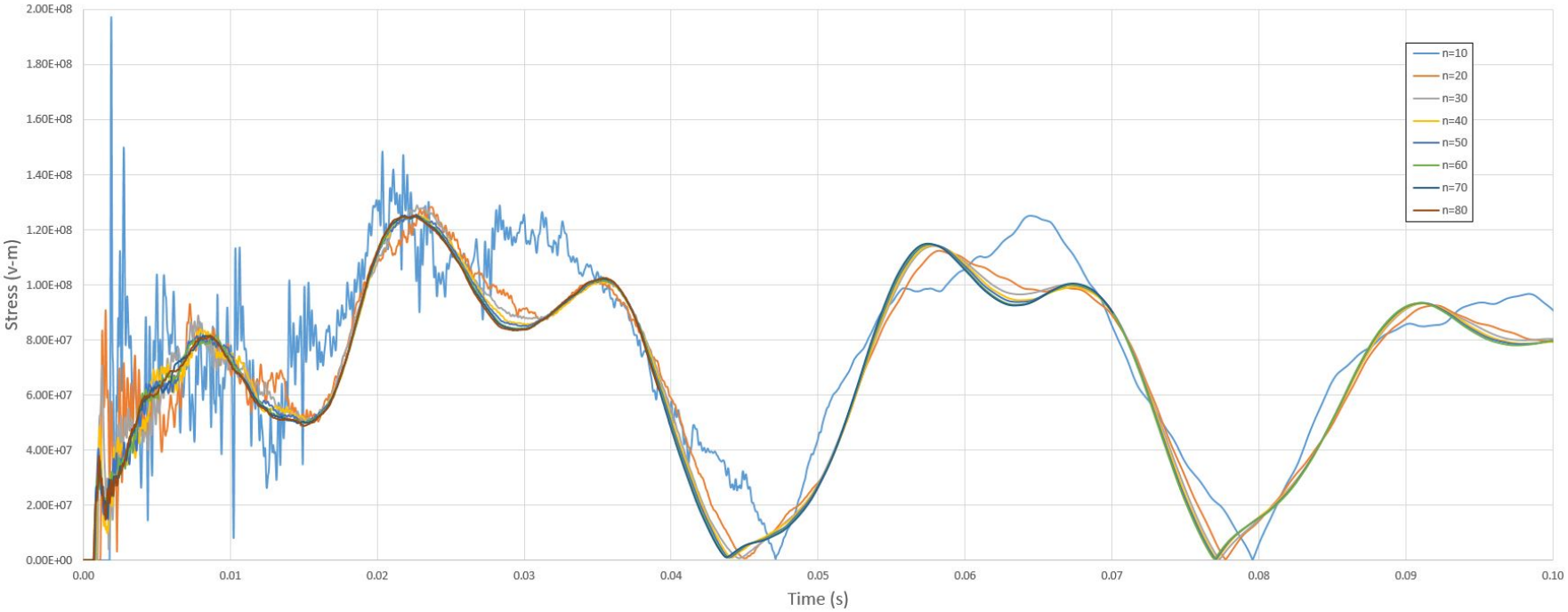

Figure 87: Sensitivity Analysis of SPH Nodes using Von Mises Stress

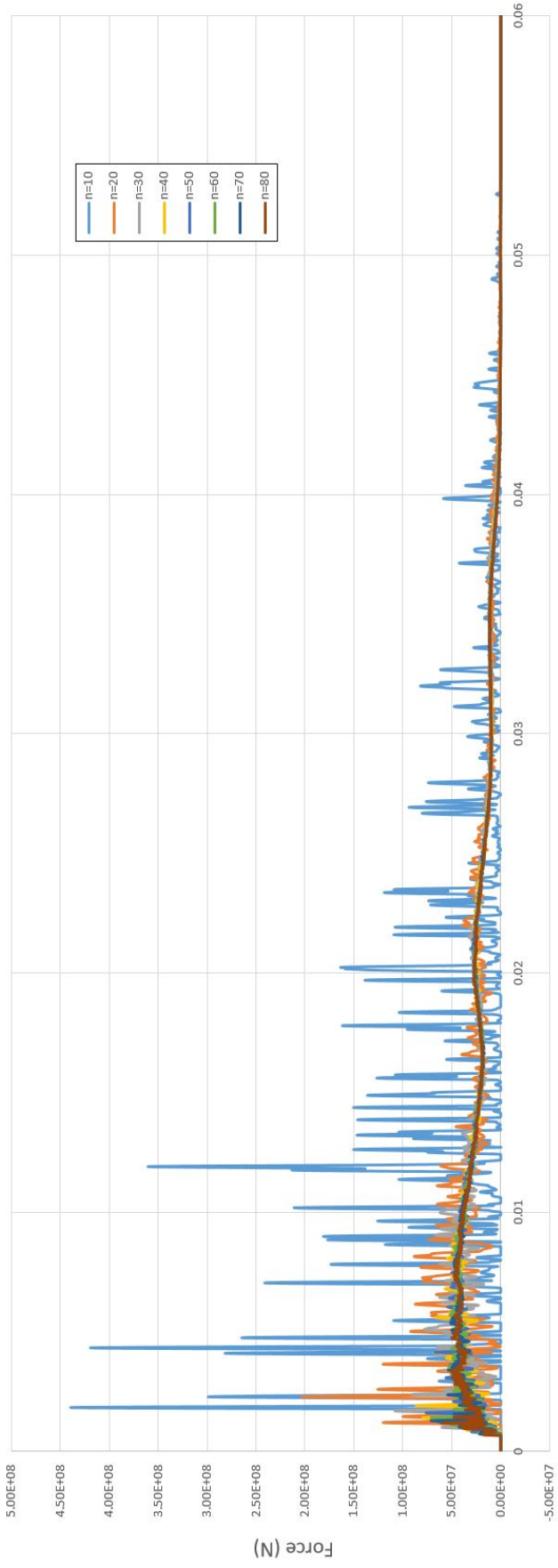

Figure 88: Sensitivity Analysis of SPH Nodes using Z Force

6.3.3 Material Properties

The material properties for the coating found in a paper by Littell et al [24] were also checked. The coating is not specifically designed for wind turbines, but is the only data available. Therefore a quick sensitivity analysis was conducted to see the effect the coating's material properties had on the results. The coating response was altered by making it either 10% harder or 10% softer (by changing the Young's modulus and stress/strain curves). Values such as the peak Von Mises, Tresca and Z Stress were then determined for each of the different material properties and the results are below in Table 42.

	Softer	**Normal**	**Harder**
Young's Modulus	2.25 GPa	2.5 GPa	2.75 GPa
	Centre of Sample		
Max Von Mises	1.57×10^7 GPa	1.59×10^7 GPa	1.6×10^7 GPa
Max Tresca	7.86×10^6 GPa	7.97×10^6 GPa	7.98×10^6 GPa
Max Z-Stress	-3.98×10^7 GPa	-3.97×10^7 GPa	-3.96×10^7 GPa
	2mm out from Centre		
Max Von Mises	4.5×10^6 GPa	4.71×10^6 GPa	4.93×10^6 GPa
Max Tresca	2.6×10^6 GPa	2.72×10^6 GPa	2.85×10^6 GPa
Max Z-Stress	-9.84×10^5 GPa	-1.09×10^6 GPa	-2.27×10^6 GPa

Table 42: Sensitivity Analysis of Gelcoat Material Properties

From Table 42 it is shown that the values are very similar even with the changes in material properties. There is a bigger change when examining the data 2mm out from the centre however it is deemed that the values still display a similar result, there is not factors of difference between the values. As stated before without accurate material properties the purpose of the modelling is to carry out parametric studies and notice trends in the erosion results and for this purpose the coating data was deemed acceptable.

6.4 Multiple Impacts

To fully understand the erosion process more than a singular droplet impact needs to be modelled. To investigate this three droplet impacts were modelled impacting a sample, the droplets were spaced a distance to replicate the time between strikes that is comparable to the ETC test rig. Figure 89 shows the setup with the sample being the composite material and coating stated in Section 6.1.4.

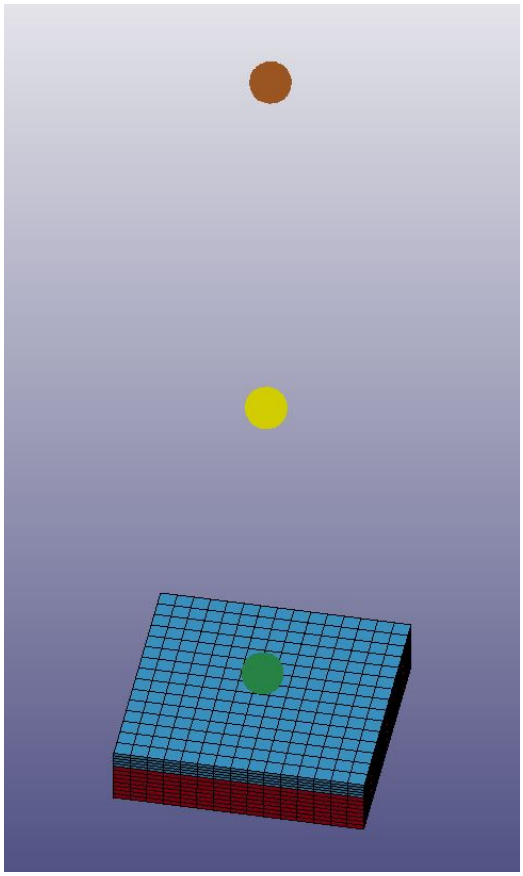

Figure 89: Arrangement of droplets to investigate multiple impacts

From this setup the accumulation of stress can be explored. Figures 90 and 91 plot the z-stress and Tresca stress. The z-axis is the axis the droplet impacts along so the z-stress becomes the compressive stress and the Tresca stress is the maximum shear stress. Both figures plot the stress against time for varying radial distances.

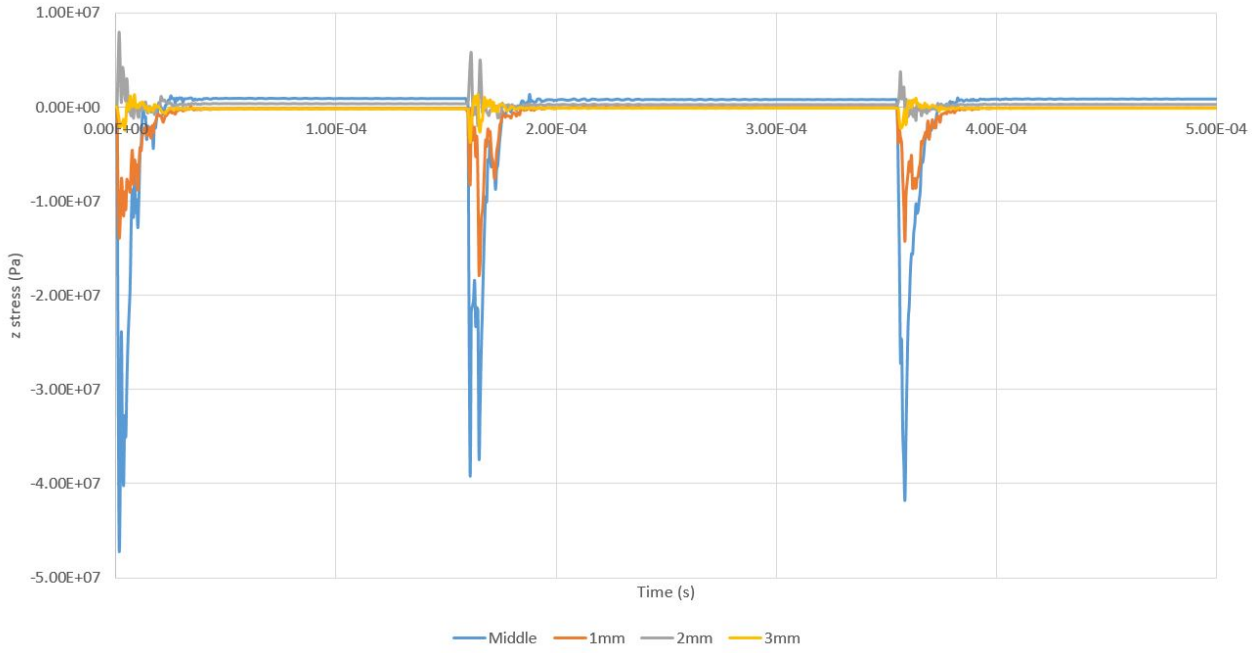

Figure 90: Z-stress against Time for multiple droplet impact plotted for varying radial distances

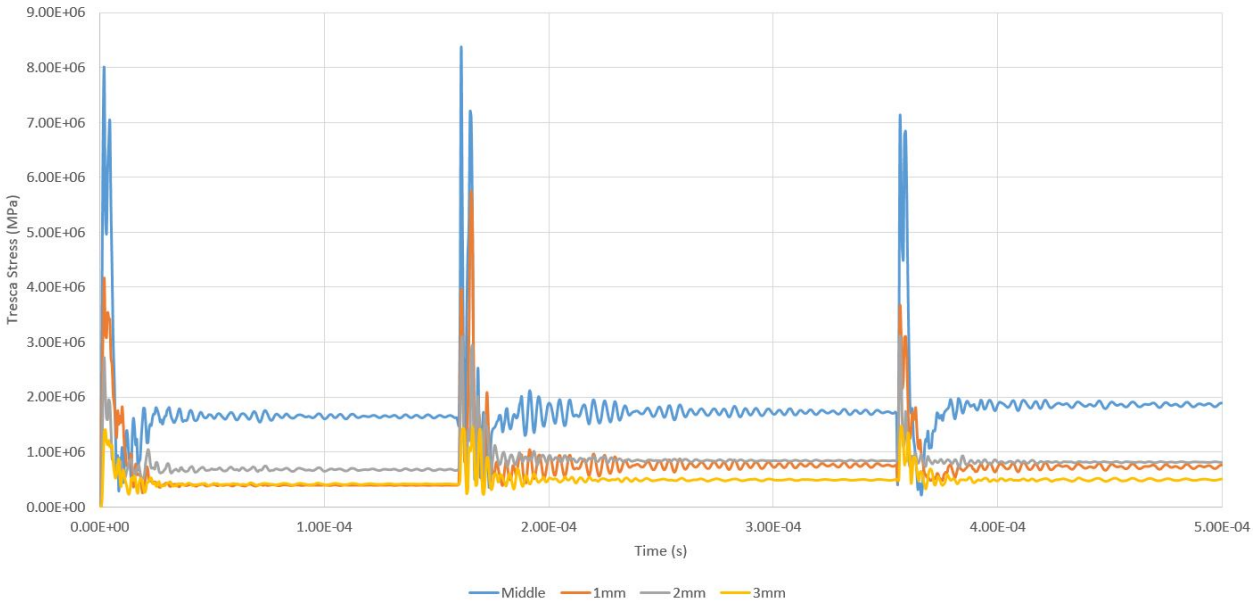

Figure 91: Tresca stress against Time for multiple droplet impact plotted for varying radial distances

Firstly the peak maximum stresses in both figures fluctuate for the three different impacts not showing a clear trend in peak stress. The compressive stress in Figure 90 returns to roughly zero after all three impacts and regardless of the radial distance. As with the singular impact the central location displays the highest peak stress and as the radius increases the peak stress decreases.

Looking at Figure 91, it is observed that the shear stress does change over time and radial distance. Firstly the centre of the sample shows a noticeable increase in shear stress compared to further away from the centre. Secondly the shear stress does not return to zero after the initial peak, there is still some residual stress present in the sample. Finally this residual stress slightly increases after each impact, the increase is very small but for all radial distances there is a slight increase.

This slight increase shows how over a very large number of impacts, the residual stress level could build to such an extent that failure occurs. This simulation required around two hours of computational time to process and therein lies the issue with using finite element software to model erosion lifetime. In Section 4.1.5 it was discovered that it can require millions of impacts to reach the end of the incubation period, this makes it impossible to use this method to predict the lifetime of samples. However LS-DYNA provides an excellent snapshot of what is occurring at a particular moment in time.

The difference in peak stress between a singular impact and multiple impacts is due to the mesh being simplified for the multiple impacts model. This was changed to reduce the computational time required to investiage multiple impacts. The aim of this model was to investigate the change in stress due to multiple impacts and not a direct comparison to a single impact.

6.5 Discussion

The development of the base model lead to many useful tips on how to develop the model. Firstly care should be taken meshing curves as the curves will be approximated with lots of very small straight lines. This works well for single layer curved shapes but difficulties can be encountered with multi-layered curved shapes.

Smoothed Particle Hydrodynamics is a useful tool for modelling water impacts. Firstly it allows the full impulse of the water to be accounted for while also allowing for lateral jetting as the water droplet collapses. From previous work, noted in the literature review, the collapse of the water droplet is an important part of the impact and SPH allows for this to be modelled.

A limited amount of data is available on the material properties. The composite material is fairly standard and by being at the base does not require as much knowledge. The coatings however are important to understand fully but companies will not publish their data. Currently this is acceptable as there is still a limited amount of modelling being conducted and even using assumptions on properties will allow for some meaningful conclusions. However if the final goal is to predict the lifetime of samples then more precise data will be required.

Another area that lacks knowledge is the contact between the layers. There is a lack of information around the adhesion between the layers plus the contact area, as voids will diminish this. Obtaining values for this is crucial to further understanding the erosion process, as in the previous section, it is observed that multi-layered systems have a larger variability and erode quicker. Leading to the conclusion that the contact and interaction between the layers is crucial.

The modelling of the base model shows a spike in compressive stress just after the droplet impact and stress waves decrease the further from the centre travelled. After this initial spike the results do tend towards zero. Also at 2mm out from the centre there is an increase in tensile stress presumably to counteract the peak in compressive stress.

The sensitivity analysis showed that the results varying number of elements started to converge around 25,600 elements and the same occurred when the number of nodes in the SPH reached 33,552. While there could be an increase in accuracy with more elements or nodes used, this number provides the ideal balance between computing time and accuracy. A quick analysis of the material properties showed that a small change in the material did not result in a change near the centre of the sample but did result in a change further from the centre. This will be

due to the centre being affected by the initial impact, and a change in the material properties of the sample will not effect this, whereas further from the centre the stress waves have travelled through the material meaning that the change in properties has an effect. However the change was deemed within an acceptable range as the main purpose of this work is to compare different parameters and as long as it is kept consistent that is fine.

Finally multiple impacts showed an increase in the residual shear stress in the sample as more droplets impacted. After the thousands of impacts a sample could experience in it is lifetime it is possible to see how this build up in residual stress could lead to failure. This analysis also showed how it is impossible to model the lifetime of a sample in LS-DYNA, this fact will be taken forwards and instead parametric studies will be conducted as well as snapshots of the erosion process rather than the full lifetime.

7 Parametric Modelling Studies

After successfully developing an efficient and realistic computational model, different parameters can be investigated to determine their effect on the erosion phenomena. As noted in Section 6.4 it is not possible to model the entire lifetime of a sample. Therefore by exploring different parameters, such as the droplet diameter and coating thickness, insight can be provided into which variables have a major or minor effect on the erosion performance of a LEP. Investigating these factors can provide knowledge and insight that can be applied to inform both experimental set-ups as well as current wind turbine design.

Without precise data on the LEPs material properties and the contact conditions between the different layers, a quantitative parametric study allows useful conclusions to be drawn, as only one parameter is being altered per model run sequence. This allows the effect of an individual parameter to be studied and compared without reliance on specific material properties.

In order to explore the influence of key parameters, some initial runs are undertaken and results presented to show the influence of droplet diameter and coating system thickness. Thereafter the focus of the work returns to looking at the effect on the LEP systems under consideration. The samples that were examined in the XCT apparatus are modelled to see how the damage inflicted on them affects the stresses present in the sample. Using the XCT to measure the change in geometry and combining with the DMA measuring the change in material properties, models can be generated of the sample throughout its lifetime. This allows the changes in the sample to be more closely examined which will provide a great understanding of the erosion process.

7.1 Droplet Diameter

In both the real world situation and experimental set-up, the droplets impacting the sample do not have a constant diameter. Most experimental set-ups, such as the ETC test rig, have spent a large amount of time analysing the droplet diameter, but this is not consistent across all experimental set ups. This parametric study looks at the effect of changing the droplet diameter and how this affects the peak stresses.

Most test rigs operate with droplets that have a diameter of between 2 and 3mm, though realistically rain production is very variable, with rainfall ranging between 0.5-10mm [68]. It

has been shown that rainfall is unlikely to achieve diameters of greater than 4 or 5mm otherwise the droplet will split in two. This study tests the range of diameters from 1mm to 5mm to explore the droplets experienced in both experimental set ups and off-shore wind turbines. The model used is the same as the base model with the material properties used stated in Section 6.1.4.

Table 43 shows the droplet diameters and the corresponding droplet volumes and impact forces they inflict on the sample, from a droplet impacting at 130m/s.

Droplet Diameter (mm)	**Droplet Volume (mm^3)**	**Force (N)**
1	4.19	13.41
2	33.51	62.02
3	113.10	132.77
4	268.08	231.50
5	523.60	382.69

Table 43: Droplet Volume and Force for each Droplet Diameter

As shown in Table 43, a small change in diameter results in a large change in droplet volume due to the cubed term in the volume of a sphere. There is also a large increase in the force experienced by the sample, which in turn will increase the peak stresses experienced by the sample. Moreover the peak stresses in the sample were analysed for the different droplet diameters. Figure 92 plots the maximum stress in the sample for both the compressive stress and Tresca (max shear stress) against the droplet diameter.

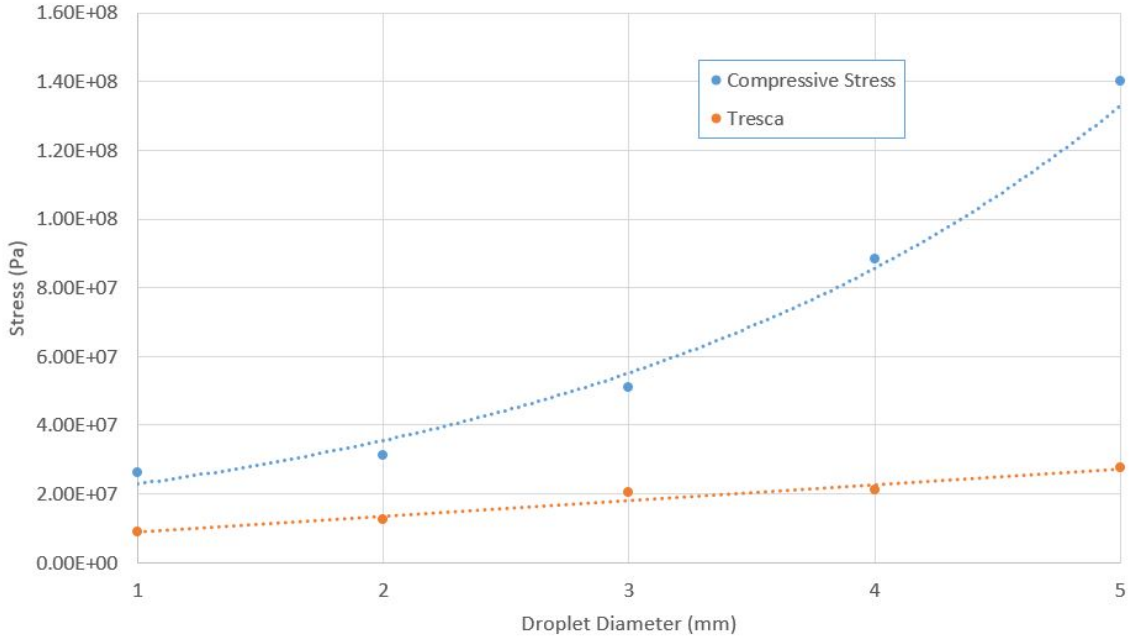

Figure 92: Compressive stress and Tresca stress vs Droplet Diameter from 1mm to 5mm diameter

Figure 92 shows there is a rapid increase in the peak compressive stress for every incremental increase in the droplet diameter. There is also an increase in the Tresca stress this is to a lesser extent when compared to compressive stress. In addition Table 43 shows that droplet volume increases rapidly with a small change in droplet diameter. Therefore, to investigate this further Figure 93 plots the stress against droplet volume.

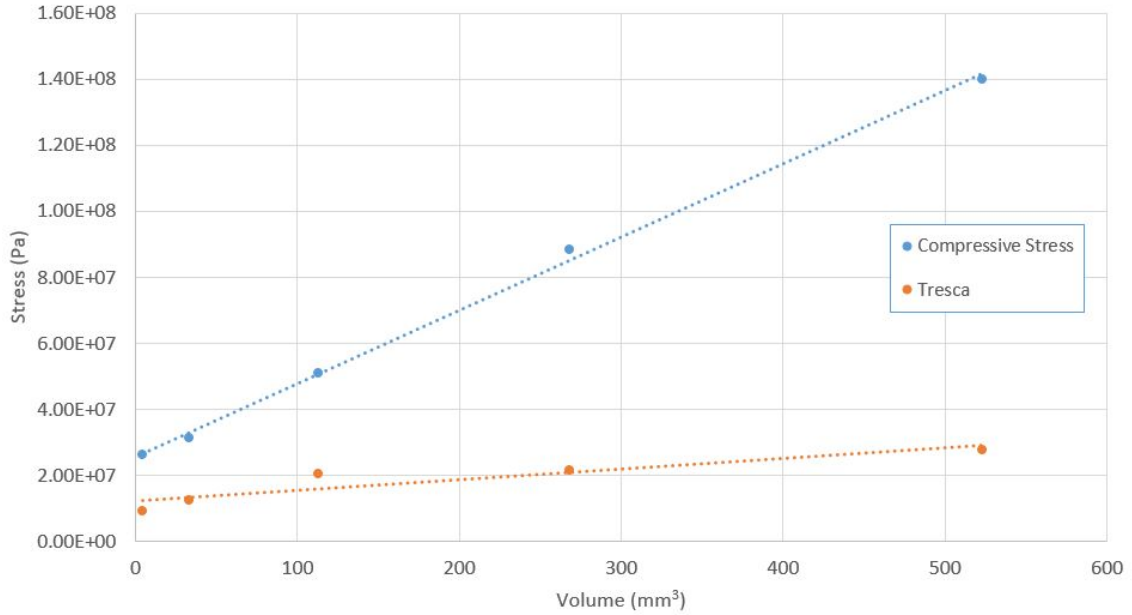

Figure 93: Compressive stress and Tresca stress vs Droplet Volume from 1mm to 5mm droplets

The alteration of the x-axis parameter to droplet volume results in a clearer linear trend for compressive stress with increased volume. By contrast, the Tresca stress appears to have a better fit when plotted against droplet diameter. This is due to the compressive stress being along the same axis as the droplet impact, therefore the total volume, and consequently the force, acting on the sample has a significant bearing. The shear stress is not as affected by droplet volume but instead increases in relation to the droplet diameter. The shear stress is a result of the lateral jetting of the droplet as it collapses on the sample, therefore the diameter will be more influential on the shear stress as this stress is acting in the radial direction.

Interestingly, these models demonstrate that when the droplet diameter is 5mm the maximum compressive stress reaches 140MPa. The compressive yield stress of the coating is only 180MPa, showing that multiple impacts with larger diameter droplets could quite quickly lead to failure. This combined with the rapid change in compressive stress shows the importance of characterising a test rig; as a small change in diameter could result in a large change in stresses experienced by the sample. This explains why the repeatable consistency of the droplet diameters is important, since increased diameter in only a small percentage of impacts could result in a large change in the stresses experienced and therefore have a major impact on the lifetime of the sample.

7.2 Thickness of Coating

In addition to understanding the influence of the droplet diameter, it is important to investigate how the thickness of the coating affects the erosion resistance of a sample. A DNV-GL Standard was published in 2006 (DNV-OS-J102) [69] which stated that all wind turbine coatings should be between 0.4mm and 0.6mm. This is currently the most up to date standard, and the influence of these values will be investigated by modelling coating thicknesses of 0.2mm, 0.4mm, 0.6mm and 0.8mm to determine if coatings could be thinner or if there is any potential benefit to having a thicker coating.

Similarly, the base model was used in the material properties for the coating and composite as stated in Section 6.1.4. Most LEPs include a filler layer and its interaction with the topcoat is important, however a lack of information about filler properties means this layer has to be neglected. This parametric study explores the compressive stress, shear stress and effective plastic strain of the coating and the composite. Measurements were taken in the centre of the sample directly beneath the impact as this relates to the worst affected area.

Figure 94 plots the compressive stress against time for the different coating thicknesses.

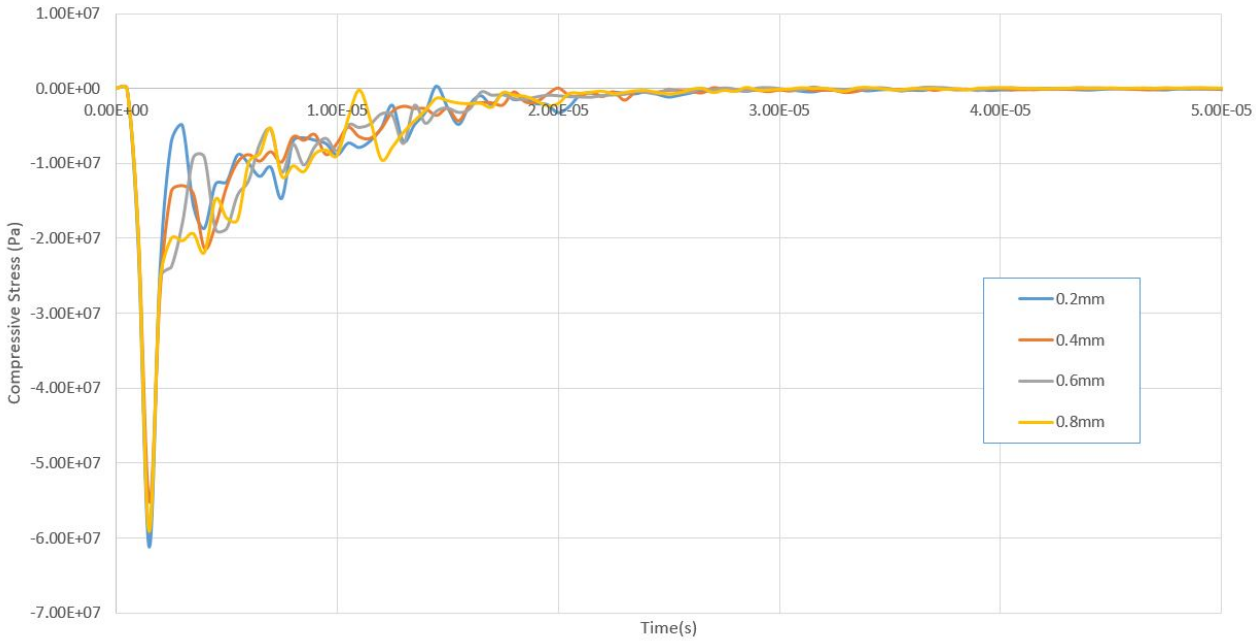

Figure 94: Compressive stress in the coating layer for varying coating thicknesses

As shown in Figure 94 there is only a slight increase in the peak compressive stress for a coating thickness of 0.2mm compared to the other thicknesses. At a thickness of 0.2mm the peak compressive stress was 6.12×10^7 Pa compared to 5.9×10^7 Pa for both 0.6mm and 0.8mm. This shows that there is a slight weakness in thinner coatings but increasing the coating thickness displayed no noticeable effect. The same trend is spotted with the shear stress; a maximum stress of 1.36×10^7 Pa at a thickness of 0.2mm compared to 1.29×10^7 Pa for 0.4mm, 1.32×10^7 Pa for 0.6mm and 1.30×10^7 Pa for 0.8mm. So there are consistent results to imply that there is a correlation between coatings below 0.4mm and an increase in peak stress. Finally from Figure 94 it is observed that the stress does not dissipate differently for changing thicknesses since all curves follow a similar trend.

Next the strain present in the coating layer was analysed, Table 44 shows the effective plastic strain for varying thicknesses.

Coating Thickness (mm)	Effective Plastic Strain
0.2	0.0111
0.4	0.0106
0.6	0.0102
0.8	0.0103

Table 44: Effective Plastic Strain for Varying Coating Thickness

Table 44 shows a coating thickness of 0.2mm leads to a higher strain value present in the coating layer, whereas increasing the thickness up to 0.8mm does not cause any significant difference when compared to 0.4 and 0.6mm.

Finally, the stress levels in the composite substrate were measured. While there may not be a great difference in the stress levels in the coating, if the composite substrate is experiencing a significant increase in stress, this can lead to cracks or subsurface failure. Cracks can cause failure mechanisms such as delamination with the coating becoming loose from the composite, as seen in Section 4.2.1 this can lead to rapid failure. To investigate this, the shear stress was examined, Figure 95 plots the Tresca stress against time for the varying coating thicknesses.

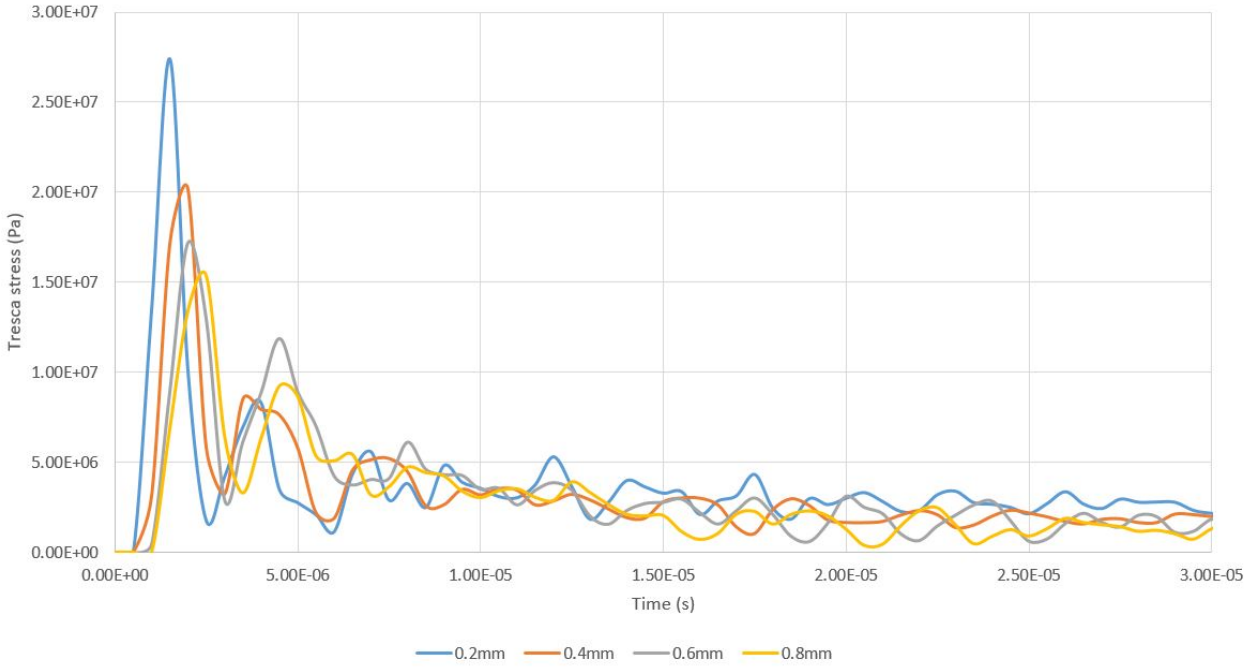

Figure 95: Tresca stress in the composite layer for varying coating thicknesses

Figure 95 displays a noticeable difference in the peak stress levels. The graph follows the trend that as the coating thickness increases the peak stress decreases. As mentioned above, the decrease in stress in the composite layer is advantageous. A lower stress level will decrease the chance of failure, this means that with the coating thickness of 0.2mm having the highest stress levels in the composite, it is the most at risk from delamination.

This parametric study shows that the DNV-GL Standard does have some basis for its requirements of coatings to be between 0.4 and 0.6mm, as coatings thinner that this results in higher peak stress in the coating and a significant increase in stress in the composite below. Similarly, increasing the coating thickness to greater than 0.6mm does not appear to provide much benefit with the peak stresses very similar and the stress in the composite only slightly better.

Finally, this study shows the importance in coating application, through experience the author has observed samples where the coating application has left all or part of the sample with a very thin layer. This implies that poor application could cause an increase in stresses and potentially lead to a different failure mechanism if the composite experiences higher stress levels than anticipated. Further work could examine samples with unequal coating application where the thickness undulates across the sample, in order to determine if this would lead to stress concentrations at the thinner points.

7.3 The Effect of Curvature

Different experimental test rigs have varying sample holders depending on their design. The effect that the variation of geometry has on the stress waves, and in turn the erosion rate is unknown. In order to examine the effect of curvature, a flat sample and a curved sample were analysed to determine the peak stresses and the stress dissipation, further assessing the effect on erosion rate.

This work was carried out in conjunction with Aerox to investigate the difference between the testing carried out by the University of Limerick and the ORE Catapult in Blyth. The University of Limerick test rig only allows the use of flat, circular samples, whereas ORE Catapult uses aerofoil shaped samples in their test rig. These two test rig's sample holders have different geometries therefore Aerox were interested to investigate the stress waves present in both. This also provides the opportunity to investigate the difference between flat and curved samples.

Aerox provided some material properties for each of the different layers along with the thicknesses of each layer. The material properties were not the most in depth with only the Young's Modulus and Density given. There was also a difference in the thickness of each layer when comparing the two samples, due to the sample holder restrictions. Table 45 shows the material properties and thicknesses for each layer. The flat samples used at Limerick have an aluminium base plate which all samples are attached to before insertion into the test rig, the properties for this are shown in the table.

Geometry	**Layer**	**Thickness (μm)**	**Density (kg/m^3)**	**Young's Modulus (Pa)**
Flat	Aluminium	1000	2700	7.1×10^{11}
	Composite	1400	1760	1.01×10^{11}
	Filler	1000	1300	3.12×10^{9}
	Putty	60	1410	1.34×10^{10}
	Topcoat	780	1160	3.48×10^{9}
Curved	Composite	3000	1760	1.01×10^{11}
	Filler	700	1300	3.12×10^{9}
	Putty	60	1410	1.34×10^{10}
	Topcoat	780	1160	3.48×10^{9}

Table 45: Material properties for Aerox samples

Table 45 shows that the thicknesses are not constant between the two samples, since the filler and composite layers are different. The topcoat and putty layer, however, are identical which should affect the peak stress levels more so a comparison can still be made. Another difference between the two experimental set ups is that the University of Limerick test rig operates with 2mm diameter droplets, whereas the ORE Catapult test rig has 2.4mm diameter droplets. This made the direct comparison between the two models more challenging, but once the results had been analysed the ability to compare the models was assessed. The set up for each of the models is shown below in Figure 96.

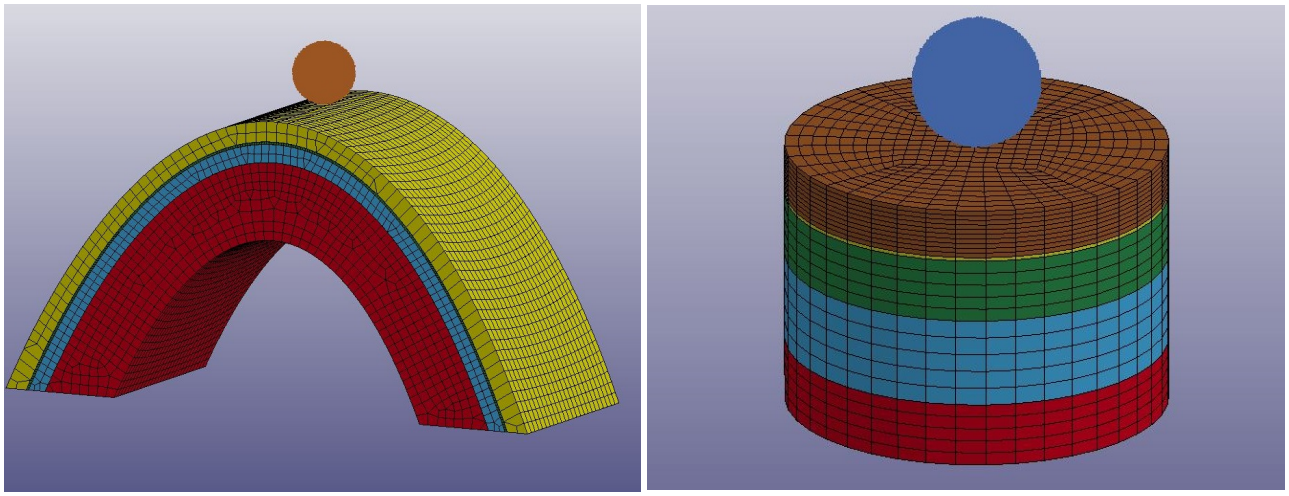

(a) Sample used in ORE Catapult Test Rig (b) Sample used in University of Limerick Test Rig

Figure 96: Model set up for both ORE Catapult and University of Limerick samples

For both models, only the area of interest with regards to stress waves was modelled, to reduce the computing time. Finally both droplets had an impact velocity of 125 m/s.

Firstly the compressive stress is analysed in the coating, the stress measurement was taken in the centre directly below the impact for both samples. Figure 97 plots the stress curves against time for both samples.

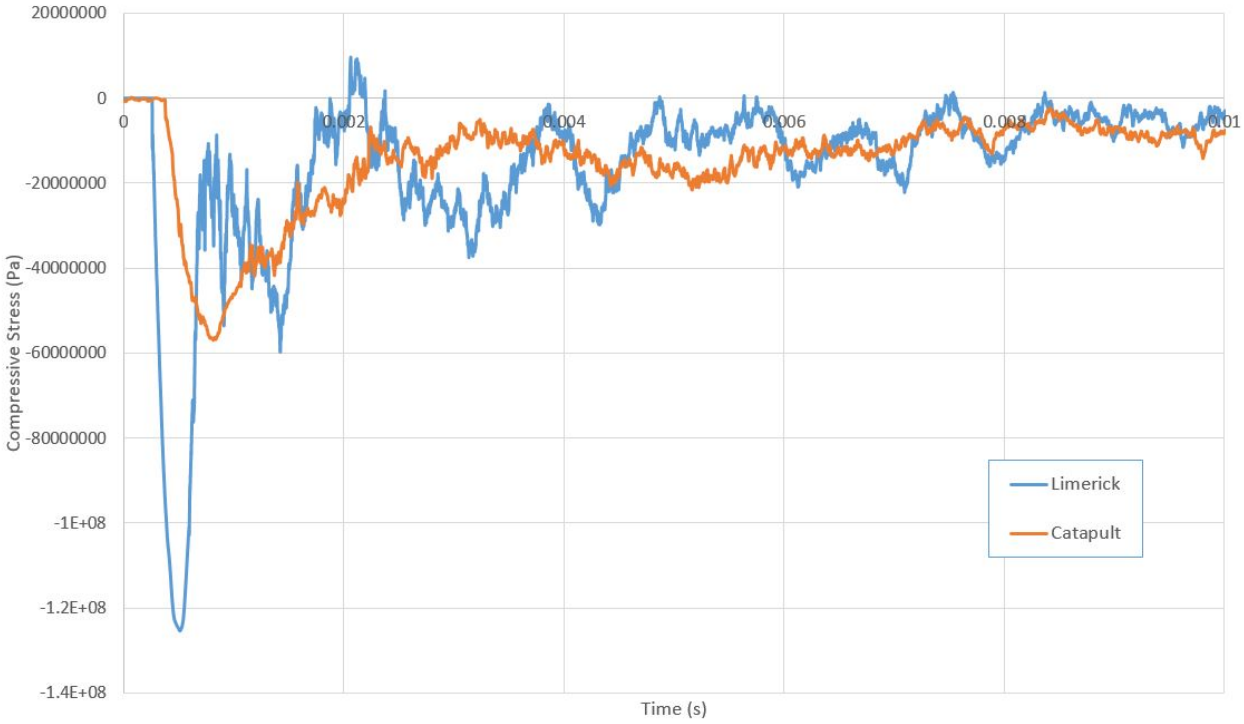

Figure 97: Compressive stress in the centre of the topcoat for both the flat and curved samples

The peak stress experienced by the Limerick sample is more than double the peak stress experienced by the Catapult sample. The Catapult sample does take longer to dissipate the stress compared to the sharp peak on the Limerick curve. As mentioned above, the Catapult sample was impacted by a larger diameter droplet therefore it would be expected that the peak stress would be slightly higher in this sample not significantly lower. This shows that the concave nature of the curved sample directs the stress away from the centre of the Catapult sample thus experiencing lower peak stress.

A very similar trend was seen when examining the shear stress. Figure 98 plots the Tresca stress in each layer for the Catapult sample and Figure 99 plots the Tresca stress in each layer for the Limerick sample.

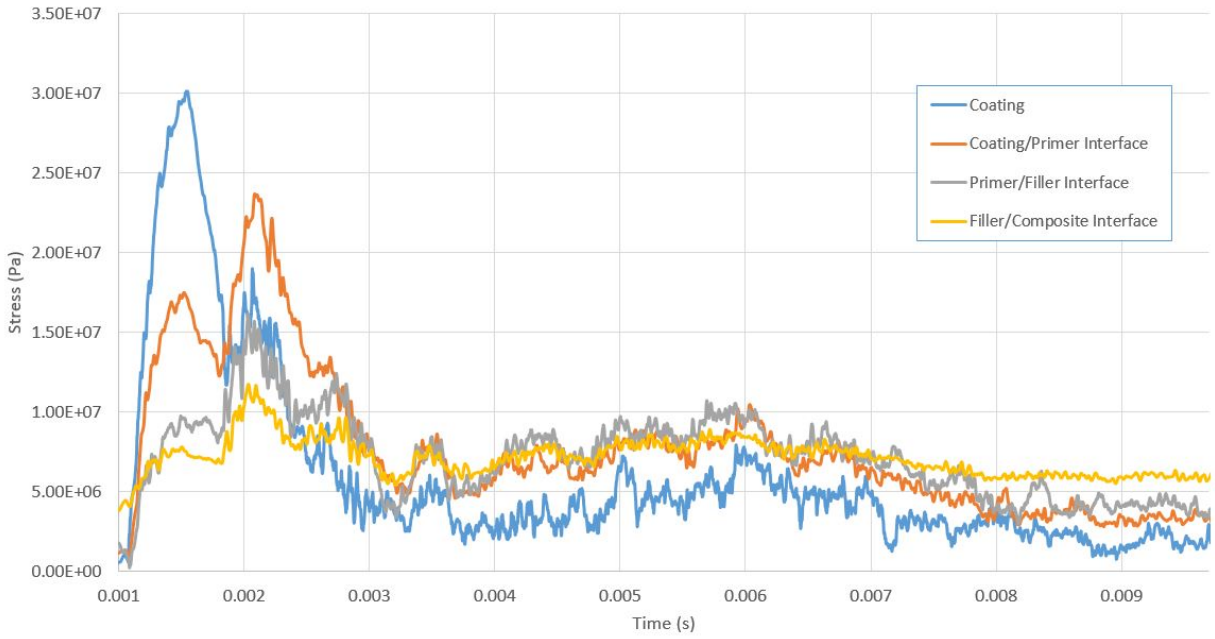

Figure 98: Tresca stress in the centre of the catapult sample

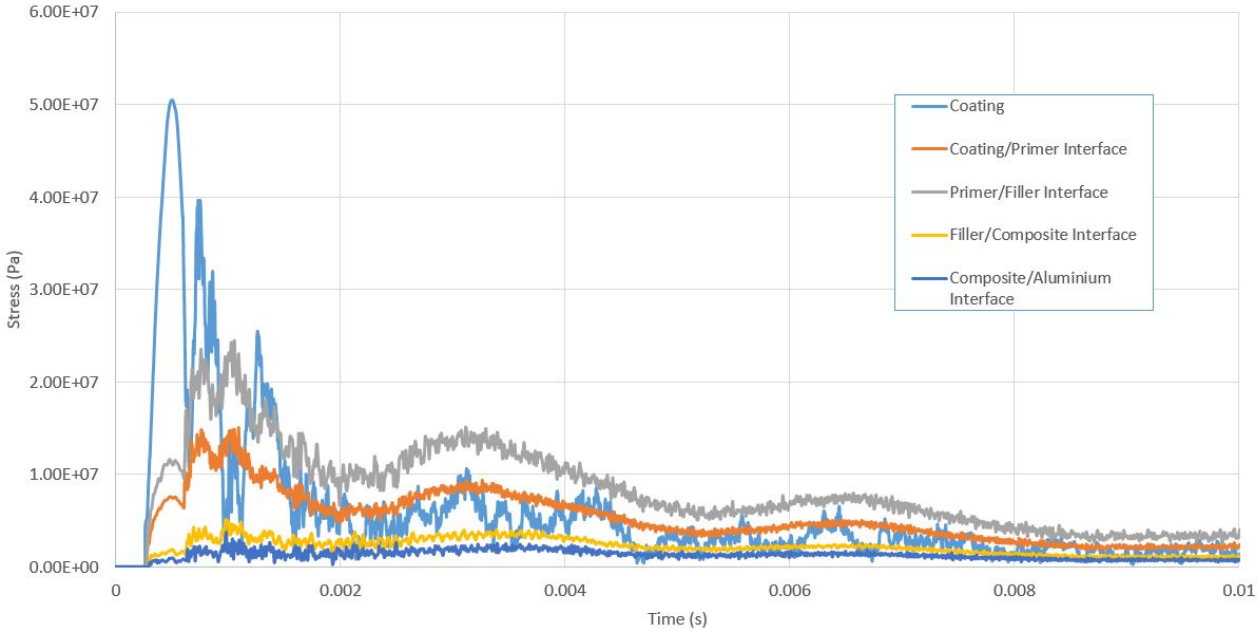

Figure 99: Tresca stress in the centre of the Limerick sample

The peak Tresca stress in the Limerick sample is 5×10^7 Pa compared to 3×10^7 Pa in the Catapult sample. This implies the main difference when comparing compressive and shear stress is that the shear stress dissipates quicker on the Limerick sample. The Catapult sample has higher stress levels through all layers compared to the Limerick sample, since the Limerick sample's coating takes the majority of the stress and the other layers record a significantly lower level, whereas in Figure 98 it is observed that even in the Filler/Composite interface there is still a stress peak at the start. Overall this makes the Catapult sample less likely to experience delamination as erosion initiates on the surface, meaning this is the area where stress should be reduced.

Another point to note, is that Figure 98 does not start at a time of 0s. This is due to the small gaps between the layers used to stop mesh instabilities, as mentioned in Section 6.1.1. Therefore there is some small stresses detected at the beginning as the layers come together before the droplet impacts, this was removed to make comparisons between the two samples clearer.

7.4 Modelling Stages of Erosion

Modelling the entire lifetime response of a rain erosion samples is not realistic using finite element techniques, and therefore a more useful approach is to examine the geometry and material properties at the various discrete stages of the erosion process. Therefore snapshots of the erosion throughout its lifetime have been used to model the changes in the geometry and material properties of the sample. The snapshots of erosion that were modelled occurred at the five different stages the XCT measured the samples, as shown in Figure 100.

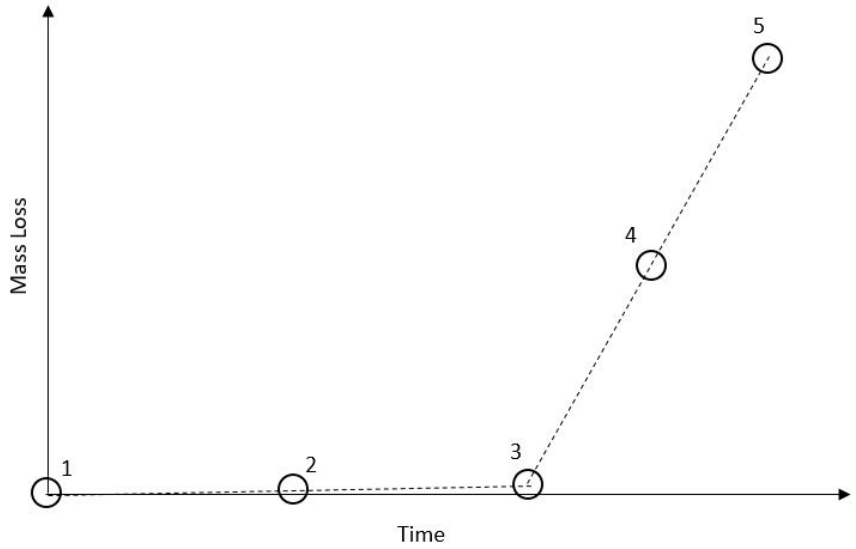

Figure 100: Five different stages of erosion used, as shown on a mass loss curve

In Section 4.2, five different flat samples were eroded and studied in XCT apparatus to investigate the sub-surface defects present in the erosion process. The XCT imagery also provided a very accurate measurement of the pit diameter and depth which can be used to accurately model the localised change in geometry. The five eroded samples were also tested in dynamic mechanical analysis apparatus (DMA) to measure the change in modulus throughout the erosion process. This allows the change in material properties to also be included in the modelling, combined with the change in geometry this provides an insight into the peak stress waves and stress dissipation present throughout the erosion process.

7.4.1 Change in Geometry

The XCT technique not only allows us to look at any sub-surface changes but also allows the geometry changes of the surface to be measured to a higher degree of accuracy than would be capable otherwise. The XCT scanner has a resolution capable of measuring distances as small as a micrometer, it also can examine the diameter of the pit throughout its depth not just measure the distance at the top. This combined allows the change in geometry to be accurately captured, through thickness which is a dramatic improvement on conventional measurement techniques.

To capture the change in geometry due to mass loss, selected elements were removed from the model. The elements were chosen to closely follow a similar pattern to that as observed from the erosion process. Building a more precise CAD model of an exact eroded sample profile was tried but there was difficulties in meshing the imported shape. The removal of discrete elements was used as a compromise, though with small enough resolution of elements, this could still provide an accurate representation.

Once the XCT scans were taken, the volumetric images were processed using the Dragonfly software system. Dragonfly software allows the user to differentiate between air and solid material by assigning colour values to measured density regions within the sample, therefore this function can be used to measure the depth of pits. By setting up a flat plate directly above the sample, the distance of air below can be measured. Figure 101 shows the output of the process mentioned, where the image shows the air depth across the full sample. The minimum distance shown in the scale at the bottom on Figure 101 shows the distance the measuring plane is above the surface of the sample, therefore to determine the maximum depth the maximum distance is subtracted from the minimum distance.

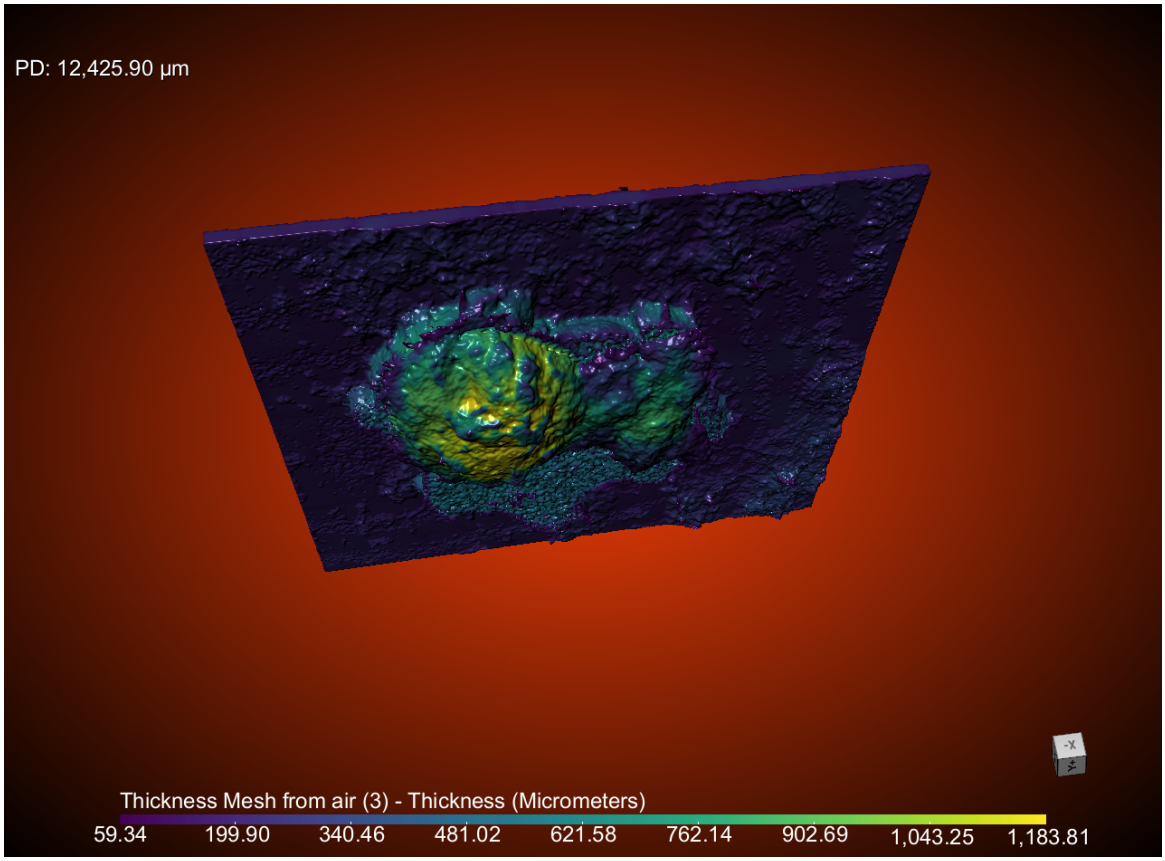

Figure 101: Depth measurements using the XCT apparatus of sample A030 at Stage 4 erosion

The sample shown in Figure 101 is at Stage 4 erosion and therefore has experienced a large amount of mass loss, the rest of the XCT depth images are in Appendix H. It is also evident that at this stage the mass loss is concentrated into one central pit, which is a common occurrence when examining samples at this stage of erosion.

This process was repeated for all samples at each stage of erosion. An average was then taken at each stage at the results for pit depth are shown in Table 46.

Stage	**Average Depth (μm)**
Stage 2	125
Stage 3	295
Stage 4	800
Stage 5	1126

Table 46: Average Depth of Pits for each Erosion Stage

The results in Table 46 show a steady increase in the pit depth until the end of incubation period has been reached at Stage 3 and then the mass loss accelerates, resulting in significant pits forming. These average depths represented the maximum depth that would be removed for the model. To decide the change in geometry as erosion occurred the pit surface area also needed to be explored, however this was not just as straightforward as measuring the pit depth. No two samples will erode with the same mass loss pattern, meaning that there is not a consistent number and size of pits forming at each stage. Some samples at Stage 3 will have 5 or 6 small pits forming, others will have one larger pit and any variation in between. To explore this, a qualitative approach was adopted to record the pits forming. Table 47 displays the notes taken for each stage of erosion, the notes are describing the extent of the damage. Each description tried to state the number of pits and the dimensions of these pits.

Stage	**Sample**	**Notes**
Stage 2	A010	- 5 pits, each around 0.25mm diameter
	A030	- 3 pits around 0.6mmx0.4mm with some smaller pits further out
	A035	- A few slashes each around 0.4mm long
	A038	NO DATA
Stage 3	A010	- 1 big pit around 2mmx1mm with other roughness around edge
	A030	- 2 pits near centre, 2mmx0.5mm and 1mmx0.5mm
	A035	- 3 or 4 pits each around 1.5mmX0.4mm
	A038	- 3 pits, 1mmx0.5mm, 0.8mmx0.4mm, 0.5mmx0.5mm
Stage 4	A010	- 1 large pit at 4.5mmx4.5mm with a 1mmx2mm area at a greater depth
	A030	- 1 large pit at 4mmx3.5mm
	A035	- 1 large pit at 4mmx3.5mm
	A038	- 1 large pit at 6mmx3mm
Stage 5	A010	- Pit extends to around 6mmx5mm
	A030	- 1 large pit at 5.5mmx4.5mm
	A035	- Pit extends to around 5mmx5mm
	A038	- 1 large pit at 8mmx4mm

Table 47: Description of surface damage and pit areas for each erosion stage

Table 47 shows common themes for each stage of erosion, the latter stages all have one large area of damage though the dimensions of this damage range from sample to sample. Stages 2 and 3 are more difficult to categorise as there can be a varying number of pits, with each

pit being a different dimension. From examining the notes, as shown in Table 47, the element size was determined. Elements were decided to have dimensions of 0.4mmx0.4mmx0.1mm, this was deemed as the largest size of element that could be used to model Stage 2 erosion. This element size is used to lower the computing time while still providing a realistic representation of the erosion stages. The combination of element dimensions combined with the maximum depth were used to determine the elements removed from the model.

Figure 102 displays the geometries used in the modelling with the appropriate elements removed for each stage. The removal of elements tried to combine accurately capturing the shape of the pits while also including the random scatter of damage typical with early stages of erosion.

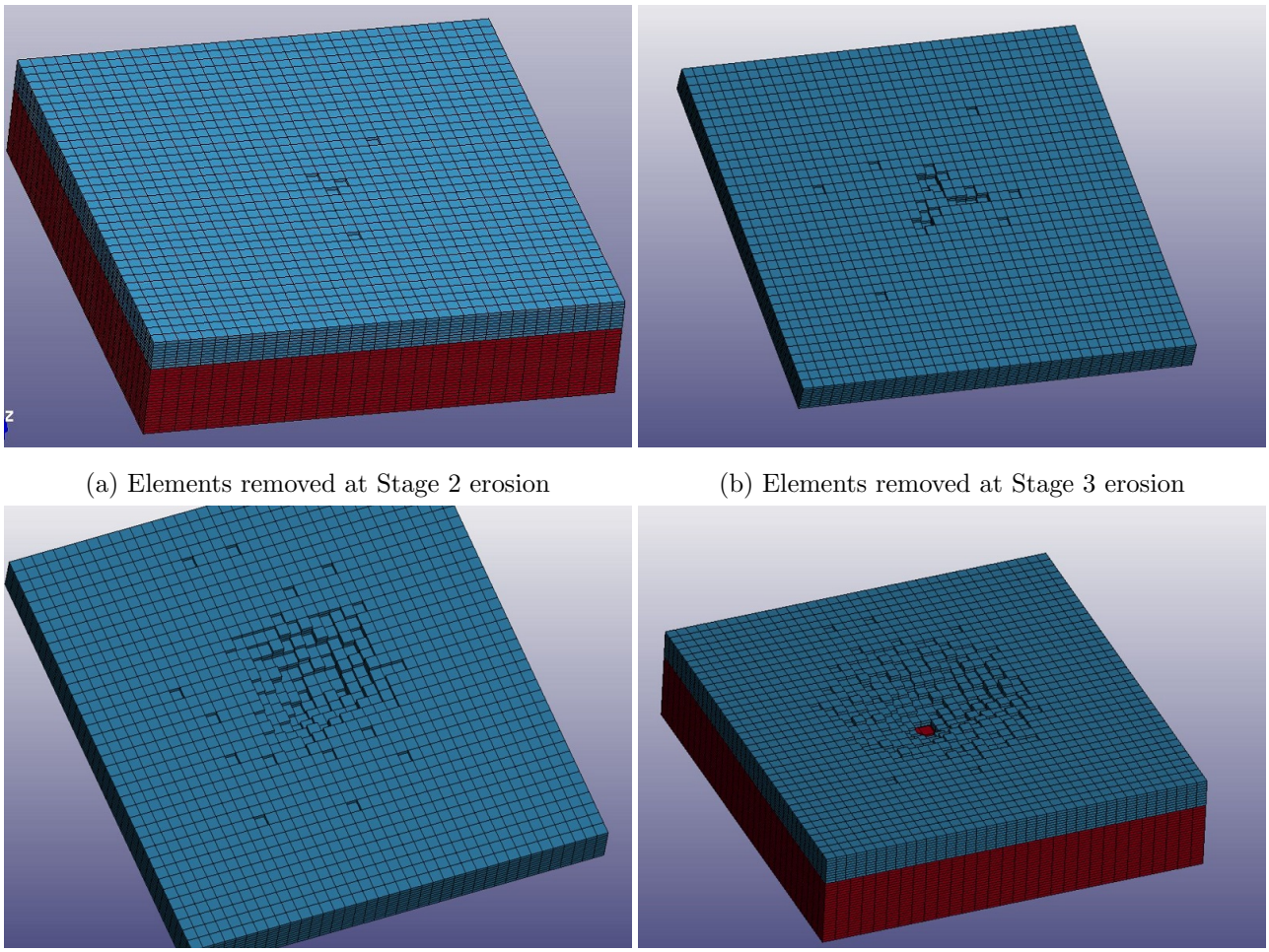

(a) Elements removed at Stage 2 erosion

(b) Elements removed at Stage 3 erosion

(c) Elements removed at Stage 4 erosion

(d) Elements removed at Stage 5 erosion

Figure 102: Elements removed at each stage of erosion, to simulate the geometry measured with the XCT

7.4.2 Effect of Variations in Material Properties

Throughout the erosion process, the samples were also tested using DMA apparatus at each erosion stage. The DMA machine uses a two point bending set up with the application of the load in the centre of the sample oscillating at different frequencies. This method calculates the storage and loss modulus of the sample, two important properties which are used when studying the visco-elastic properties of a material.

For each stage, four different samples were tested to determine how the moduli changed as the sample was eroded. These material property changes can be inputted into the model alongside the change in geometry. Table 48 displays all the results from the DMA measurements.

		Before Erosion		After Erosion		Change		Average Percentage Change	
Stage	**Sample**	**Storage**	**Loss**	**Storage**	**Loss**	**Storage**	**Loss**	**Storage**	**Loss**
2	A06	5648	340.2	5050	277	598	63.2	15.4 %	16.4 %
	A13	7533	328.1	5967	260.3	1566	67.8		
	A26	4688	353	3995	305.5	693	47.5		
	A28	6665	325.4	5640	283.7	1025	41.7		
3	A18	6687	314.4	6138	288.8	549	25.6	10.7 %	10.8 %
	A22	5882	334.9	5155	285.9	727	49		
	A49	6347	310.6	5688	279.1	659	31.5		
	A53	4620	343.8	4064	308.9	556	34.9		
4	A01	5856	266.4	5614	242.1	242	24.3	6.4 %	12.6 %
	A27	5364	329.3	4909	270.8	455	58.5		
	A29	5967	276.8	5337	211.8	630	65		
	A54	4222	298.3	4121	298.4	101	-0.1		
5	A20	6002	299.8	5779	269.1	223	30.7	6.4 %	15.1 %
	A23	6343	305.9	6083	260.9	260	45		
	A32	5174	318	5212	279	-38	39		
	A52	4112	308	3872	236.8	240	71.2		

Table 48: Results from DMA Measurements

The results displayed in Table 48 show a large variation of measurements for the storage modulus, with all 16 samples being made of exactly the same material the results should exhibit a smaller variation. Each sample was only eroded once, the same sample was not repeat measured. Therefore the average percentage change in the last two columns, states the change in moduli with respect to an uneroded sample, not the change from the previous erosion stage. Taking this into regard, the results from the DMA show that there is a 15.4% decrease in the storage modulus before the storage modulus recovers throughout the erosion process. The value for loss modulus decreases by 16.4% but then fluctuates in value as erosion occurs.

Storage and loss modulus are visco-elastic material properties, the ratio between the loss and storage material is defined as $tan\delta$ and provides the measure of damping in the material. For example a material with greater $tan\delta$ will exhibit more damping. The more damping present in the material, the more visco-elastic a material behaves whereas for little damping the material is effectively behaving elastically. Figure 103 provides a graphical representation of the relationship between storage and loss modulus.

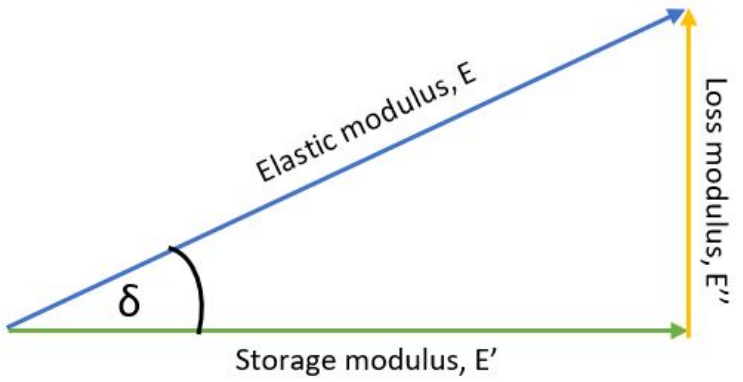

Figure 103: Graphical representation of relation between storage, loss and elastic modulus

The ratio of loss over storage modulus is 0.04, and the tan value of this is still 0.04. Therefore with a very small phase angle the sample is behaving elastically, thus the storage modulus can be assumed to equal the elastic modulus. This means when examining the results in Table 48, only the storage modulus will be used as it equates to the change in Young's modulus.

There were a few issues with the process and procedure used in the DMA measurements. Firstly the samples were 50mm long to fit in the DMA apparatus however the supports for the two point bending were a distance of 50mm apart meaning that the sample was perched on the edge of the supports. This results in the variance in measurement of storage and loss modulus, in fact if the same sample was measured twice some differences in measurement could

be obtained. Secondly as the erosion process occurs, the sample experiences mass loss thus changing the thickness and volume of the sample. The thickness and volume of the material is crucial as it is an important parameter to measure the stiffness of the material, thus from Stage 3 onwards as the sample volume changed the values for change in storage and loss modulus were compromised. Finally the DMA measurements do not isolate the separate layers of the sample, the storage and loss modulus are measured for a bulk material of the full sample. This means that any changes in the moduli are changes for the full system even though it is expected that the coating will experience the most change.

For the reasons stated above the change in modulus will be ignored after Stage 2 as the erosion has affect the thickness and volume of the sample making the measurement invalid. Therefore estimations will need to be made for the change in moduli throughout the erosion process, with only the change between Stage 1 and Stage 2 known. The average time taken to reach each stage was determined based off the results in Table 29 and therefore knowing that the sample took an average of 65 mins to reach Stage 2 and during that time lost 15 % of its modulus these results can be extrapolated. Assuming that the material properties changed at the same rate per time throughout the erosion process, the change in modulus can be determined for the other stages.

Table 49 shows the average time to reach each stage, the corresponding change in material properties based on the assumption made above. This percentage change is then applied to the material properties as stated in Section 6.1.4.

Erosion Stage	**Average Time to Reach Stage**	**Percentage Change in Properties**	**Young's Modulus**	**Tensile Yield Stress**	**Compressive Yield Stress**	**Compressive Stress at Break**
Stage 1	-	-	2.5 GPa	90 MPa	120 MPa	180 MPa
Stage 2	65 mins	15 %	2.13 GPa	76.5 MPa	102 MPa	153 MPa
Stage 3	102.5 mins	23.65 %	1.91 GPa	68.71 MPa	91.62 MPa	137.42 MPa
Stage 4	121.25 mins	27.98 %	1.8 GPa	64.82 MPa	86.42 MPa	129.63 MPa
Stage 5	128.75 mins	29.71 %	1.76 GPa	63.26 MPa	84.35 MPa	126.52 MPa

Table 49: Change in Material Properties for each Erosion Stage

The results in Table 49 show the change in Young's modulus and how this change will affect the tensile and compressive stress strain curves inputted into the model. Combining this work with the change in geometry provides a representation of the changes in the sample which can then be modelled to see the affect on the stress levels and stress locations in the sample.

7.4.3 Results

The set-up for the modelling is, as shown in Figure 104. A 2.3mm droplet is impacting a sample with the altered properties of the materials as stated in Section 6.1.4. Only the properties of the coating are altered during the erosion process, the composite properties remain the same.

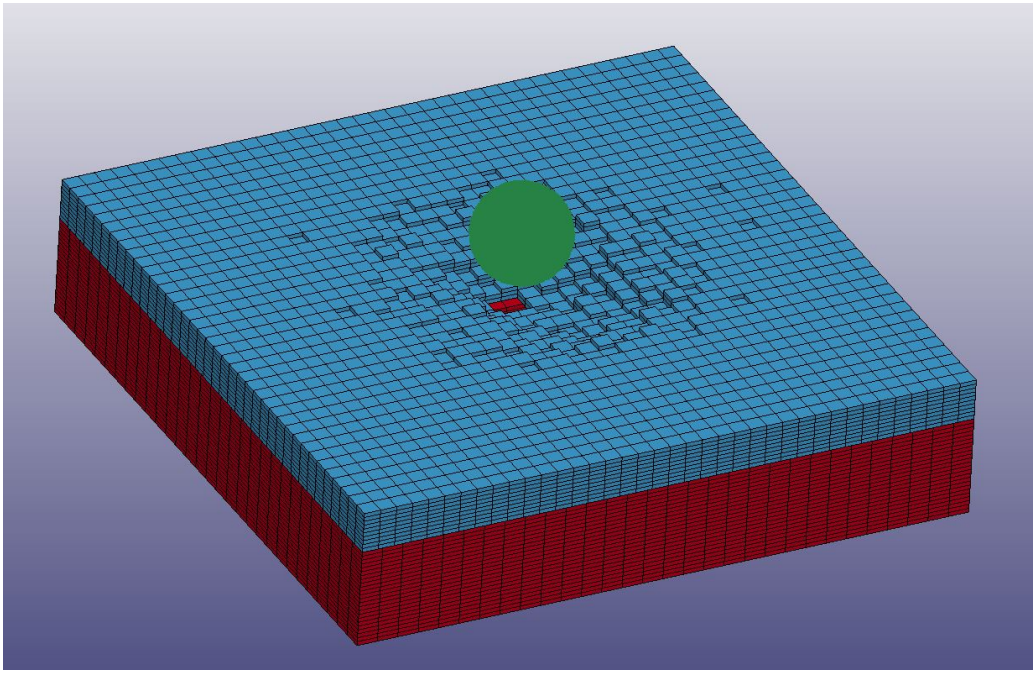

Figure 104: Model set-up for Stage 5 of Erosion Modelling

The stress waves were analysed at each stage to determine if there was a correlation between the stage of erosion and the stress waves. For each stage the compressive and shear stress was analysed in the coating layer and the composite layer.

Firstly, the compressive stresses at varying radial distances were analysed for Stage 1 and 5 erosion. Figures 105 and 106 plot the compressive stress in the coating layer at the centre of the sample and at increments progressively of one radius out.

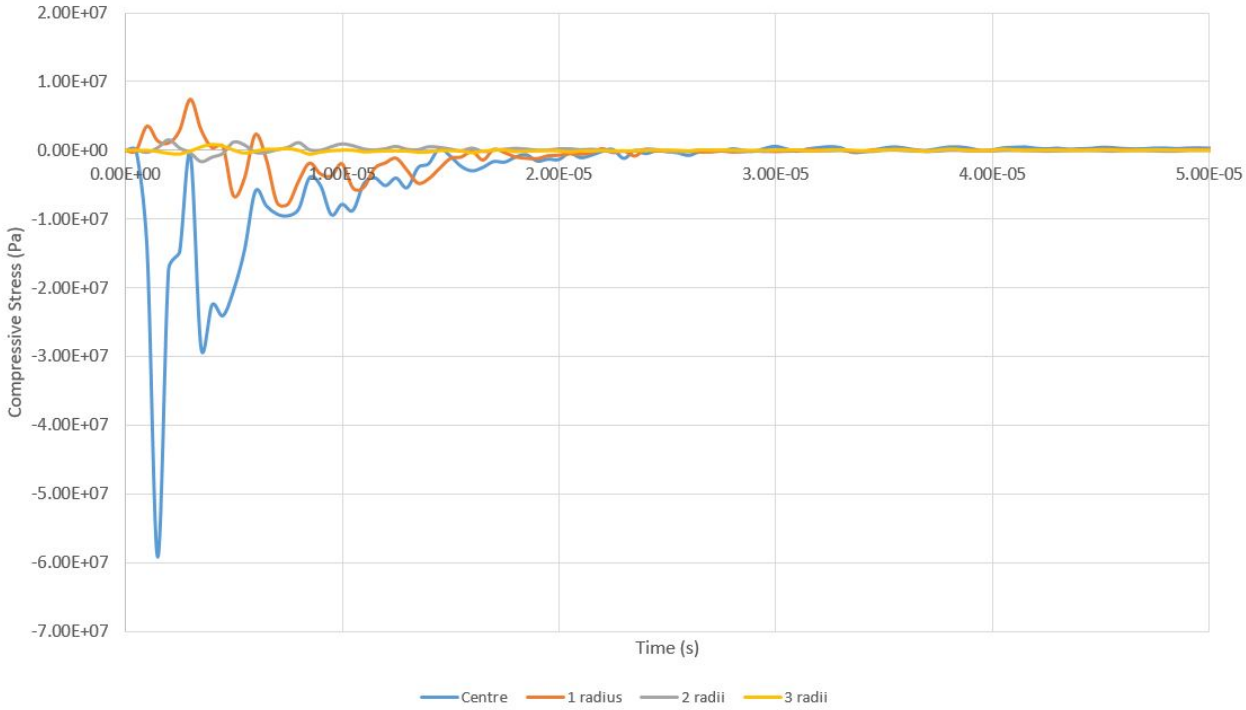

Figure 105: Compressive stress in the coating layer for Stage 1 erosion

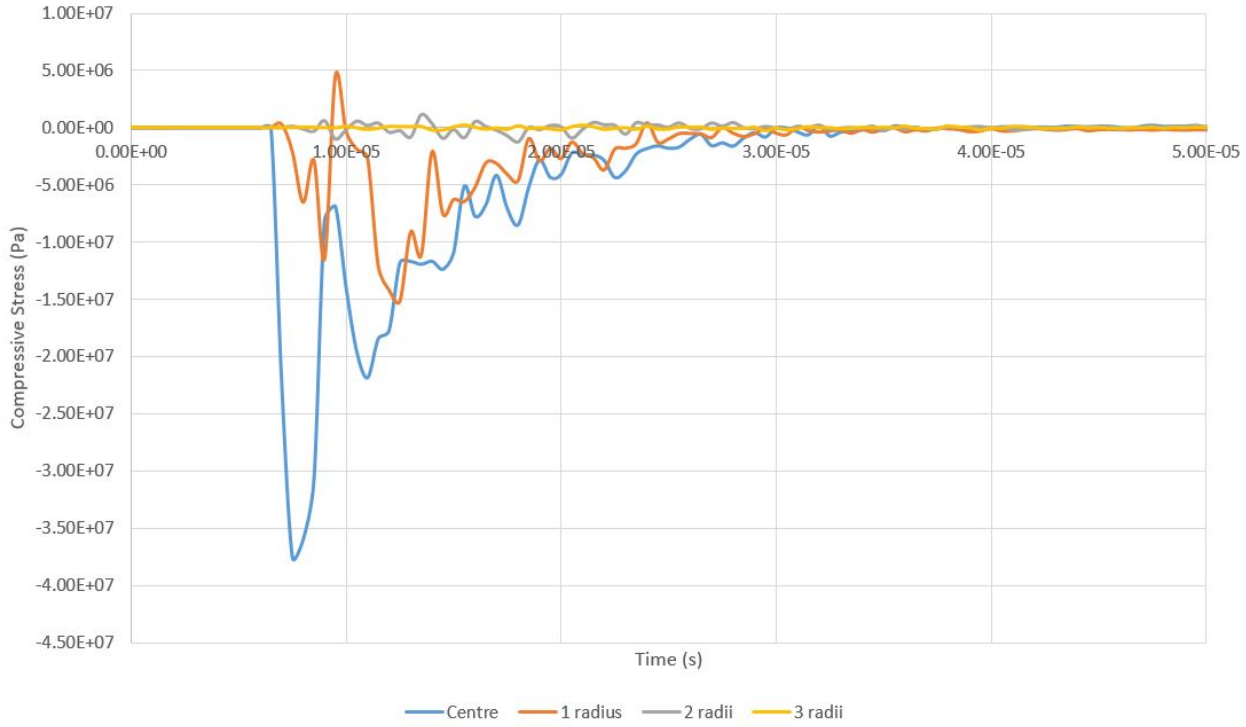

Figure 106: Compressive stress in the coating layer for Stage 5 erosion

Figures 105 and 106 show a similar trend even at the different stages of erosion. There is significantly larger stress present at one radius out, however at Stage 5 the damage has become so severe that the area of damage is larger than a one radius distance from the centre. Therefore the stress concentrations in the pit are recorded at this distance out. The time before the initial impact is much longer in Figure 106 this is solely due to the removal of elements, therefore resulting in a greater distance to travel before the droplet impacts a surface.

The other noticeable difference between the two figures is at Stage 5 the peak stress is significantly lower. To investigate this the compressive stresses for the centre of each coating, at all five stages, was plotted in Figure 107.

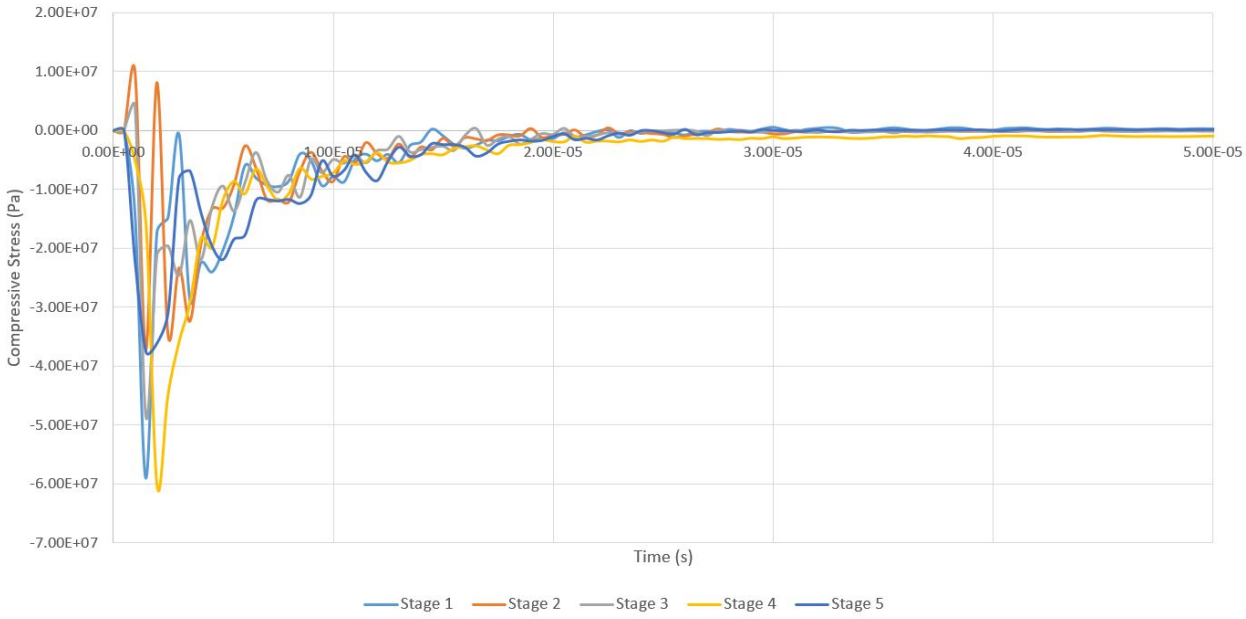

Figure 107: Compressive stress in the centre of the coating layer for each of the Stages of Erosion

Figure 107 shows no correlation between the peak compressive stress and the stage of erosion. The peak stress ranges between 3.5×10^7 Pa and 6×10^7 Pa, the difference in stress is a result of the location of the point measured and the removed elements surrounding it. To try and replicate brittle fracture, where small chunks fall off, the removal of elements was not overtaken in a uniform manner. Rather the overall shape of the pit that was seen in the XCT was followed, but certain areas of the pit could be a few elements lower than the element beside it. This could account for the difference in stress peaks, as this roughness will result in stress concentrations occurring and depending on the location of the measurements the peak stress could vary.

The Tresca stress was also investigated to see if a similar trend occurred for the shear stress.

The Tresca stress was plotted at the centre of the coating for each of the five stages, see Figure 108.

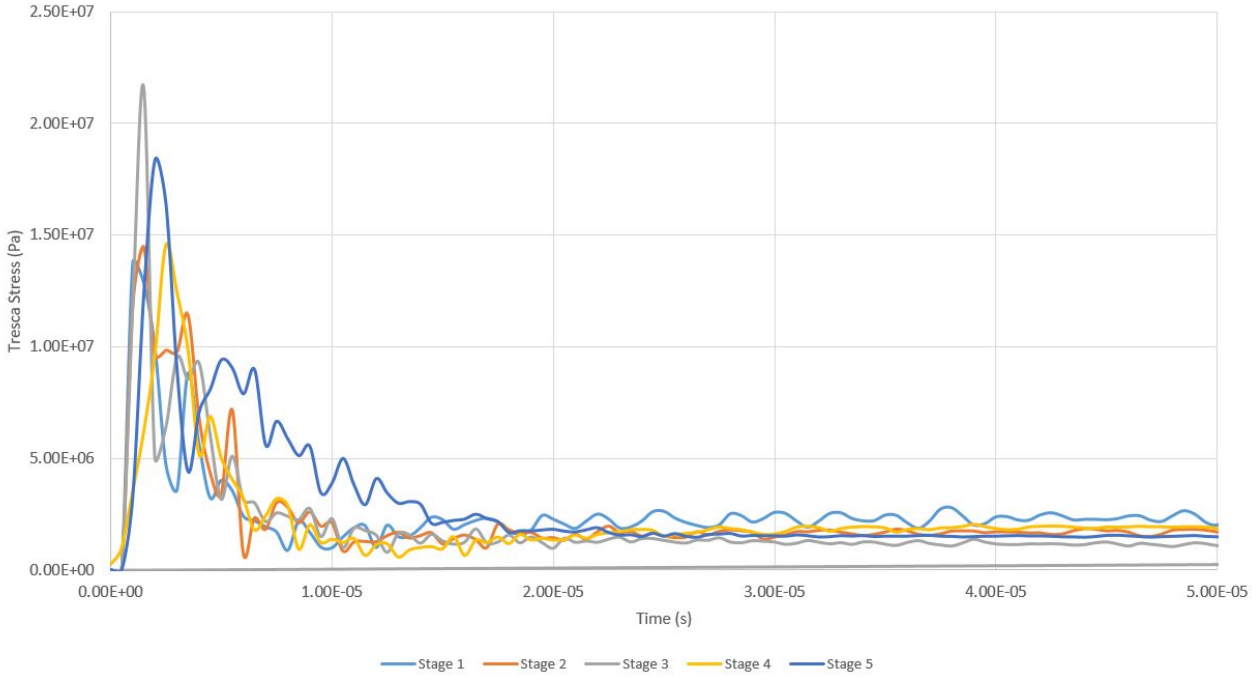

Figure 108: Tresca stress in the centre of the coating layer for each of the Stages of Erosion

The results displayed in Figure 108 show a similar lack of correlation between peak stress at the stage of erosion for shear stress. The only difference with Stage 5 erosion is that the stress wave takes longer to dissipate compared to earlier in the erosion process. The same trend is visible in the compressive stress graph, Figure 107, showing the inclusion of pits does concentrate the stress centrally and stop it from dissipating.

There is a lack of correlation between peak stress and the stage of erosion, the main conclusion from this modelling approach is the stress concentrating around areas of damage. Figure 109 shows the compressive stress plots for the sample at Stage 3 erosion and Figure 110 shows the Tresca stress plots of the sample at Stage 5 erosion.

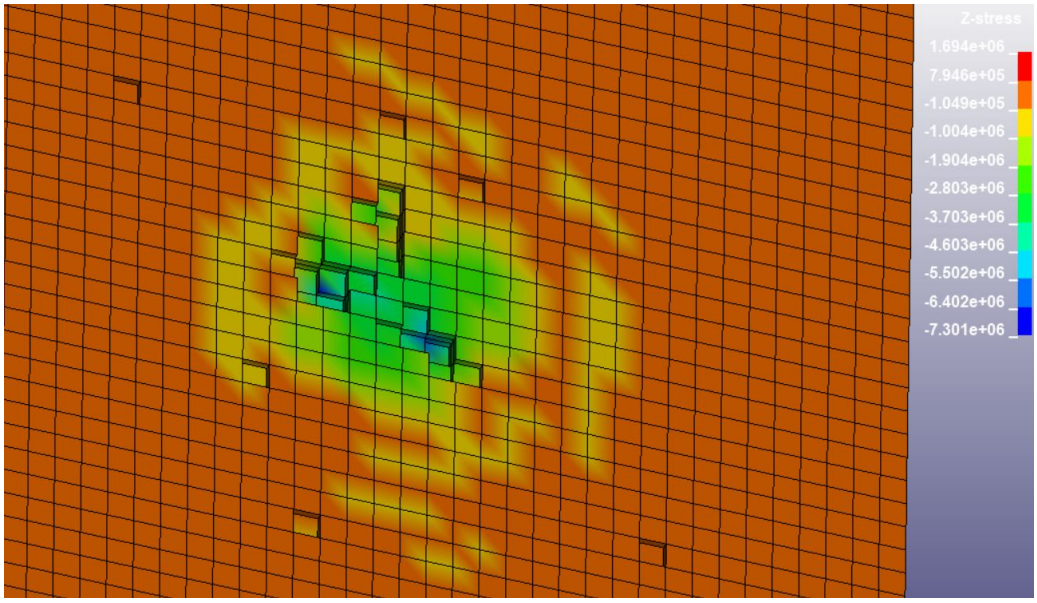

Figure 109: Compressive stress in the coating layer for a sample at Stage 3 erosion

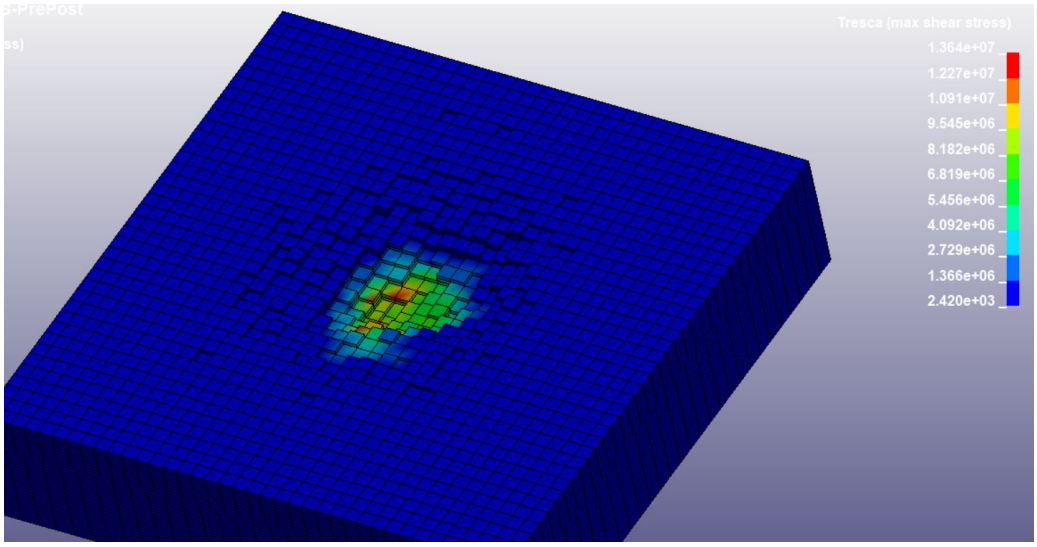

Figure 110: Tresca stress in the coating layer for a sample at Stage 5 erosion

Figure 109 shows that the peak compressive stresses are present in the deepest pits and are concentrated to those areas. Figure 110 displaying the shear stress also shows that all of the stress waves are concentrated into the damage in the centre of the sample rather than spreading out, as would usually be expected. This shows that while the maximum stress levels are not increasing the stress is being concentrated to the areas that already damaged thus escalating the erosion.

Examining the stress levels at a die-out distance of 3 radii out from the centre shows the trend

of stress being concentrated into the already damaged areas. Table 50 displays the compressive and Tresca stress throughout the five stages of erosion.

Stage	**Compressive Stress (Pa)**	**Tresca Stress (Pa)**
Stage 1	5.38×10^5	1.77×10^6
Stage 2	3.07×10^5	6.37×10^5
Stage 3	2.86×10^5	6.38×10^5
Stage 4	2.67×10^5	5.89×10^5
Stage 5	2.26×10^5	5.64×10^5

Table 50: Compressive and Tresca stress at a distance of 3 radii from the centre of the coating for each of the five erosion stages

From the results in Table 50, a clear correlation can be seen between lower stress levels, and the further distance, as the level of erosion increase. This consolidates the view on the damage leading to stress concentrations which results in an accumulation of stress in the centre of the sample.

7.5 Discussion

Parametric investigation is a powerful approach when undertaking modelling studies. It allows insight to be gained and quantified which cannot be realistically achieved by experimental testing. Such studies allow a certain area to be investigated that would either be too complex to experimentally test or much cheaper using a modelling approach. Initial studies on the influence of droplet diameter showed clearly the effect on the peak stresses and distribution arising in the erosion process. The first area explored was droplet diameter and how it affected the stresses involved in the erosion process. The results showed a linear trend between droplet volume and the compressive stress experienced by the sample upon impact. As the equation for the volume of a sphere includes a r^3, a small change in droplet diameter can result in a large change in the stress in the sample. This shows the importance of accurate measurement of droplet diameter when commissioning a test rig, as a range of 1mm between the largest and smallest diameter droplets can result in a large difference in stress experienced in the sample. Finally when modelling a 5mm diameter droplet the peak compressive stress observed was 140MPa which is not far from the 180MPa yield stress for that material system, as an example. This indicates how erosion could be initiated in off-shore wind turbines, as heavier rainfall

results in larger droplet formation. A spell of larger droplet impacts could initiate damage earlier than expected due to the larger stress waves experienced.

Next the coating thickness was investigated to determine if there was a thin enough thickness that resulted in increased stress, and if there was a point reached of diminishing returns where increasing the coating thickness had no bearing on the stresses present in the sample. The results showed that at the thinnest thickness of 0.2mm there was a slight increase in the peak compressive and shear stress. There was also no difference in the coating layer between the thicknesses of 0.4 - 0.8mm showing that a plateau in performance had been reached. However when examining the composite layer, the thicker the coating layer the less stress experienced by the composite. Depending on the failure mechanism present in an LEP, this does show that there is a potential benefit to increase the coating thickness.

The difference between flat and curved samples were analysed using Aerox material data. The models were designed to replicate the two different test rigs at the the University of Limerick and ORE Catapult. There was a very slight difference in droplet diameter though they were similar enough to compare flat and curved samples. Even with the curved samples being impacted by a droplet with a larger diameter it showed significantly smaller peak stresses in the coating layer, though the Limerick sample did dissipate the stress quicker than the Catapult sample. This showed that ideally test rigs should operate with curved samples, as this is more representative of real world wind turbine blades and by solely testing with flat samples the peak stresses will increase thus adversely predicting the erosion lifetime.

The flat samples that were eroded and examined under XCT apparatus were also modelled to determine if the mass loss and material property changes affected the stress waves inside the material. Firstly the geometrical changes had to be examined, using the imagery obtained from the XCT apparatus and accurate measurement of pit depth could be established and an average taken for each stage of erosion. When examining pit location and surface area, quantifying the differences was not as simple. Due to the random nature of mass loss, the same pits were not seen in all five samples, with some samples having a singular larger pit, at earlier stages of erosion, and others having many smaller pits. Therefore a qualitative approach was adopted to provide a representation of the erosion at each stage. While not being an ideal solution, this did provide an adequate alternate that captured the trends associated with erosion.

Next a DMA machine was used to measure the storage and loss modulus changes throughout the erosion lifetime. The testing procedure did have some flaws which resulted in a large variance in results, it this work was to be conducted again, increasing the length of samples to 60mm

would resolve the issue the samples being on the edge of the supports and hopefully provide more reliable results. Whilst the experimental set-up was not ideally configured, taking an average of all samples provides a fairly accurate value for the modulus. The next issue encountered was the change in sample volume as the sample eroded, with the volume being an important input into the DMA machinery this will affect the measurements recorded. As Stage 2 has negligible mass loss the results for the stage could be deemed accurate, therefore using the time taken to reach Stage 2 the results could be extrapolated forwards to estimate the other stages. While these solutions might not result in fully accurate modelling of the sample they allow trends to be explored and generalised conclusions made.

Analysing both the compressive and shear stress at each of the erosion stages showed that the peak stress levels were not impacted by the changes due to erosion. This is to be expected as the peak stresses are primarily driven by the impact substance, as the droplet is not changing then the peak stresses should not change. The one situation this might differ is when thinking about the coating thickness, as shown above the very thin coatings do resolve in a higher peak stress. Therefore this phenomena might have been visible at the latter stages of erosion. The one noticeable change as the erosion progressed is that the stress concentrating in the areas already damaged. For all modelled stages, it was evident that the stress was concentrating in or around the pits. This shows why the erosion process accelerates once the end of incubation period is reached, as stress concentrations occur in more localised areas.

8 Conclusions and Future Work

Combining the work of experimental testing with computer modelling helps to validate and progress both fields. Experimental testing provides an opportunity to examine samples in an environment similar to that experienced on wind turbines, while modelling allows certain parameters to be explored that would not be feasible with an experimental set-up. This combination will advance the field and lead us towards a time where both experimental and modelling solutions are applicable to what is observed.

8.1 Experimental Work

One of the aims with the experimental test rig was to provide a highly controllable and repeatable set-up allowing outcomes to be analysed and results to be determined. Issues with other test rigs include a high number of variables that are not well understood, leading to results that were not true when put into practice. Currently, a lot of the results seen from experimental test rigs are not translating to results in the real world, this is due to the large amount of variables and uncertainties involved in the current testing methodology. To improve this, there was a focus on characterisation which can turn these unknowns to knowns.

The characterisation of the ETC rig covered all potential variables that could affect the erosion process, with the goal to make the test rig as scientific and specific as possible, this is a goal not shared by all experimental test rigs. A lack of continuity between different research groups makes it difficult for the research to progress and build on each other. DNV-GL released a standard to provide guidance on erosion testing, however it is based on the R&D-AS set-up and has some shortcomings which will be discussed shortly.

The first area investigated by the characterisation of the ETC test rig was how the rotational speed affected the number of droplets and number of impacts. The results show that at speeds greater than 1200rpm, the turbulence generated by the rotating arm starts to affect the droplets resulting in less consistent results. It would be expected that the number of droplets would not be affected by rotational speed; however, above 1200 rpm, the number produced started to decrease. Droplets are formed by water collecting on the end of the needle. A greater aerodynamic wake this will cause the water to be blown off before droplets can form. Fewer droplets results in fewer impacts on the sample and the number of impacts is also decreased due to turbulence in the test rig causing the droplets to be deflected. These two phenomena

combined show that keeping the speed at 1200rpm or lower will provide more consistent results, with 75% of the droplets impacting the sample at this speed compared to the 67% impacting at 1300rpm. This does not sound like a large difference but over thousands of impacts it will have an effect.

The strike location was also analysed, for a radial viewpoint, as it is important to determine where the droplets impact: if all droplets were deflected towards the edge of the sample, this would provide a different result than expected. Similar to the previous result, speeds of 1100rpm and 1200rpm provide the most impacts in the centre of the sample: around half of the impacts were located in the centre, with another quarter slightly above centre. Viewing the samples tangentially was also examined, where it was discovered that below a speed of 1100rpm all impacts were located in the centre of the sample. The maximum number of deflections occurred at 1100rpm, though only 20% of impacts were deflected outside the middle third of the sample. The strike location is an important variable to understand, as if the strikes impacting the centre were too low then the number of impacts would have to be adjusted.

The droplet diameter was initially determined using a stationary test rig: with the test rig at the highest pressure head the average droplet diameter was measured at 2.27mm. The effect on the droplet diameter of reducing the number of operational needles was explored, as this is a condition often used when experimentally testing whether erosion is occurring too quickly. With 36 needles operating, the droplet diameter was 2.13mm; at 24 needles the diameter was 2.08mm. This is another area where the ETC test rig is more scientific as this trend allows an estimation of droplet diameter for any available needles operating. The droplet diameter was investigated with the test rig operating at various rotational speeds. This provided ambiguous results as the turbulence present distorted the droplets, resulting in a much larger variance in diameters measured. The main flaw in this process was that images were taken to determine the droplet diameters. The distortion of the droplets can cause non-spherical shapes to form: since the measurements were taken from a 2D image - which is a 2D representation of a 3D situation - the results might not be a fair representation of the droplet size. Further work should be conducted to investigate this area further, as it is crucial to determine the droplet diameter while the test rig is spinning. The rotation of the test rig will result in a change of aerodynamics, which will cause the droplets to detach from the needles early, resulting in a change in diameter and diameter distribution. A preferable method for calculating droplet size could be to measure the droplet volume rather than diameter as it will account for the distortion due to aerodynamics. Achieving this while operating a rotating arm at speeds of 1200rpm could be difficult, but would provide a step forward in the repeatability of experimental test rigs.

Finally, the standoff height in the test rig was explored. The standoff height is the distance between the needles and the sample. The DNV-GL standard states a minimum standoff distance of 200mm however this does not take into account the shrouds used on the ETC test rig. The shrouds protect the tips of the needles thereby allowing droplet formation to occur outside the turbulent air. The inclusion of shrouds results in a standoff height of 50mm providing the most straight falling droplets and therefore an increase in impacts. With the shrouds being 35mm long, the droplets are only in the airstream for 15mm, clearly showing the reason why. At a standoff height of 50mm and speeds of 120m/s or below, the number of straight falling droplets is around 90%, whereas at the speed of 140m/s this drops to 55%. This again shows that the higher speeds increase the turbulent air, resulting in less precise experimentation. Many other test rigs have the capability of rotating at speeds much greater than the ETC test rig; this work provides a warning that faster speeds are not always beneficial and that care should be taken to investigate the aerodynamic effects of high rotational speeds.

Droplet break up is another important consideration when characterising a test rig. The turbulent air present can cause droplets to implode, thus creating lots of tiny droplets. These tiny droplets will stay in the airstream and inevitably some will impact the sample. While these tiny droplets will not cause a great impact energy, this is a phenomenon that will not occur in the lifetime of actual turbines. Therefore even though an individual impact will have a negligible effect, the combination of these impacts over a 6 hour test could result in differing results to those seen on wind turbines. Using a high speed camera, image analysis showed that all droplet break up occurs shortly after the passing of the arm, within a quarter of its rotation around the test rig. Future work should focus on engineering a solution for droplet release to reduce the number of imploded droplets, thus eliminating one of the differences between experimental testing and the real world.

The DNV-GL standard, along with the majority of operational test rigs, does not place enough importance on the aerodynamics at work in a test rig. This is the main difference between wind turbines and experimental test rigs as wind turbines have much lower rotational speeds. Therefore, the wake off the back of the blade has time to dissipate before another blade passes. A key consideration should be the number of arms on an experimental test rig as increasing the number of arms will result in a shorter time between passes. The DNV-GL standard states a maximum number of three arms allowed on a test rig, though CFD work carried on the ETC test rig showed that the aerodynamic wake off the back of an arm is present for 200°, therefore even having two arms rotating will result in the arms being affected by the turbulence from the previous arm. Obviously the arm radius affects these results as larger radii will increase the

time between passes. This is another area where work should be conducted to investigate the ratio between the radius and the rotational speed and how this links to the aerodynamics of a test rig.

All of the above characterisation provides a good basis for experimental testing; without this work the results will not have the same validity. The characterisation work is the beginning of commissioning a test rig; the next step is to investigate the erosion rate and how the impact speed and frequency affects this. To explore these areas, a homogeneous and reliable material must be used and aluminium was chosen to achieve this. The aluminium samples provided consistent results, that could be trusted, allowing parameters such as impact to speed to be explored in detail.

The aluminium samples were tested from speeds of 1100 to 1300rpm to investigate how the impact speed affected the lifetime of the samples. The method for tracking the change in erosion is to measure the mass loss in the material, which can then be used to produce mass loss curves, a common tool used in industry. When comparing the mass loss with either time or number of impacts there was a clear correlation with the impact speed. This allows for the accurate prediction of lifetime for other impact speeds even without testing. The goal is to reach such a level of confidence with testing that this prediction method can also be used with Leading Edge Protection systems (LEPs). However, LEPs do not currently have the same repeatability as aluminium providing a larger variation in results. It is only once this stage is reached that experimental testing will provide accurate lifetime prediction for LEPs.

The aluminium mass loss curves were also created using kinetic energy as a method of comparison. This provided an interesting result as for speeds of 1200, 1250 and 1300rpm there was a very tight grouping indicating that the kinetic energy required to reach the end of the incubation period was independent of impact speed. However, the two slower speeds, 1100 and 1150pm did not continue this trend and were drastically different. As the set up of the test rig changed during the tests, resulting in the speeds of 1200, 1250 and 1300rpm being tested with the new set up it is unclear whether the results show a trend towards a similar kinetic energy or whether the speed of 1200rpm is an outlier. Further work should be carried out to investigate this, as well as providing a larger sample size for the results.

Next the XCT apparatus was used to investigate sub-surface damage and its effect on the erosion process. The erosion process was categorised into five different stages to make examining the process easier. Firstly, the void volume was used as a measure of quality to determine if this correlated to the lifetime of the samples, however no trend was noticed between the void volume

at Stage 1 and the lifetime. When examining the location of the voids, it was determined that most occurred near the composite interface and subsequently had less effect on the sample lifetime. The biggest impact on the lifetime of a sample, was for sample A007 which had a noticeable depression on the surface before any erosion had taken place. This imperfection may have caused stress concentrations to occur, leading to cracks and in turn delamination. The rest of the samples failed due to brittle fracture, with small fractions of material falling off.

The location of voids was examined to determine if any near the surface were causing stress concentrations which would lead to erosion initiation. No visible voids were detected near the surface that were in the same area as the erosion damage, any noticeable voids occurred elsewhere in the sample. The ETC test rig does have a very precise impact location thereby the droplets might never impact near an area with significant voids. There will be a small range of impacts as the aerodynamics of the test rig will cause some droplet deflection, though it is hard to determine if there was enough variation in impact location. This is an area where future work could be conducted using a test rig with a wider spread of impact locations to either show whether ot not voids near the surface will lead to erosion initiation. One trend that was noticed was an increase in void volume in the filler as erosion occurred. This volume increased even before mass loss had been experienced in this layer. The reasons for this occurring are either minuscule voids collating due to the stress waves from the droplet impacts causing the thin walls between them to break or the particulates in the filler layer causing crack initiation. The XCT imagery was not set up to achieve a high enough resolution to detect these minute cracks or voids. If this work was to be conducted again then higher resolution image should be used to focus on a smaller area just around the impact zone rather than the full sample.

Two different styles of LEP were tested: a long-standing industry standard elastic LEP and a highly flexible visco-elastic LEP. Both LEPs had a similar correlation between impact speed and time to reach the end of the incubation period, though there was a linear trend for long-standing elastic LEP whereas the highly visco-elastic LEP followed a logarithmic trend, similar to the aluminium samples. This shows that the visco-elastic LEP is designed to perform better at higher impact speeds, which is evident when examining the time for each stage in Figure 75. The time to reach the end of incubation period is proportionally greater at the higher speeds. This leads to an interesting thought that should LEPs be designed for a particular situation in mind, on wind turbines in certain environments the LEP could be chemically altered to increase its lifetime for that environment.

Studying the impact frequency in the long-standing elastic LEP showed that the lifetime of the

sample was unaffected by the frequency, as the same number of impacts was required to reach the end of the incubation period. This shows that the recovery time of this LEP is shorter than the time between impacts meaning that residual stress is not increasing rapidly due to a shorter recovery time. When examining the impact frequency on the flexible visco-elastic LEP the longer recovery time resulted in a shorter lifetime, again indicating the visco-elastic LEP had been designed to operate under specific conditions.

For both LEPs there was a restricted number of samples available meaning that the sample size was small. Due to a fault in testing, and a limited sample size, there are not results for each speed. It can be difficult to draw conclusions about the LEPs lifetime and how this is affected by the number of impacts or kinetic energy, without a large enough sample size. Therefore, further work could be done to increase the confidence in the results by testing a larger sample size. Another area for extra research is to investigate a larger range of impact frequencies. For the long-standing elastic LEP there will be an impact frequency where the LEP does not have time to recover therefore seeing a change in the number of impacts to reach the end of incubation. Also for the visco-elastic LEP with only two frequencies measured it is difficult to estimate the trend between impact frequency and lifetime. More frequencies are required to determine a trend. Linking the material properties to a LEP's preferred impact frequency could provide interesting conclusions on the erosion process and how best to prolong the lifetime.

8.2 Computational Modelling Work

Modelling provides a good tool to investigate certain parameters such as the impact frequency. Before carrying out any parametric studies a base model needed to be developed. LS-DYNA was the finite element software chosen due to its expertise in impact modelling and the ability to include smoothed particle hydrodynamics (SPH). SPH is the ideal tool for modelling water as it allows initial conditions to be applied to the full droplet while still allowing for the collapse of the droplet on impact and the ability to model the lateral jetting that occurs. Due to a lack of material data available, a sensitivity analysis was used to determine the effect of material properties on the stress levels measured. Making the material slightly stiffer and slightly softer hardly caused an insignificant change to the peak stresses experienced in the coating. These test results gave confidence that the parametric studies conducted would give results consistent with what was observed in eroded sample, even though there was incomplete material data.

The main goal in researching erosion is to determine the lifetime of coating materials, to achieve

this thousands of droplet impacts would need to be modelled. This is not achievable to model as the computational time would be too great, though the effect of multiple impacts was investigated. Three simultaneous impacts were modelled to determine if this resulted in any changes in the stresses detected in the sample. The compressive stresses showed not noticeable change after repeated impacts, however the shear stress did. The residual shear stress in the sample increased by a minuscule amount after each impact, showing that with the thousands of impacts experienced in a lifetime the shear stress could increase to a level where failure is possible.

Now that a base model had been developed, certain parametric studies could be conducted. Firstly, the effect of altering the droplet diameter was investigated, which is an important parameter to study as wind turbines are impacted by a variety of droplet diameters throughout their lifetime. The studied showed a drastic increase in the peak stresses when the droplet diameter was increased, this is due to the cubed term in the volume of a sphere thus the mass increases significantly with a small increase in diameter. This result shows the importance of test rigs, accurately measuring the average droplet diameter and distribution of droplet diameters. The droplet diameter variance should be a controlled, with the DNV-GL standard having a requirement that test rigs need to meet. The distribution is important to understand the range of droplets impacting and how they can affect the lifetime. If a test rig has a high variance in diameters then the results will be less repeatable, due to significant difference in peak stress impacted by various droplet diameters.

Another parametric study was analysing the effects of a flat or curved sample and how this impacted the peak stresses in the coating layer. It was observed that the flat samples had peak stresses of around double those experienced by the curved sample. This showed that ideally test rigs should operate with curved samples, as this is more representative of real-world wind turbine blades and by solely testing with flat samples the peak stresses will increase thus adversely predicting the erosion lifetime. One benefit to the flat samples was that the majority of the stresses were present in the coating layer, whereas the curved samples had higher stress levels in the composite. Higher stress levels in the composite layer can lead to delamination, which can lead to early failure as shown in Section 4.2.1, therefore this should be avoided. However, this case might not only be applicable for this particular LEP and is not necessarily transferable to all LEPs.

As finite element modelling of the full lifetime of a sample is unachievable, an approach was adopted to examine the geometry and material properties at various discrete stages of erosion.

XCT apparatus was used to look at sub-surface defects in the sample but was also useful in providing high resolution measurements of pits on the sample surface. The XCT imagery provided useful data on the pit depths which could be used to determine an average pit depth for each stage of erosion. However averaging the location and surface area of the pits was not as simple, each sample showed different locations and number of pits. Therefore a qualitative approach was adopted to provide a best estimate of the erosion at each stage. Ideally this is an area to develop further, a large sample size could provide an expected erosion pattern for a given LEP which could be used in modelling processes.

To measure the change in the material properties, DMA analysis was conducted. The testing procedure did have some flaws which resulted in a large variance in results, it this work was to be conducted again, increasing the length of samples to 60mm would resolve the issue the samples being on the edge of the supports and hopefully provide more reliable results. Whilst the experimental set-up was not ideally configured, taking an average of all samples provides a fairly accurate value for the modulus. The next issue encountered was the change in sample volume as the sample eroded, with the volume being an important input into the DMA machinery this will affect the measurements recorded. As Stage 2 has negligible mass loss the results for the stage could be deemed accurate, therefore using the time taken to reach Stage 2 the results could be extrapolated forwards to estimate the other stages. While these solutions might not result in fully accurate modelling of the sample they allow trends to be explored and generalised conclusions made.

Using the changes in geometry, combined with the material property changes the different stages of erosion could be modelled. The results showed that the peak compressive and shear stress were not impacted by the changes in erosion. The main change between the different stages was that the latter stages would experience more stress concentrations in the already damaged areas. This indicates why the mass loss accelerates once the end of incubation period is reached, as once the initial erosion has occurred the process accelerates with the stress concentrating to the already damaged areas.

8.3 Final Comments

To fully prevent erosion occurring on wind turbines, future coatings need to be developed which require experimental techniques operating at a high standard. The characterisation work carried out within this thesis is not common place amongst most test rig operators, but only by undertaking this work will there be a solid basis for all results. The aerodynamic effects of having a rotating arm spinning at rotational speeds much greater than experienced on a wind turbine is not fully appreciated and more work needs to be conducted to understand the influence turbulence in an experimental test rig and minimise it where possible.

The experimental testing showed that all samples tested followed the mass loss curves first developed by Springer. Though different materials, different impact speeds and different imapct frequencies will change the shape of the graph, by increasing or decreasing the length of the incubation period and altering the rate of erosion once significant mass loss has begun. The experimental testing has shown that the understanding has reached a high level for homogeneous materials such as aluminium, however the picture is not as clear when examining multi-layered systems. The difference in the effect of impact frequency shows that each LEP does not behave in a similar manner and currently there is not an agreement in the industry on the best LEP make-up. The changes in the void volume during the erosion process shows that there are sub-surface changes occurring though it is currently unclear exactly what these are. Through the experimental samples tested in the XCT and the parallel modelling work it was seen that the initiation of damage concentrates the stress, leading to acceleration of the erosion and more severe failure. Once this stage of the mass loss curve has been reached it is difficult to stop the coating erosion from escalating, therefore future work should be focused on elongating the incubation period as this is the key to increasing the erosion lifetime.

The modelling work showed that the compressive and shear stresses were the most prevalent during droplet impacts, as initially stated by Woods. The parametric studies displayed that an accurate droplet diameter measurement is crucial when operating experimental test rigs and that coating application plays an important role in its lifetime, as poorly applied coatings can lead to stress concentrations in the thinner areas of coating. Modelling the change in sample material properties and geometry showed that the compressive and shear stresses remained similar throughout, exhibiting that the Woods model remains valid during the erosion process. Further work could be carried out analysing the initiation of erosion, either by: increasing the number of impacts, in a multiple impact study, to a stage where there is a noticeable increase in residual stress; or by narrowing the focus to the point around the end of the incubation period

and modelling that time interval to determine any changes. These two steps will help inform and provide knowledge that can be used to predict the lifetime. Industry presently uses a modified Springer model, which has a number of known inherent limitations. The work presented herein, provides new insight and guidance on experimental testing, material characterisation and numerical modelling which helps develop the understanding of wind turbine blade leading edge erosion.

8.4 Suggestions for Future Work

This work has provided unique insight into both experimental and modelling techniques, though further work could be conducted to advance from this knowledge. One possibility would be to expand experimental testing of the different LEPs to explore the relaxation time effects on the impacted materials and their potential interaction with droplet impingement frequency. As shown in this thesis, the impact frequency of droplets does affect the lifetime of the LEPs (especially with respect to materials with viscoelastic properties), and not always with the expected correlation of higher impact frequency leading to shorter lifetime. The rest period between testing intervals is another area where stress relaxation could affect results, as when testing LEPs there are periods of downtime during experimentation while the sample is examined. When comparing samples, the testing programme was kept identical to avoid the rest period affecting the results, however this is an important area to investigate as real-world application will not provide consistent breaks between droplet impacts. Therefore, it would be interesting to further explore the stress relaxation: both in terms of droplet frequency and the rest period between testing intervals.

The analysis of samples with the XCT apparatus provided a novel method for examining the subsurface defects present in samples, however there are a couple of ways in which this analysis could be improved. Firstly, the experimental set-up provided a very localised area of impacts, but to better determine the effect of voids the droplets should ideally impact the full width of the sample. Currently the lack of erosion initiation around voids could be due to the droplet impacts being located elsewhere, so by spreading the impacts over the full sample this effect could be measured much more accurately. Finally, the stress models used in the modelling approach could be refined to predict behaviours more precisely by following the morphology of the samples, as observed in the XCT results. The voids detected in the XCT analysis were not included in the modelling and could provide an extra layer of detail. As the models become more complex and model the interaction between the layers to a greater detail than

currently possible, then the inclusion of voids (especially near these interfaces) could make the stress reflections and transmissions more realistic with stress concentrations present around the voids.

When examining the modelling techniques used in this thesis, the overall standard of modelling was improved from previous levels but there are clear areas for potential improvement. Firstly, a water droplet impacting a sample is a high strain rate phenomena, therefore the material properties of the impacted material need to also be measured at high strain rates. The author was aware of this but currently there is no obvious techniques to measure material properties at the strain rates required. These high strain rate material properties will increase the level of accuracy and allow the viscoelastic element of erosion to be modelled fully. Secondly, when modelling the composite it was assumed to be a homogeneous anisotropic material. Future work could look at modelling the fibres and matrix separately, which would tie in with the modelling of voids; as from the XCT analysis it was observed that a greater number of voids were present at the composite interface between the fibres. Finally, the modelling of the contact between the layers could be improved, as for the work in this thesis the contact between layers was assumed to be perfect. Experimental work would need to be conducted initially to determine the adhesion and contact between layers before these findings could be included into the model. This extra detail would affect the transmission and reflection of stress waves between layers which is an important area to consider with the multiple impacts present in leading edge erosion.

References

[1] Global wind statistics 2019. *Global Wind Energy Council*, Dec 2019.

[2] Peter Enevoldsen and George Xydis. Examining the trends of 35 years growth of key wind turbine components. *Energy for sustainable development*, 50:18–26, 2019.

[3] Richard D Woods. Screening of surface waves in soils. *Am Soc Civil Engr J Soil Mech*, 1968.

[4] Min Ku Lee, Whung Whoe Kim, Chang Kyu Rhee, and Won Jong Lee. Liquid impact erosion mechanism and theoretical impact stress analysis in tin-coated steam turbine blade materials. *Metallurgical and Materials Transactions A*, 30(4):961–968, 1999.

[5] Emil André Valaker, S Armada, and Shawn Wilson. Droplet erosion protection coatings for offshore wind turbine blades. *Energy Procedia*, 80:263–275, 2015.

[6] N Gaudern. A practical study of the aerodynamic impact of wind turbine blade leading edge erosion. In *Journal of Physics: Conference Series*, volume 524, page 012031. IOP Publishing, 2014.

[7] Anthony O'Carroll. Correlation of mechanical properties to rain erosion resistance of polymeric materials. 2018.

[8] S Armada, A Bjørgum, OØ Knudsen, C Simon, and M Pilz. Organic coatings reinforced with ceramic particles: an erosion study. 2010.

[9] SC Nolet. Composite wind blade engineering and manufacturing, tpi composites, inc. january 20, 2011.

[10] George Marsh. Meeting the challenge of wind turbine blade repair. *Reinforced Plastics*, 55:32–36, 07 2011.

[11] Rain erosion test apparatus. Technical report, University of Dayton Research Institute, 2019.

[12] William F Adler. Rain impact retrospective and vision for the future. *Wear*, 233:25–38, 1999.

[13] EF Tobin, TM Young, D Raps, and O Rohr. Comparison of liquid impingement results from whirling arm and water-jet rain erosion test facilities. *Wear*, 271(9-10):2625–2631, 2011.

[14] Hamish Macdonald. *The infuence of hail on wind turbine blade leading edge erosion and damage*. PhD thesis, University of Strathclyde, 2017.

[15] William F Adler. Waterdrop impact modeling. *Wear*, 186:341–351, 1995.

[16] Gal deBotton. The interaction of a coated target and an impinging waterdrop. *Wear*, 219(1):60–72, 1998.

[17] Mark Hugh Keegan, David Nash, and Margaret Stack. *Wind Turbine Blade Leading Edge Erosion: An investigation of rain droplet and hailstone impact induced damage mechanisms*. PhD thesis, University of Strathclyde, 2014.

[18] Na Li, Qulan Zhou, Xi Chen, Tongmo Xu, Shien Hui, and Di Zhang. Liquid drop impact on solid surface with application to water drop erosion on turbine blades, part i: Nonlinear wave model and solution of one-dimensional impact. *International Journal of Mechanical Sciences*, 50(10-11):1526–1542, 2008.

[19] B Amirzadeh, A Louhghalam, M Raessi, and M Tootkaboni. A computational framework for the analysis of rain-induced erosion in wind turbine blades, part i: Stochastic rain texture model and drop impact simulations. *Journal of Wind Engineering and Industrial Aerodynamics*, 163:33–43, 2017.

[20] B Amirzadeh, A Louhghalam, M Raessi, and M Tootkaboni. A computational framework for the analysis of rain-induced erosion in wind turbine blades, part ii: Drop impact-induced stresses and blade coating fatigue life. *Journal of Wind Engineering and Industrial Aerodynamics*, 163:44–54, 2017.

[21] Leon Mishnaevsky Jr, Søren Fæster, Lars P Mikkelsen, Yukihiro Kusano, and Jakob Ilsted Bech. Micromechanisms of leading edge erosion of wind turbine blades: X-ray tomography analysis and computational studies. *Wind Energy - Volume 23*, 2019.

[22] Ting Ye, Dingyi Pan, Can Huang, and Moubin Liu. Smoothed particle hydrodynamics (sph) for complex fluid flows: Recent developments in methodology and applications. *Physics of Fluids*, 31(1):011301, 2019.

[23] Costantino Menna, Domenico Asprone, Giancarlo Caprino, Valentina Lopresto, and Andrea Prota. Numerical simulation of impact tests on gfrp composite laminates. *International Journal of Impact Engineering*, 38(8-9):677–685, 2011.

[24] Justin D Littell, Charles R Ruggeri, Robert K Goldberg, Gary D Roberts, William A Arnold, and Wieslaw K Binienda. Measurement of epoxy resin tension, compression, and shear stress–strain curves over a wide range of strain rates using small test specimens. *Journal of Aerospace Engineering*, 21(3):162–173, 2008.

[25] History of wind energy, 2016. Available at `http://windenergyfoundation.org/about-wind-energy/history/`.

[26] Anonymous. 2020 climate energy package, Feb 2017. Available at `https://ec.europa.eu/clima/policies/strategies/2020_en`.

[27] Adam Vaughan. Uk sets ambitious new 2030s carbon target, Jun 2016. Available at `https://www.theguardian.com/environment/2016/jun/30/uk-sets-ambitious-new-2030s-carbon-target`.

[28] The world wind energy association. *WWEA Half-year Report: Worldwind wind capacity reached 456 GW*, Oct 2016.

[29] Ian Johnstone. Developing world invests more in renewable energy than rich countries for first time, new study says, May 2016. Available at `https://www.independent.co.uk/environment/climate-change/renewable-energy-investment-developed-world-developing-world-ren21-report-a7058436.html`.

[30] Global wind report chapter on global offshore. *Global Wind Energy Council*, 2015.

[31] Uk government affirms 40 gw offshore wind energy commitment - evwind. Dec 2019. Available at `https://www.evwind.es/2019/12/19/uk-government-affirms-40-gw-offshore-wind-energy-commitment/72645`.

[32] Ryan Wiser, Maureen Hand, Joachim Seel, and Bentham Paulos. Berkeley lab. *Reducing Wind Energy Costs through Increased Turbine Size: Is the Sky the Limit?*, Nov 2016.

[33] George S Springer, Cheng-I Yang, and Poul S Larsen. Analysis of rain erosion of coated materials. *Journal of Composite Materials*, 8(3):229–252, 1974.

[34] Matthias Schramm, Hamid Rahimi, Bernhard Stoevesandt, and Kim Tangager. The influence of eroded blades on wind turbine performance using numerical simulations. *Energies*, 10(9):1420, 2017.

[35] How long does a wind turbine last?, 2015. Available at https://www.renewablesfirst.co.uk/windpower/windpower-learning-centre/how-long-do-wind-turbines-installations-last/.

[36] DNV GL. Rp-0171 "testing of rotor blade erosion protection systems". 2018.

[37] Frank Philip Bowden and John Edwin Field. The brittle fracture of solids by liquid impact, by solid impact, and by shock. *Proceedings of the Royal Society of London. Series A. Mathematical and Physical Sciences*, 282(1390):331–352, 1964.

[38] Omid Gohardani. Impact of erosion testing aspects on current and future flight conditions. *Progress in Aerospace Sciences*, 47(4):280–303, 2011.

[39] HM Slot, ERM Gelinck, C Rentrop, and E Van Der Heide. Leading edge erosion of coated wind turbine blades: Review of coating life models. *Renewable energy*, 80:837–848, 2015.

[40] JP Dear and JE Field. High-speed photography of surface geometry effects in liquid/solid impact. *Journal of Applied Physics*, 63(4):1015–1021, 1988.

[41] Rong Liu, Kuiying Chen, Ju Chen, Jingrong Zhao, and Ming Liang. Simulation studies of solid-particle and liquid-drop erosion of nial alloy. *Simulation*, 1:10001184, 2015.

[42] Shizhong Zhang, Kim Dam-Johansen, Sten Nørkjær, Pablo L Bernad Jr, and Søren Kiil. Erosion of wind turbine blade coatings–design and analysis of jet-based laboratory equipment for performance evaluation. *Progress in Organic Coatings*, 78:103–115, 2015.

[43] Mark Hugh Keegan, David Nash, and Margaret Stack. Numerical modelling of hailstone impact on the leading edge of a wind turbine blade. *EWEA Annual Wind Energy Event 2013*, 2013.

[44] Junlei Chen, Jihui Wang, and Aiqing Ni. A review on rain erosion protection of wind turbine blades. *Journal of Coatings Technology and Research*, 16(1):15–24, 2019.

[45] JR Hutchinson, PJ Schubel, and NA Warrior. A cost and performance comparison of lrtm and vi for the manufacture of large scale wind turbine blades. *Renewable energy*, 36(2):866–871, 2011.

[46] Chia Chen Ciang, Jung-Ryul Lee, and Hyung-Joon Bang. Structural health monitoring for a wind turbine system: a review of damage detection methods. *Measurement science and technology*, 19(12):122001, 2008.

[47] Bent F Sørensen, Lars Lading, Peter Sendrup, Malcolm McGugan, Christian P Debel, Ole JD Kristensen, Gunner Chr Larsen, Anders M Hansen, Jørgen Rheinländer, Jens Rusborg, et al. Fundamentals for remote structural health monitoring of wind turbine blades-a preproject. 2002.

[48] Drone inspection of wind turbines - on and off shore. Available at `https://forcetechnology.com/en/services/drone-inspection-of-wind-turbines-onshore-and-offshore`.

[49] Charles J Hurley and George F Schmitt Jr. Development and calibration of a mach 1.2 rain erosion test apparatus. Technical report, Dayton Univ Oh Research Inst, 1970.

[50] Anonymous. R&d group. Available at `https://www.rd-as.com/rain-erosion-tester/`.

[51] SAAB. Rain erosion test facility. Available at `https://www.saabgroup.com`.

[52] ASTM ASTM. G73-10 "standard test method for liquid impingement erosion using rotating apparatus". *ASTM: West Conshohocken, PA, USA*, 2013.

[53] Joe J Monaghan. Smoothed particle hydrodynamics. *Annual review of astronomy and astrophysics*, 30(1):543–574, 1992.

[54] Rad A Dalrymple and BD Rogers. Numerical modeling of water waves with the sph method. *Coastal engineering*, 53(2-3):141–147, 2006.

[55] Tarek Mabrouki, K Raissi, and A Cornier. Numerical simulation and experimental study of the interaction between a pure high-velocity waterjet and targets: contribution to investigate the decoating process. *Wear*, 239(2):260–273, 2000.

[56] Qulan Zhou, Na Li, Xi Chen, Tongmo Xu, Shien Hui, and Di Zhang. Liquid drop impact on solid surface with application to water drop erosion on turbine blades, part ii: Axisymmetric solution and erosion analysis. *International Journal of Mechanical Sciences*, 50(10-11):1543–1558, 2008.

[57] E Cortés, F Sánchez, L Domenech, A Olivares, TM Young, A O'Carroll, and F Chinesta. Manufacturing issues which affect coating erosion performance in wind turbine blades. In *AIP Conference Proceedings*, volume 1896, page 030023. AIP Publishing LLC, 2017.

[58] Offshore Renewable Energy Catapult. Blade leading edge erosion: Droplet impact modelling and characterisation, internal ore catapult. 2015.

[59] Needle gauge table, 2020. Available at https://darwin-microfluidics.com/blogs/tools/syringe-needle-gauge-table.

[60] R Herring, K Dyer, A MacLeod, and C Ward. Computational fluid dynamics methodology for characterisation of leading edge erosion in whirling arm test rigs. In *Journal of Physics: Conference Series*, volume 1222, page 012011. IOP Publishing, 2019.

[61] Willi A Kalender. X-ray computed tomography. *Physics in Medicine & Biology*, 51(13):R29, 2006.

[62] I Ouachan, M Kuball, D Liu, K Dyer, C Ward, and I Hamerton. Understanding of leading-edge protection performance using nano-silicates for modification. In *Journal of Physics: Conference Series*, volume 1222, page 012016. IOP Publishing, 2019.

[63] How matlab represents pixel colors, 2006. Available at https://uk.mathworks.com/company/newsletters/articles/how-matlab-represents-pixel-colors.html.

[64] Joe J Monaghan. Smoothed particle hydrodynamics. *Annual review of astronomy and astrophysics*, 30(1):543–574, 1992.

[65] MB Liu, GR Liu, KY Lam, and Z Zong. Smoothed particle hydrodynamics for numerical simulation of underwater explosion. *Computational Mechanics*, 30(2):106–118, 2003.

[66] R Vacondio, BD Rogers, and PK Stansby. Accurate particle splitting for smoothed particle hydrodynamics in shallow water with shock capturing. *International Journal for Numerical Methods in Fluids*, 69(8):1377–1410, 2012.

[67] Mark Hugh Keegan, DH Nash, and MM Stack. On erosion issues associated with the leading edge of wind turbine blades. *Journal of Physics D: Applied Physics*, 46(38):383001, 2013.

[68] CE Lapple. Characteristics of particles and particle dispersoids. *Stanford Research Institute Journal*, 5:95, 1961.

[69] Det Norske Veritas. Dnv-os-j102, design and manufacture of wind turbine blades. *Oct-2006*, 2010.

Appendices

A Radial Nozzle Position

Needle	Position	Needle	Position	Needle	Position
1	69.3	26	76.9	51	64.5
2	71.9	27	77.3	52	65.0
3	75.8	28	77.6	53	66.0
4	75.1	29	76.9	54	66.2
5	74.5	30	76.9	55	64.4
6	76.1	31	77.7	56	68.5
7	75.6	32	76.7	57	69.2
8	73.9	33	75.9	58	71.4
9	74.4	34	74.6	59	73.2
10	74.5	35	73.5	60	72.2
11	74.6	36	70.4	61	70.7
12	73.6	37	68.8	62	70.8
13	72.2	38	70.3	63	71.9
14	72.4	39	70.8	64	73.6
15	72.2	40	70.2	65	73.7
16	72.7	41	67.9	66	74.8
17	72.8	42	65.6	67	75.3
18	70.7	43	65.7	68	76.3
19	70.0	44	63.8	69	74.9
20	71.5	45	65.1	70	74.8
21	72.1	46	64.7	71	72.6
22	72.9	47	64.1	72	69.5
23	73.4	48	63.7		
24	73.9	49	64.1		
25	75.1	50	64.0		

Table 51: Radial Position of Needles

B Strike Locations

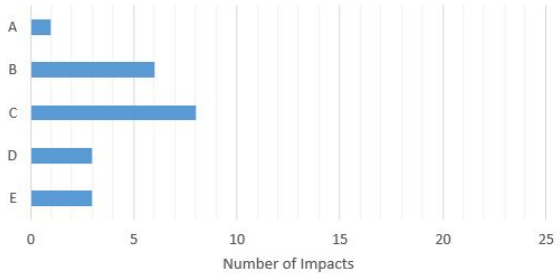

(a) Strike location for a sample at 700rpm

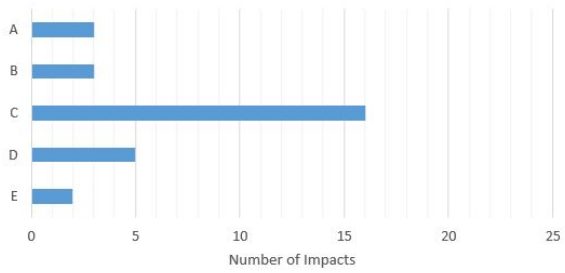

(b) Strike location for a sample at 800rpm

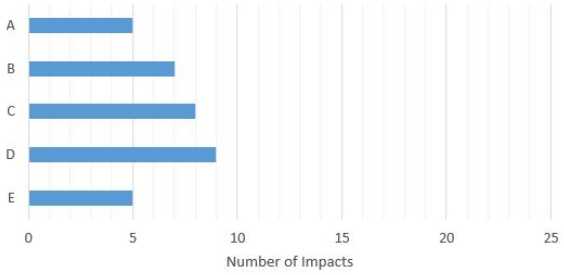

(c) Strike location for a sample at 900rpm

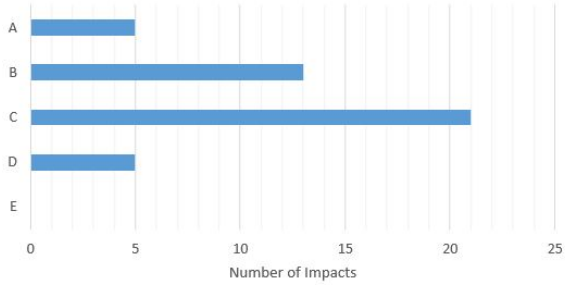

(d) Strike location for a sample at 1100rpm

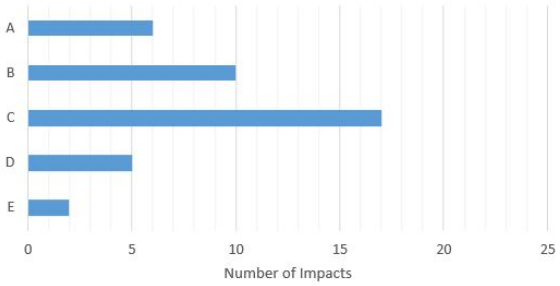

(e) Strike location for a sample at 1200rpm

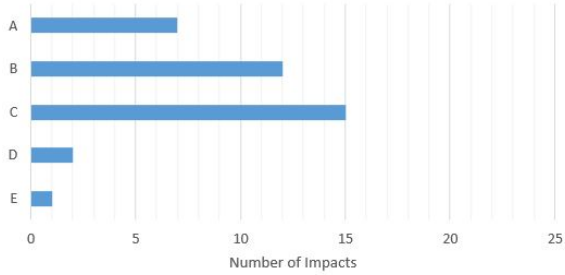

(f) Strike location for a sample at 1300rpm

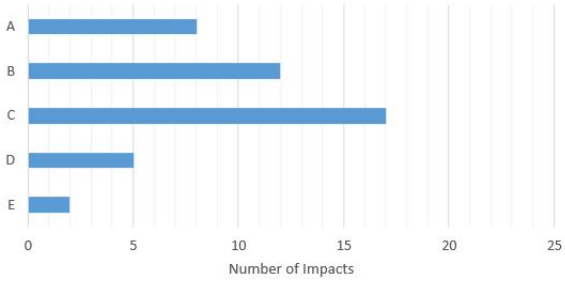

(g) Strike location for a sample at 1400rpm

Figure 111: Strike Locations for aerofoil at varying speeds of 700-1400rpm

C Mass Loss Curve Estimations

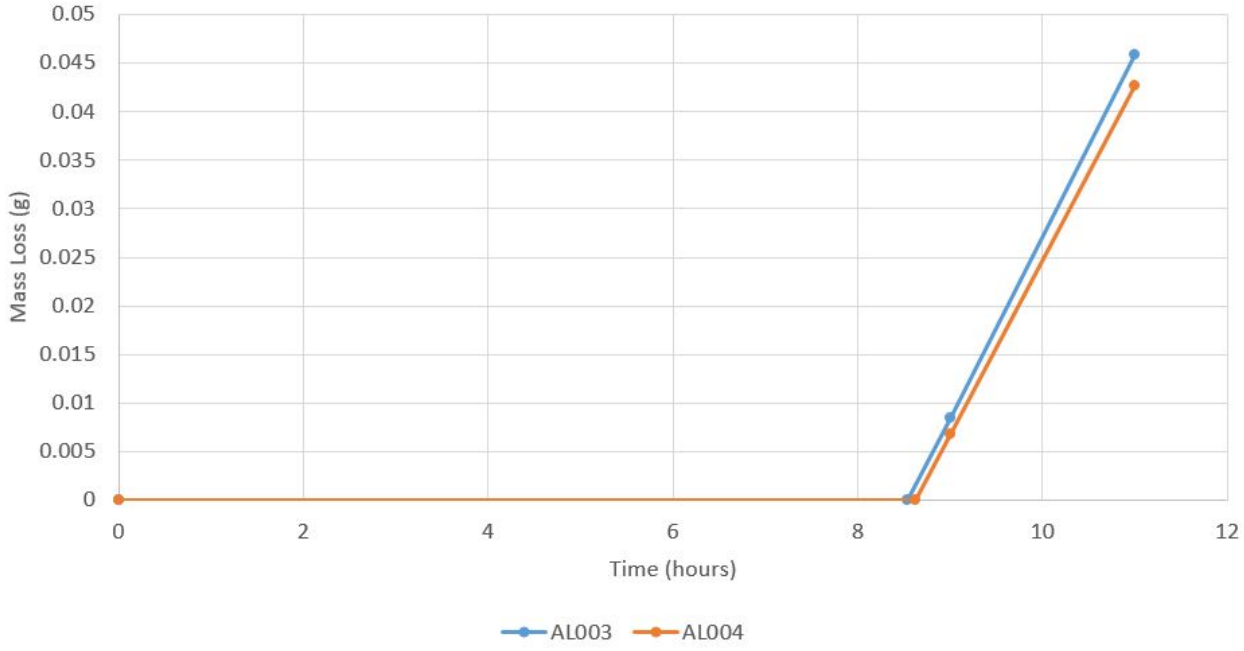

Figure 112: Mass loss curve estimation, for all samples. Impact velocity of 1100rpm.

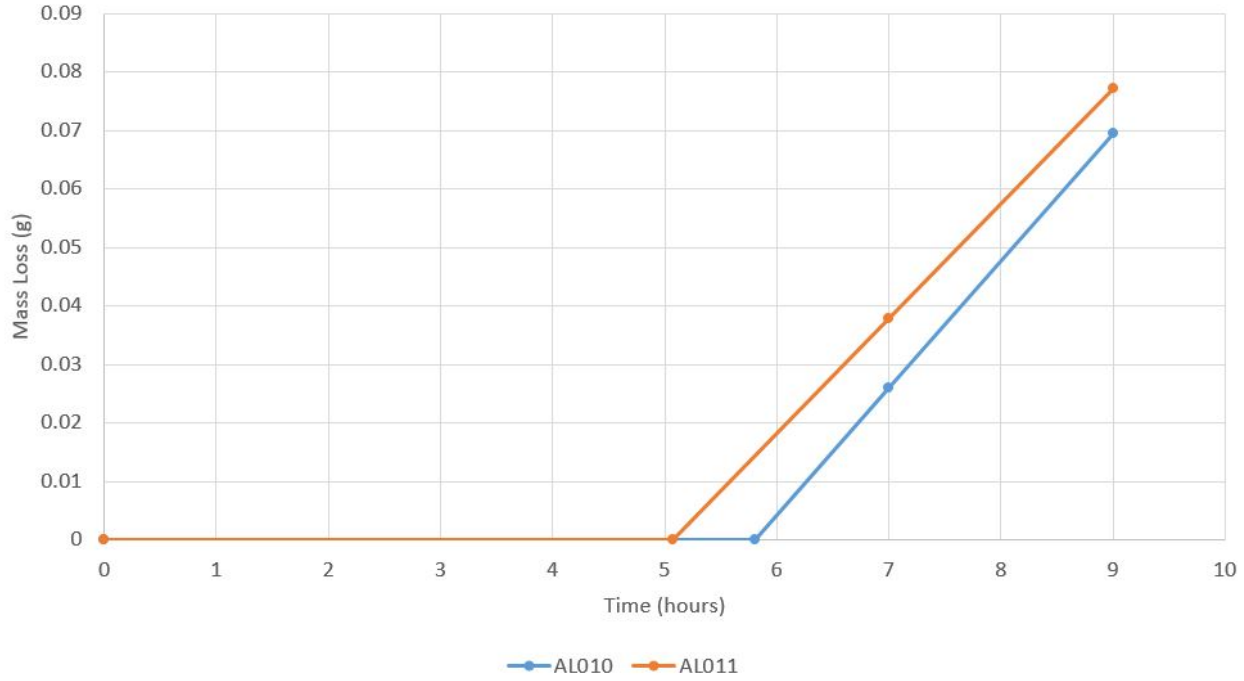

Figure 113: Mass loss curve estimation, for all samples. Impact velocity of 1150rpm.

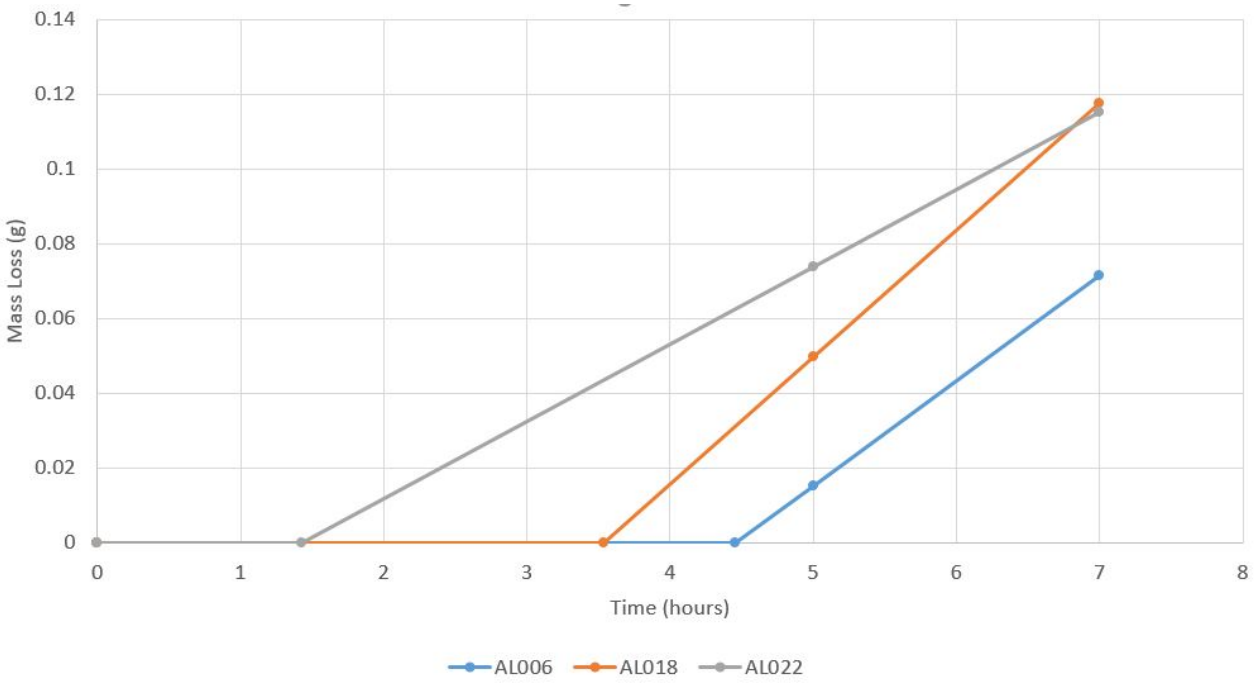

Figure 114: Mass loss curve estimation, for all samples. Impact velocity of 1200rpm.

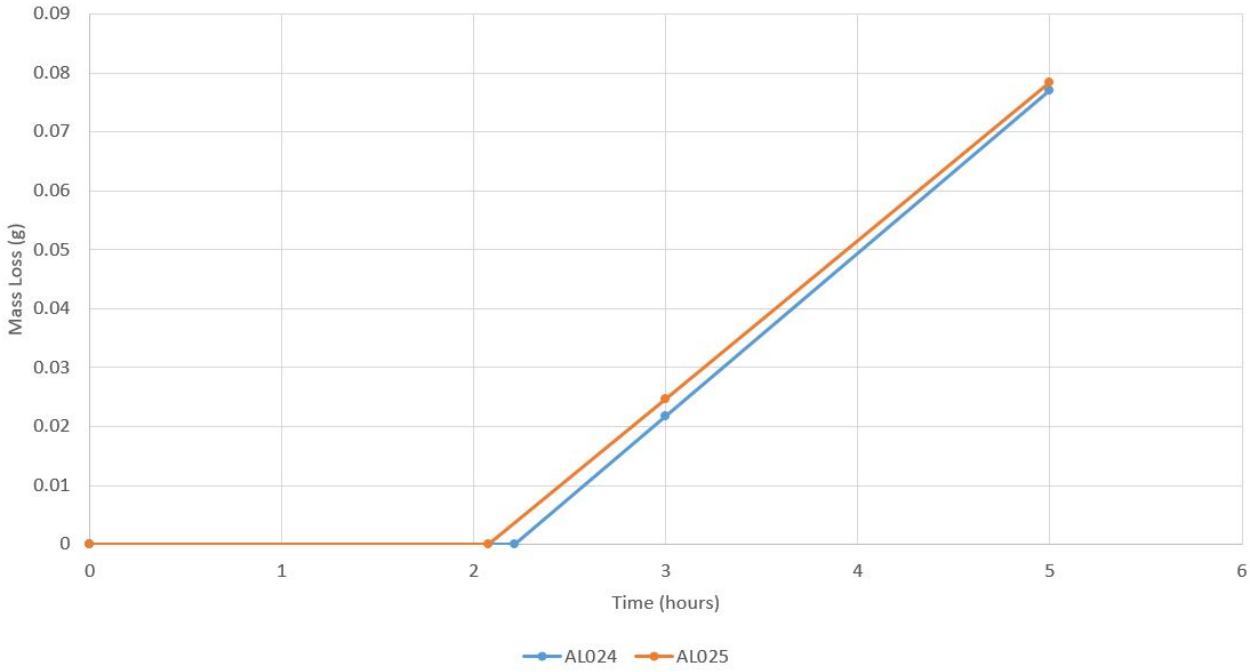

Figure 115: Mass loss curve estimation, for all samples. Impact velocity of 1250rpm.

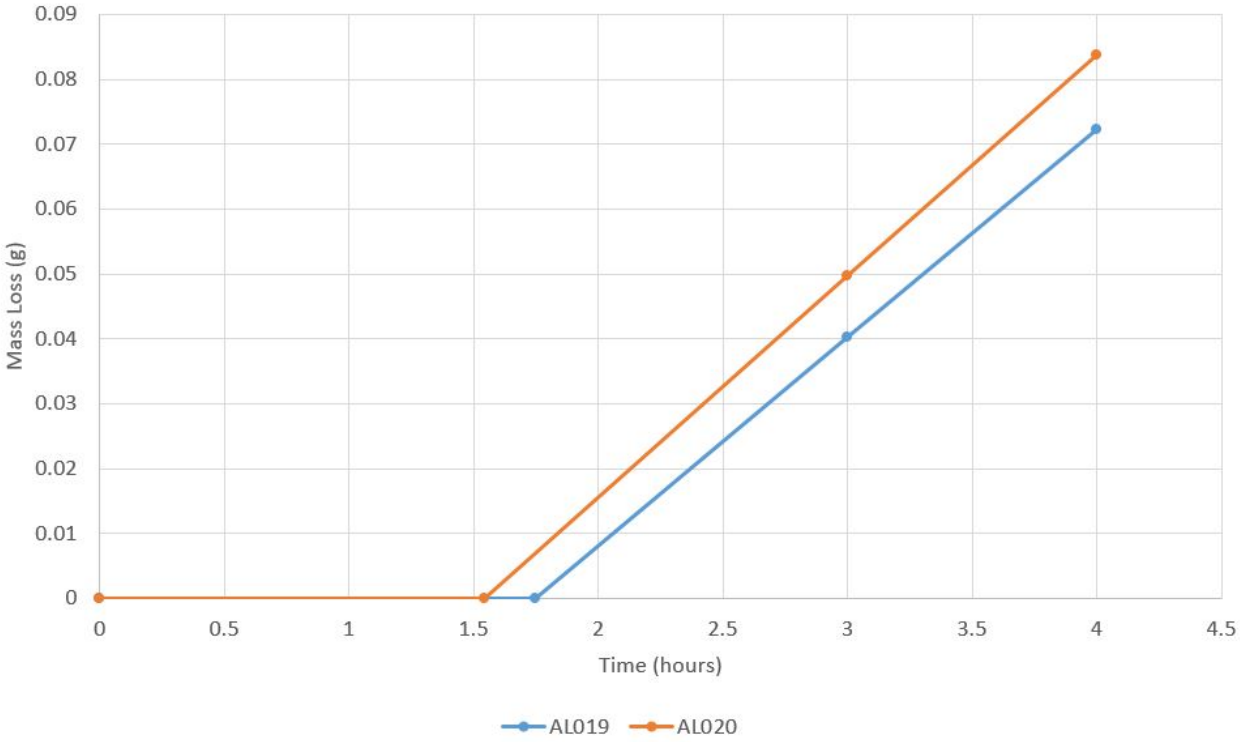

Figure 116: Mass loss curve estimation, for all samples. Impact velocity of 1300rpm.

C.1 Number of Needles vs Kinetic Energy

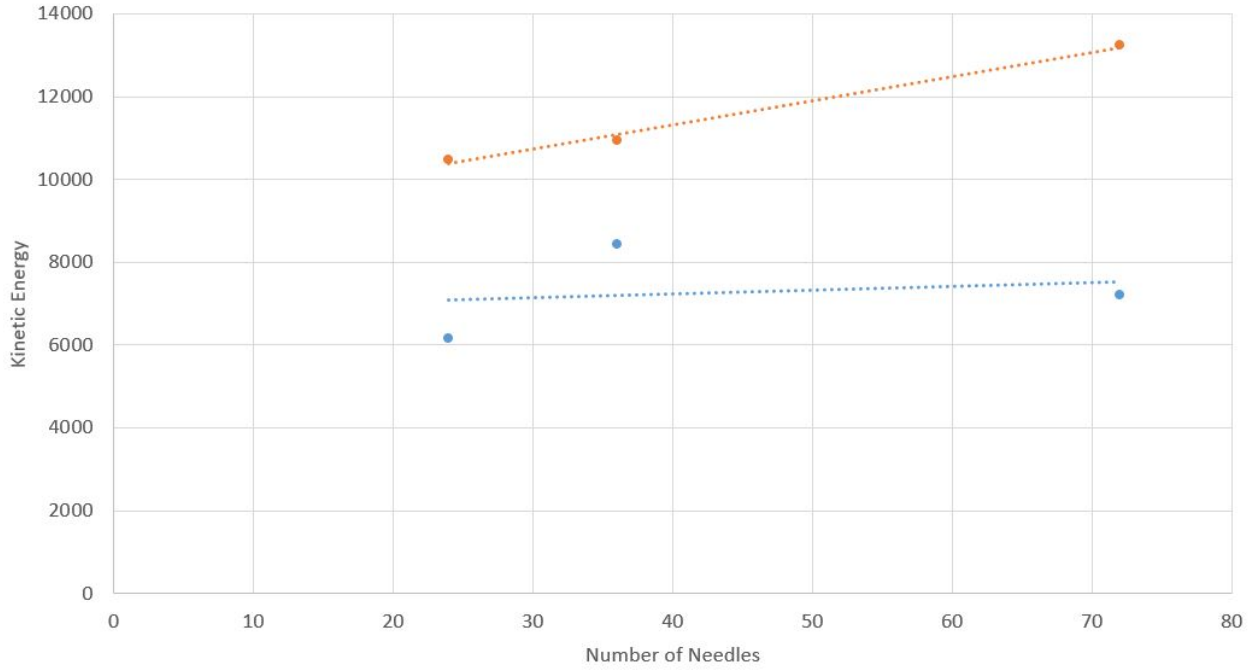

Figure 117: Number of Needles vs Kinetic Energy to reach the end of Incubation Period (blue) and Breakthrough (orange)

D Pixel Detection Photos

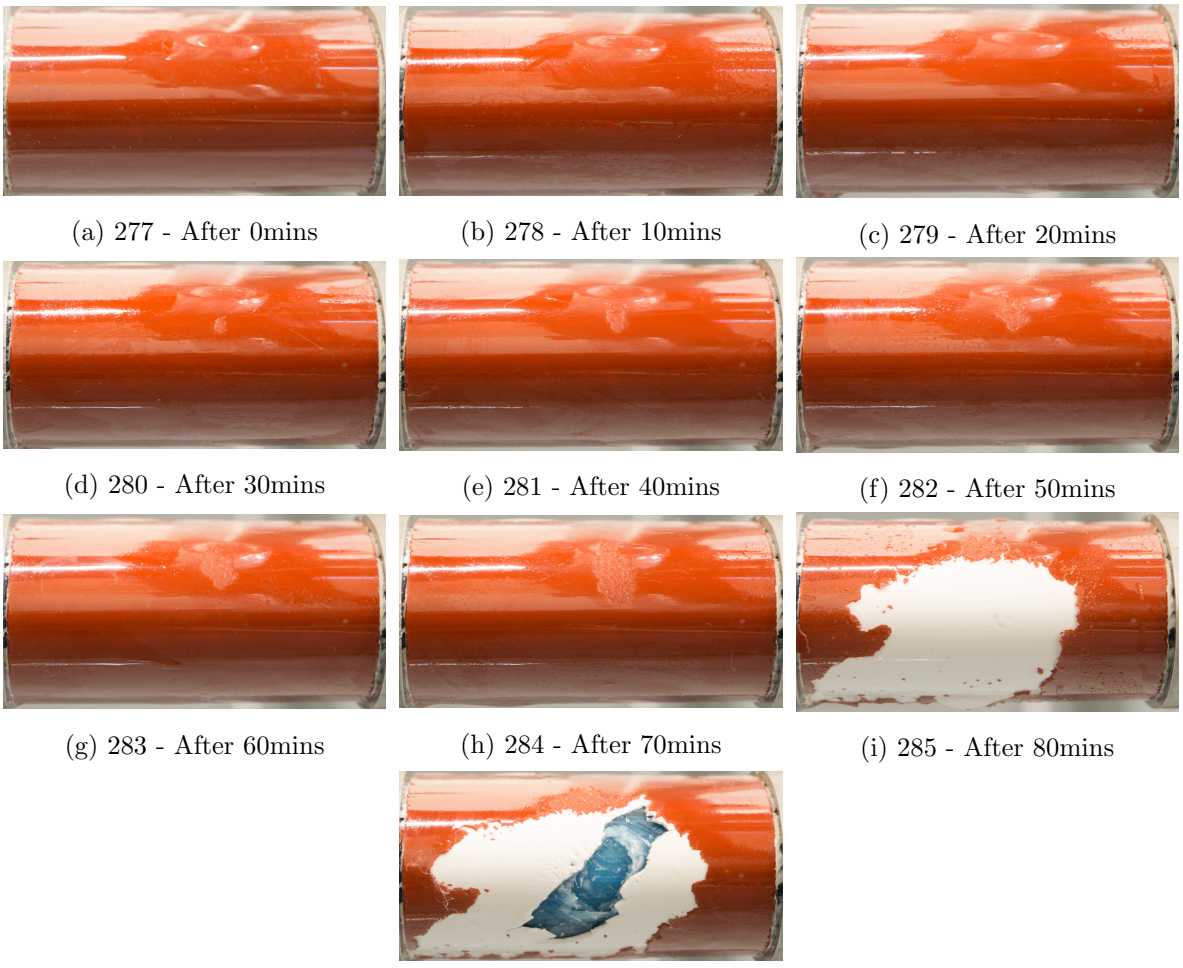

(a) 277 - After 0mins

(b) 278 - After 10mins

(c) 279 - After 20mins

(d) 280 - After 30mins

(e) 281 - After 40mins

(f) 282 - After 50mins

(g) 283 - After 60mins

(h) 284 - After 70mins

(i) 285 - After 80mins

(j) 286 - After 90mins

Figure 118: Photos taken of Sample C008 to test Matlab script

(a) 292 - After 0mins (b) 293 - After 10mins (c) 294 - After 20mins

(d) 295 - After 30mins (e) 296 - After 40mins (f) 297 - After 50mins

(g) 298 - After 60mins (h) 299 - After 70mins (i) 300 - After 80mins

(j) 301 - After 90mins (k) 302 - After 100mins (l) 303 - After 110mins

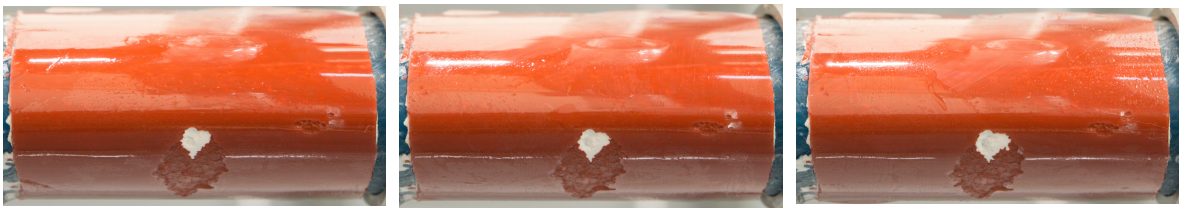

(m) 304 - After 120mins (n) 305 - After 130mins (o) 306 - After 140mins

Figure 119: Photos taken of Sample C008 to test Matlab script

E Matlab Script to Detect Red Pixels

```
close all
clear all
clc

%%Load image
rgb = imread('Erosion306cropped.jpg');
figure(1)
imshow(rgb)
%%Find red points
redPoints = rgb(:,:,1)>=50 & rgb(:,:,2)<=170 & rgb(:,:,3)<=170;
percentRed = 100*(sum(sum(redPoints))/(size(rgb,1)*size(rgb,2)));
fprintf('Image has %d red pixels\n',sum(sum(redPoints)))
fprintf('Image is %.2f percent red\n',percentRed)
%%Highlight red on image
rgbRed = uint8(cat(3,redPoints,redPoints,redPoints)).*rgb;
figure(2)
imshow(rgbRed)
```

Figure 120: Matlab script used to Detect Red Pixels

F Voids in Filler Layer

F.1 Sample A30

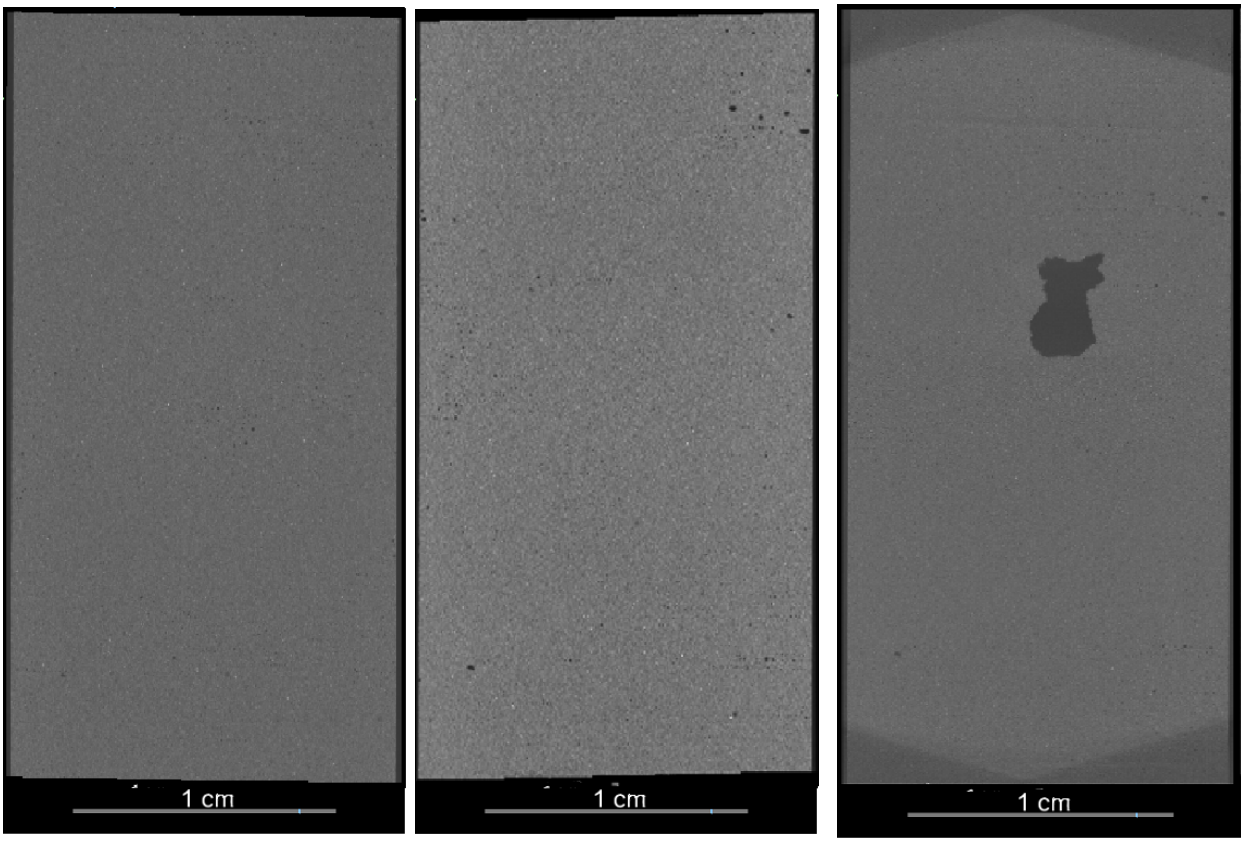

(a) Stage 2 (b) Stage 3 (c) Stage 4

Figure 121: Voids in Filler layer for Sample A30

F.2 Sample A35

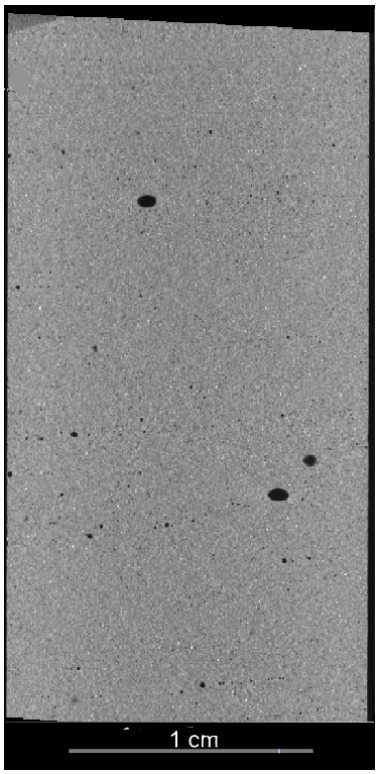

(a) Stage 2

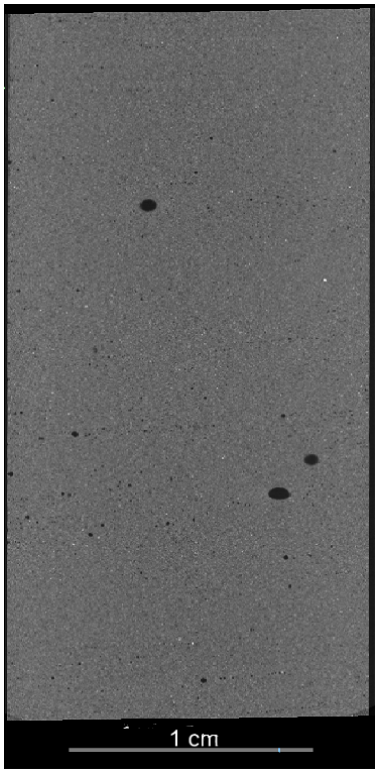

(b) Stage 3

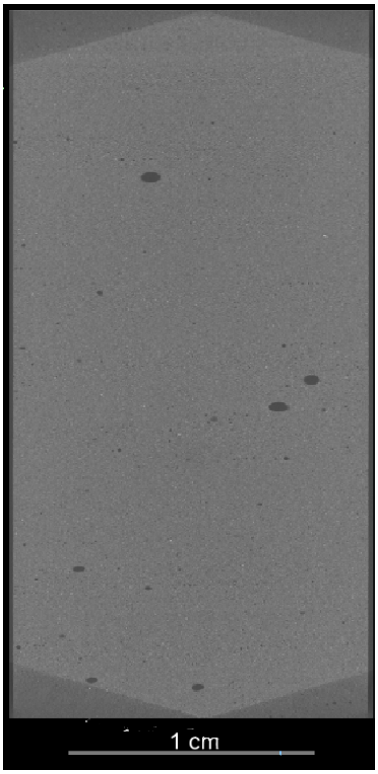

(c) Stage 4

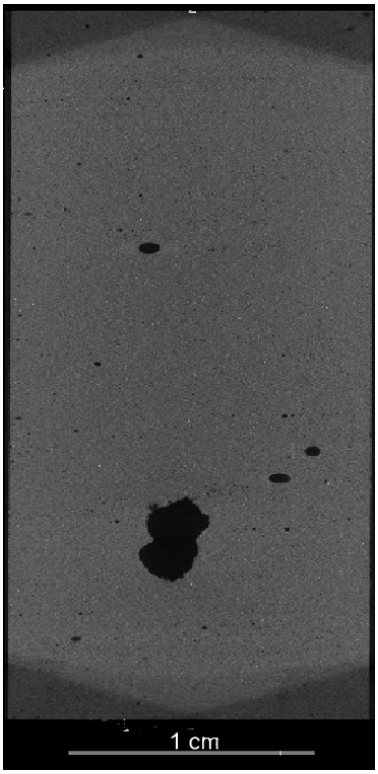

(d) Stage 5

Figure 122: Voids in Filler layer for Sample A35

F.3 Sample A38

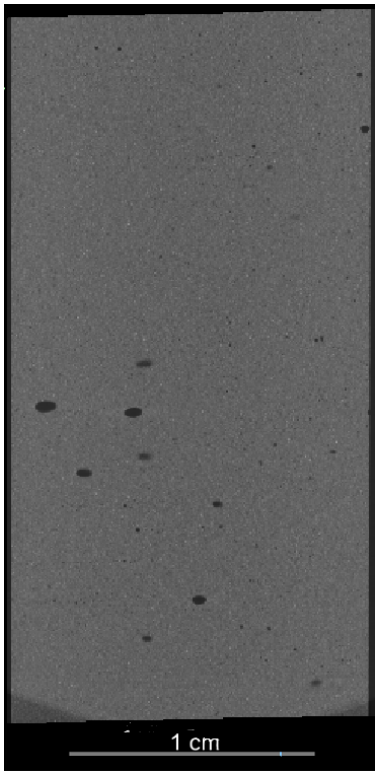

(a) Stage 2

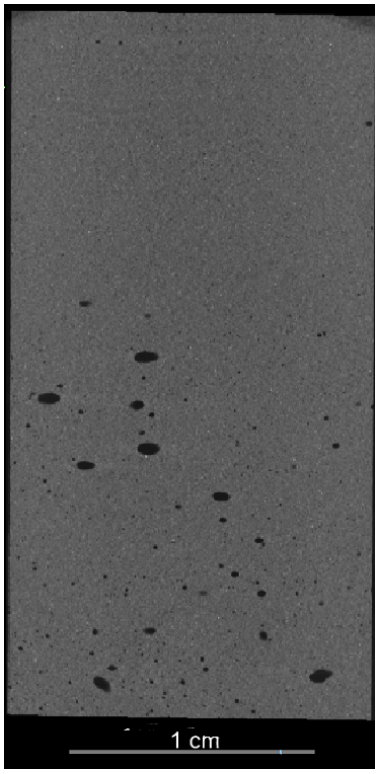

(b) Stage 3

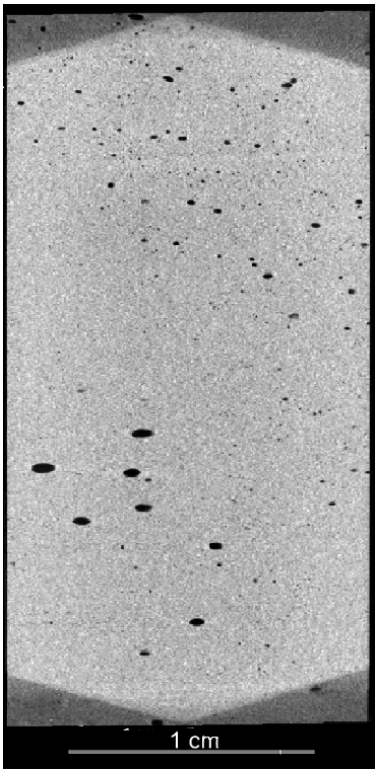

(c) Stage 4

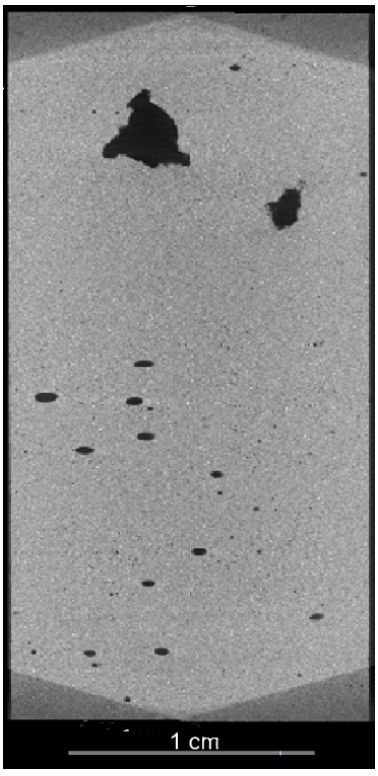

(d) Stage 5

Figure 123: Voids in Filler layer for Sample A38

G Stress Plots of Curved Samples

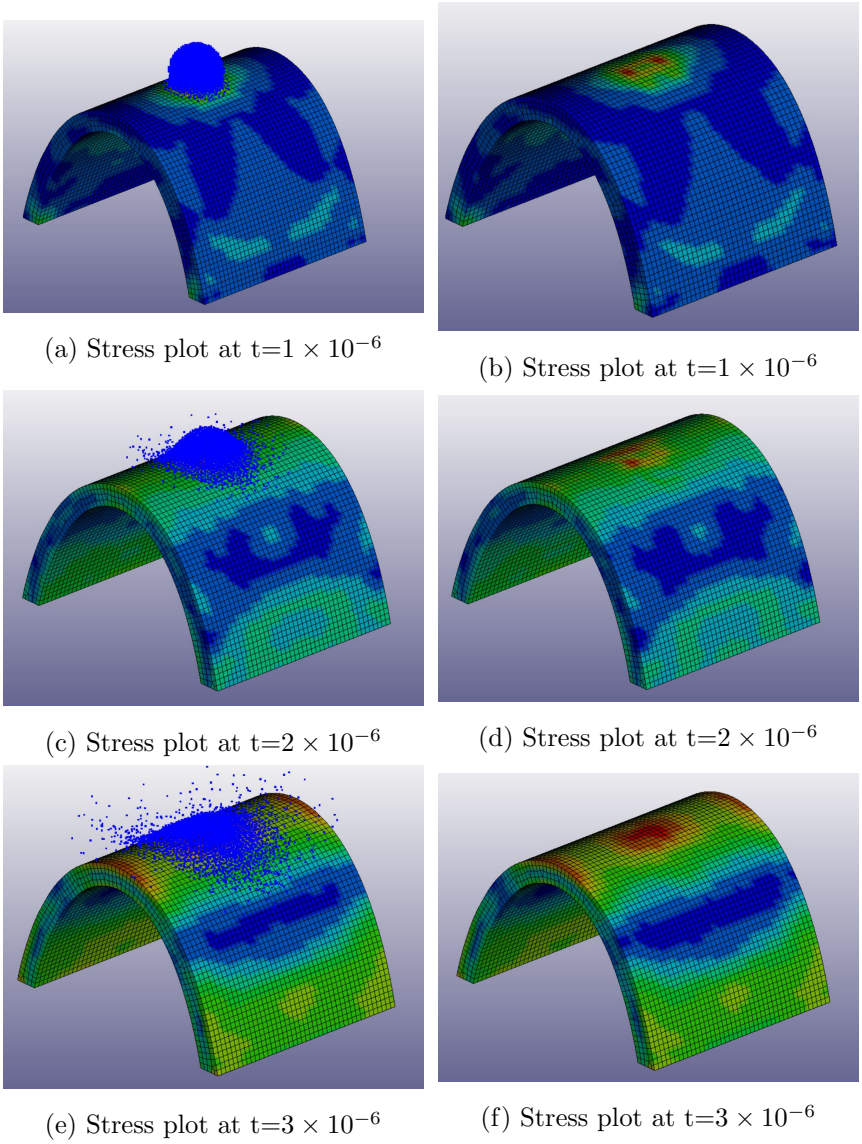

(a) Stress plot at t=1 $\times$ 10^{-6}

(b) Stress plot at t=1 $\times$ 10^{-6}

(c) Stress plot at t=2 $\times$ 10^{-6}

(d) Stress plot at t=2 $\times$ 10^{-6}

(e) Stress plot at t=3 $\times$ 10^{-6}

(f) Stress plot at t=3 $\times$ 10^{-6}

Figure 124: Progression of stress plots for curved model with and without droplet

H XCT Depth Measurements

H.1 Sample A10

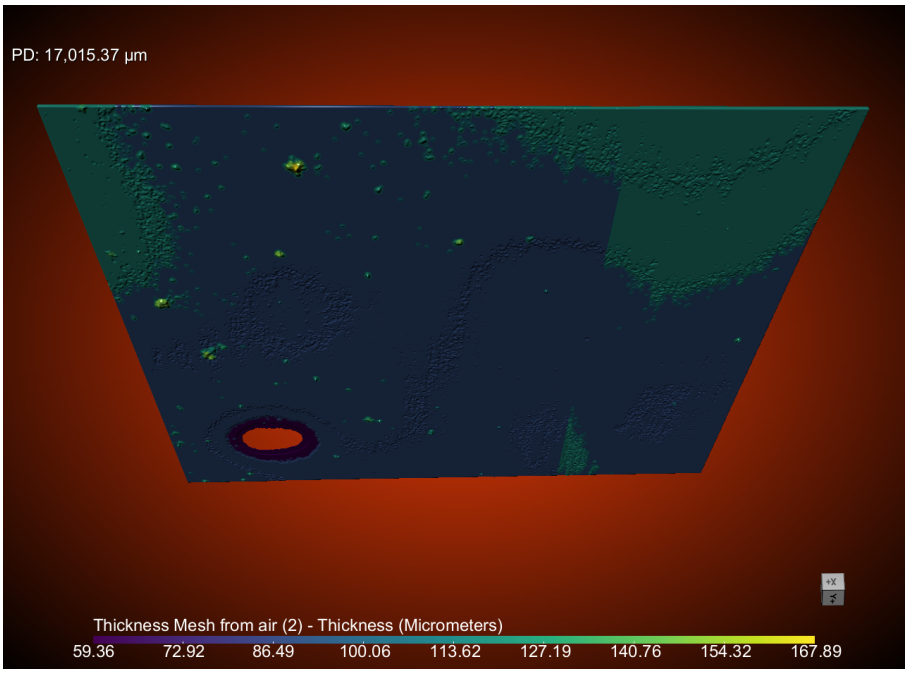

Figure 125: Depth measurements using the XCT apparatus of sample A010 at Stage 2 erosion

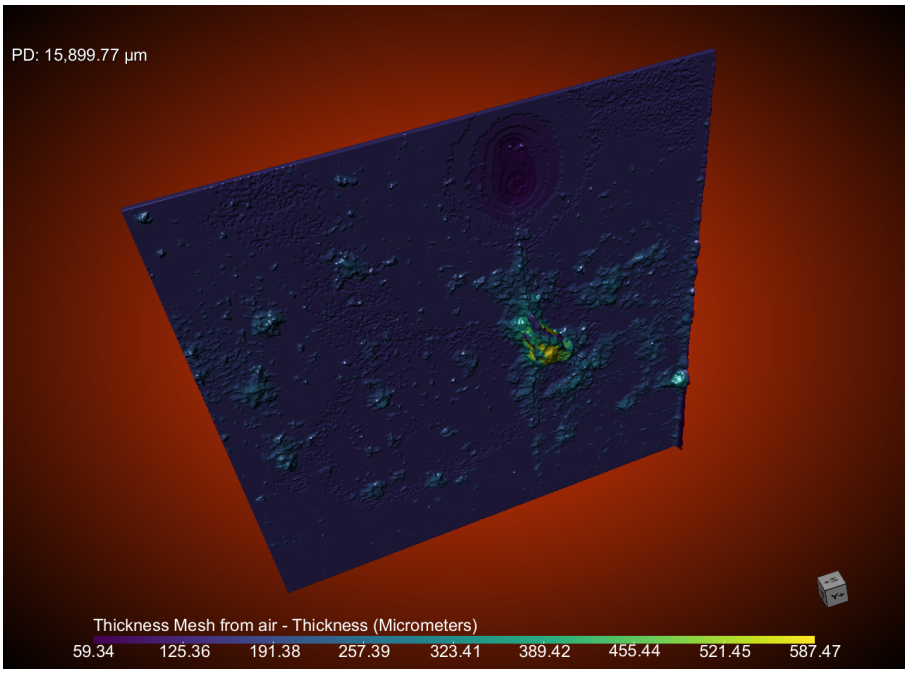

Figure 126: Depth measurements using the XCT apparatus of sample A010 at Stage 3 erosion

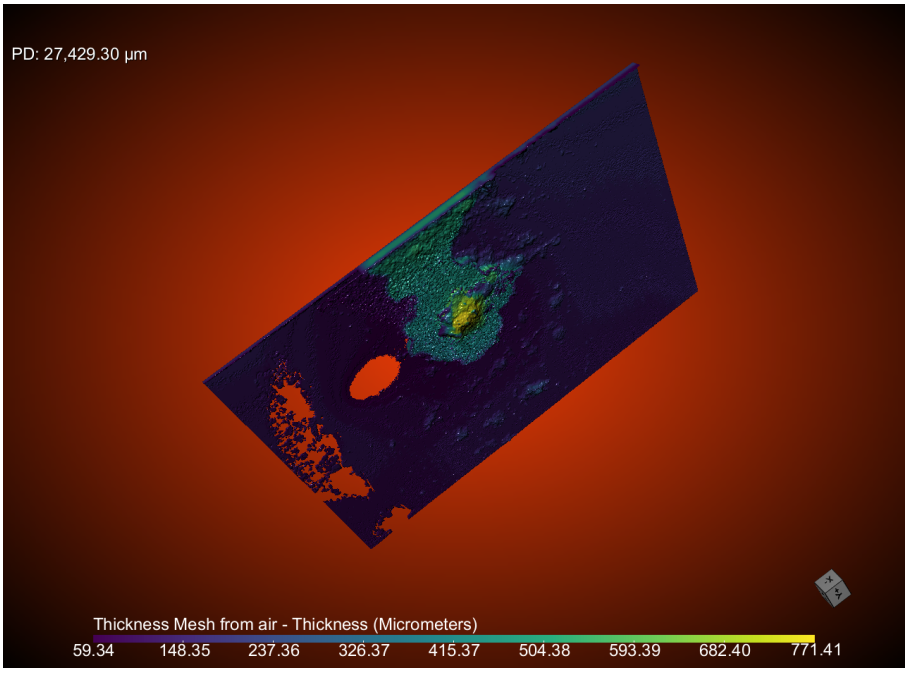

Figure 127: Depth measurements using the XCT apparatus of sample A010 at Stage 4 erosion

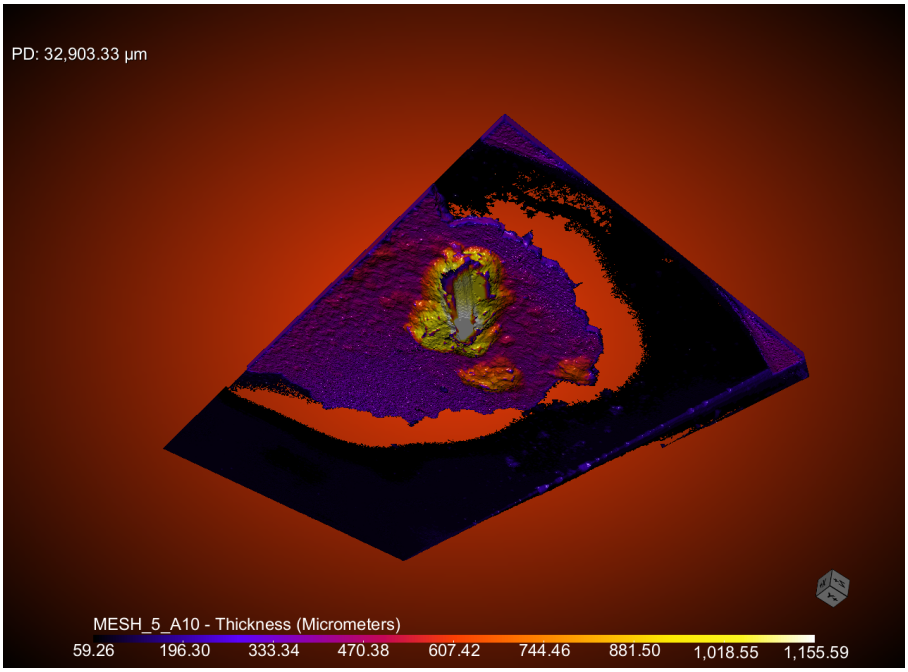

Figure 128: Depth measurements using the XCT apparatus of sample A010 at Stage 5 erosion

H.2 Sample A30

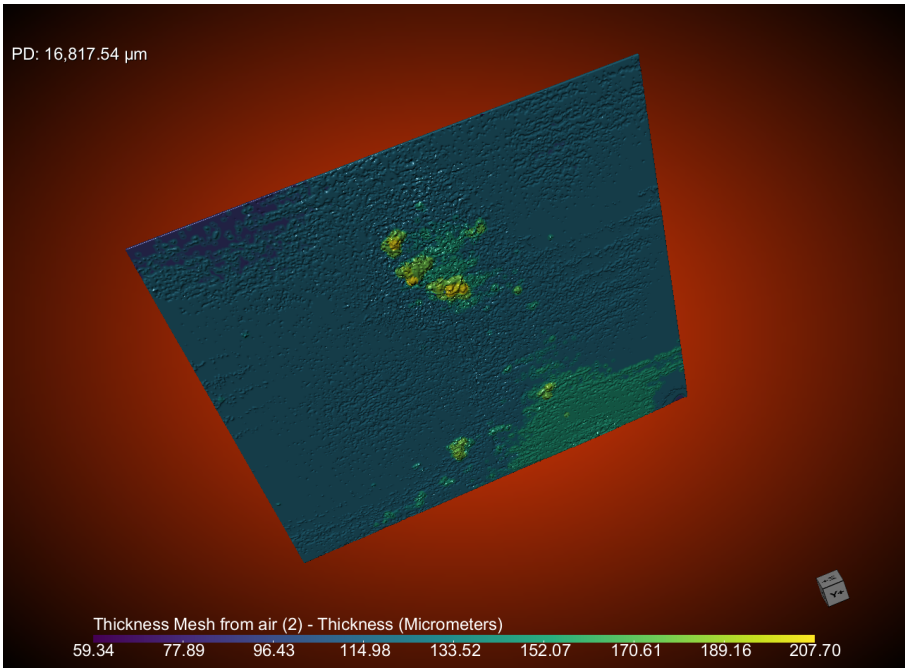

Figure 129: Depth measurements using the XCT apparatus of sample A030 at Stage 2 erosion

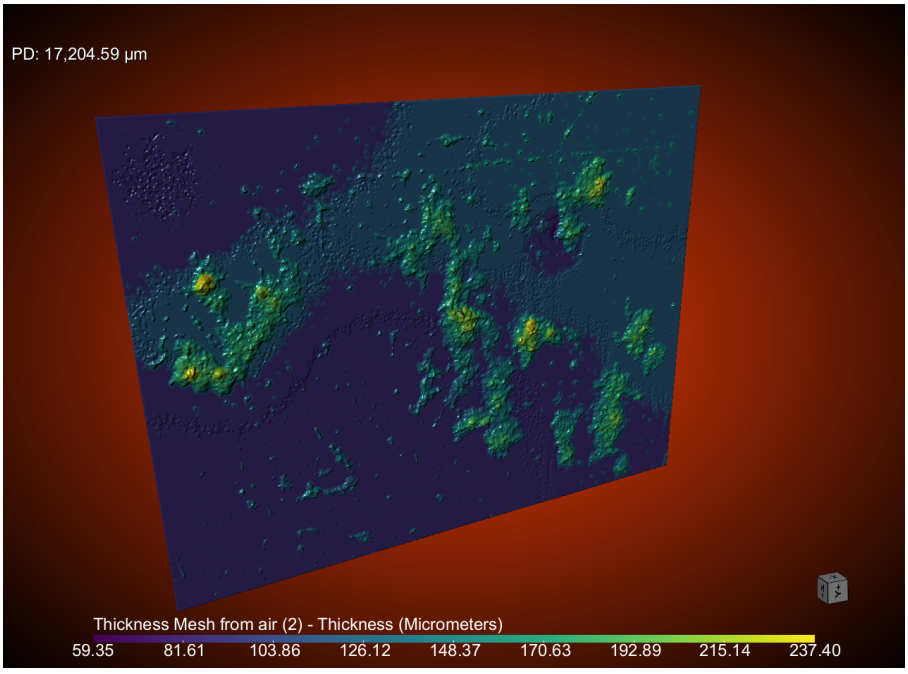

Figure 130: Depth measurements using the XCT apparatus of sample A030 at Stage 3 erosion

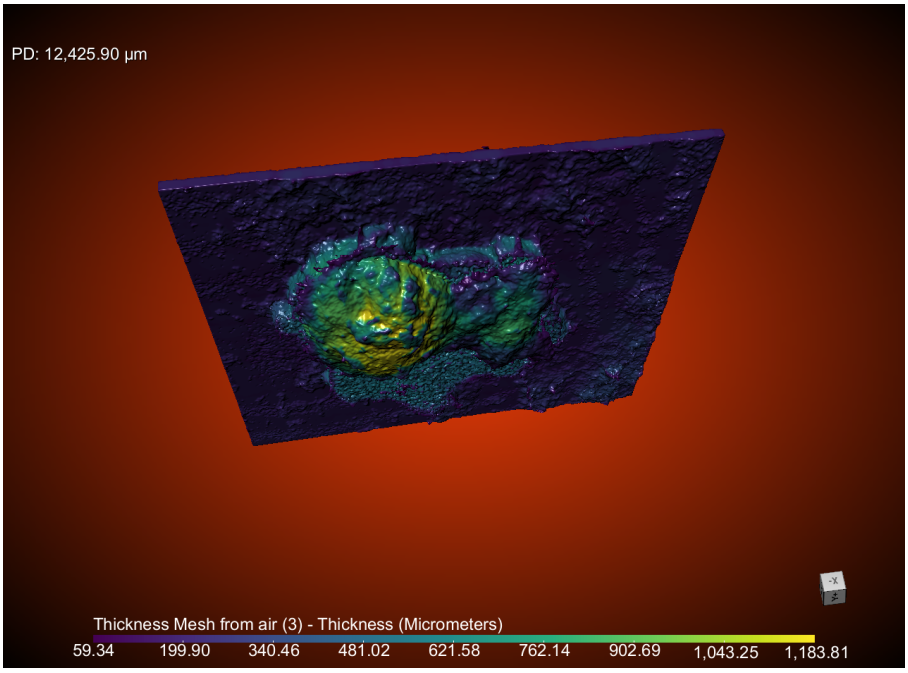

Figure 131: Depth measurements using the XCT apparatus of sample A030 at Stage 4 erosion

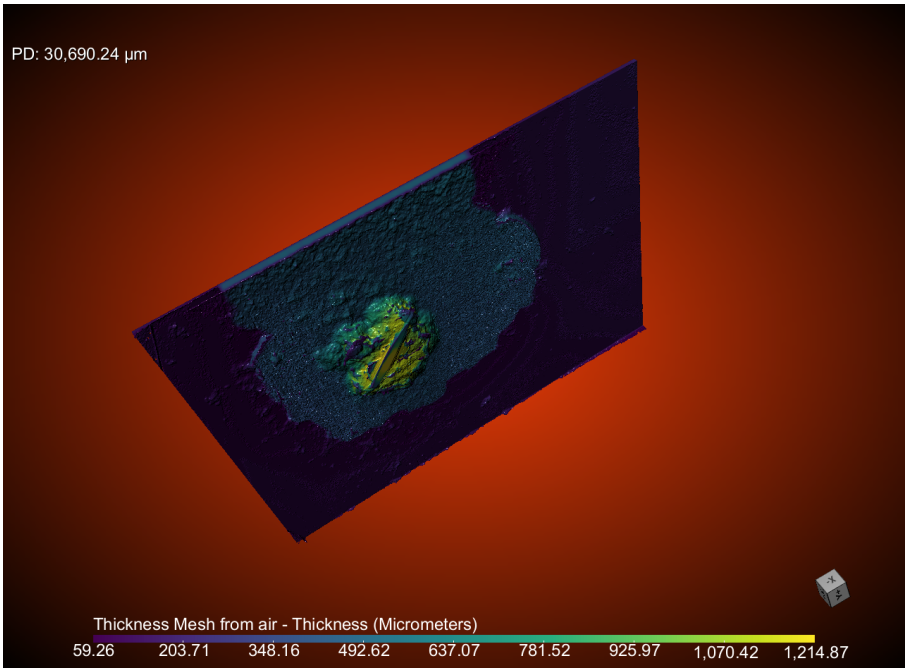

Figure 132: Depth measurements using the XCT apparatus of sample A030 at Stage 5 erosion

H.3 Sample A35

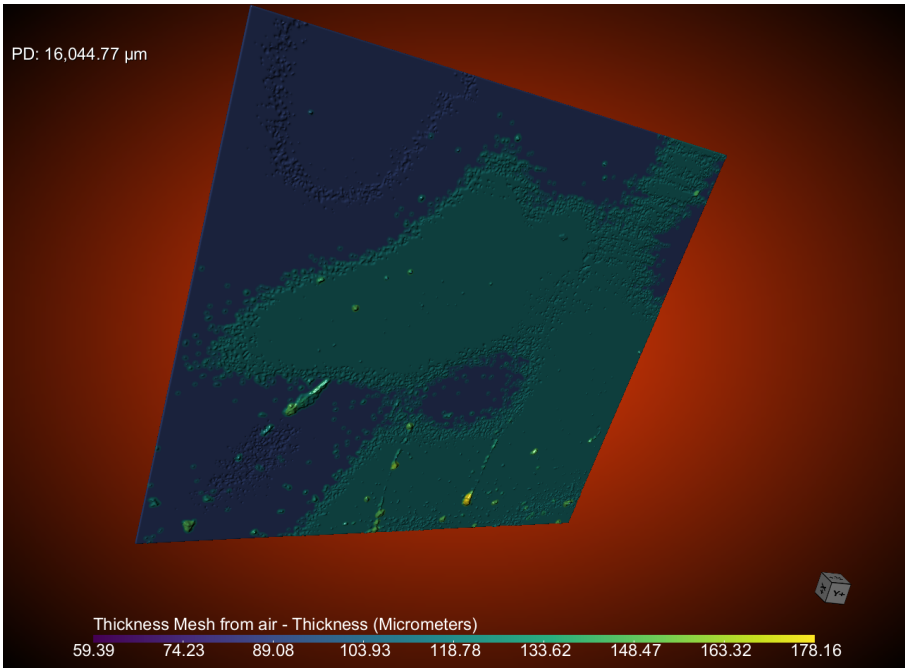

Figure 133: Depth measurements using the XCT apparatus of sample A035 at Stage 2 erosion

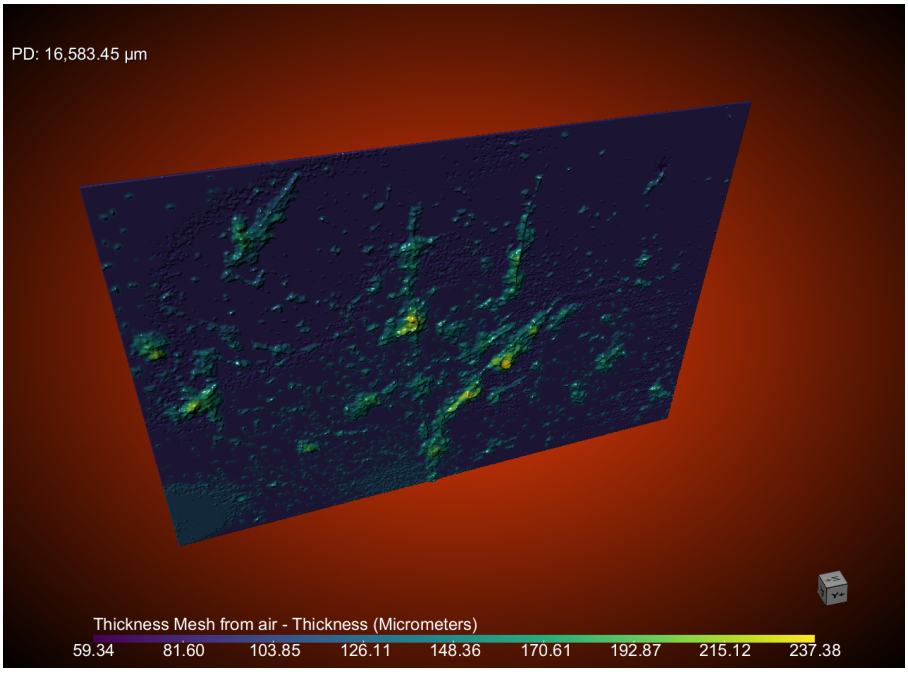

Figure 134: Depth measurements using the XCT apparatus of sample A035 at Stage 3 erosion

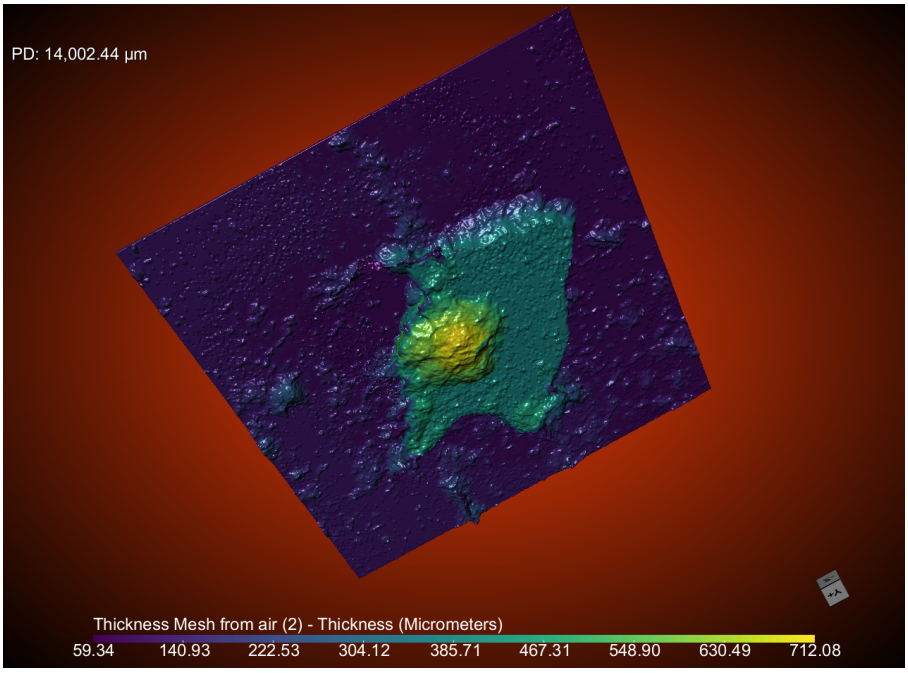

Figure 135: Depth measurements using the XCT apparatus of sample A035 at Stage 4 erosion

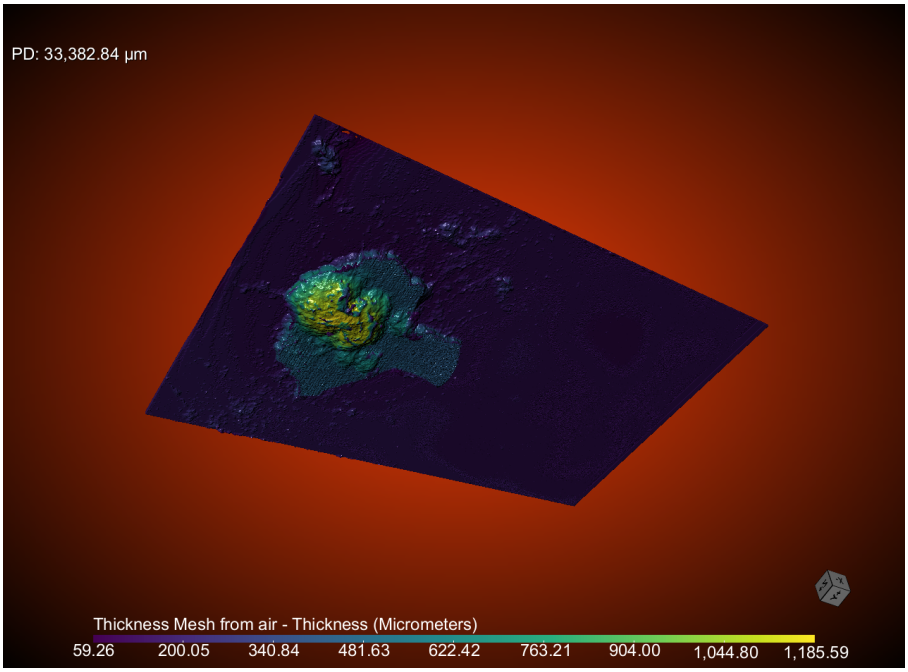

Figure 136: Depth measurements using the XCT apparatus of sample A035 at Stage 5 erosion

H.4 Sample A38

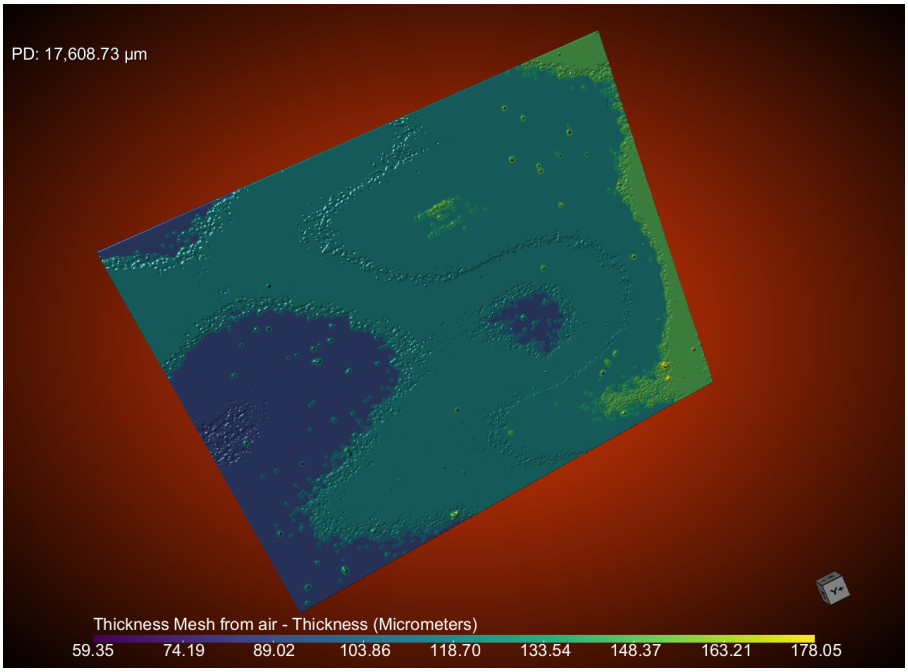

Figure 137: Depth measurements using the XCT apparatus of sample A038 at Stage 2 erosion

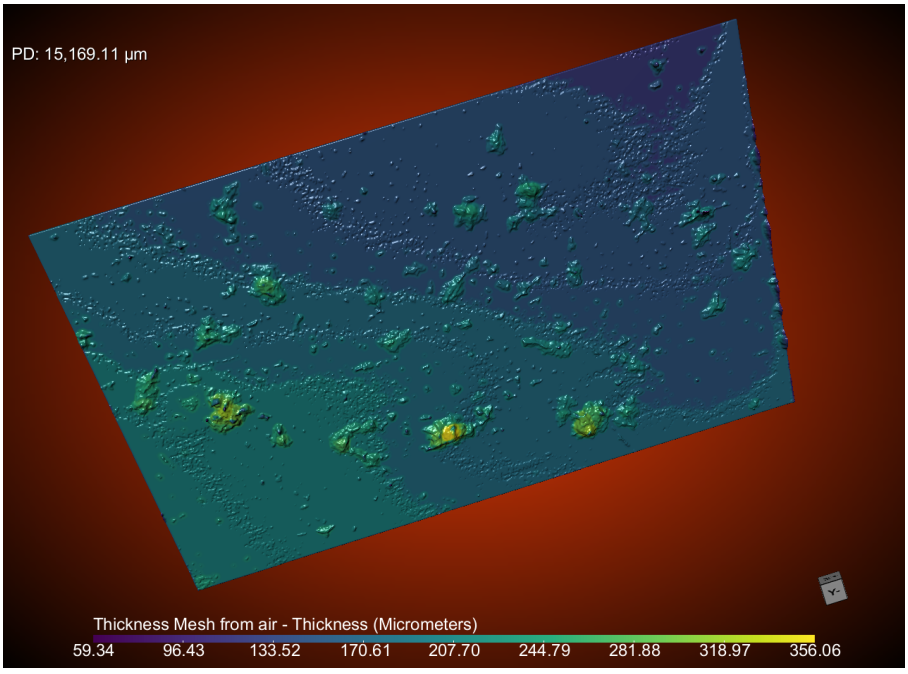

Figure 138: Depth measurements using the XCT apparatus of sample A038 at Stage 3 erosion

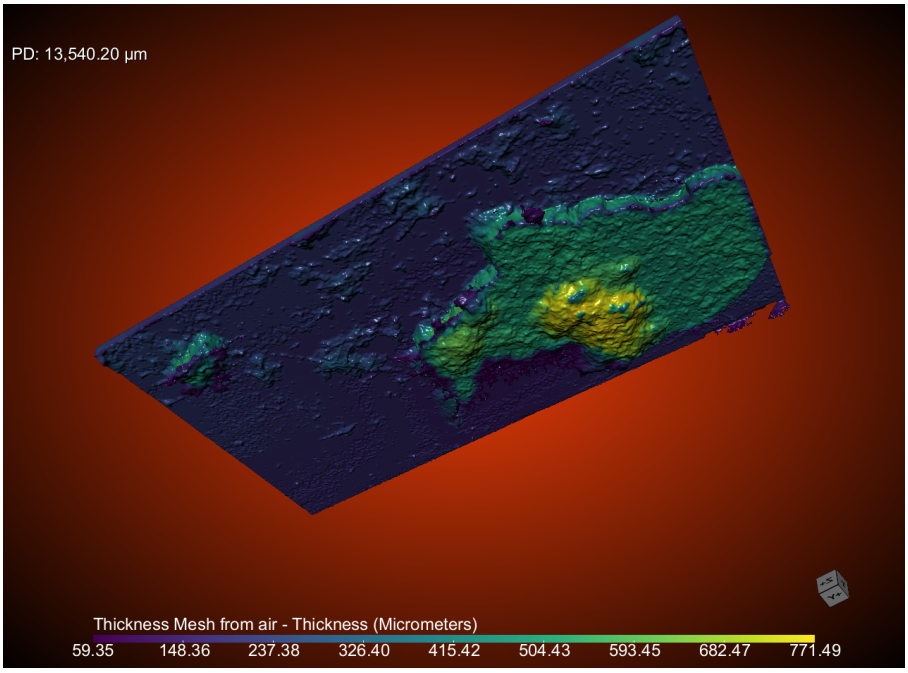

Figure 139: Depth measurements using the XCT apparatus of sample A038 at Stage 4 erosion